NATO Science for Peace and Security Series - B:
Physics and Biophysics

Low-Dimensional Functional Materials

Edited by
Reinhold Egger
Davron Matrasulov
Khamdam Rakhimov

Springer

NATO OTAN

This publication is supported by:

The NATO Science for Peace and Security Programme

Low-Dimensional Functional Materials

NATO Science for Peace and Security Series

This Series presents the results of scientific meetings supported under the NATO Programme: Science for Peace and Security (SPS).

The NATO SPS Programme supports meetings in the following Key Priority areas: (1) Defence Against Terrorism; (2) Countering other Threats to Security and (3) NATO, Partner and Mediterranean Dialogue Country Priorities. The types of meeting supported are generally "Advanced Study Institutes" and "Advanced Research Workshops". The NATO SPS Series collects together the results of these meetings. The meetings are co-organized by scientists from NATO countries and scientists from NATO's "Partner" or "Mediterranean Dialogue" countries. The observations and recommendations made at the meetings, as well as the contents of the volumes in the Series, reflect those of participants and contributors only; they should not necessarily be regarded as reflecting NATO views or policy.

Advanced Study Institutes (ASI) are high-level tutorial courses to convey the latest developments in a subject to an advanced-level audience

Advanced Research Workshops (ARW) are expert meetings where an intense but informal exchange of views at the frontiers of a subject aims at identifying directions for future action

Following a transformation of the programme in 2006 the Series has been re-named and re-organised. Recent volumes on topics not related to security, which result from meetings supported under the programme earlier, may be found in the NATO Science Series.

The Series is published by IOS Press, Amsterdam, and Springer, Dordrecht, in conjunction with the NATO Emerging Security Challenges Division.

Sub-Series

A.	Chemistry and Biology	Springer
B.	Physics and Biophysics	Springer
C.	Environmental Security	Springer
D.	Information and Communication Security	IOS Press
E.	Human and Societal Dynamics	IOS Press

http://www.nato.int/science
http://www.springer.com
http://www.iospress.nl

Series B: Physics and Biophysics

Low-Dimensional Functional Materials

edited by

Reinhold Egger
Institut für Theoretische Physik
Heinrich-Heine-Universität, Düsseldorf, Germany

Davron Matrasulov
Department of Energy, Laboratory for Advanced Studies
Turin Polytechnic University in Tashkent, Tashkent, Uzbekistan

and

Khamdam Rakhimov
Department of Physics
National University of Uzbekistan, Tashkent, Uzbekistan

Published in Cooperation with NATO Emerging Security Challenges Division

Proceedings of the NATO Advanced Research Workshop on
Recent Trends in Energy Security (with Special Emphasis on Low-Dimensional Functional Materials)
Tashkent, Uzbekistan
15–19 October 2012

Library of Congress Control Number: 2013940537

ISBN 978-94-007-6666-2 (PB)
ISBN 978-94-007-6617-4 (HB)
ISBN 978-94-007-6618-1 (e-book)
DOI 10.1007/978-94-007-6618-1

Published by Springer,
P.O. Box 17, 3300 AA Dordrecht, The Netherlands.

www.springer.com

Printed on acid-free paper

Preface

This book presents proceedings of the NATO Advanced Research Wokshop "Recent Trends in Energy Security: With Special Emphasis on Low-Dimensional Functional Materials" held in Tashkent, October 15–19, 2012. The objective of the conference was to discuss recent advances, problems and prospects in the physics of low-dimensional nanoscale materials from the viewpoint of their practical application in energy and resource saving. Currently such materials are being considered to play key role in the development of contemporary nanotechnology. The workshop brought together experts working on different issues of nanoscale physics such as quantum transport, organic photovoltaics, hydrogen storage, carbon nanostructures, superconductivity and others. Talks presented by the speakers were concentrated on photovoltaic elements on the basis of low-dimensional materials, graphene, CNT, fullerene, particle and heat transport in low-dimensional nanoscale systems, thermoelectric effect on low-dimensional materials, quantum networks and hydrogen in low-dimensional materials. Special focus was brought to practical applications of low-dimensional functional materials in renewable energy, energy conversion and storage. Total 55 talks were presented by senior and young speakers as 35- and 15-min long and short talks, respectively.

Broad audience of experimental and theoretical physicists was attracted by extensive panel discussions which were very helpful for deeper understanding of different issues of the physics of low-dimensional functional materials. Concluding remarks have been presented to some of the speakers at the end of Workshop.

The Workshop has been efficiently and successfully organized due to the local organizing committee with members T. Muminov, A.A. Saidov, K. Sharipov, K. Nakamura, B. Eshchanov, J. Yusupov, D. Otajanov, B. Umrzakov and B. Oksengendler. A group of young researchers and students from Turin Polytechnic University in Tashkent and National University of Uzbekistan assisted for several important organizational matters.

In addition, we would like to thank Jambul Yusupov, Doniyor Babajanov and Davran Otajanov for their valuable assistance in preparing this proceedings. Also, our special thanks go to Olga Karpova for her great help with the secretarial duties, before, during and after the conference.

Finally, we wish to thank NATO Science for Peace and Security Program for the financial support, Applied Physics Institute, Physical Society of Uzbekistan and Turin Polytechnic University in Tashkent for additional funding and organizational support.

Düsseldorf, Germany — *Reinhold Egger*
Tashkent, Uzbekistan — *Davron Matrasulov*
January, 2013 — *Khamdam Rakhimov*

Contents

Contributors

Bakhodir Abdullaev Institute of Applied Physics, National University of Uzbekistan, Tashkent, Uzbekistan

Boris Abdurakhmanov Institute of Ion-Plasma and Laser Technologies, Uzbek Academy of Sciences, Tashkent, Uzbekistan

Khatam Ashurov Institute of Ion-Plasma and Laser Technologies, Uzbek Academy of Sciences, Tashkent, Uzbekistan

Atabek E. Atamuratov Department of Physics, Urganch State University, Urganch, Uzbekistan

Zuhra Atamuratova Department of Physics, Urganch State University, Urganch, Uzbekistan

Donyor Babajanov Department of Energy, Turin Polytechnic University in Tashkent, Tashkent, Uzbekistan

Szymon Bauch Institute of Physics, Polish Academy of Sciences, Warszawa, Poland

Bernd Braunecker Departamento de Física Teórica de la Materia Condensada, Universidad Autónoma de Madrid, Madrid, Spain

Luis Brey Instituto de Ciencia de Materiales de Madrid (CSIC) Cantoblanco, Madrid, Spain

Tina Brower Nanostructures Laboratory, Howard University, Washington, DC, USA

Andrey Chaves Departamento de Física, Universidade Federal do Ceará, Fortaleza-CE, Brazil

Alexander Cook Deptartment of Physics, University of Texas at Dallas, USA

Alessandro De Martino Department of Mathematical Science, City University London, London, UK

Flyra Djurabekova Institute of Ion-Plasma and Laser Technologies, Uzbek Academy of Sciences, Tashkent, Uzbekistan

Reinhold Egger Institut für Theoretische Physik, Heinrich-Heine-Universit, Düsseldorf, Germany

Valijon Eshniyozov Physics Department, National University of Uzbekistan, Tashkent, Uzbekistan

Gil de Aquino Farias Departamento de Física, Universidade Federal do Ceará, Fortaleza-CE, Brazil

Tatsuya Fujii Institute for Solid State Physics, University of Tokyo, Kashiwa, Chiba, Japan

Ralf Granzner Department of Solid-State Electronics, Institute of Micro- and Nanotechnologies, Ilmenau University of Technology, Ilmenau, Germany

Mahkam Halillaev Department of Physics, Urganch State University, Urganch, Uzbekistan

Antonio Hill Institut für Physik, Universität Augsburg, Augsburg, Germany

Jongbae Hong Department of Physics, Pohang University of Science and Technology, Pohang, Gyeongbuk, Korea

Asia Pacific Center for Theoretical Physics, Pohang, Gyeongbuk, Korea

Tito Huber Nanostructures Laboratory, Howard University,Washington, DC, USA

Oleh Hul Institute of Physics, Polish Academy of Sciences, Warszawa, Poland

Artur Hütten Institut für Theoretische Physik, Heinrich-Heine-Universität, Düsseldorf, Germany

Roland Hützen Institut für Theoretische Physik, Heinrich-Heine-Universität, Düsseldorf, Germany

Inomjon Ibragimov Department of Energy, Turin Polytechnic University in Tashkent, Tashkent, Uzbekistan

Valentin Irkhin Institute of Metal Physics, Ekaterinburg, Russia

Scott Johnson Department of Physical Sciences and Engineering, Prince George's Community College, USA

Bekir Kandemir Faculty of Sciences, Department of Physics, Ankara University, Tandoğan, Ankara, Turkey

Mario Kittler Department of Solid-State Electronics, Institute of Micro- and Nanotechnologies, Ilmenau University of Technology, Ilmenau, Germany

Andreas Knorr Institut für Theoretische Physik, Nichtlineare Optik und Quantenelektronik, Technische Universität Berlin, Berlin, Germany

Leonid Konopko Institute of Applied Physics, Academy of Sciences of Moldova, Chisinau, Moldova

Sherzod Kuchkanov Institute of Ion-Plasma and Laser Technologies, Uzbek Academy of Sciences, Tashkent, Uzbekistan

Marek Kuś Center for Theoretical Physics, Polish Academy of Sciences, Warszawa, Poland

Michał Ławniczak Institute of Physics, Polish Academy of Sciences, Warszawa, Poland

Alfredo Levy Yeyati Departamento de Física Teórica de la Materia Condensada, Universidad Autónoma de Madrid, Madrid, Spain

Sergey Maksimov Institute of Ion-Plasma and Laser Technologies, Uzbek Academy of Sciences, Tashkent, Uzbekistan

Ermin Malić Institut für Theoretische Physik, Nichtlineare Optik und Quantenelektronik, Technische Universität Berlin, Berlin, Germany

Murad Marasulov Polymer Physics Institute, Uzbek Academy of Sciences, Uzbekistan

Davron Matrasulov Department of Energy, Laboratory for Advanced Studies, Turin Polytechnic University in Tashkent, Tashkent, Uzbekistan

Kamil Mielczarek Deptartment of Physics, University of Texas at Dallas, USA

Alexander Morozkin Department of Physics, Lomonosov Moscow State University, Len Gory, Moscow, Russia

Vladimir Nikiforov Department of Physics, Lomonosov Moscow State University, Len Gory, Moscow, Russia

Albina Nikolaeva Institute of Applied Physics, Academy of Sciences of Moldova, Chisinau, Moldova

Sardor Nuraliev Polymer Physics Institute, Uzbek Academy of Sciences, Uzbekistan

Akira Oguri Department of Physics, Osaka City University, Sumiyoshiku, Osaka, Japan

Boris Oksengendler Polymer Physics Institute, Uzbek Academy of Sciences, Uzbekistan

Tomi Paananen Faculty of Physics, Universitat Bielefeld, Finanzbuchhaltung, Bielefeld, Germany

Khamdam Rakhimov Department of Physics, National University of Uzbekistan, Tashkent, Uzbekistan

Karimjon Sabirov Department of Physics, National University of Uzbekistan, Tashkent, Uzbekistan

Zarif Sabirov Department of Energy, Turin Polytechnic University in Tashkent, Tashkent, Uzbekistan

Rui Sakano Institute for Solid State Physics, University of Tokyo, Kashiwa, Chiba, Japan

Reum Scott Nanostructures Laboratory, Howard University, Washington, DC, USA

Frank Schwierz Department of Solid-State Electronics, Institute of Micro- and Nanotechnologies, Ilmenau University of Technology, Ilmenau, Germany

Leszek Sirko Institute of Physics, Polish Academy of Sciences, Warszawa, Poland

Adam Sawicki Center for Theoretical Physics, Polish Academy of Sciences, Warszawa, Poland

Nigora Turaeva Department of Biology, Webster University, Louis, MO, USA

Torben Winzer Institut für Theoretische Physik, Nichtlineare Optik und Quantenelektronik, Technische Universität Berlin, Berlin, Germany

Jambul Yusupov Department of Energy, Turin Polytechnic University in Tashkent, Tashkent, Uzbekistan

Anvar Zakhidov Deptartment of Physics, University of Texas at Dallas, Richardson, TX, USA

Alex Zazunov Institut für Theoretische Physik, Heinrich-Heine-Universit, Düsseldorf, Germany

Klaus Ziegler Institut für Physik, Universität Augsburg, Augsburg, Germany

Chapter 1
On the Finite-Size Excitonic Instability in Interacting Graphene Quantum Dots

Tomi Paananen and Reinhold Egger

Abstract Using Hartree-Fock simulations, exact diagonalization and perturbative calculations, we study ground-state properties of clean circular quantum dots formed in a graphene monolayer. With chemical potential at the neutrality point, we study $N \leq 15$ interacting particles, where the fine structure constant α parametrizes the Coulomb interaction. We explore Sucher's positive projection ("no-pair") approach, a more general Hamiltonian conserving both N and the number of additional electron-hole pairs, and the full QED problem, where only N is conserved. We find electron-hole pair production for $\alpha > 1$, where the filled Dirac sea is reconstructed and a finite-size excitonic instability occurs. We also address the case of an orbital magnetic field.

1.1 Introduction

Coulomb interaction effects in monolayer graphene [1, 2] are nowadays attracting much interest, see Ref. [3] for a detailed review, primarily motivated by the possibility of realizing a strong-coupling version of QED in a readily accessible two-dimensional (2D) system. In fact, the (bare) fine structure constant is rather large, $\alpha = e^2/(\hbar\kappa v_F) \simeq 2.2/\kappa$, with the effective substrate dielectric constant κ and the Fermi velocity $v_F \approx c/300 \approx 10^6$ m/s. Retardation effects are irrelevant here, i.e., we effectively have 2D massless Dirac fermions interacting via the Coulomb potential. Similar physics can be expected for the surface state in 3D topological

T. Paananen
Faculty of Physics, Universitat Bielefeld, Finanzbuchhaltung, Postfach 101133, 33511 Bielefeld, Germany

R. Egger (✉)
Institut für Theoretische Physik, Heinrich-Heine-Universit, D-40225 Düsseldorf, Germany
e-mail: egger@thphy.uni-duesseldorf.de

R. Egger et al. (eds.), *Low-Dimensional Functional Materials*, NATO Science for Peace and Security Series B: Physics and Biophysics, DOI 10.1007/978-94-007-6618-1_1,

insulators [4], but interactions are expected to be much weaker due to the large κ in the relevant materials.

In graphene, the situation away from the Dirac point (defined as zero of energy) can be reasonably well understood in terms of Fermi liquid theory [3, 5] but the picture is more complicated near the Dirac point. At a critical interaction strength α_c, a semimetal-insulator transition is theoretically expected [6] due to electron-hole proliferation. For $\alpha > \alpha_c$, a finite gap corresponding to an excitonic insulator is formed and the ground state undergoes reconstruction. On the other hand, quantum critical behavior is expected [7,8] as a precursor of the instability for $\alpha < \alpha_c$. Recent lattice quantum Monte Carlo simulations [9] found the critical value $\alpha_c \approx 1.1$ for an infinitely extended ("bulk") graphene monolayer. Similar values were also obtained analytically from the dynamical polarization function approach [10] and under the ladder approximation to the Bethe-Salpeter equation [11]. However, so far no experimental signature of this *excitonic instability* has been reported.

It has also been recognized that the excitonic instability for the bulk many-body problem is related to the simpler "supercritical" instability of the hydrogen problem in graphene [3], where α corresponds to the (attractive) potential strength of the nucleus. Above a critical value for α, the nucleus captures an electron to screen its positive charge below criticality, while at the same time a hole escapes to infinity in order to maintain charge neutrality. In atomic physics, essentially the same phenomenon should also take place for superheavy atoms [12]. The creation of an electron-hole pair thus also accompanies the supercritical instability. In the presence of an homogeneous orbital magnetic field B, the hole escape process is disturbed by the formation of closed Landau orbits. For the bulk many-body problem, the resulting magnetic catalysis phenomenon [13] implies a lowering of α_c with increasing B.

We have recently studied [14] a finite-size version of the excitonic instability realizable in graphene quantum dots. The present article gives a summary of (some of) our results. Quantum dots in conventional 2D systems have been studied extensively [15,16], and experimental results for lithographically prepared graphene dots were reported recently [17–21]. Within the single-particle picture, theoretical proposals on how to model such a dot have been reviewed in Ref. [2]. We here adopt the probably simplest route by imposing the so-called "infinite-mass boundary condition" [22, 23] where no current is allowed to flow through the circle $r = R$ defining the dot's boundary. While disorder limits the quality of the boundary in existing dots [21], such a boundary condition captures at least their qualitative physics. Moreover, future experimental progress is likely to yield well-defined boundaries.

We investigate the ground state of N interacting electrons in a closed circular graphene dot, where N particles are added on top of the filled Dirac sea, i.e., relative to the chemical potential $\mu = 0$. This problem has been studied before within the Hartree-Fock (HF) approach [24–27]. However, when going beyond effective single-particle theory, one has to deal with the "Brown-Ravenhall disease" [28, 29], i.e., the possibility to excite electron-hole pairs with small energy by combining a hole and an electron both very far away from the Fermi surface.

While such processes are physically suppressed by the finite bandwidth, the infinitely deep filled Dirac sea present in the Dirac theory renders naive approaches mathematically ill-defined. For $\alpha \ll 1$ and when a gap separates electron and hole states, Sucher [29] showed that one can circumvent the Brown-Ravenhall problem by a suitable projection Λ_+ of the basic QED Hamiltonian H to a well-defined no-pair Hamiltonian $H_+ = \Lambda_+ H \Lambda_+$, where the filled Dirac sea is effectively treated as completely inert. The projection operator Λ_+ eliminates negative-energy (hole) states from the single-particle Hilbert space.

We here study the validity of the no-pair approach for graphene dots and find that for $\alpha < 1$, it is indeed meaningful, see also Ref. [30]. On a quantitative level, however, it is accurate only for $\alpha \ll 1$. As also discussed by Sucher [29], if one wishes to go beyond the positive projection scheme, a QED approach is indicated. The QED Hamiltonian H, see Eq. (1.11) below, does not conserve the number N_{eh} of electron-hole pairs. In fact, only the particle number N – defined as the imbalance of electron and hole numbers – is conserved, and a superposition of states with different N_{eh} determines the ground state for strong interactions. Once electron-hole pairs proliferate, a reconstruction of the ground state takes place.

We encounter this phenomenon for $\alpha > 1$ in graphene dots, similar to the reported critical value [9] for the bulk excitonic instability. However, in our finite-size system this is a smooth crossover and not a phase transition. We stress that our "N-particle problem" defines N as the difference of electron and hole numbers, which allows for the excitation of an arbitrary number N_{eh} of electron-hole pairs. For $\alpha \to 0$, this definition reduces to having N electrons on top of the filled Dirac sea.

The structure of the remainder of this paper is as follows. In Sect. 1.2 we introduce the model and discuss the various theoretical approaches employed to find the ground state. An intermediate approach is to generalize the no-pair approach (where $N_{eh} = 0$) to allow for a fixed but finite number N_{eh} of electron-hole pairs. The Hamiltonian $H_{\rm fix}$ is obtained from H by neglecting all terms that do not conserve N_{eh}. A sufficient (but not necessary) condition for the breakdown of the no-pair Hamiltonian H_+ arises when the ground-state energy of $H_{\rm fix}$ is lowered for some $N_{eh} > 0$. We assess the validity of the no-pair scheme in Sect. 1.3 by comparing to results obtained under $H_{\rm fix}$ and from the QED Hamiltonian H. We perform these calculations using exact diagonalization (ED) for $N = 2$ and $N = 3$ particles in the dot. In Sect. 1.4, we use H_+ to carry out detailed HF calculations for up to $N = 15$ particles and relatively weak interactions, $\alpha \leq 1$. We present results for the addition energy as function of N. Finally, in Sect. 1.5 we provide a discussion of our main results.

1.2 Model and Theoretical Approaches

In this section, we describe the model employed in our study of the electronic properties of interacting graphene quantum dots. We will then turn to different theoretical approaches to obtain the ground-state properties.

1.2.1 Single-Particle Problem

It is well established that on low energy scales, quasiparticles in graphene are described by the Dirac Hamiltonian [2]

$$H_0 = v_F \boldsymbol{\sigma} \cdot \left(\mathbf{p} + \frac{e}{c}\mathbf{A} \right) + M(r)\sigma_z\tau_z - \mu_B \mathbf{s}\cdot\mathbf{B}, \tag{1.1}$$

where $\mathbf{p} = -i\hbar(\partial_x, \partial_y)^T$ and $-e$ is the electronic charge. The Pauli matrices $\boldsymbol{\sigma} = (\sigma_x, \sigma_y)$ and σ_z refer to graphene's sublattice structure, while the Pauli matrix τ_z corresponds to the valley degree of freedom, i.e., to the two K points. A static vector potential $\mathbf{A}(\mathbf{r})$ [with $\mathbf{r} = (x,y)^T$] allows for the inclusion of a constant orbital magnetic field B_z, where we choose the symmetric gauge, $\mathbf{A} = \frac{1}{2}B_z(-y,x)^T$. Since we neglect spin-orbit couplings in Eq. (1.1), spin Pauli matrices $\mathbf{s} = (s_x, s_y, s_z)$ only appear in the Zeeman term. With μ_B denoting Bohr's magneton and putting the Landé factor to $g_e = 2$ [21], this term couples to the full (homogeneous) magnetic field, $\mathbf{B} = (B_x, B_y, B_z)$ with $B = |\mathbf{B}|$.

Switching to polar coordinates (r,ϕ), we consider a clean circular quantum dot in a graphene monolayer modelled by the well-known infinite-mass boundary condition [22] where the mass $M(r)$ in Eq. (1.1) is zero for $r < R$ but tends to $+\infty$ for $r > R$. This choice ensures that no current flows through the boundary at $r = R$. Eigenstates can be classified by the conserved total angular momentum, $J_z = -i\hbar\partial_\phi + \hbar\sigma_z/2$, with eigenvalue $\hbar j$ for half-integer $j = m + 1/2$ (with integer m).

While the eigenfunctions can be found in analytical form even in the presence of the magnetic field [23], the Coulomb interaction matrix elements are readily available [27] only in the $B = 0$ basis. We therefore first describe the solution for $B = 0$ and later include the homogeneous magnetic field. Note that different valleys ($\tau = \pm$) are decoupled and spin ($s = \pm$) then simply yields a twofold degeneracy. For given (m, τ, s), we first discuss the $E > 0$ solutions to $H_0\Phi^{(+)} = E\Phi^{(+)}$, where the spinor has the sublattice structure

$$\Phi^{(+)}(r,\phi) = e^{im\phi} \begin{pmatrix} \psi_{1,m}(r) \\ ie^{i\phi}\psi_{2,m}(r) \end{pmatrix}. \tag{1.2}$$

The infinite-mass boundary condition implies [22, 23]

$$\psi_{1,m}(R) = \tau\psi_{2,m}(R). \tag{1.3}$$

With the Bessel functions $J_m(kr)$ of the first kind, $k = E/\hbar v_F$, and normalization constant A, the Dirac equation for $r < R$ is solved by the *Ansatz*

$$\psi_{1,m}(r) = AJ_m(kr), \quad \psi_{2,m} = AJ_{m+1}(kr).$$

The quantization condition (1.3) then determines the eigenenergies $E_a > 0$ with $a \equiv (n, m, \tau, s)$,

$$J_m(E_a/\Delta_0) = \tau J_{m+1}(E_a/\Delta_0), \tag{1.4}$$

where $\Delta_0 \equiv \hbar v_F/R$ is the single-particle level spacing of the dot and $n = 1, 2, \ldots$ labels different solutions for given (m, τ, s). Equation (1.4) is easily solved numerically and the eigenstates to energy $E_a > 0$ are

$$\Phi_a^{(+)}(r, \phi) = A_a e^{im\phi} \begin{pmatrix} J_m(k_a r) \\ i e^{i\phi} J_{m+1}(k_a r) \end{pmatrix}, \tag{1.5}$$

where $k_a = E_a/\hbar v_F$ and the normalization factor is

$$A_a = [\pi(J_m^2 - J_{m-1}J_{m+1} + J_{m+1}^2 - J_m J_{m+2})]^{-1/2} \tag{1.6}$$

with $J_m \equiv J_m(E_a/\Delta_0)$.

Time-reversal invariance implies the Kramers degeneracy relation $E_{n,m,\tau,s} = E_{n,-m-1,-\tau,-s}$. Negative-energy (hole) solutions, $\Phi_{\tilde{a}}^{(-)}(r, \phi)$, follow by using the electron-hole symmetry property of the Hamiltonian, $E_{n,m,-\tau,s} = -E_{n,m,\tau,s}$. We use the multi-index $a(\tilde{a})$ to count states with positive (negative) energy. There is no zero-energy solution for $B = 0$, and we have a finite gap around the Dirac point.

Next we add the magnetic field. Expressed in terms of the eigenstates $\Phi_a^{(+)}$ and $\Phi_{\tilde{a}}^{(-)}$, the vector potential part in H_0 has a matrix structure diagonal both in the quantum numbers (m, τ, s) and the conduction/valence band index $\pm$, i.e., only different n states are mixed. By numerical diagonalization, it is straightforward to obtain the resulting eigenenergies $\tilde{E}_a > 0$ and $\tilde{E}_{\tilde{a}} < 0$, and the corresponding eigenstates. The indices n and thus a ($\tilde{a}$) are redefined to take into account the unitary transformation diagonalizing H_0.

Finally, we include the Zeeman term. Choosing the spin quantization axis along $\mathbf{B}$, where $s = \pm 1$ corresponds to spin-up or spin-down states, the full eigenenergy $E_a > 0$ is given by[1]

$$E_a = \tilde{E}_a - s\mu_B B, \tag{1.7}$$

and similary for $E_{\tilde{a}} < 0$. In a slight abuse of notation, E_a now denotes the full eigenenergy and not the solution to Eq. (1.4) anymore. The Zeeman term is generally quite small [2] but breaks the spin degeneracy of the levels, while the vector potential breaks the valley degeneracy, see Eq. (1.3). The resulting eigenstates are denoted by $\Phi_a^{(+)}(r, \phi)$ and $\Phi_{\tilde{a}}^{(-)}(r, \phi)$.

[1] In the HF calculations, it is sometimes advantageous to include a small mixing term in the single-particle Hamiltonian, $H_{\text{mix}} = \delta_K \tau_x + \delta_s s_x$. Inclusion of H_{mix} in the construction of the eigenenergies and -states is straightforward. This allows us to probe all spin and valley states in one run, and by careful extrapolation $\delta_K, \delta_s \to 0$, we can extract the ground state.

1.2.2 Many-Body Interactions

We now include the Coulomb interaction among the particles. The noninteracting reference problem is characterized by a filled Dirac sea ($\mu = 0$), i.e., all $E_{\tilde{a}} < 0$ states are filled. The QED Hamiltonian H describing this problem can be expressed in terms of electron annhilation operators, c_a, corresponding to the single-particle states $\boldsymbol{\Phi}_a^{(+)}$, and hole creation operators, $d_{\tilde{a}}^\dagger$, with single-particle states $\boldsymbol{\Phi}_{\tilde{a}}^{(-)}$. The full field operator is written as

$$\Psi(\mathbf{r}) = \sum_a \boldsymbol{\Phi}_a^{(+)}(\mathbf{r}) c_a + \sum_{\tilde{a}} \boldsymbol{\Phi}_{\tilde{a}}^{(-)}(\mathbf{r}) d_{\tilde{a}}^\dagger. \tag{1.8}$$

Since the Hamiltonian commutes with τ_z and $\mathbf{s}\cdot\mathbf{B}$, we can write $\Psi(\mathbf{r}) = \sum_{\tau s} \Psi_{\tau s}(\mathbf{r})$.

The Hamiltonian is then given by $H = H_k + H_I$, with the kinetic part (note that $E_{\tilde{a}} < 0$)

$$H_k = \sum_a E_a c_a^\dagger c_a + \sum_{\tilde{a}} |E_{\tilde{a}}| d_{\tilde{a}}^\dagger d_{\tilde{a}} \tag{1.9}$$

and the interaction term

$$H_I = \frac{\hbar v_F \alpha}{2} \sum_{\tau\tau' ss'} \int \frac{\mathrm{d}\mathbf{r}\mathrm{d}\mathbf{r}'}{|\mathbf{r}-\mathbf{r}'|} : \Psi_{\tau s}^\dagger(\mathbf{r}) \Psi_{\tau' s'}^\dagger(\mathbf{r}') \Psi_{\tau' s'}(\mathbf{r}') \Psi_{\tau s}(\mathbf{r}) :, \tag{1.10}$$

where the colons denote normal ordering.

Inserting the field operator expansion (1.8) into Eq. (1.10),

$$H = H_{\mathrm{fix}} + H'. \tag{1.11}$$

H_{fix} commutes separately with both the electron and the hole number operator, $\hat{N}_e = \sum_a c_a^\dagger c_a$ and $\hat{N}_h = \sum_{\tilde{a}} d_{\tilde{a}}^\dagger d_{\tilde{a}}$. The full Hamiltonian, however, only commutes with $\hat{N} = \hat{N}_e - \hat{N}_h$. We thus define the N-particle problem by having N excess electrons and $N_{eh} = N_h$ electron-hole pairs on top of the filled Dirac sea. Only N is conserved, while N_{eh} can fluctuate. Under H_{fix} alone, the number N_{eh} of electron-hole pairs is conserved,

$$\begin{aligned} H_{\mathrm{fix}} = H_k &+ \frac{1}{2} \sum_{aba'b'} \left(V_{abb'a'} - \delta_{ss'} V_{aba'b'} \right) c_a^\dagger c_b^\dagger c_{b'} c_{a'} \\ &+ \frac{1}{2} \sum_{\tilde{a}\tilde{b}\tilde{a}'\tilde{b}'} \left(V_{\tilde{a}\tilde{b}\tilde{b}'\tilde{a}'} - \delta_{ss'} V_{\tilde{a}\tilde{b}\tilde{a}'\tilde{b}'} \right) d_{\tilde{a}}^\dagger d_{\tilde{b}}^\dagger d_{\tilde{b}'} d_{\tilde{a}'} \\ &- \sum_{aa',\tilde{b}\tilde{b}'} \left(V_{a\tilde{b}\tilde{b}'a'} - \delta_{ss'} V_{a\tilde{b}a'\tilde{b}'} \right) c_a^\dagger d_{\tilde{b}}^\dagger d_{\tilde{b}'} c_{a'}. \end{aligned} \tag{1.12}$$

All terms not commuting with $\hat{N}_{e,h}$ are collected in the remaining part, $H' = h + h^\dagger$, with

$$\begin{aligned} h = & \frac{1}{2} \sum_{ab\tilde{a}'\tilde{b}'} \left(V_{ab\tilde{b}'\tilde{a}'} - \delta_{ss'} V_{ab\tilde{a}'\tilde{b}'} \right) c_a^\dagger c_b^\dagger d_{\tilde{b}'}^\dagger d_{\tilde{a}'}^\dagger \\ & + \frac{1}{2} \sum_{aa'\tilde{b}\tilde{b}'} \delta_{s,-s'} V_{a\tilde{b}\tilde{a}'b'} c_a^\dagger d_{\tilde{a}'}^\dagger d_{\tilde{b}} c_{b'} \\ & + \sum_{abb'\tilde{a}'} \left(V_{abb'\tilde{a}'} - \delta_{ss'} V_{bab'\tilde{a}'} \right) c_a^\dagger d_{\tilde{a}'}^\dagger c_b^\dagger c_{b'} \\ & - \sum_{a\tilde{a}'\tilde{b}\tilde{b}'} \left(V_{a\tilde{b}\tilde{b}'\tilde{a}'} - \delta_{ss'} V_{a\tilde{b}\tilde{a}'\tilde{b}'} \right) c_a^\dagger d_{\tilde{a}'}^\dagger d_{\tilde{b}'}^\dagger d_{\tilde{b}}. \end{aligned} \tag{1.13}$$

In Eqs. (1.12) and (1.13), the spin quantum numbers are given by $s = s_a = s_{a'}$ and $s' = s_b = s_{b'}$ (when hole states are involved, $a \to \tilde{a}$ etc.). These spin selection rules are encoded in the interaction matrix elements $V_{aa'b'b}$ which have been derived in a form useful for numerical evaluation in Ref. [26]. We quote them for the convenience of the reader next.

A finite matrix element follows only when the valley selection rule, $\tau_a = \tau_{a'}$ and $\tau_b = \tau_{b'}$, and angular momentum conservation, $m_a + m_{a'} = m_b + m_{b'}$, are satisfied. When all selection rules are met,

$$\begin{aligned} V_{aa'b'b} = & (4\pi)^2 \alpha \Delta_0 A_a A_{a'} A_{b'} A_b \sum_{l=0}^{\infty} C_{q,l} \\ & \times \int_0^1 \mathrm{d}r\, r^{-l} \left(J_{m_a}(E_a r) J_{m_b}(E_b r) + J_{m_a+1}(E_a r) J_{m_b+1}(E_b r) \right) \\ & \times \int_0^r \mathrm{d}r'\, (r')^{l+1} \left(J_{m_{a'}}(E_{a'} r') J_{m_{b'}}(E_{b'} r') + J_{m_{a'}+1}(E_{a'} r') J_{m_{b'}+1}(E_{b'} r') \right), \end{aligned}$$

with E_a in units of $\Delta_0 = \hbar v_F / R$ and $q \equiv |m_b - m_a|$. The coefficient $C_{q,l}$ vanishes when $l + q$ is odd or when $l < q$. For $q = l = 0$, we have $C_{0,0} = 1/2$, while otherwise

$$C_{q,l} = \frac{(2l-1)!!}{2^{l+1} l!} \prod_{n=1}^{(l+q)/2} \frac{(n-1/2)(n-l-1)}{n(n-l-1/2)}.$$

1.2.3 Calculation Approaches

A standard way to proceed is to employ the no-pair approach [27]. With the projector Λ_+ to the subsector $E_a > 0$ of the single-particle Hilbert space (for each particle), we thus consider the N-particle problem with respect to the filled Dirac sea. The projected Hamiltonian $H_+ = \Lambda_+ H \Lambda_+ = \Lambda_+ H_{\mathrm{fix}} \Lambda_+$ is given by

$$H_+ = \sum_a E_a c_a^\dagger c_a + \frac{1}{2}\sum_{aba'b'} \left(V_{abb'a'} - \delta_{ss'} V_{aba'b'}\right) c_a^\dagger c_b^\dagger c_{b'} c_{a'}. \tag{1.14}$$

As detailed in Refs. [26,27], this allows for a straightforward implementation of the HF approach, and we will report HF results in Sect. 1.4. Given the converged self-consistent density matrix, one can obtain the ground-state energy $E(N)$ and other observables of interest.

On a more general level, we allow for a fixed number of electron-hole pairs by employing the Hamiltonian $H_{\rm fix}$ (Eq. 1.12). The no-pair Hamiltonian H_+ follows from $H_{\rm fix}$ with $N_{eh} = 0$. When the ground-state energy of $H_{\rm fix}$ is minimized for some $N_{eh} > 0$, the no-pair approach breaks down. Interactions are then able to overcome the gap between valence and conduction band, and one cannot treat the Dirac sea as inert anymore. $H_{\rm fix}$ as well as the QED model H are studied by exact diagonalization and perturbation theory in Sect. 1.3. For given α, ED results can be obtained within a few minutes on a standard desktop computer.

1.3 Particle-Hole Pair Production and Reconstruction of the Ground State

We now compare the different theoretical approaches by using ED for $N = 2$. We here consider only the simpler spinless single-valley version of graphene; for the full case, see Ref. [14].

Figure 1.1 shows results for the α-dependence of the ground-state energy for $N = 2$ using $H_{\rm fix}$ and H. For $\alpha > 1$, we observe that the ground state undergoes

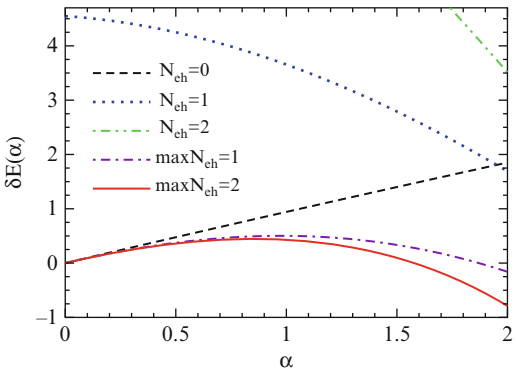

Fig. 1.1 ED results for the interaction energy $\delta E(\alpha) = E(\alpha) - E(0)$ (in units of Δ_0) vs. α for $N = 2$ and $B = 0$. The curves for $N_{eh} = 0, 1, 2$ correspond to the Hamiltonian $H_{\rm fix}$ with N_{eh} electron-hole pairs, i.e., the ground state then has no electron-hole pair for $\alpha < 1.9$. However, the full QED Hamiltonian Eq. (1.11), where we truncate the Hilbert space to at most one or two electron-hole pairs ($\max(N_{eh}) = 1, 2$), has a significantly lower energy already for $\alpha > 0.5$

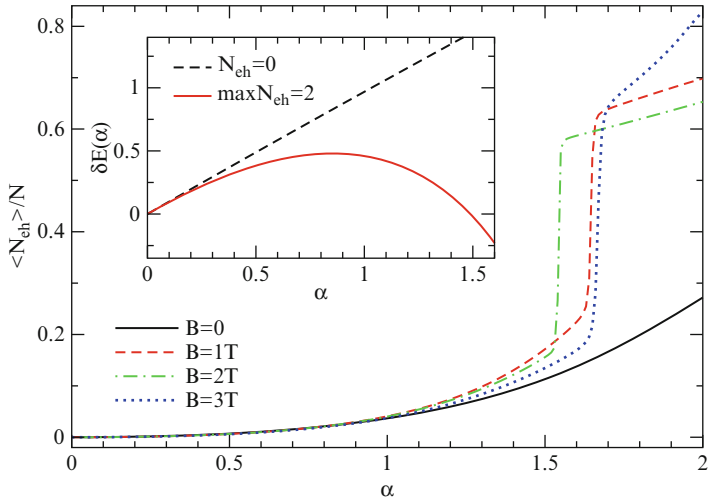

Fig. 1.2 Main panel: relative number of electron-hole pairs in the ground state, $\langle N_{eh}\rangle/N$, vs. α for $N = 2$ and several values of the magnetic field. We take the dot radius $R = 30$ nm. The results were obtained using the QED Hamiltonian but with the Hilbert space truncated to at most two electron-hole pairs. Inset: Interaction correction δE vs. α for $N = 2$ and $B = 1$ T. Shown are ED results using H_+ ($N_{eh} = 0$) and for the full H, where the Hilbert space was truncated at $\max(N_{eh}) = 2$

reconstruction and involves at least one electron-hole pair. The full interaction correction to the energy is significantly lowered by including H' and may even change sign for large α. In these calculations, the Hilbert space was truncated to contain at most one or two electron-hole pairs. For $\alpha < 1.5$, this appears to be sufficient. Similar results were found for $N = 3$ [14].

The effect of H' can also be evaluated analytically by using second-order perturbation theory (the first order vanishes identically). Second-order perturbation theory captures the ED data quite well, especially for $\alpha < 1$ [14]. The combination of ED (or HF) calculations for $H_{\rm fix}$ supplemented with a perturbative treatment of H' should in general provide a good approximation of the ground state.

Let us proceed by discussing the case of finite magnetic field, again for $N = 2$ (we have also studied the $N = 3$ case, again with very similar results).

The main panel of Fig. 1.2 shows the average number of electron-hole pair excitations in the ground state for several values of the magnetic field. The shown results are for a dot radius $R = 30$ nm. A magnetic field of $B = 1$ T corresponds to the magnetic length $l_B = (c/eB)^{1/2} \approx 26$ nm, which is of the same order of magnitude as the radius. Evidently, in a magnetic field, the proliferation of electron-hole pairs becomes more important. We interpret this effect as the finite-size analogue of the magnetic catalysis phenomenon [13].

The interaction correction to the ground-state energy is shown for $B = 1$ T in the inset of Fig. 1.2. While the result shows qualitatively similar behavior as for $B = 0$, the now more significant deviations between the ED data and the no-pair result are consistent with magnetic catalysis again. We note in passing that for

(approximately) $\alpha > 1.5$, the basis size used in our ED calculations is most likely not sufficient, and probably $N_{eh} > 2$ states also contribute to the ground state. The steplike features in Fig. 1.2 are then presumably smeared out.

We conclude that the no-pair Hamiltonian is quantitatively reliable only for weak interactions, $\alpha < 0.5$, and for not too large magnetic fields. For stronger interactions and/or fields, the ground state undergoes reconstruction and electron-hole pair proliferation. Using $H_{\rm fix}$ (Eq. 1.12) is not sufficient to get more accurate results, and one has to include H' (Eq. 1.13) which does *not* conserve the electron and hole numbers separately. However, for $\alpha < 1$, quite accurate results for the ground-state energy are obtained by combining ED (or HF) calculations for the no-pair Hamiltonian with subsequent second-order perturbation theory in H'.

Here only two or three particles have been addressed, where electron-hole proliferation takes place around $\alpha \approx 1$. Since the bulk case, which follows from the above model by a suitable limiting procedure with $N \to \infty$ and $R \to \infty$, has a phase transition at $\alpha \approx 1.1$, the finite-size crossover apparently depends on N only weakly.

1.4 Addition Spectrum and Ground-State Properties

Let us now turn to HF results for the ground state of the N-electron dot with $N \leq 15$ using the no-pair Hamiltonian H_+ (Eq. 1.14). As discussed in Sect. 1.3, this approximation is reliable only for weak interactions, and we focus on the regime $\alpha \leq 1$ below.

The spin and valley degrees of freedom are fully included in our self-consistent HF calculations. We note that the spin filling sequence found in our calculations [14] can be measured experimentally by Coulomb blockade spectroscopy [21]. Both the spin and valley filling sequences obtained by HF theory have been independently confirmed by ED of the no-pair Hamiltonian for $N \leq 4$.

To estimate the accuracy of the HF approximation for the no-pair model, we have also determined the relative difference between the HF ($E_{\rm HF}$) and the ED ($E_{\rm ED}$) energy,

$$\delta(N) = \frac{E_{\rm HF}(N,\alpha) - E_{\rm ED}(N,\alpha)}{E_{\rm ED}(N,\alpha) - E_{\rm ED}(N,0)}.$$

In all studied cases ($N \leq 4$), $\delta(N)$ was found to be rather small. For instance, even when taking the large value $\alpha = 1.5$, we obtain $\delta(2) = 0.107$, $\delta(3) = 0.175$ and $\delta(4) = 0.148$. As long as the no-pair approach stays valid, we conclude that HF theory yields quite accurate results.

Our HF results for the *addition energy* [16] which follows from the ground-state energy $E(N)$ using the relation

$$\Delta(N) = E(N+1) + E(N-1) - 2E(N), \tag{1.15}$$

are shown in Fig. 1.3 for $B = 0$ and several α. Similar HF results were discussed in Ref. [27].

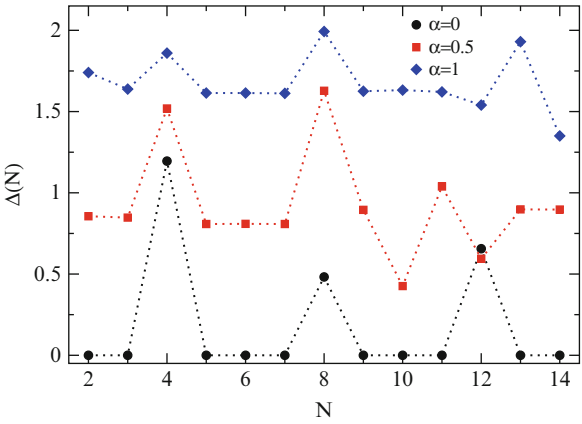

Fig. 1.3 Addition energy (1.15) in units of Δ_0 vs. N for several α from HF calculations for H_+ with $B = 0$

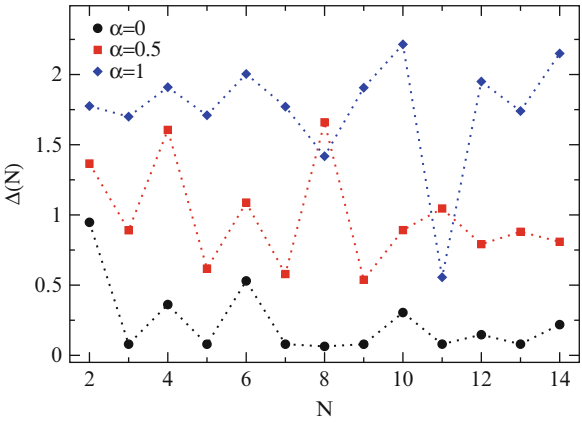

Fig. 1.4 Same as Fig. 1.3 but with $B_x = 15$ T and $B_z = 3$ T (for $R = 30$ nm)

Peaks in $\Delta(N)$ signify especially stable dot configurations (magic numbers). While for $\alpha = 0$, $\Delta(N)$ shows a four-periodicity due to spin-valley degeneracy [14], the addition energy peaks become less pronounced with interactions, and the four-periodicity is not always visible.

Interestingly, while there are magic numbers $N = 4, 8, 12, \ldots$ related to completely filled "energy shells" in the noninteracting case, the addition energy curves $\Delta(N)$ are rather featureless and almost flat for strong interactions. This indicates that a constant interaction model [31] provides a reasonable description, where the microscopic Coulomb interaction is replaced by the electrostatic charging energy of an effective capacitor.

The addition energy $\Delta(N)$ for $B \neq 0$ is shown in Fig. 1.4. The in-plane part B_x of the magnetic field here acts to increase the spin Zeeman field.

However, Zeeman effects in graphene are weak [2], and indeed almost the same results as those in Fig. 1.4 were found for $B_x = 0$ and $B_z = 3$ T. As a consequence of the broken spin degeneracy, only an (approximate) two-periodicity in $\Delta(N)$ is observed in the magnetic field case.

1.5 Conclusions

In this work, we have studied the ground state properties of N particles in a disorder-free circular graphene quantum dot, with the filled Dirac sea as the point of reference. The boundary of the dot has been modelled by the infinite-mass boundary condition, and the particles interact via the unscreened Coulomb potential whose prefactor is proportional to the bare dimensionless fine structure constant α. In contrast to atomic physics where $\alpha = 1/137$ is very small, in graphene (e.g., by the variation of the substrate dielectric parameter) α may be tuned up to a maximum value of $\alpha \approx 2.2$ (reached for freely suspended samples). For instance, a recent experiment [21] using Coulomb blockade spectroscopy for a graphene dot reported $\alpha \approx 1$.

We have studied the N-particle problem in a graphene dot on various levels of complexity – from the no-pair Hamiltonian to the full QED model – and by a number of different techniques. Our main results are as follows.

By using exact diagonalization (ED) for $N = 2$ and 3 particles, we found that the no-pair Hamiltonian H_+ originally proposed by Sucher [29], where the filled Dirac sea is assumed to be inert, is quantitatively reliable only for $\alpha \ll 1$. While this represents the standard situation in atomic physics [32], it can easily be violated in graphene. For $\alpha > 0.5$, our calculations indicate that electron-hole pair excitations contribute to the ground state energy. For $\alpha > 1$, these excitations proliferate and eventually cause a completely restructured ground state. Technically, the projection operator Λ_+ defining the vacuum should thus be changed to include interaction effects in a self-consistent manner.

Mittleman [33] has shown that this goal can be achieved by first minimizing the ground state energy $E(N,\Lambda_+)$ for given Λ_+, followed by the maximization of the energy over all possible Λ_+. The final result for $E(N)$ should then be equivalent to the QED results obtained numerically by ED (in the limit of infinite basis size).

We here argue that graphene dots realize a finite-size crossover version of the bulk semimetal-insulator phase transition. We find that the crossover scale is set by $\alpha \approx 1$, consistent with the bulk result $\alpha_c \approx 1.1$ [9].

When an orbital magnetic field is applied – the Zeeman field plays no significant role – electron-hole pair proliferation sets in earlier and implies a lowering of α_c, consistent with the magnetic catalysis scenario [13]. Even on a qualitative level, the no-pair Hamiltonian H_+ is thus reliable only on the semimetallic side of the transition ($\alpha < 1$).

For the regime $\alpha \leq 1$, we have reported detailed results using Hartree-Fock theory for H_+ and $N \leq 15$ particles in Sect. 1.4, taking into account the spin and

valley degrees of freedom. We find a four- (two-)periodicity in the spin filling sequence in the absence (presence) of a magnetic field, which can be understood from the single-particle picture and remains unaffected by weak interactions. However, the valley filling sequence is more intricate, especially when $B \neq 0$. This is related to subtle differences between the intra- and inter-valley scattering matrix elements of the Coulomb interaction. We have observed a strong tendency towards valley polarization induced by interactions in this N-body problem. Importantly, our analysis of the addition energy spectrum reveals that the constant interaction model can provide a reasonable description.

In a previous HF study of the spinless single-valley no-pair problem [27], we found that Wigner molecule formation sets in for strong interactions. Since that regime corresponds precisely to the onset of electron-hole proliferation, $\alpha > 1$, where the no-pair model becomes unreliable, we have analyzed the question of Wigner molecule formation using ED for $N = 3$ under the full QED model again. The Wigner molecule is identified from pronounced density correlations, and our numerical results (not shown here) are very similar to what we reported in Ref. [27]. We thus expect that the Wigner molecule formation is only weakly affected by the electron-hole pair proliferation reported in this paper.

References

1. Geim AK, Novoselov KS (2007) Nat Mater 6:183
2. Castro Neto AH, Guinea F, Peres NMR, Novoselov KS, Geim A (2009) Rev Mod Phys 81:109
3. Kotov VN, Uchoa B, Pereira VM, Castro Neto AH, Guinea F (2012) Rev Mod Phys 84:1067
4. Hasan MZ, Kane CL (2010) Rev Mod Phys 82:3045
5. González J, Guinea F, Vozmediano MAH (2001) Phys Rev B 63:134421
6. Khveshchenko DV (2009) J Phys Condens Matter 21:075303
7. Son DT (2007) Phys Rev B 75:235423
8. Müller M, Schmalian J, Fritz L (2009) Phys Rev Lett 103:025301
9. Drut JE, Lähde TA (2009) Phys Rev Lett 102:026802; (2009) Phys Rev B 79:165425
10. Gamayun OV, Gorbar EV, Gusynin VP (2010) Phys Rev B 81:075429; (2011) Phys Rev B 83:235104
11. Wang J, Fertig HA, Murthy G, Brey L (2011) Phys Rev B 83:035404
12. Greiner W, Müller B, Rafelski J (1985) Quantum electrodynamics of strong fields. Springer, Berlin
13. Gusynin VP, Miransky VA, Shovkovy IA (1994) Phys Rev Lett 73:3499
14. Paananen T, Egger R (2012) Phys Rev B 84:155456
15. Kouwenhoven LP, Austing DG, Tarucha S (2001) Rep Prog Phys 64:701
16. Reimann SM, Manninen M (2002) Rev Mod Phys 74:1283
17. Ponomarenko LA, Schedin F, Katsnelson MI, Yang R, Hill EW, Novoselov KS, Geim AK (2008) Science 320:356
18. Todd K, Chou HT, Amasha S, Goldhaber-Gordon D (2009) Nano Lett 9:416
19. Ritter KA, Lyding JW (2009) Nat Mater 8:235
20. Güttinger J, Stampfer C, Libisch F, Frey T, Burgdorfer J, Ihn T, Ensslin K (2009) Phys Rev Lett 103:046810
21. Güttinger J, Frey T, Stampfer C, Ihn T, Ensslin K (2010) Phys Rev Lett 105:116801
22. Berry MV, Mondragon RJ (1987) Proc R Soc Lond A 412:53

23. Schnez S, Ensslin K, Sigrist M, Ihn T (2008) Phys Rev B 78:195427
24. Wunsch B, Stauber T, Guinea F (2008) Phys Rev B 77:035316
25. Ezawa M (2008) Phys Rev B 77:155411
26. Egger R, De Martino A, Siedentop H, Stockmeyer E (2010) J Phys A Math Theor 43:215202
27. Paananen T, Egger R, Siedentop H (2011) Phys Rev B 83:085409
28. Brown GE, Ravenhall DG (1951) Proc R Soc Lond A 208:552
29. Sucher J (1957) Phys Rev 107:1448; (1958) Phys Rev 109:1010; (1980) Phys Rev A 22:348; (1984) Int J Quantum Chem 25:3
30. Häusler W, Egger R (2009) Phys Rev B 80:161402(R)
31. Grabert H, Devoret MH (eds) (1992) Single charge tunneling, vol 294, NATO ASI series B, physics. Plenum Press, New York
32. Reiher M, Wolf A (2009) Relativistic quantum chemistry. Wiley VCH, Weinheim
33. Mittleman MH (1981) Phys Rev A 24:1167

Chapter 2
Two-Dimensional Lattice Fermions with Random Gap

Antonio Hill and Klaus Ziegler

Abstract We calculate the localization lengths for lattice fermions with random gap in two dimensions. This is done by means of the transfer matrix approach. Numerical results are analyzed for finite-size scaling and they exhibit a metal-insulator and a insulator-insulator transition. At these transitions we calculate the critical exponent of the localization length.

2.1 Introduction

Dirac fermions in two dimensions play a crucial role in graphene and on the surface of topological insulators. A remarkable observation in graphene is the robust electronic transport in the vicinity of the two Dirac nodes. At these nodes two electronic bands touch each other with linear dispersion [1, 2]. The latter is a direct consequence of the lattice structure of graphene, since the honeycomb lattice decomposes into two triangular lattices.

It has been claimed from the theoretical side that transport in the presence of disorder [3] is very sensitive whether inter-node scattering is present or not. This is in contrast to the experimentally observed robust transport properties. In particular, the prediction has been made that electronic states are localized in the presence of inter-node scattering but delocalized in its absence. This has been elucidated by changing the symmetry class of the underlying Hamiltonian from orthogonal to symplectic [4, 5]. These statements are based on weak-localization calculations [3, 5], which predict weak (anti-)localization (with) without inter-node scattering.

A. Hill • K. Ziegler (✉)
Institut für Physik, Universität Augsburg, D-86135 Augsburg, Germany
e-mail: klaus.ziegler@physik.uni-augsburg.de

R. Egger et al. (eds.), *Low-Dimensional Functional Materials*, NATO Science for Peace and Security Series B: Physics and Biophysics, DOI 10.1007/978-94-007-6618-1_2,

Indeed, we have shown in our previous work [6] that lifting the node degeneracy has a drastic effect on the localization behavior. Since we have studied a single node located in the center of the Brillouin zone, it would be interesting to investigate whether this behavior changes when the node is shifted. For this reason, we apply the transfer matrix method, originally introduced for calculations of the Schrödinger Hamiltonian [7, 8], to lattice Dirac fermions in two dimensions with broken node symmetry.

The aim of this work is to understand the scaling behavior of the localization length for a single node, away from the center. In the presence of a random gap in the Dirac spectrum a metal-insulator transition has been observed in graphene [9–11] recently. If fluctuations of the random gap are weak in comparison to the average gap the system is insulating, whereas it is metallic when fluctuations are strong [12, 13]. Moreover, we will verify if there is a phase boundary separating two insulating phases, where a insulator-insulator transition can be observed.

2.2 Model

A tight-binding description of electrons in graphene results in the famous energy dispersion with two separate nodes (or neutrality points) in the Brillouin zone. In the vicinity of these nodes the momentum dependence of the spectrum is linear and the low-energy behavior of quasi particles can well be described by the Dirac equation $H\psi(x,y) = E\psi(x,y)$ with the Hamiltonian

$$H = -i\hbar v_F\,(\sigma\cdot\nabla) + v_F^2\, m\,\sigma_3, \tag{2.1}$$

where v_F is the Fermi velocity, σ is the vector of Pauli matrices and $\psi = (\varphi_1, \varphi_2)$ is the two component spinor wave function. In the following we set $\hbar$ and v_F to unity.

For a numerical treatment of the Dirac equation a discretization in space is required. However, the naive discretization through replacing the differential operator by a difference operator leads to additional new nodes. This phenomenon is often called fermion doubling or multiplication [14]. In real space there are two methods to avoid this problem [4, 15, 16]. One that we will apply in this work goes back to an idea by Susskind [14]. Discretization of the differential operator in a symmetric way is given by

$$\partial_x f(x) \approx \frac{1}{2\Delta}(f_{l+\Delta} - f_{l-\Delta})\,, \tag{2.2}$$

where Δ is the lattice constant which we set to unity in the following. The discrete Dirac equation for $m = 0$ reads

$$-\frac{i}{2}\sigma_1\left\{\psi_{l+1,n} - \psi_{l-1,n}\right\} - \frac{i}{2}\sigma_2\left\{\psi_{l,n+1} - \psi_{l,n-1}\right\} = E\,\sigma_0\,\psi_{l,n} \tag{2.3}$$

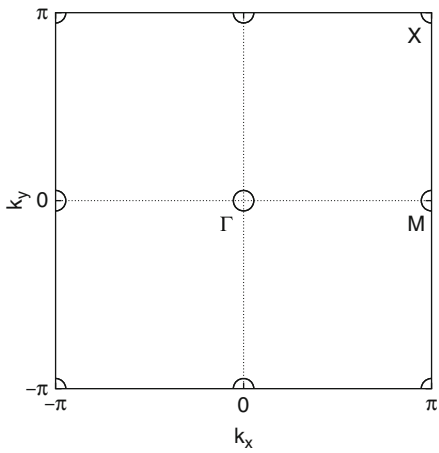

Fig. 2.1 Brillouin zone of the discrete Dirac equation, where circles depict the location of Dirac cones

with lattice points given by the coordinates (l,n), where l and n are integer. Fourier transformation leads to eigenvalues $E = \pm\sqrt{sin(k_x)^2 + sin(k_y)^2}$ which have four nodal points in the Brillouin zone corresponding to four Dirac fermions. In order to open a gap at nodes independently, we add a lattice operator [17] which acts on a wave function as

$$\hat{B}\,\psi_{l,n} = \frac{1}{2}\left\{\psi_{l+1,n} + \psi_{l-1,n} + \psi_{l,n+1} + \psi_{l,n-1}\right\}. \tag{2.4}$$

By including the lattice operator $\hat{B}$ and a random gap term, we get for the discrete Hamiltonian (Eq. 2.1)

$$H \to H + \delta(\hat{B} - 2)\sigma_3 + m_{l,n}\,\sigma_3. \tag{2.5}$$

In Fourier representation with uniform gap m our new Hamiltonian reads

$$H = \begin{pmatrix} m + \delta(cos(k_x) + cos(k_y) - 2) & \sin(k_x) + i\sin(k_y) \\ \sin(k_x) - i\sin(k_y) & -m - \delta(cos(k_x) + cos(k_y) - 2) \end{pmatrix} \tag{2.6}$$

and the corresponding energy dispersion is given by

$$E = \pm\sqrt{sin(k_x)^2 + sin(k_y)^2 + (m + \delta cos(k_x) + \delta cos(k_y) - 2\delta)^2}. \tag{2.7}$$

For $m = 2\delta$ there is a node at point M and additional nodes for $m = 0, \delta = 0$ at Γ and X (cf. Fig. 2.1). Nodal degeneracy can be lifted via the parameter δ using this model. We consider the node to be located at M for our calculations in the following. In Fig. 2.2 the dispersion of Eq. (2.7) is shown for the four-fold degeneracy (dashed line) and for the node at M without gap (solid line) and with gap (thick solid line).

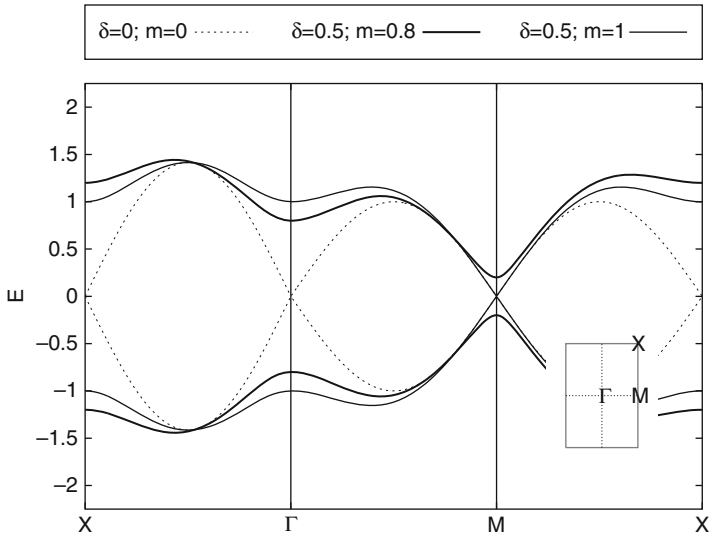

Fig. 2.2 Bandstructure for lattice fermions with preserved node symmetry without gap (*dashed line*), for broken node symmetry ($\delta = 0.5,\ m = 0.8$) with gap (*thick solid line*) and for $m = 1$ (*thin solid line*). The inset shows the Brillouin zone schematically

The index n is absorbed with the help of matrix representation and we write for the wave function

$$\psi_{l+1} = H^Y\ \psi_l + H^D\ \psi_{l-1}. \tag{2.8}$$

Each spinor component is now an M-component vector, where M is the strip width and thus $n = 1, 2, \ldots, M$. The matrices H^Y, H^D are written as

$$H^Y_{n,n} = 2S^{-1}\left[E\,\sigma_0 + (2\delta - m)\sigma_3\right] \tag{2.9}$$

$$H^Y_{n,n+1} = S^{-1}\left[i\sigma_2 - \delta\sigma_3\right] \tag{2.10}$$

$$H^Y_{n,n-1} = -S^{-1}\left[i\sigma_2 + \delta\sigma_3\right] \tag{2.11}$$

$$H^D_{n,n} = -S^{-1}\left[i\sigma_1 + \delta\sigma_3\right] \tag{2.12}$$

with $S = -i\sigma_1 + \delta\sigma_3$ and where H^Y has periodic boundary conditions imposed in the y-direction. The latter allows us to construct a transfer matrix T_l through the equation [7]

$$\begin{pmatrix} \psi_{l+1} \\ \psi_l \end{pmatrix} = \begin{pmatrix} H^Y & H^D \\ 1 & 0 \end{pmatrix} \begin{pmatrix} \psi_l \\ \psi_{l-1} \end{pmatrix} \equiv T_l \begin{pmatrix} \psi_l \\ \psi_{l-1} \end{pmatrix}. \tag{2.13}$$

Different random potentials, e.g. random scalar potential, can be introduced accordingly.

2.3 Method

2.3.1 Lyapunov Exponents

According to [7, 8] Lyapunov characteristic exponents (LCE) can be calculated using the transfer matrix T_l, defined in Eq. (2.13). The iteration of Eq. (2.13) provides ψ_L by the product matrix

$$M_L = \prod_{l=1}^{L} T_l. \tag{2.14}$$

For disordered systems this is a product of random matrices satisfying Oseledec's theorem [18]. The latter guarantees the existence of a limiting matrix

$$\Gamma = \lim_{L\to\infty} (M_L^{\dagger} M_L)^{1/2L}. \tag{2.15}$$

The eigenvalues of Γ can be written as exponential functions $\exp(\gamma_i)$, where γ_i is the LCE. Implementing the numerical algorithm described in Ref. [7], the whole Lyapunov spectrum can be calculated. Most commonly, the smallest LCE is identified with the inverse localization length [8] and can be used for scaling analysis.

2.3.2 Finite-Size Scaling

Let us denote the localization length (i.e. the inverse of the smallest LCE) as $\Lambda = 1/\gamma_{min}$. The localization length Λ increases with the system width M according to a power law:

$$\Lambda \propto M^{\alpha}, \tag{2.16}$$

where the exponent α determines the present phase. For $\alpha > 1$ ($\alpha < 1$) the system is in the regime of extended (localized) states, and $\alpha = 1$ in the critical regime. If the system is in the exponentially localized regime, we expect $\Lambda \propto const$. According to the one-parameter scaling theory by MacKinnon and Kramer [19], the localization length normalized by strip width $\tilde{\Lambda} = \Lambda/M$ obeys the equation

$$\frac{d\ln\tilde{\Lambda}}{d\ln M} = \chi(\ln\tilde{\Lambda}), \tag{2.17}$$

where the scaling function χ must be determined numerically, with solutions of the form

$$\tilde{\Lambda}(M,W) = f(\xi(W)/M). \tag{2.18}$$

Here, the parameter W characterizes the disorder strength and ξ is a characteristic length of the system. The main statement of the one-parameter scaling theory is that $\tilde{\Lambda}$ does not depend on M and W separately. As a consequence, any change of disorder strength W can be compensated by a change of the system width M. Moreover, from the behavior of $\tilde{\Lambda}$ in the vicinity of a scale-invariant point it is possible to extract the critical exponent ν of the correlation length [7], corresponding to the localization length of the infinite system. This can be done by Taylor expansion

$$\begin{aligned} \ln\tilde{\Lambda} &= \ln\tilde{\Lambda}_c + \sum_{s=1}^{S} A_s \left(|W-W_c|M^{1/\nu}\right)^s \\ &= \ln\tilde{\Lambda}_c + \sum_{s=1}^{S} A_s \left(\frac{\xi}{M}\right)^{-s/\nu}, \end{aligned} \tag{2.19}$$

with $\xi = |W-W_c|^{-\nu}$. Comparing the latter with Eq. (2.18), the scaling function ξ is interpreted as the characteristic length scale. If the scaling argument holds, the raw data should collapse onto a single curve by rescaling the data with $M \to \xi/M$.

2.4 Metal-Insulator Transition

In our previous work [6] we have discussed the scaling behavior of lattice fermions with preserved node symmetry ($\delta = 0$) and broken node symmetry ($\delta = 0.5$). Furthermore, we have chosen parameters such that the single node was located in the center of the Brillouin zone. In this work we will focus only on lifted degeneracy of the node structure, but consider the node to be located at the border of the Brillouin zone (cf. Point M in Fig. 2.1). This can be achieved by setting $m = 2\delta$. In this case the Dirac cone at the border has no gap. Setting $m = 0.8$ opens a gap and corresponds to $m = 0.2$ for the node in the center of the Brillouin zone.

In the following we set $\bar{m} = 0.8$ for the mean value of the random gap (i.e., $\bar{m} = \langle m \rangle$) and calculate localization lengths by means of the transfer matrix approach using Eq. (2.13). This is done for several combinations of strip width M and disorder strength W. We use for the random gap m a box distribution on the interval $[\bar{m} - W/2, \bar{m} + W/2]$ and calculations are restricted to the Dirac point (i.e. $E = 0$).

Considering the disorder dependence of the rescaled localization length $\tilde{\Lambda}$, our data exhibits two critical points. Below transition point I ($W_{c1} \approx 3.047$) the system is insulating, meaning that $\tilde{\Lambda}$ decays with increasing system size. Between the first and the second point ($W_{c2} \approx 7.727$), the rescaled localization length is growing with system size, indicating metallic behavior. For even stronger disorder the system is insulating again. Results are shown in Fig. 2.3 on a logarithmic scale.

In order to compute the critical quantities, we have calculated $\tilde{\Lambda}$ in vicinity of transition point I and fitted the data to Eq. (2.19) for $S = 5$. The finite-size scaling

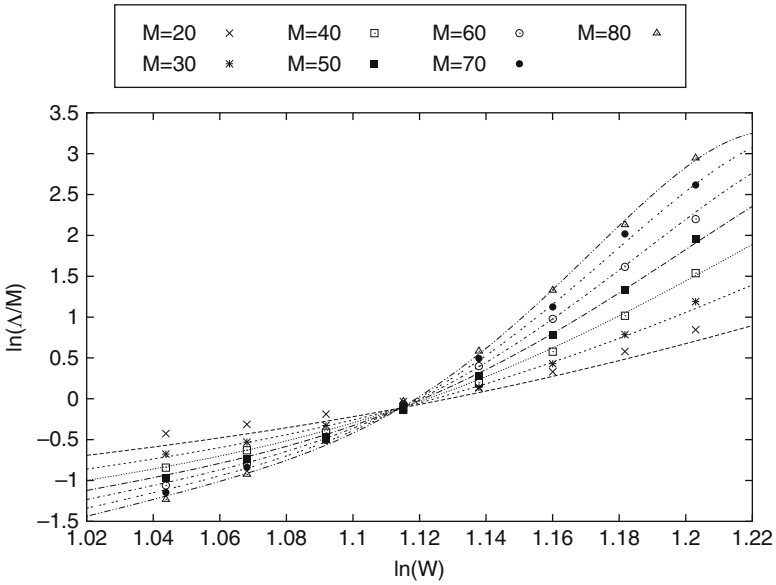

Fig. 2.3 Logarithm of the normalized localization length in the vicinity of critical point I for $\delta = 0.5$ and $\bar{m} = 0.8$. *Dashed lines* are the result of fitting Eq. (2.19) to the data

Table 2.1 Critical values for $\bar{m} = 0.8$ and $\delta = 0.5$ obtained from fitting the data to equation

Critical point	I	II
Exponent ν	1.217 ± 0.017	1.451 ± 0.024
W_c	3.047 ± 0.004	7.727 ± 0.01
Λ_c	0.893 ± 0.013	0.479 ± 0.007
Disorder range	$2.7 \leq W \leq 3.33$	$6.6 \leq W \leq 8.4$
System sizes	$20 \leq M \leq 80$	$20 \leq M \leq 80$

analysis leads to the critical exponent ν, which can be taken from Table 2.1. It also yields the scaling function ξ, which we use to rescale the data onto a single curve. Figure 2.4 shows that all points collapse nicely either on the metallic or the insulating branch.

The same procedure has been performed in vicinity of critical point II. In Fig. 2.5 it can be seen, that $\ln(\tilde{\Lambda})$ is growing with system size, left of the transition point. On the other hand, it is decaying with system size, on the right of the critical point. The dashed lines in Fig. 2.5 are the result of fitting the data to Eq. (2.19) for $S = 5$ and the critical quantities can be taken from Table 2.1. The resulting scaling function could then be used to rescale the raw data onto a single curve, which is shown Fig. 2.6. Again, the rescaled data has a metallic and an insulating branch. This clearly demonstrates the appearance of an Anderson transition at critical points I and II.

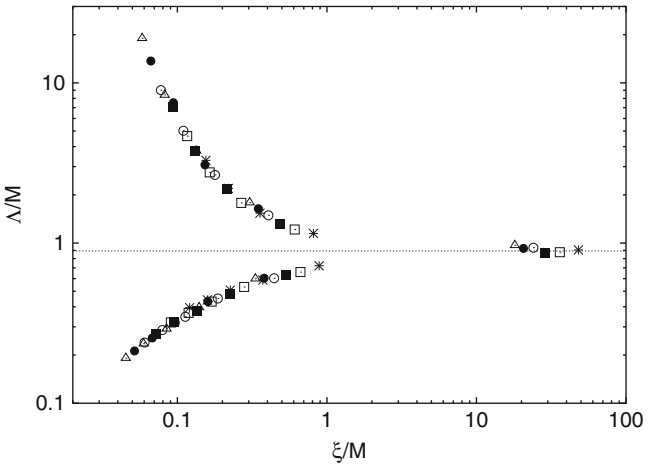

Fig. 2.4 Rescaled data in vicinity of critical point I, symbols are identical to those used in Fig. 2.3. The *dashed line* corresponds to $\tilde{\Lambda}_c$

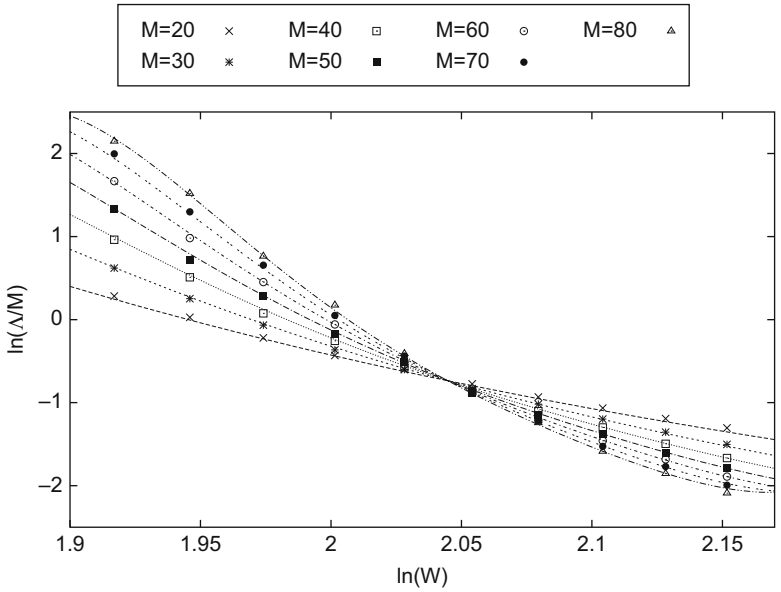

Fig. 2.5 Logarithm of the normalized localization length in the vicinity of critical point II for $\delta = 0.5$ and $\bar{m} = 0.8$. *Dashed lines* are the result of fitting Eq. (2.19) to the data

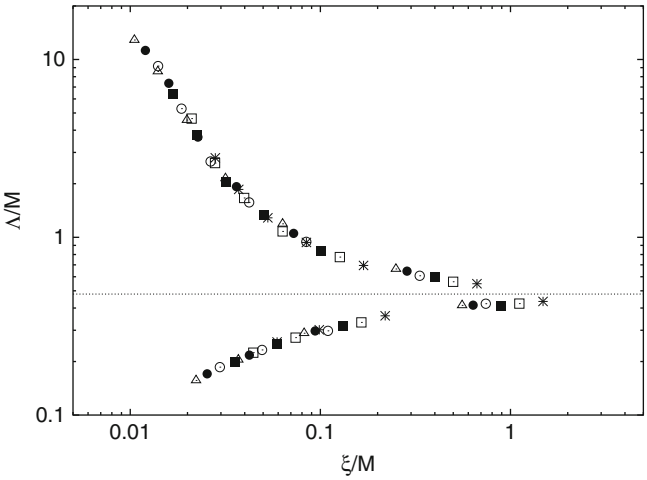

Fig. 2.6 Rescaled data in vicinity of critical point II, symbols are identical to those used in Fig. 2.5. The *dashed line* corresponds to $\tilde{\Lambda}_c$

2.5 Insulator-Insulator Transition

Let us now consider $\bar{m} = 2\delta$, in this case the node at the border of the Brillouin zone is ungapped. We expect that the system behaves critical for disorder strengths smaller than W_{c1}. This means, that if we change $\bar{m}$ for fixed disorder, the system should undergo a insulator-insulator transition. In order to confirm this assumption, we fix disorder strength to $W = 1$ and calculate Λ for different strip widths M as a function of $\bar{m}$. Discussing the inverse of the normalized localization length $z = M\gamma_{min}$ (or normalized Lyapunov exponent) is equivalent to discussing Λ/M [20] and numerical results are shown in Fig. 2.7. Indeed, it can be seen that there is a critical point at $\bar{m} = 1$. The critical exponent can be obtained by fitting the data to

$$z = \frac{M}{\Lambda} \approx z_c + c\ (\bar{m} - m_c) M^{1/\nu} \tag{2.20}$$

and gives for our data

$$\nu = 1.006 \pm 0.005 \quad (W = 1,\ m_c = 1). \tag{2.21}$$

Using the resulting scaling function

$$\xi = |\bar{m} - m_c|^{-\nu}\ , \tag{2.22}$$

the raw data, shown in Fig. 2.7, can be rescaled and all points collapse onto a single curve. In this case only a insulating branch exists as can be seen in Fig 2.8.

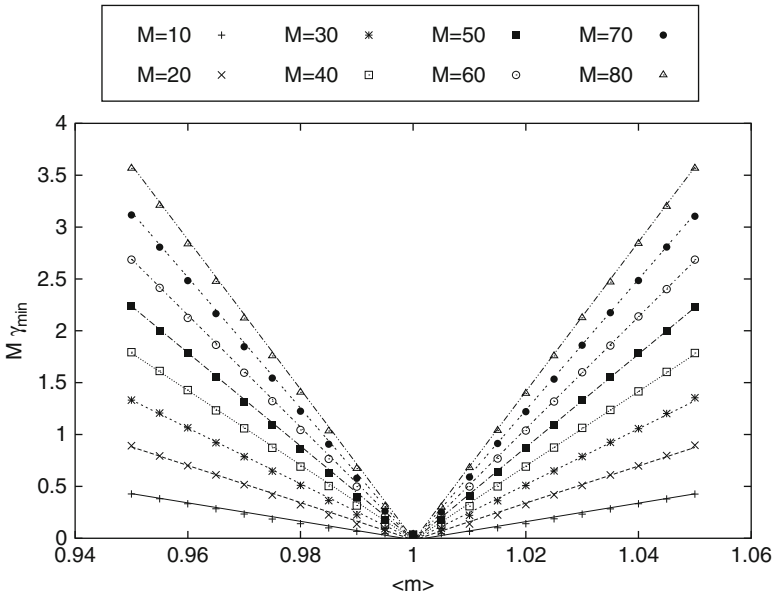

Fig. 2.7 Normalized Lyapunov exponent at the insulator-insulator transition for $\delta = 0.5$, $\bar{m} = 1$ and $W = 1$. *Dashed lines* correspond to the result of fitting Eq. (2.20) to the data

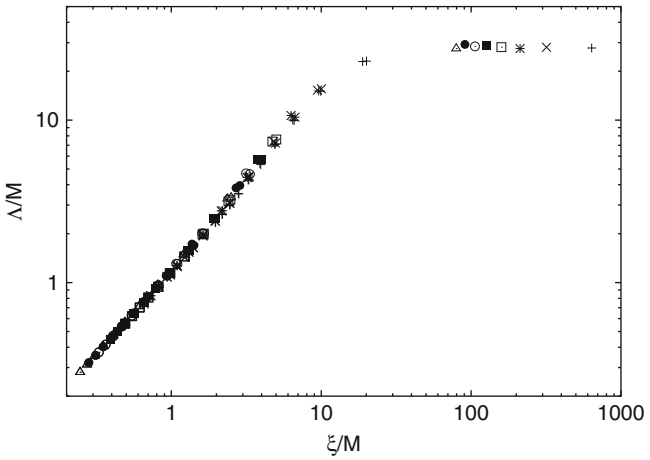

Fig. 2.8 Rescaled data in vicinity of the insulator-insulator transition, symbols are identical to those used in Fig. 2.7

2.6 Discussion

Our results are summarized in the following. The localization length Λ for $\delta = 0.5$ always increases with M according to the power law of Eq. (2.16), where the exponent α depends on the model parameters:

$$\begin{cases} \alpha = 0 & \text{for } \bar{m} = 0.8,\ W \leq W_{c1} \\ \alpha > 1 & \text{for } \bar{m} = 0.8,\ W_{c1} \leq W \leq W_{c2} \\ 0 < \alpha < 1 & \text{for } \bar{m} = 0.8,\ W > W_{c2} \\ \alpha = 1 & \text{for } \bar{m} = 1,\ W < W_c \end{cases} . \tag{2.23}$$

For the single node located at the border of the Brillouin zone, finite-size scaling of the localization lengths shows a typical Anderson transition at two points. States are exponentially localized for weak disorder (i.e. $W < W_{c1}$), since $\alpha = 0$. In the intermediate phase for $W_{c1} \leq W \leq W_{c2}$ the exponent is $\alpha > 1$, indicating metallic behavior. For stronger disorder states are decaying but not exponentially (i.e. $0 < \alpha < 1$). This indicates two metal-insulator transitions, one from $\alpha = 0$ to $\alpha > 1$ and a second from $\alpha > 1$ to $0 < \alpha < 1$.

The localization length Λ for $\delta = 0.5$, $\bar{m} = 1$ and $W < W_c$ is critical, thus independent of M (i.e. $\alpha = 1$). Since the model shows insulating behavior for $\bar{m} = 0.8$, it has to undergo a transition from $\alpha = 0$ to $\alpha = 1$ when increasing $\bar{m}$ to $\bar{m}_c = 1$. The exact value for W_c is not known yet, therefore needs to evaluated by further calculations. Moreover, it is not clear how α changes for stronger disorder $W > W_c$.

2.7 Conclusion

We have introduced a model for Dirac fermions on a lattice with several nodes which allows us to perform numerical calculations of the localization length by means of the transfer matrix formalism. Using the Hamiltonian in Eq. (2.6) it is possible to break the node symmetry in the Brillouin zone and by an appropriate choice of $\bar{m}$ the location of a node can be chosen between three points (Γ, M, X). In this work we have set $\delta = 0.5$ and considered the node to be on the border of the Brillouin zone.

We have calculated localization lengths for several strip widths and for different strength of the random gap. In all cases the localization length can be described by $\Lambda \sim M^{\alpha}$. However, the exponent α depends on the model parameters (cf. Eq. 2.23). In particular, our numerical result indicates $\alpha = 0$ for non-degenerate nodes, finite gap and weak disorder. On the other hand, we have a metallic phase (i.e $\alpha > 1$) only for intermediate disorder strength. The metallic phase is separated from the insulating phases by two Anderson transitions. At these transitions one-parameter scaling holds and we have been able to extract critical exponents.

In the special case of $\bar{m} = 1$, where the node is gapless, $\tilde{\Lambda}$ shows critical behavior, at least for weak disorder. The latter represents a phase boundary, separating two insulating phases, where a insulator-insulator transition occurs. By means of finite-size scaling we have calculated the critical exponent.

References

1. Novoselov KS, Geim AK, Morozov SV, Jiang D, Katsnelson MI, Grigorieva IV, Dubonos SV, Firsov AA (2005) Nature 438:197
2. Zhang Y, Tan Y-W, Stormer HL, Kim P (2005) Nature 438:201
3. Shon NH, Ando T (1998) J Phys Soc Jpn 67:2421
4. Tworzydło J, Groth CW, Beenakker CWJ (2008) Phys Rev B 78:235438
5. Suzuura H, Ando T (2002) Phys Rev Lett 89:266603
6. Hill A, Ziegler K. arXiv:1211.2329
7. MacKinnon A, Kramer B (1983) Z Phys B Condens Matter 13:1546
8. Pichard JL, Sarma G (1981) J Phys C Solid State Phys 14:L127
9. Bostwick A, McChesney JL, Emtsev KV, Seyller T, Horn K, Kevan SD, Rotenberg E (2009) Phys Rev Lett 103:056404
10. Elias DC, Nair RR, Mohiuddin TMG, Morozov SV, Blake P, Halsall MP, Ferrari AC, Boukhvalov DW, Katsnelson MI, Geim AK, Novoselov KS (2009) Science 323:610
11. Ponomarenko LA, Geim AK, Zhukov AA, Jalil R, Morozov SV, Novoselov KS, Cheianov VV, Fal'ko VI, Watanabe K, Taniguchi T, Gorbachev RV (2011) Nat Phys 7:958
12. Abergel DSL, Apalkov V, Berashevich J, Ziegler K, Chakraborty T (2010) Adv Phys 59:261
13. Ziegler K (2009) Phys Rev Lett 102:126802; (2009) Phys Rev B 79:195424
14. Susskind L (1977) Phys Rev D 16:3031
15. Stacey R (1982) Phys Rev D 26:468
16. Medvedyeva MV, Tworzydło J, Beenakker CWJ (2010) Phys Rev B 81:214203
17. Ziegler K (1996) Phys Rev B 53:9653
18. Oseledec V (1968) Trans Mosc Math Soc 19:197
19. MacKinnon A, Kramer B (1981) Phys Rev Lett 47:21
20. Markos P (2006) Acta Phys Slovaca 56:561

Chapter 3
Dielectric Constant and Screened Interactions in AA Stacked Bilayer Graphene

Luis Brey

Abstract *AA* stacked bilayer graphene has a band structure consisting of two Dirac cones, bonding and antibonding, displaced in energies. In absence of interaction between electrons, the system is metallic and the Fermi surface consists of circles in the bonding and antibonding bands which coincides exactly. In presence of interaction between electrons the system is unstable to the condensation of bonding-like electrons and antibonding-like holes. The properties and the critical temperature of this gapped phase depends strongly on the screening on the interaction between pairs at large distances. In this work we study the polarizability and the intra and interlayer screened Coulomb interactions of a AA-stacked bilayer graphene for different energy gaps in the spectrum. We obtain that the existence of a gap suppress the screening at small wavevectors. Our results indcates the importance of a self-consistent treatment of the screening in the study of gapped phases in *AA* stacked bilayer graphene.

3.1 Introduction

Graphene is a two-dimensional zero gap semiconductor with exotic electronic properties [1]. In graphene, carbon atoms arrange in a triangular lattice with two atoms *A* and *B* per unit cell. The unusual properties of monolayer graphene triggered in the last years the study of bilayer graphene systems. The electronic properties of bilayer graphene depends strongly on the orientation of the constituent layers. The more studied [2] and more natural form of the bilayer graphene is the so-called Bernal or *AB* stacking for which high quality samples have been obtained. Few layer graphene films grown by chemical vapor deposition methods, often

L. Brey (✉)
Instituto de Ciencia de Materiales de Madrid (CSIC), Cantoblanco, E-28049 Madrid, Spain
e-mail: brey@icmm.csic.es

R. Egger et al. (eds.), *Low-Dimensional Functional Materials*, NATO Science for Peace and Security Series B: Physics and Biophysics, DOI 10.1007/978-94-007-6618-1_3,

show rotations of successive graphene layers. Therefore exfoliation from these films produces twisted bilayer graphene [3, 4]. Finally, experimental observations of bilayers graphene with *AA* stacking have been reported [5]. This stacking is less natural than Bernal stacking and there are not many theoretical studies on the properties of *AA*-stacking bilayer graphene [6–10].

In the *AA* bilayer graphene, all carbon atoms of the left layer are tunnel coupled with the equivalent atoms of the right layer. The band structure of the system consists of two Dirac cones, with the Dirac points separated in energy by $2t_1$, being t_1 the interlayer hopping parameter. These two Dirac cones correspond to the bonding and anti-bonding combination of the Dirac cones of the constituent monolayers. In undoped systems, the Fermi surface coincides with the region in momentum space where the bonding and the antibonding Dirac cones crosses, and consists of two concentric circles of radius $k_c = t_1/\hbar v_F$. Here v_F is the Fermi velocity of monolayer graphene. In this case the particle hole symmetry of the Hamiltonian, Eq. (3.1) ensures perfect nesting between the electron Fermi spheres in the bonding and antibonding bands, thereby driven the electron-hole condensation [11,12]. Estimates of the critical temperature of the condensate depends strongly on the model and approximations used for describing the electron-electron interaction. The long range character of the unscreened Coulomb interaction produces large gaps in the spectra and critical temperatures near room temperature [13, 14]. On the opposite limit, in the metallic AA stacked bilayer graphene the electron hole excitations provide metallic screening at long distances, and the gap of the condensate obtained using this screening is extremely small [15–17]. The appearance of an energy gap in the condensate induces changes in the electron polarizability and can modify the pairing interaction considerably [18–20]. In this work we study the polarizability and the intra and interlayer screened Coulomb interactions of a AA-stacked bilayer graphene for different energy gaps in the spectrum.

3.2 Hamiltonian

Near a Dirac point the one-electron Hamiltonian of the *AA* stacked bilayer graphene takes the form

$$H_0 = \hbar v_F \sum_{\mathbf{k},i=L,R} (k_x - ik_y) c^+_{Ai\mathbf{k}} c_{Bi\mathbf{k}} - t_1 \sum_{\mathbf{k},\alpha=A,B} c^+_{\alpha L\mathbf{k}} c_{\alpha R\mathbf{k}} + h.c. \tag{3.1}$$

here the operator $c^+_{\alpha i\mathbf{k}}$ creates an electron in the sublattice α, in the layer i and with momentum $\mathbf{k}$. t_1 is the interlayer hopping, that we consider to get a values $t_1 \sim 0.12t$ [2], being t the first neighbour interlayer hopping, $\hbar v_F = \frac{\sqrt{3}}{2} ta$ and a is the monolayer graphene lattice parameter. Valley and spin degrees of freedom are not explicitly treated. The eigenvalues of Hamiltonian Eq. (3.1) are $\varepsilon(k) \pm t_1$, which are the bonding $(-)$ and antibonding $(+)$ combination of the left and right layer graphene wavefunctions. The monolayer graphene dispersion is $\varepsilon(k) = s\hbar v_F k$, where $s = \pm 1$

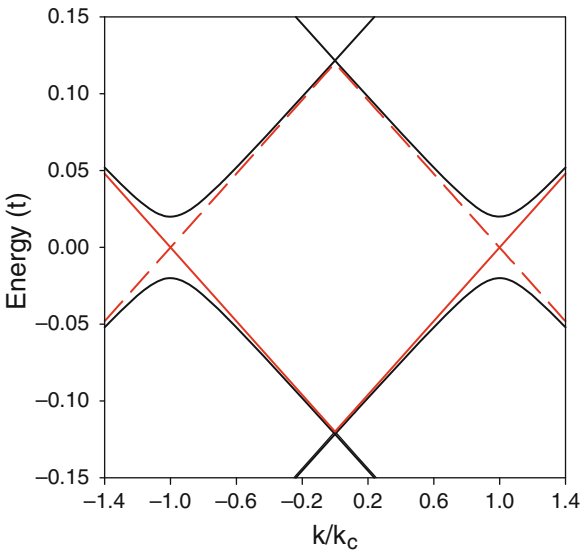

Fig. 3.1 Continuous *black lines* correspond to the gapped energy bands. In *red* we plot the four bands of the gapless AA stacked bilayer graphene, here continuous (*dashed*) lines represent the bonding (antibonding) combinations (color figure online)

indicates the valence and conduction bands of each graphene layer. We create a gap in the system at the Fermi energy by including a coupling, $E_g/2$, between the electron-like band of the symmetric Dirac cone band and the hole like band of the antisymmetric Dirac cone.

Figure 3.1 illustrates the band structure of the AA bilayer as a function of the momentum near a Dirac point. When the system is undoped, the Fermi surface corresponds with a circle of radius $k_c = t_1/\hbar v_F$ at which the hole-like antibonding band spectrum crosses the electron-like bonding band spectrum.

3.3 Dielectric Constant and Effective Interactions

The electron electron Coulomb interactions induce charge screening that modifies the interaction between particles. In bilayer graphene, charges located in different layers participate in the screening process. Within the Random Phase Approximation (RPA) the dielectric function is a 2×2 matrix of the form,

$$\varepsilon_{\alpha,\beta}(\mathbf{q},\omega) = \varepsilon_0\delta_{\alpha,\beta} - \sum_l V^{ext}(\mathbf{q})_{\alpha,\gamma}\Pi^0_{\gamma,\beta}(\mathbf{q},\omega)\,, \tag{3.2}$$

where ε_0 is a background dielectric constant due to the substrate upon which graphene is deposited. The external Coulomb interactions for intralayers and interlayers are $V^{ext}_{L,L}(\mathbf{q})$=$V^{ext}_{R,R}(\mathbf{q})$=$v_q$ and $V^{ext}_{L,R}(\mathbf{q})$=$V^{ext}_{R,L}(\mathbf{q})$=$v_q e^{-qd}$ respectively, being v_q=$2\pi e^2/q$ the bare Coulomb interaction and d the distance between the graphene layers. The polarizability matrix takes the form,

$$\Pi^0_{\alpha,\beta}(q,\omega) = -\frac{g_s g_v}{S}\sum_{\mathbf{k},s,s'}\frac{f(\varepsilon_{s,\mathbf{k}}) - f(\varepsilon_{s',\mathbf{k}'})}{\omega + \varepsilon_{s,\mathbf{k}} - \varepsilon_{s',\mathbf{k}'}} F^{\alpha,\beta}_{s,s'}(\mathbf{k},\mathbf{k}') \tag{3.3}$$

where $\mathbf{k}'=\mathbf{k}'+\mathbf{q}$, $g_s = 2$ and $g_v = 2$ are the spin and valley degeneracy, S is the sample area and $\varepsilon_{s,\mathbf{k}}$ are the eigenvalues of the band s corresponding to the wavevector $\mathbf{k}$. In Eqs. (3.2) and (3.3), the index α and β are the layer indices and $f(E)$ is the Fermi-Dirac distribution. The couplings F have the form

$$F^{\alpha,\beta}_{s,s'}(\mathbf{k},\mathbf{k}') = < s,\mathbf{k}|P_\alpha|s',\mathbf{k}' >< s',\mathbf{k}'|P_\beta|s,\mathbf{k} > \tag{3.4}$$

where P_α is a layer projection operator,

$$\rho_L = \begin{pmatrix} 1&0&0&0\\ 0&1&0&0\\ 0&0&0&0\\ 0&0&0&0 \end{pmatrix} \text{ and } \rho_R = \begin{pmatrix} 0&0&0&0\\ 0&0&0&0\\ 0&0&1&0\\ 0&0&0&1 \end{pmatrix} \tag{3.5}$$

These operators are written in the basis LA, LB, RA, RB. In the expression of the polarizability, Eq. (3.3), both the eigenvalues and eigenvectors depends on the value of the gap E_g. By symmetry $\Pi^0_{L,L} = \Pi^0_{R,R}$ and $\Pi^0_{L,R} = \Pi^0_{R,L}$. The response function $\Pi^0_{\alpha,\beta}$ indicates the electric polarization created in layer α by and electric field acting on layer β. The sum

$$\Pi^0(q) = \Pi^0_{L,L} + \Pi^0_{R,R} + \Pi^0_{L,R} + \Pi^0_{R,L}, \tag{3.6}$$

plays the role of the effective polarizability of the whole system, and gives and indication of the screening ability of the AA-stacked bilayer graphene.

In Fig. 3.2 we plot Π^0 for different values of the energy gap E_g. In the gapless case, the polarization takes the form [21, 22],

$$\Pi^0(q, E_g = 0) = D_0\left[1 - \Theta(q-2k_c)\frac{q}{4k_c}\left(\frac{2k_c}{q}\sqrt{1-\left(\frac{2k_c}{q}\right)^2} - \arccos\left(\frac{2k_c}{q}\right)\right)\right] \tag{3.7}$$

where $D_0 = 2g_s g_v \frac{t_1}{2\pi v_F^2}$ is the density of states at the Fermi energy of the AA staked bilayer. The finite value of $\Pi^0(q, E_g = 0)$ at zero wavevector indicates the metallic behaviour of the system at long distances.

When the gap is finite, the polarizability of the system is suppressed at small wavevectors, indicating that the system is unable to screen long-wavelength perturbations. We observe that as larger is the energy gap larger is the region in reciprocal space where the screened is suppressed.

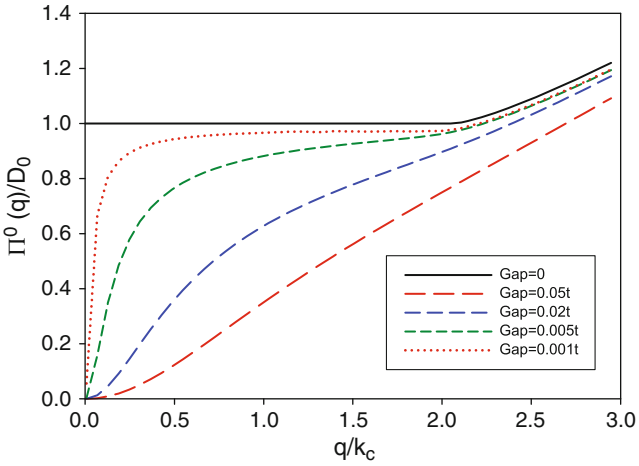

Fig. 3.2 The effective static polarizability of a *AA* staked bilayer graphene as function of the wavevector k for different values of the energy gap. The polarizability is plotted in units of the density of states D_0

From the definition of the RPA dielectric constant, Eq. (3.2) and using the previous expressions for the polarizabilities, the obtain the intra and interlayer effective interactions,

$$\begin{pmatrix} V_{LL}(q) & V_{LR}(q) \\ V_{LR}(q) & V_{LL}(q) \end{pmatrix} =$$

$$\frac{v(q)}{\varepsilon_0}\left[\begin{pmatrix} 1 & 0 \\ 0 & 1 \end{pmatrix} + \frac{v(q)}{\varepsilon_0}\begin{pmatrix} 1 & e^{-qd} \\ e^{-qd} & 1 \end{pmatrix}\begin{pmatrix} \Pi^0_{LL}(q) & \Pi^0_{LR}(q) \\ \Pi^0_{LR}(q) & \Pi^0_{LL}(q) \end{pmatrix}\right]^{-1}\begin{pmatrix} 1 & e^{-qd} \\ e^{-qd} & 1 \end{pmatrix} \quad (3.8)$$

And from this equation we obtain

$$V_{LL}(q) = \frac{v(q)}{\varepsilon_0}\frac{1+\frac{v(q)}{\varepsilon_0}\Pi^0_{LL}(q)(1-e^{-2qd})}{\left(1+\frac{v(q)}{\varepsilon_0}\Pi^0_{LL}(q)+\frac{v(q)}{\varepsilon_0}\Pi^0_{LR}(q)e^{-qd}\right)^2-\left(\frac{v(q)}{\varepsilon_0}\Pi^0_{LR}(q)+\frac{v(q)}{\varepsilon_0}e^{-qd}\Pi^0_{LL}(q)\right)^2}$$

$$V_{LR}(q) = \frac{v(q)}{\varepsilon_0}\frac{e^{-qd}+\frac{v(q)}{\varepsilon_0}\Pi^0_{LR}(q)(e^{-2qd}-1)}{\left(1+\frac{v(q)}{\varepsilon_0}\Pi^0_{LL}(q)+\frac{v(q)}{\varepsilon_0}\Pi^0_{LR}(q)e^{-qd}\right)^2-\left(\frac{v(q)}{\varepsilon_0}\Pi^0_{LR}(q)+\frac{v(q)}{\varepsilon_0}e^{-qd}\Pi^0_{LL}(q)\right)^2} \quad (3.9)$$

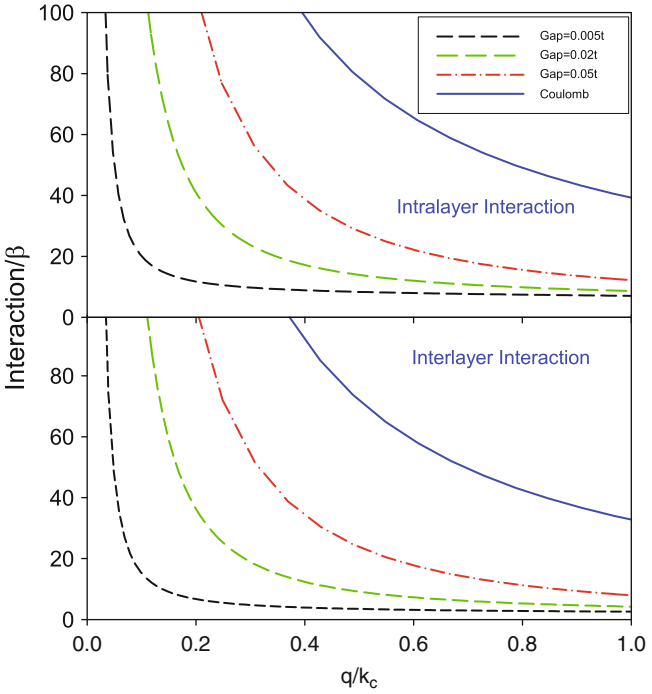

Fig. 3.3 Inter and intralayer interactions as functions of the wavevector q for different values of the gap E_g. In this figure the effective fine-structure factor is $\beta = 1.2$

In Fig. 3.3 we plot the effective interactions as function of the wavevector q, for different values of the gap E_g. In graphene the strength of the Coulomb interaction with respect the kinetic energy is characterised by an effective fine structure constant β=$e^2/\varepsilon_0\hbar v_F$. The results in Fig. 3.3 correspond to $\beta = 1.2$, but the conclusions we get are rather independent of the precise value of this parameter. For large values of the wavevector q, both intra and interlayer interactions are highly reduced from the bare Coulomb interaction. That is an indication of the ability of the system for screening short period perturbations by creating electron hole pairs. However for values of q below $\sim E_g/\hbar v_F$, the interactions $V^{LL}(q)$ and $V^{LR}(q)$ are not fully screened and both of them have a Coulomb like $1/q$ divergence. The suppression of the screening of the electron electron interaction at large distances, caused by the existence of a gap, is going to be crucial for the study of possible excitonic condensates in *AA* stacked bilayer graphene. A estimation of the critical temperature of condensate will require a selfconsistent treatment of the gap, so that the screened interactions must be computed self-consistently with energies and wave-functions obtained from the many body Hamiltonian.

Acknowledgements The author wants to thank Prof. H.A.Fertig for enlightening discussions. Funding for the work described here was provided by MICINN-SPAIN via grant No. FIS2009-08744.

References

1. Castro-Neto AH, Guinea F, Peres NMR, Novoselov KS, Geim AK (2009) The electronic properties of graphene. Rev Mod Phys 81:109
2. McCann E, Koshino M (2013) The electronic properties of bilayer graphene. Rep Prog Phys 76:056503
3. Lopes dos Santos JMB, Peres NMR, Castro Neto AH (2007) Graphene bilayer with a twist: electronic structure. Phys Rev Lett 99:256802
4. Suárez Morell E, Vargas P, Chico L, Brey L (2011) Charge redistribution and interlayer coupling in twisted bilayer graphene under electric fields. Phys Rev B 84:195421
5. Liu Z, Suenaga K, Harris PJF, Iijima S (2009) Open and closed edges of graphene layers. Phys Rev Lett 102:015501
6. de Andres PL, Ramirez R, Vergés JA (2008) Strong covalent bonding between two graphene layers. Phys Rev B 77:045403
7. Prada E, San-Jose P, Brey L, Fertig HA (2011) Band topology and the quantum spin hall effect in bilayer graphene. Solid State Commun 151(16):1075–1083
8. Berashevich J, Chakraborty T (2011) Interlayer repulsion and decoupling effects in stacked turbostratic graphene flakes. Phys Rev B 84:033403
9. Tabert CJ, Nicol EJ (2012) Dynamical conductivity of AA-stacked bilayer graphene. Phys Rev B 86:075439
10. Rakhmanov AL, Rozhkov AV, Sboychakov AO, Nori F (2012) Instabilities of the AA-stacked graphene bilayer. Phys Rev Lett 109:206801
11. Keldysh LV, Kopoev YV (1965) Possible instability of semimetallic state toward coulomb interaction. Sov Phys Solid State 6:2219
12. Lozovik YE, Yudson VI (December 1975) Feasibility of superfluidity of paired spatially separated electrons and holes; a new superconductivity mechanism. Sov J Exp Theor Phys Lett 22:274
13. Min H, Bistritzer R, Su J-J, MacDonald AH (2008) Room-temperature superfluidity in graphene bilayers. Phys Rev B 78:121401
14. Zhang C-H, Joglekar YN (2008) Excitonic condensation of massless fermions in graphene bilayers. Phys Rev B 77:233405
15. Kharitonov MY, Efetov KB (2008) Electron screening and excitonic condensation in double-layer graphene systems. Phys Rev B 78:241401
16. Kharitonov MY, Efetov KB (2010) Excitonic condensation in a double-layer graphene system. Semicond Sci Technol 25(3):034004
17. Abergel DSL, Sensarma R, Das Sarma, S (2012) Density fluctuation effects on the exciton condensate in double layer graphene. Phys Rev B 86:161412(R)
18. Sodemann I, Pesin DA, MacDonald AH (2012) Interaction-enhanced coherence between two-dimensional Dirac layers. Phys Rev B 85:195136
19. Lozovik YE, Ogarkov SL, Sokolik AA (2010) Electronelectron and electronhole pairing in graphene structures. Philos Trans R Soc A Math Phys Eng Sci 368(1932):5417–5429
20. Lozovik YE, Ogarkov SL, Sokolik AA (2012) Condensation of electron-hole pairs in a two-layer graphene system: correlation effects. Phys Rev B 86:045429
21. Wunsch B, Stauber T, Sols F, Guinea F (2006) Dynamical polarization of graphene at finite doping. New J Phys 8(12):318
22. Hwang EH, Das Sarma S (2007) Dielectric function, screening, and plasmons in two-dimensional graphene. Phys Rev B 75:205418

Chapter 4
Graphene Bloch Equations

Torben Winzer, Ermin Malić, and Andreas Knorr

Abstract The ultrafast carrier dynamics in graphene has been intensively investigated in recent years. From the theoretical side the graphene Bloch equations have been successfully applied to explain linear absorption and various features observed in optical pump-probe experiments. Here, we present a detailed derivation of the graphene Bloch equations and discuss different contributions resulting from the electron-electron and electron-phonon interaction.

4.1 Introduction

Carbon nanostructures, such as graphene and carbon nanotubes, provide unique optical and electronic properties [1–3]. In recent years, their investigations attract enormous interest in both theoretical and experimental research. From the theoretical side, the density matrix theory turned out to be an ideal technique to study the properties of these low-dimensional nanostructures. In particular, this approach allows the microscopic inclusion of many-particle effects resulting in a realistic description of the system [4, 5].

Within the density matrix formalism various features of absorption spectra of carbon structures can be studied, such as Coulomb-induced renormalization of the band structure, excitonic effects, the formation of phonon-induced sidebands and ultrafast carrier scattering [6–12]. Recently also the influence of the functionalization of carbon nanotubes with spinopyran molecules has been investigated predicting a high potential of carbon nanotubes as substrate for molecular switches [13].

T. Winzer • E. Malić • A. Knorr (✉)
Institut für Theoretische Physik, Nichtlineare Optik und Quantenelektronik,
Technische Universität Berlin, Hardenbergstr. 36, 10623 Berlin, Germany
e-mail: torben.winzer@tu-berlin.de; ermin.malic@tu-berlin.de;
andreas.knorr@physik.tu-berlin.de

R. Egger et al. (eds.), *Low-Dimensional Functional Materials*, NATO Science for Peace and Security Series B: Physics and Biophysics, DOI 10.1007/978-94-007-6618-1_4,

For graphene one recent focus of investigations, based on the density matrix formalism, lies on the ultrafast carrier dynamics. Kinetic equations for electrons and phonons describe the optical excitation and the Coulomb- and phonon-induced relaxation processes of photo-excited carries [10, 14, 15]. Within these microscopic calculations the typical bi-exponential decay measured in differential pump-probe experiments, can be well described and explained [16, 17]. Here, the strength of the approach is that the efficiency of each scattering channel can be analyzed separately to shed light on experimentally observed phenomena from a microscopic point of view. Processes like momentum [10, 15] and orientational relaxation [10, 18] can be ascribed to the corresponding responsible scattering mechanism. Therewith, the role of experimental parameters, such as the pump fluence can be studied in detail [19], resulting e.g. in a microscopic explanation of the optical saturation behavior of graphene [20]. Moreover, the microscopic description of the relaxation dynamics allows to predict various fundamental new phenomena in graphene arising from its unique band structure:

- It has been demonstrated that depending on the excitation regime, Coulomb-induced Auger processes give rise to a multiplication of photo-excited carriers, which may optimize the efficiency of graphene-based photodetectors [12, 21]. Meanwhile, there are several experimental studies revealing the important role of Auger processes in graphene [22–25].
- A recent pump-probe experiment has observed a transient population inversion in graphene [26]. Here, microscopic calculations have shown that efficient optical phonon scattering is the crucial formation mechanism [27]. Furthermore, in a gain excitation regime Auger-processes are found to be the predominant recombination mechanism being responsible for the experimentally observed transience of the population inversion on a 100 fs timescale [26, 27].
- Another graphene specific phenomenon concerns the relaxation of a current. In contrast to semiconductors, the decay of current corresponds only to the orientational relaxation, where Coulomb scattering is a crucial channel at high carrier densities [28].

In this work,[1] we present a detailed derivation of the graphene Bloch equations (GBEs) underlaying all above mentioned investigations. The GBEs describe the coupled dynamics of carriers, phonons, and microscopic polarization on a consistent footing based on density matrix theory. The Coulomb and carrier-phonon interaction are treated within the second-order Born-Markov approximation and the electron-light interaction is considered within a semi-classical approach [5]. Furthermore, a derivation of the optical and the Coulomb matrix element is presented.

[1] This work is part of the dissertation of Torben Winzer.

4.2 Hamilton Operator

The quantum mechanical properties of graphene's carrier and phonon system interacting with external electromagnetic fields is described by the Hamilton operator

$$H = H_0 + H_{cf} + H_{cc} + H_{cp}, \tag{4.1}$$

accounting for the free energy of carriers and phonons H_0, the carrier-field coupling H_{cf}, the carrier-carrier interaction H_{cc} and the carrier-phonon interaction H_{cp}. Applying electron field operators, a classical electromagnetic field, and quantized displacements of the ions we transform the Hamilton operator into the representation of second quantization [5]. All contributions of Eq. (4.1) can be expressed in terms of creation and annihilation operators, where $a_{\mathbf{a}}^{(\dagger)}$ annihilates (creates) an electron in the state $\mathbf{a} = (\mathbf{k}_a, \lambda_a)$ with the electron wave vector $\mathbf{k}_a$ in the band $\lambda_a = v, c$. The corresponding phonon operators $b_{\mathbf{n}}^{(\dagger)}$ acts on the phonon state $\mathbf{n} = (\mathbf{q}_n, j_n)$ with the phonon momentum $\mathbf{q}$ in the mode j. Due to their fermionic nature the electronic operators fulfill the anti-commutator relations

$$[a_{\mathbf{a}}, a_{\mathbf{b}}^\dagger]_+ = \delta_{\mathbf{a},\mathbf{b}} \quad \text{and} \quad [a_{\mathbf{a}}^{(\dagger)}, a_{\mathbf{b}}^{(\dagger)}]_+ = 0. \tag{4.2}$$

Consequently, the phonon operators obey the bosonic commutator relations

$$[b_{\mathbf{n}}, b_{\mathbf{m}}^\dagger]_- = \delta_{\mathbf{n},\mathbf{m}} \quad \text{and} \quad [b_{\mathbf{n}}^{(\dagger)}, b_{\mathbf{m}}^{(\dagger)}]_- = 0. \tag{4.3}$$

Therewith, the free Hamiltonian reads

$$H_0 = \sum_{\mathbf{a}} \varepsilon_{\mathbf{a}} a_{\mathbf{a}}^\dagger a_{\mathbf{a}} + \sum_{\mathbf{n}} \hbar\omega_{\mathbf{n}} \left(b_{\mathbf{n}}^\dagger b_{\mathbf{n}} + \frac{1}{2} \right), \tag{4.4}$$

where $\varepsilon_{\mathbf{a}}$ denotes graphene's electronic band structure, discussed in Sect. 4.3.1, and $\hbar\omega_{\mathbf{n}}$ is the phonon dispersion.

Within the radiation gauge [29] the carrier-field coupling is given by

$$H_{cf} = i\hbar \frac{e_0}{m_0} \sum_{\mathbf{ab}} \mathbf{M}_{\mathbf{a},\mathbf{b}} \cdot \mathbf{A}(t) a_{\mathbf{a}}^\dagger a_{\mathbf{b}} + \frac{e_0^2}{2m_0} \mathbf{A}(t)^2 \sum_{\mathbf{a}} a_{\mathbf{a}}^\dagger a_{\mathbf{a}}, \tag{4.5}$$

with the positive elementary electron charge e_0 and the free electron mass m_0. The optical matrix element $\mathbf{M}_{\mathbf{a},\mathbf{b}} = \langle \Psi_{\mathbf{a}}(\mathbf{r}) | \nabla_{\mathbf{r}} | \Psi_{\mathbf{b}}(\mathbf{r}) \rangle$ determines the coupling strength between the electronic system and an external field in terms of its vector potential $\mathbf{A}(t)$, where $\Psi_{\mathbf{a}}(\mathbf{r})$ denotes the single-particle wave function having energies $\varepsilon_{\mathbf{a}}$, cf. Eq. (4.4). The optical matrix element of graphene will be discussed in detail in Sect. 4.3.2.

The Hamilton operator of the Coulomb interaction reads

$$H_{cc} = \frac{1}{2} \sum_{\mathbf{abcd}} V_{\mathbf{cd}}^{\mathbf{ab}} a_{\mathbf{a}}^{\dagger} a_{\mathbf{b}}^{\dagger} a_{\mathbf{d}} a_{\mathbf{c}}, \tag{4.6}$$

and couples to two initial ($\mathbf{a}$, $\mathbf{b}$) and two final electron states ($\mathbf{c}$, $\mathbf{d}$). The corresponding matrix element is given by $V_{\mathbf{cd}}^{\mathbf{ab}} = \langle \Psi_{\mathbf{a}}(\mathbf{r}) \Psi_{\mathbf{b}}(\mathbf{r}') | V(\mathbf{r}-\mathbf{r}') | \Psi_{\mathbf{d}}(\mathbf{r}') \Psi_{\mathbf{c}}(\mathbf{r}) \rangle$ with the Coulomb potential $V(\mathbf{r}-\mathbf{r}')$. A more detailed discussion of graphene's Coulomb matrix element is presented in Sect. 4.3.3.

The electron-phonon Hamilton operator, describing the interaction between both systems, reads in second quantization:

$$H_{cp} = \sum_{\lambda_1 \lambda_2 \mathbf{k}} \sum_{j\mathbf{q}} \left[g_{\mathbf{k},\mathbf{q}}^{\lambda_1 \lambda_2 j} a_{\mathbf{k}}^{\lambda_1 \dagger} a_{\mathbf{k}-\mathbf{q}}^{\lambda_2} b_{\mathbf{q}}^{j} + g_{\mathbf{k},\mathbf{q}}^{\lambda_1 \lambda_2 j *} a_{\mathbf{k}-\mathbf{q}}^{\lambda_2 \dagger} a_{\mathbf{k}}^{\lambda_1} b_{\mathbf{q}}^{j \dagger} \right]. \tag{4.7}$$

The first term describes an electronic transition from $\mathbf{k}-\mathbf{q}$ to $\mathbf{k}$ initiated by the absorption of a phonon with the momentum $\mathbf{q}$. The second term is the inverse process induced by the emission of a phonon. The applied matrix elements $g_{\mathbf{k},\mathbf{q}}^{\lambda_1 \lambda_2 j}$ are taken from DFT-calculations for the optical phonons [30] and from Ref. [31] for the acoustic phonons.

4.3 Bandstructure and Matrix Elements

To determine the Hamilton operator explicitly, the band structure and the matrix elements need to be known. In this section, tight-binding wave functions are applied to work out graphene's band structure, the optical as well as the Coulomb matrix element analytically.

4.3.1 Bandstructure of Graphene

The band structure of graphene is formed by the four valence electrons of both carbon atom in the unit cell. Respectively, three electrons configure a sp^2-hybridization being responsible for the extremely strong in-plane binding in graphene [32]. The corresponding σ-bands are energetically separated and therefore not relevant for phenomena resulting from optical excitations in the infrared and THz regime [33]. Consequently, this work focuses on the fourth electron, which has a $2p_z$-shaped orbital. Due to the localization of these orbitals at the atomic positions, the electronic wave function $\Psi(\mathbf{k})$ can be described in a tight-binding approach [34,35] as a linear combination of both equivalent sublattices A and B

$$\Psi(\mathbf{k},\mathbf{r}) = c_A(\mathbf{k}) \Phi_A(\mathbf{k},\mathbf{r}) + c_B(\mathbf{k}) \Phi_B(\mathbf{k},\mathbf{r}), \tag{4.8}$$

where $c_l(\mathbf{k})$ are the tight-binding coefficients and $\Phi_l(\mathbf{k})$ the sublattice wave function with $l = A, B$. The latter are the normalized functions

$$\Phi_l(\mathbf{k}, \mathbf{r}) = \frac{1}{\sqrt{N}} \sum_{\mathbf{R}_l} e^{i\mathbf{k}\cdot\mathbf{R}_l} \phi(\mathbf{r} - \mathbf{R}_l), \tag{4.9}$$

which are periodic on the sublattice $\mathbf{R}_l$. N is here the number of unit cells in the system and $\phi(\mathbf{r})$ is the atomic orbital. With this ansatz the Schrödinger equation

$$H\Psi(\mathbf{k}, \mathbf{r}) = \varepsilon_{\mathbf{k}} \Psi(\mathbf{k}, \mathbf{r}) \tag{4.10}$$

can be solved analytically. To this end Eq. (4.10) is multiplied with $\Phi_A^*(\mathbf{k})$ and $\Phi_B(\mathbf{k})$ respectively and integration yields

$$\begin{pmatrix} H_{AA} - \varepsilon_{\mathbf{k}} S_{AA} & H_{AB} - \varepsilon_{\mathbf{k}} S_{AB} \\ H_{BA} - \varepsilon_{\mathbf{k}} S_{BA} & H_{BB} - \varepsilon_{\mathbf{k}} S_{BB} \end{pmatrix} \begin{pmatrix} c_A(\mathbf{k}) \\ c_B(\mathbf{k}) \end{pmatrix} = 0, \tag{4.11}$$

with $H_{ij} = \langle \Phi_i(\mathbf{k}) | H | \Phi_j(\mathbf{k}) \rangle$ and $S_{ij} = \langle \Phi_i(\mathbf{k}) | \Phi_j(\mathbf{k}) \rangle$. Taking into account the symmetry relations $H(S)_{AA} = H(S)_{BB}$ and $H(S)_{AB} = H(S)_{BA}^*$, arising from the equivalence of both sublattices, Eq. (4.11) exhibits non-trivial solutions, if the eigenvalues fulfill

$$\varepsilon_{\mathbf{k}}^{\pm} = -\Theta \pm \sqrt{\Theta^2 - H_{AA}^2 + |H_{AB}|^2}, \tag{4.12}$$

with

$$\Theta = \frac{\Re[H_{AB} S_{AB}^*] - H_{AA} S_{AA}}{|S_{AA}|^2 - |S_{AB}|^2}. \tag{4.13}$$

It remains to determine the matrix elements H_{ij} and S_{ij}, e.g.

$$H_{AB} = \frac{1}{N} \sum_{\mathbf{R}_A, \mathbf{R}_B} e^{i\mathbf{k}(\mathbf{R}_B - \mathbf{R}_A)} \langle \phi(\mathbf{r} - \mathbf{R}_A) | H | \phi(\mathbf{r} - \mathbf{R}_B) \rangle. \tag{4.14}$$

Due to the localization of the atomic orbital, H_{AB} can be treated within the next neighbor approximation, i.e. for each summand $\mathbf{R}_A$ only the three adjacent B atoms at $\mathbf{R}_{B_1}$, $\mathbf{R}_{B_2}$, and $\mathbf{R}_{B_3}$ are considered [36]. In particular, one has $\mathbf{R}_{B_i} - \mathbf{R}_A = \mathbf{b}_i$ and the three tight-binding integrals $\gamma_0 = \langle \phi(\mathbf{r} - \mathbf{R}_A) | H | \phi(\mathbf{r} - \mathbf{R}_{B_i}) \rangle$ are constant and independent of i, since the $2p_z$-orbital depends only on distance $\phi(\mathbf{r}) \equiv \phi(|\mathbf{r}|)$ [35]. Common values for γ_0 are in the range between -2.5 and $-3.0\,\mathrm{eV}$ [35, 37]. Therewith Eq. (4.14) yields:

$$H_{AB} = \gamma_0 e(\mathbf{k}), \tag{4.15}$$

with the nearest neighbor sum

$$e(\mathbf{k}) = \sum_{i=1}^{3} e^{i\mathbf{k}\mathbf{b}_i}. \tag{4.16}$$

The other matrix elements can be treated analogously: H_{AA} is a constant, which is chosen to be zero to benchmark the energy scale with respect to the Fermi level. The normalization of the sublattice wave function Eq. (4.9) directly yields $S_{AA} = 1$, and S_{AB} is given by $S_{AB} = s_0 e(\mathbf{k})$ with the overlap integral $s_0 = \langle \phi(\mathbf{r}) | \phi(\mathbf{r} - \mathbf{b}_1) \rangle$, here common values are between 0.06 and 0.13 [35,38]. Later in this work the overlap integral will be neglect providing still a good description around the Dirac point. Considering all matrix elements and with Eqs. (4.12) and (4.13) the band structure reads:

$$\varepsilon_{\mathbf{k}}^{\lambda} = \frac{-\sigma_\lambda \gamma_0 |e(\mathbf{k})|}{1 - \sigma_\lambda s_0 |e(\mathbf{k})|}, \tag{4.17}$$

where $\lambda = c$ ($\lambda = v$) denotes the conduction (valence) band with $\sigma_c = 1$ ($\sigma_v = -1$). The shape of the band structure is mainly determined by the function:

$$|e(\mathbf{k})| = \sqrt{3 + 2\cos(a_0 k_y) + 4\cos\left(\frac{\sqrt{3}a_0}{2} k_x\right) \cos\left(\frac{a_0}{2} k_y\right)}, \tag{4.18}$$

offering a saddle at the M point $\left(\mathbf{M} = \frac{2\pi}{a_0\sqrt{3}}\mathbf{e}_x\right)$ and the characteristic linear band crossing around the K/K′ point $\left(\mathbf{K}/\mathbf{K}' = \pm\frac{4\pi}{3a_0}\mathbf{e}_y\right)$, where $a_0 = 0.2461\,\text{nm}$ is graphene's lattice constant [36].

Finally, with Eqs. (4.17) and (4.11) and with the normalization of the sublattice wave function, the tight-binding coefficients can be determined:

$$c_B^{\lambda}(\mathbf{k}) = \frac{1}{\sqrt{2}} \frac{1}{\sqrt{1 - \sigma_\lambda s_0 |e(\mathbf{k})|}} \quad \text{and} \quad c_A^{\lambda}(\mathbf{k}) = -\sigma_\lambda \frac{e(\mathbf{k})}{|e(\mathbf{k})|} c_B^{\lambda}(\mathbf{k}). \tag{4.19}$$

Therewith, the entire tight-binding wave function is available, which is utilized to calculate the optical and Coulomb matrix element in Sects. 4.3.2 and 4.3.3.

Linear Band Approximation

Close to the Dirac point the band structure from Eq. (4.17) can be approximated linearly. Therefore, the overlap integral s_0 is neglected and the nearest neighbor sum (Eq. 4.16) is expand up to the first order around the Dirac point:

$$e(\mathbf{k}) \approx e(\mathbf{K}) + [\nabla_{\mathbf{k}} e(\mathbf{k})]\Big|_{\mathbf{k}=\mathbf{K}} (\mathbf{k} - \mathbf{K}) = -\frac{a_0\sqrt{3}}{2} \left(i\tilde{k}_x + \tilde{k}_y\right), \tag{4.20}$$

with $\mathbf{K} = \frac{4\pi}{3a_0}\mathbf{e}_y$ and $\tilde{\mathbf{k}} = \mathbf{k} - \mathbf{K}$ is the electron wave vector with respect to the Dirac point. Therewith the band structure reads:

$$\varepsilon_{\mathbf{k}}^{\lambda} = \sigma_{\lambda} v_F \tilde{k}, \tag{4.21}$$

with $v_F = -\gamma_0 a_0 \sqrt{3}/2 \approx 0.605\,\mathrm{eVnm}$ corresponding to a Fermi velocity of $0.92\,\mathrm{nm/fs}$.

Density of States

The density of states is defined by

$$D(\varepsilon) = \frac{1}{A} \sum_{s\lambda\mathbf{k}} \delta(\varepsilon - \varepsilon_{\mathbf{k}}^{\lambda}), \tag{4.22}$$

where A is the area of the graphene sheet. For small energies ε the linear band structure Eq. (4.21) can be applied and the $\mathbf{k}$-sum is restricted to the regions around the K and K' point. Considering the degeneracy of spin Eq. (4.22) results in a linear density of states:

$$D(\varepsilon) = \frac{8}{3\pi\gamma_0^2 a_0^2} |\varepsilon|. \tag{4.23}$$

In particular, the density of states vanishes at the Dirac point.

4.3.2 Optical Matrix Element

The optical matrix element from Eq. (4.5) determines the strength of coupling between the electronic system and an external field in terms of its vector potential $\mathbf{A}(t)$. In second quantization the matrix element is given by [5]:

$$\mathbf{M}_{\mathbf{k},\mathbf{k}'}^{\lambda,\lambda'} = \langle \Psi^{\lambda}(\mathbf{k},\mathbf{r}) | \nabla_{\mathbf{r}} | \Psi^{\lambda'}(\mathbf{k}',\mathbf{r}) \rangle. \tag{4.24}$$

Applying the tight-binding wave function (Eq. 4.8), the optical matrix element can be treated within the next-neighbor approximation [39,40]. Exploiting the symmetry properties of the $2p_z$-orbital yields

$$\mathbf{M}_{\mathbf{k},\mathbf{k}'}^{v,c} = \delta_{\mathbf{k},\mathbf{k}'} \frac{1}{\sqrt{1 - s_0^2 |e(\mathbf{k})|^2}} \frac{M}{|e(\mathbf{k})|} \Re \left[e^*(\mathbf{k}) \sum_{i=1}^{3} e^{i\mathbf{k}\mathbf{b}_i} \frac{\mathbf{b}_i}{|\mathbf{b}_i|} \right], \tag{4.25}$$

and

$$\mathbf{M}^{v,v}_{\mathbf{k},\mathbf{k}'} = \delta_{\mathbf{k},\mathbf{k}'} \frac{i}{\sqrt{1-s_0^2|e(\mathbf{k})|^2}} \frac{M}{|e(\mathbf{k})|} \Im \left[e^*(\mathbf{k}) \sum_{i=1}^{3} e^{i\mathbf{k}\mathbf{b}_i} \frac{\mathbf{b}_i}{|\mathbf{b}_i|} \right], \tag{4.26}$$

for interband and intraband processes, respectively [39, 40]. A detailed derivation and a Cartesian parametrization is found in the Appendix 4.A.1. The Kronecker $\delta_{\mathbf{k},\mathbf{k}'}$ allows only direct optical transitions neglecting the quantum mechanical momentum of the photons.[2] Note, the optical matrix element is a imaginary number for $\lambda = \lambda'$, whereas interband transitions $\lambda \neq \lambda'$ are described by a real-valued coupling. Close to the Dirac point the influence of the overlap s_0 is small and will be neglect in the following. Then, the optical matrix element fulfills the symmetry relations $\mathbf{M}^{v,c}_{\mathbf{k}} = \mathbf{M}^{c,v}_{\mathbf{k}}$ and $\mathbf{M}^{v,v}_{\mathbf{k}} = -\mathbf{M}^{c,c}_{\mathbf{k}}$.

Optical Matrix Element Close to the Dirac Point

For excitation energies in the THz and near infrared regime the optical matrix elements can be further simplified. Regarding the optical elements as a vector field around the Dirac point, it can be shown that $\mathbf{M}^{vc}_{\mathbf{k}}$ is close to a pure rotational field, whereas the intraband matrix element is approximately a pure radial field. Therefore, both vector fields are separated in their rotational and radial parts:

$$\mathbf{M} = M_{(k)}\mathbf{e}_k + M_{(\phi)}\mathbf{e}_\phi, \tag{4.27}$$

with $M_{(i)} = \mathbf{M}\cdot\mathbf{e}_i$. Neglecting the divergence of the interband matrix element and the rotation of $\mathbf{M}^{cc}_{\mathbf{k}}$, the $M_{(i)}$ can be expanded at the Dirac point by applying l'Hôpital's rule. The simplified optical matrix elements read:

$$\mathbf{M}^{vc}_{\mathbf{k}} = \frac{3}{2} M \mathbf{e}_\phi \quad \text{and} \quad \mathbf{M}^{cc}_{\mathbf{k}} = i\frac{3}{2} M \mathbf{e}_k. \tag{4.28}$$

In particular, the intraband matrix element is directly related to the band structure via $\mathbf{M}^{cc}_{\mathbf{k}} \propto \nabla_{\mathbf{k}}\varepsilon_{\mathbf{k}}$. For the interband matrix element the direction of rotation reverses at the K' point.

4.3.3 Coulomb Matrix Element

The Coulomb matrix element in second quantization is given by [4]:

$$V^{\mathbf{ab}}_{\mathbf{cd}} = \langle \Psi_{\mathbf{a}}(\mathbf{r}), \Psi_{\mathbf{b}}(\mathbf{r}') | V(\mathbf{r}-\mathbf{r}') | \Psi_{\mathbf{d}}(\mathbf{r}'), \Psi_{\mathbf{c}}(\mathbf{r}) \rangle. \tag{4.29}$$

[2] In the following the optical matrix element will be denoted only with a single electron wave vector. Nevertheless, it still contains the Kronecker $\delta_{\mathbf{k},\mathbf{k}'}$.

Applying the tight-binding wave functions (Eq. 4.8) and the $2p_z$-function with an effective charge number $Z \approx 4.6$ for the atomic orbitals, the Coulomb matrix element can be treated analytically within the next-neighbor approximation. The derivation in Appendix 4.A.2 results in

$$V_{\mathbf{cd}}^{\mathbf{ab}} = V_q \mathscr{V}_q^2 f(\mathbf{a},\mathbf{c}) f(\mathbf{b},\mathbf{d}) \delta_{\mathbf{k}_1+\mathbf{k}_2,\mathbf{k}_3+\mathbf{k}_4}, \tag{4.30}$$

with $q = |\mathbf{k}_3 - \mathbf{k}_1|$. Here, $V_q = \frac{1}{L^2}\frac{e_0^2}{2\varepsilon_0 q}$ is the Fourier transform of the two-dimensional Coulomb potential. The modification of the Coulomb potential $\mathscr{V}_q = \left[(qa_B/Z)^2 + 1\right]^{-3}$ arises from the integral over the $2p_z$-orbitals. In the case of large momentum transfers, $\mathscr{V}_q$ causes an effective decay of the Coulomb potential $\propto q^{-13}$ [41] . However, for all processes taking place within one Dirac valley it is $q \ll a_B/Z$ and therewith $\mathscr{V}_q \approx 1$. The Kronecker $\delta_{\mathbf{k}_1+\mathbf{k}_2,\mathbf{k}_3+\mathbf{k}_4}$ ensures the conservation of momentum for Coulomb-induced processes. The graphene specific form factor

$$f(\mathbf{a},\mathbf{c}) = \frac{1}{2}\left[1 + \sigma_{\lambda_\mathbf{a}}\sigma_{\lambda_\mathbf{c}} \frac{e^*(\mathbf{k}_a)}{|e(\mathbf{k}_a)|}\frac{e(\mathbf{k}_c)}{|e(\mathbf{k}_c)|}\right] \tag{4.31}$$

results directly from the tight-binding ansatz. Within the linear approximation for the nearest neighbor sum (Eq. 4.20) the form factor describes the angle dependence of each Coulomb process

$$f(\mathbf{a},\mathbf{c}) = \frac{1}{2}\left[1 + \sigma_{\lambda_\mathbf{a}}\sigma_{\lambda_\mathbf{c}} e^{-i(\phi_c - \phi_a)}\right], \tag{4.32}$$

where ϕ_a is here the polar angle of $\mathbf{k}_a$. Therewith, the Coulomb matrix element becomes maximal for parallel processes within a band, whereas it vanishes for anti-parallel electron wave vectors (backscattering). For interband processes the situation is reversed.

Screening

The Coulomb potential V_q is screened due the presence of other carriers. Throughout this work the screened Coulomb potential $W_\mathbf{q} = V_q/\varepsilon_{sub}\varepsilon(\mathbf{q})$ is applied considering the influence of the substrate ε_{sub} as well as graphene's intrinsic carriers.

Assuming that the substrate located only on one side of the graphene monolayer, the corresponding screening can be considered simply by $\varepsilon_{sub} = (\varepsilon_{r,sub} + \varepsilon_{r,vac})/2$ [42].

The intrinsic screening can be derived within the density matrix formalism resulting in the static limit [43, 44]:

$$\varepsilon(\mathbf{q}) = 1 - \frac{2}{\gamma_0} V_q \mathscr{V}_q^2 \sum_\mathbf{k} \frac{1}{|e(\mathbf{k}-\mathbf{q})| + |e(\mathbf{k})|}\left(1 - \Re\left[\frac{e^*(\mathbf{k})e(\mathbf{k}-\mathbf{q})}{|e(\mathbf{k})||e(\mathbf{k}-\mathbf{q})|}\right]\right). \tag{4.33}$$

Within the tight-binding approach the dielectric function $\varepsilon(\mathbf{q})$ can be evaluated numerically. For $T = 0\,\mathrm{K}$ and small momentum transfers (within one Dirac valley) the resulting screening is approximately constant $\varepsilon(\mathbf{q}) \approx 4.66$ [10, 44].

4.4 Graphene Bloch Equations

With the knowledge about the Hamilton operator, the matrix elements, and the dispersion of electrons and phonons we have all ingredients to determine the dynamics of an arbitrary operator quantity $\mathscr{O}(t)$. Its temporal evolution is described by the Heisenberg equation of motion:

$$i\hbar \frac{d}{dt}\mathscr{O}(t) = [\mathscr{O}(t), H]_-. \tag{4.34}$$

The relevant quantities in the coupled electron-phonon system are the carrier occupation $\rho_{\mathbf{k}}^{\lambda} = \langle a_{\mathbf{k}}^{\lambda\dagger} a_{\mathbf{k}}^{\lambda} \rangle$, the microscopic polarization $p_{\mathbf{k}} = \langle a_{\mathbf{k}}^{v\dagger} a_{\mathbf{k}}^{c} \rangle$ which is a measure for the transition probability between both bands, and the phonon population $n_{\mathbf{q}}^{j} = \langle b_{\mathbf{q}}^{j\dagger} b_{\mathbf{q}}^{j} \rangle$. In equilibrium $\rho_{\mathbf{k}}^{\lambda}$ and $n_{\mathbf{q}}^{j}$ are given by a Fermi-Dirac and a Bose-Einstein distribution, respectively.

4.4.1 Free Energy and Carrier-Light Coupling

The optical properties of the free carrier system are described by the Hamilton operators H_0 (Eq. 4.4) and H_{cf} (Eq. 4.5). The Heisenberg equation (4.34) yields the Bloch equations:

$$\frac{d}{dt}\rho_{\mathbf{k}}^{c} = -\frac{d}{dt}\rho_{\mathbf{k}}^{v} = 2\Im\left[\Omega_{\mathbf{k}}^{vc*} p_{\mathbf{k}}\right], \tag{4.35}$$

$$\frac{d}{dt}p_{\mathbf{k}} = -i\left[\Delta\omega_{\mathbf{k}} - \Omega_{\mathbf{k}}^{vv} + \Omega_{\mathbf{k}}^{cc}\right] p_{\mathbf{k}} - i\Omega_{\mathbf{k}}^{vc}\left[\rho_{\mathbf{k}}^{c} - \rho_{\mathbf{k}}^{v}\right], \tag{4.36}$$

with $\Delta\omega_{\mathbf{k}} = (\varepsilon_{\mathbf{k}}^{c} - \varepsilon_{\mathbf{k}}^{v})/\hbar$ and $\Omega_{\mathbf{k}}^{\lambda\lambda'} = i\frac{e_0}{m_0}\mathbf{M}_{\mathbf{kk}}^{\lambda\lambda'}\mathbf{A}(t)$. In the presence of an external field, the Rabi frequency $\Omega_{\mathbf{k}}^{vc}$ couples the dynamics of the carrier occupation and $p_{\mathbf{k}}$. The real-numbered optical intraband contribution $\Omega_{\mathbf{k}}^{\lambda\lambda}$ as well as the free energy part gives rise to oscillations of the microscopic polarization.

4.4.2 Many-Particle Interactions

The treatment of many-particle interactions, such as the carrier-carrier or carrier-phonon coupling leads to Boltzmann-like scattering equations describing the relaxation dynamics after an optical excitation. The derivation of the equations of motion needs more effort and certain approximations, which are described in the following.

Correlation Expansion

Applying the Heisenberg equation of motion (Eq. 4.34) for a many-particle Hamilton operator, e.g. H_{cc} or H_{cp}, the dynamics of an arbitrary two-operator expectation value (EV) $\langle 2\rangle = \langle c_{\mathbf{a}} c_{\mathbf{b}}\rangle$, like $\rho^{\lambda}_{\mathbf{k}}$, $p_{\mathbf{k}}$, or $n^{j}_{\mathbf{q}}$, couples to the dynamics of higher order EVs $\langle n\rangle = \langle c_{\mathbf{a}} c_{\mathbf{b}} \cdots c_{\mathbf{n}}\rangle$ with $n > 2$. The latter couples again to the next higher order resulting in an infinite hierarchy of equations, which describes the many-particle system exactly [45]. However, to obtain an manageable finite set of equations the correlation expansion is applied allowing a decoupling at a desired order [45]. The idea is to factorize a n-th order EV into all possible permutation of same- and lower-order correlations:

$$\begin{aligned}
\langle c_{\mathbf{a}}\rangle &= \langle c_{\mathbf{a}}\rangle^{c} \\
\langle c_{\mathbf{a}} c_{\mathbf{b}}\rangle &= \langle c_{\mathbf{a}} c_{\mathbf{b}}\rangle^{c} + \langle c_{\mathbf{a}}\rangle^{c}\langle c_{\mathbf{b}}\rangle^{c} \\
\langle c_{\mathbf{a}} c_{\mathbf{b}} c_{\mathbf{c}}\rangle &= \langle c_{\mathbf{a}} c_{\mathbf{b}} c_{\mathbf{c}}\rangle^{c} + (-1)^{\sigma_f(abc)}\langle c_{\mathbf{a}}\rangle^{c}\langle c_{\mathbf{b}} c_{\mathbf{c}}\rangle^{c} + (-1)^{\sigma_f(cab)}\langle c_{\mathbf{c}}\rangle^{c}\langle c_{\mathbf{a}} c_{\mathbf{b}}\rangle \\
&\quad + (-1)^{\sigma_f(bca)}\langle c_{\mathbf{b}}\rangle^{c}\langle c_{\mathbf{c}} c_{\mathbf{a}}\rangle^{c} + \langle c_{\mathbf{a}}\rangle^{c}\langle c_{\mathbf{b}}\rangle^{c}\langle c_{\mathbf{c}}\rangle^{c} \\
&\cdots ,
\end{aligned} \tag{4.37}$$

where $\sigma_f(\cdots)$ is the number of permutations of fermion operators. Supposing that, the higher the order the less important is the contribution of the corresponding correlation, the set of equations can be closed at a certain order n by neglecting $\langle n\rangle^{c}$. This also corresponds to perturbation theory in the screened interaction $W_{\mathbf{q}}$. Since the number of fermions have to be conserved only terms with the same number of electron creation and annihilation operators contributes.

Markov-Approximation

The Markov approximation is a procedure to approximately solve intermediate differential equations, emerging in the derivation of the scattering equations. The structure of these intermediate equations reads [4]:

$$\frac{d}{dt}x(t) = (i\tilde{\omega} - \gamma)x(t) + iQ(t). \tag{4.38}$$

For $x(-\infty) = 0$ a formal integration yields

$$x(t) = i \int_0^\infty dt' e^{(i\tilde{\omega}-\gamma)t'} Q(t-t'). \tag{4.39}$$

The idea of the Markov-approximation is that the memory kernel $-t'$ of Q can be neglected, if $Q(t-t')$ varies slowly compared to the oscillation $e^{-i\tilde{\omega}t'}$. However, in this work $Q(t-t')$ typically contains two-operator or more EVs $\langle a_{\mathbf{a}}^\dagger a_{\mathbf{b}} \rangle(t)$ having fast oscillations arising from the free energy, cf. Eqs. (4.4) and (4.36). The memory kernel of this oscillations have to be considered via

$$\langle a_{\mathbf{a}}^\dagger a_{\mathbf{b}} \rangle(t-t') \approx e^{-\frac{i}{\hbar}(\varepsilon_{\mathbf{a}}-\varepsilon_{\mathbf{b}})t'} \langle a_{\mathbf{a}}^\dagger a_{\mathbf{b}} \rangle(t), \tag{4.40}$$

resulting in $Q(t-t') \approx Q(t)e^{-i\omega t'}$, where ω contains all memory oscillations. Then, $Q(t)$ can be taken out of the integral, which can be evaluated analytically subsequently. Integration yields the Heitler-zeta function [46]:

$$x(t) = Q(t) \left[i \frac{\gamma}{\Delta\omega^2 + \gamma^2} - \mathscr{P}\left(\frac{\Delta\omega}{\Delta\omega^2 + \gamma^2} \right) \right], \tag{4.41}$$

with $\Delta\omega = \tilde{\omega} - \omega$ and $\mathscr{P}(\cdot)$ denotes the principal value. In the case of a vanishing γ the integral in Eq. (4.39) yields:

$$x(t) = Q(t) \left[i\pi\delta(\Delta\omega) - \mathscr{P}\left(\frac{1}{\Delta\omega} \right) \right], \tag{4.42}$$

where the sharp δ-function represents the conservation of energy in the considered scattering processes.

4.4.3 Coulomb Interaction

In this section the Coulomb-induced dynamics is considered up to the second order in correlation expansion. The obtained equations are responsible for the ultrafast dephasing of polarization and redistribution of optically excited carriers in graphene.

Starting from the Heisenberg equation (4.34) the Hamiltonian for the Coulomb interaction yields:

$$i\hbar \frac{d}{dt} \langle a_{\mathbf{1}}^\dagger a_{\mathbf{2}} \rangle \Big|_{H_{cc}} = \sum_{\mathbf{abc}} \left[V_{\mathbf{bc}}^{\mathbf{2a}} \langle a_{\mathbf{1}}^\dagger a_{\mathbf{a}}^\dagger a_{\mathbf{c}} a_{\mathbf{b}} \rangle - V_{\mathbf{1c}}^{\mathbf{ab}} \langle a_{\mathbf{a}}^\dagger a_{\mathbf{b}}^\dagger a_{\mathbf{c}} a_{\mathbf{2}} \rangle \right] \tag{4.43}$$

Here, the dynamics of an electronic density matrix element couples to four-operators EVs. Applying the correlation expansion for the four-operator EVs, they can be

divided into the first-order Hartree-Fock contribution (HF) and the second-order correlation term ($corr$) with

$$i\hbar\frac{d}{dt}\langle a_{\mathbf{1}}^{\dagger}a_{\mathbf{2}}\rangle\Big|_{HF} = \sum_{\mathbf{abc}}\Big\{V_{\mathbf{bc}}^{\mathbf{2a}}\left[\langle a_{\mathbf{1}}^{\dagger}a_{\mathbf{b}}\rangle\langle a_{\mathbf{a}}^{\dagger}a_{\mathbf{c}}\rangle - \langle a_{\mathbf{1}}^{\dagger}a_{\mathbf{c}}\rangle\langle a_{\mathbf{a}}^{\dagger}a_{\mathbf{b}}\rangle\right] - V_{\mathbf{1c}}^{\mathbf{ab}}\left[\langle a_{\mathbf{a}}^{\dagger}a_{\mathbf{2}}\rangle\langle a_{\mathbf{b}}^{\dagger}a_{\mathbf{c}}\rangle - \langle a_{\mathbf{a}}^{\dagger}a_{\mathbf{c}}\rangle\langle a_{\mathbf{b}}^{\dagger}a_{\mathbf{2}}\rangle\right]\Big\} \tag{4.44}$$

and

$$i\hbar\frac{d}{dt}\langle a_{\mathbf{1}}^{\dagger}a_{\mathbf{2}}\rangle\Big|_{corr} = \sum_{\mathbf{abc}}\left[V_{\mathbf{bc}}^{\mathbf{2a}}\langle a_{\mathbf{1}}^{\dagger}a_{\mathbf{a}}^{\dagger}a_{\mathbf{c}}a_{\mathbf{b}}\rangle^{c} - V_{\mathbf{1c}}^{\mathbf{ab}}\langle a_{\mathbf{a}}^{\dagger}a_{\mathbf{b}}^{\dagger}a_{\mathbf{c}}a_{\mathbf{2}}\rangle^{c}\right]. \tag{4.45}$$

For reasons of a better readability the notations $\sigma_{\mathbf{12}} = \langle a_{\mathbf{1}}^{\dagger}a_{\mathbf{2}}\rangle, \sigma_{1}^{12} = \langle a_{\mathbf{k}_1}^{\lambda_1\dagger}a_{\mathbf{k}_1}^{\lambda_2}\rangle$ and $\Lambda_{\mathbf{34}}^{\mathbf{12}} = \langle a_{\mathbf{1}}^{\dagger}a_{\mathbf{2}}^{\dagger}a_{\mathbf{3}}a_{\mathbf{4}}\rangle$ are used in following.

Hartree-Fock Contribution

Neglecting the higher-order correlations the Hartree-Fock factorization is a mean-field approximation. Within this Hartree-Fock approximation

$$\langle a_{\mathbf{1}}^{\dagger}a_{\mathbf{2}}^{\dagger}a_{\mathbf{3}}a_{\mathbf{4}}\rangle \approx \langle a_{\mathbf{1}}^{\dagger}a_{\mathbf{4}}\rangle\langle a_{\mathbf{2}}^{\dagger}a_{\mathbf{3}}\rangle - \langle a_{\mathbf{1}}^{\dagger}a_{\mathbf{3}}\rangle\langle a_{\mathbf{2}}^{\dagger}a_{\mathbf{4}}\rangle \tag{4.46}$$

Coulomb-induced modification of linear absorption spectra can be described [47].

In a spatial homogeneous system only density matrix elements, which are diagonal with respect to the electronic wave vector, have a non-vanishing EV: $\sigma_{\mathbf{12}} = \sigma_{1}^{12}\delta_{\mathbf{k}_1,\mathbf{k}_2}(1 \mathrel{\hat{=}} k_1)$. Therewith the Hartree-Fock contribution (4.44) can be rewritten as:

$$i\hbar\frac{d}{dt}\sigma_{1}^{12}\Big|_{HF} = \sum_{\mathbf{k}_b}\sum_{\lambda_a\lambda_b\lambda_c}\left[V_{\mathbf{k}_1\,\mathbf{k}_b\,\lambda_1\,\lambda_c}^{\mathbf{k}_b\,\mathbf{k}_1\,\lambda_b\,\lambda_a}\sigma_{b}^{bc}\sigma_{1}^{a2} - V_{\mathbf{k}_b\,\mathbf{k}_1\,\lambda_c\,\lambda_a}^{\mathbf{k}_1\,\mathbf{k}_b\,\lambda_2\,\lambda_b}\sigma_{b}^{bc}\sigma_{1}^{1a}\right]. \tag{4.47}$$

For the dynamics of the carrier occupation in the conduction band Eq. (4.47) yields:

$$\begin{aligned}\frac{d}{dt}\rho_{\mathbf{k}}^{c}\Big|_{HF} = &\frac{i}{\hbar}\sum_{\mathbf{k}'}\left[V_{\mathbf{k}'\,\mathbf{k}\,v\,v}^{\mathbf{k}\,\mathbf{k}'\,c\,v}\rho_{\mathbf{k}'}^{v} + V_{\mathbf{k}'\,\mathbf{k}\,c\,v}^{\mathbf{k}\,\mathbf{k}'\,c\,c}\rho_{\mathbf{k}'}^{c}\right]p_{\mathbf{k}}^{*}\\ &-\frac{i}{\hbar}\sum_{\mathbf{k}'}\left[V_{\mathbf{k}\,\mathbf{k}'\,c\,v}^{\mathbf{k}'\,\mathbf{k}\,v\,v}\rho_{\mathbf{k}'}^{v} + V_{\mathbf{k}\,\mathbf{k}'\,c\,c}^{\mathbf{k}'\,\mathbf{k}\,c\,v}\rho_{\mathbf{k}'}^{c}\right]p_{\mathbf{k}}\\ &+\frac{i}{\hbar}\sum_{\mathbf{k}'}\left[V_{\mathbf{k}'\,\mathbf{k}\,c\,v}^{\mathbf{k}\,\mathbf{k}'\,c\,v}p_{\mathbf{k}'} + V_{\mathbf{k}'\,\mathbf{k}\,v\,v}^{\mathbf{k}\,\mathbf{k}'\,c\,c}p_{\mathbf{k}}^{*}\right]p_{\mathbf{k}}^{*}\\ &-\frac{i}{\hbar}\sum_{\mathbf{k}'}\left[V_{\mathbf{k}\,\mathbf{k}'\,c\,c}^{\mathbf{k}'\,\mathbf{k}\,v\,v}p_{\mathbf{k}'} + V_{\mathbf{k}\,\mathbf{k}'\,c\,v}^{\mathbf{k}'\,\mathbf{k}\,c\,v}p_{\mathbf{k}'}^{*}\right]p_{\mathbf{k}}.\end{aligned} \tag{4.48}$$

The band index combinations of the Coulomb matrix elements in first two lines, where three indices are equal, denote Auger-like terms. Within the linear band approximation the corresponding matrix element is antisymmetric with respect to the Dirac point [41]. Therefore, these terms vanish for an isotropic carrier distribution. The last two lines are nonlinear in the microscopic polarization, which are only relevant in the presence of nonlinear optical excitations. Consequently, the terms in Eq. (4.48) are typically not considered in description of optical properties in the limit of weak excitations.

The equation of motion for the microscopic polarization within the Hartree-Fock approximation reads

$$\begin{aligned}\frac{d}{dt}p_{\mathbf{k}}\Big|_{HF} = &\frac{i}{\hbar}\sum_{\lambda\mathbf{k}'}\left[V^{\mathbf{k}\,\mathbf{k}'\,c\,\lambda}_{\mathbf{k}'\,\mathbf{k}\,\lambda\,c}\rho^{\lambda}_{\mathbf{k}'} - V^{\mathbf{k}'\,\mathbf{k}\,\lambda\,v}_{\mathbf{k}\,\mathbf{k}'\,v\,\lambda}\rho^{\lambda}_{\mathbf{k}'}\right]p_{\mathbf{k}}\\ &-\frac{i}{\hbar}\sum_{\mathbf{k}'}[V^{\mathbf{k}'\,\mathbf{k}\,v\,c}_{\mathbf{k}\,\mathbf{k}'\,v\,c}p_{\mathbf{k}'} + V^{\mathbf{k}\,\mathbf{k}'\,c\,c}_{\mathbf{k}'\,\mathbf{k}\,v\,v}p^{*}_{\mathbf{k}'}](\rho^{c}_{\mathbf{k}} - \rho^{v}_{\mathbf{k}})\\ &-\frac{i}{\hbar}\sum_{\lambda\mathbf{k}'}[V^{\mathbf{k}\,\mathbf{k}'\,c\,\lambda}_{\mathbf{k}'\,\mathbf{k}\,\lambda\,v}\rho^{\lambda}_{\mathbf{k}'}](\rho^{c}_{\mathbf{k}} - \rho^{v}_{\mathbf{k}})\\ &-\frac{i}{\hbar}\sum_{\lambda\mathbf{k}'}[(V^{\mathbf{k}'\,\mathbf{k}\,v\,v}_{\mathbf{k}\,\mathbf{k}'\,v\,c} - V^{\mathbf{k}\,\mathbf{k}'\,c\,v}_{\mathbf{k}'\,\mathbf{k}\,c\,c})p_{\mathbf{k}'} + (V^{\mathbf{k}'\,\mathbf{k}\,c\,v}_{\mathbf{k}\,\mathbf{k}'\,v\,v} - V^{\mathbf{k}\,\mathbf{k}'\,c\,c}_{\mathbf{k}'\,\mathbf{k}\,v\,c})p^{*}_{\mathbf{k}'}]p_{\mathbf{k}}. \quad (4.49)\end{aligned}$$

The last two lines can be neglected for the same reasons as in Eq. (4.48). Commonly, the first two lines are treated within the limit of linear optics and Eq. (4.49) can be simplified to:

$$\frac{d}{dt}p_{\mathbf{k}}\Big|_{HF} = \frac{i}{\hbar}\varepsilon^{HF}_{\mathbf{k}}p_{\mathbf{k}} - \frac{i}{\hbar}\sum_{\mathbf{k}'}\left[V^{\mathbf{k}'\,\mathbf{k}\,v\,c}_{\mathbf{k}\,\mathbf{k}'\,v\,c}p_{\mathbf{k}'} + V^{\mathbf{k}\,\mathbf{k}'\,c\,c}_{\mathbf{k}'\,\mathbf{k}\,v\,v}p^{*}_{\mathbf{k}'}\right], \quad (4.50)$$

with $\varepsilon^{HF}_{\mathbf{k}} = \sum_{\mathbf{k}'}\left[V^{\mathbf{k}\,\mathbf{k}'\,c\,c}_{\mathbf{k}'\,\mathbf{k}\,c\,c} - V^{\mathbf{k}'\,\mathbf{k}\,c\,v}_{\mathbf{k}\,\mathbf{k}'\,v\,c}\right]$. The first term in Eq. (4.50) has the same structure as the free energy contribution, cf. Eq. (4.36). This Coulomb-induced renormalization of the band structure results in a blue-shift of the free energy peak in absorption spectra [7–11]. The second term represents a renormalization of the Rabi-frequency resulting in a deformation and a red-shift of the absorption peak, which can be interpreted as the formation of saddle point excitons [7–11].

Carrier-Carrier Scattering

This section goes beyond the Hartree-Fock level focusing on the second-order correlation term, cf. Eq. (4.45). As shown below, these terms result in a Boltzmann-like scattering equation for the carrier occupation and a diagonal as well as a off-diagonal dephasing for the microscopic polarization.

To describe the dynamics of $\sigma_{\mathbf{12}}$ beyond the Hartree-Fock level, the temporal evolution each correlation $\Lambda_{\mathbf{34}}^{\mathbf{12}c}$, Eq. (4.37), needs to be known.[3] Therefore, again the correlation expansion is applied

$$\Lambda_{\mathbf{34}}^{\mathbf{12}c} = \Lambda_{\mathbf{34}}^{\mathbf{12}} + \sigma_{\mathbf{13}}\sigma_{\mathbf{24}} - \sigma_{\mathbf{14}}\sigma_{\mathbf{23}} \tag{4.51}$$

and the dynamics of each term is determined using the Heisenberg equation. The free particle Hamiltonian directly yields

$$\frac{d}{dt}\Lambda_{\mathbf{34}}^{\mathbf{12}c}\Big|_{H_0} = \frac{i}{\hbar}\Delta\tilde{\varepsilon}\Lambda_{\mathbf{34}}^{\mathbf{12}c}, \tag{4.52}$$

with $\Delta\tilde{\varepsilon} = \varepsilon_{\mathbf{1}} + \varepsilon_{\mathbf{2}} - \varepsilon_{\mathbf{3}} - \varepsilon_{\mathbf{4}}$. The Coulomb-induced dynamics of $\Lambda_{\mathbf{34}}^{\mathbf{12}}$ couple to six-operator EVs reading

$$\begin{aligned} i\hbar\frac{d}{dt}\Lambda_{\mathbf{34}}^{\mathbf{12}}\Big|_{H_{cc}} = &\sum_{\mathbf{abc}} V_{\mathbf{1c}}^{\mathbf{ab}}\left[\langle a_{\mathbf{a}}^\dagger a_{\mathbf{b}}^\dagger a_{\mathbf{2}}^\dagger a_{\mathbf{c}} a_{\mathbf{3}} a_{\mathbf{4}}\rangle - \Lambda_{\mathbf{34}}^{\mathbf{ab}}\delta_{\mathbf{2c}}\right] \\ &- \sum_{\mathbf{abc}} V_{\mathbf{2c}}^{\mathbf{ab}}\langle a_{\mathbf{a}}^\dagger a_{\mathbf{b}}^\dagger a_{\mathbf{1}}^\dagger a_{\mathbf{c}} a_{\mathbf{3}} a_{\mathbf{4}}\rangle \\ &+ \sum_{\mathbf{abc}} V_{\mathbf{bc}}^{\mathbf{3a}}\langle a_{\mathbf{1}}^\dagger a_{\mathbf{2}}^\dagger a_{\mathbf{a}}^\dagger a_{\mathbf{4}} a_{\mathbf{c}} a_{\mathbf{b}}\rangle \\ &- \sum_{\mathbf{abc}} V_{\mathbf{bc}}^{\mathbf{4a}}\left[\langle a_{\mathbf{1}}^\dagger a_{\mathbf{2}}^\dagger a_{\mathbf{a}}^\dagger a_{\mathbf{3}} a_{\mathbf{c}} a_{\mathbf{b}}\rangle - \Lambda_{\mathbf{cb}}^{\mathbf{12}}\delta_{\mathbf{3a}}\right]. \end{aligned} \tag{4.53}$$

To obtain a closed set of equations at this level, the six-operator quantities are disassembled according to the correlation expansion (4.37). Within the second order Born-approximation the highest occurring order of correlations is neglect. Furthermore, some terms are canceled by the second term in Eq. (4.51) given by:

$$\begin{aligned} i\hbar\frac{d}{dt}\left[\sigma_{\mathbf{13}}\sigma_{\mathbf{24}} - \sigma_{\mathbf{14}}\sigma_{\mathbf{23}}\right]\Big|_{H_{cc}} = &\sum_{\mathbf{abc}}\Big\{V_{\mathbf{1c}}^{\mathbf{ab}}\left[\Lambda_{\mathbf{c4}}^{\mathbf{ab}}\sigma_{\mathbf{23}} - \Lambda_{\mathbf{c3}}^{\mathbf{ab}}\sigma_{\mathbf{24}}\right] \\ &+ V_{\mathbf{2c}}^{\mathbf{ab}}\left[\Lambda_{\mathbf{c3}}^{\mathbf{ab}}\sigma_{\mathbf{14}} - \Lambda_{\mathbf{c4}}^{\mathbf{ab}}\sigma_{\mathbf{13}}\right] + V_{\mathbf{bc}}^{\mathbf{3a}}\left[\Lambda_{\mathbf{cb}}^{\mathbf{1a}}\sigma_{\mathbf{24}} - \Lambda_{\mathbf{cb}}^{\mathbf{2a}}\sigma_{\mathbf{14}}\right] \\ &+ V_{\mathbf{bc}}^{\mathbf{4a}}\left[\Lambda_{\mathbf{cb}}^{\mathbf{2a}}\sigma_{\mathbf{13}} - \Lambda_{\mathbf{cb}}^{\mathbf{1a}}\sigma_{\mathbf{23}}\right]\Big\}. \end{aligned} \tag{4.54}$$

[3] Due to the Kronecker $\delta_{\mathbf{k_1}+\mathbf{k_2},\mathbf{k_3}+\mathbf{k_4}}$ in the Coulomb matrix element only the dynamics of momentum conserving correlations have to be determined. Nevertheless, for a more clear notation the equation of motion for a general $\Lambda_{\mathbf{34}}^{\mathbf{12}c}$ is derived.

Finally, the Coulomb-induced dynamics of $\Lambda^{\mathbf{12}c}_{\mathbf{34}}$ is found to be

$$
\begin{aligned}
i\hbar\frac{d}{dt}\Lambda^{\mathbf{12}c}_{\mathbf{34}}\Big|_{H_{ee}} = & \sum_{\mathbf{abcd}} \left(V^{\mathbf{ab}}_{\mathbf{dc}} - V^{\mathbf{ba}}_{\mathbf{dc}}\right)\left[\sigma_{\mathbf{1d}}\sigma_{\mathbf{2c}}\sigma^{\dagger}_{\mathbf{b3}}\sigma^{\dagger}_{\mathbf{a4}} - \sigma^{\dagger}_{\mathbf{1d}}\sigma^{\dagger}_{\mathbf{2c}}\sigma_{\mathbf{b3}}\sigma_{\mathbf{a4}}\right] \\
& - \sum_{\mathbf{a}}\left[\varepsilon^{corr}_{\mathbf{1a}}\Lambda^{\mathbf{a2}c}_{\mathbf{34}} + \varepsilon^{corr}_{\mathbf{2a}}\Lambda^{\mathbf{1a}c}_{\mathbf{34}} - \varepsilon^{corr*}_{\mathbf{3a}}\Lambda^{\mathbf{12}c}_{\mathbf{a4}} - \varepsilon^{corr*}_{\mathbf{4a}}\Lambda^{\mathbf{12}c}_{\mathbf{3a}}\right] \\
& + \sum_{\mathbf{abcd}} V^{\mathbf{ab}}_{\mathbf{dc}}\left[\Lambda^{\mathbf{ab}c}_{\mathbf{34}}\left(\sigma_{\mathbf{1d}}\sigma_{\mathbf{2c}} - \sigma^{\dagger}_{\mathbf{1d}}\sigma^{\dagger}_{\mathbf{2c}}\right) + \Lambda^{\mathbf{12}c}_{\mathbf{cd}}\left(\sigma^{\dagger}_{\mathbf{b3}}\sigma^{\dagger}_{\mathbf{a4}} - \sigma_{\mathbf{b3}}\sigma_{\mathbf{a4}}\right)\right] \\
& + 2\sum_{\mathbf{abcd}} V^{\mathbf{ab}}_{\mathbf{dc}}\left[\Lambda^{\mathbf{2a}c}_{\mathbf{c4}}\left(\sigma_{\mathbf{1d}}\sigma^{\dagger}_{\mathbf{3b}} - \sigma_{\mathbf{b3}}\sigma^{\dagger}_{\mathbf{d1}}\right) + \Lambda^{\mathbf{2a}c}_{\mathbf{c3}}\left(\sigma_{\mathbf{b4}}\sigma^{\dagger}_{\mathbf{d1}} - \sigma_{\mathbf{d1}}\sigma^{\dagger}_{\mathbf{4b}}\right)\right. \\
& \left. + \Lambda^{\mathbf{a1}c}_{\mathbf{d4}}\left(\sigma_{\mathbf{b3}}\sigma^{\dagger}_{\mathbf{c2}} - \sigma_{\mathbf{2c}}\sigma^{\dagger}_{\mathbf{3b}}\right) + \Lambda^{\mathbf{a1}c}_{\mathbf{d3}}\left(\sigma_{\mathbf{2c}}\sigma^{\dagger}_{\mathbf{4b}} - \sigma_{\mathbf{b4}}\sigma^{\dagger}_{\mathbf{c2}}\right)\right], \qquad (4.55)
\end{aligned}
$$

with $\varepsilon^{corr}_{\mathbf{1a}} = 2\sum_{\mathbf{bc}} V^{\mathbf{ab}}_{\mathbf{1c}}\sigma_{\mathbf{bc}}$ and $\varepsilon^{corr*}_{\mathbf{3a}} = 2\sum_{\mathbf{bc}} V^{\mathbf{3b}}_{\mathbf{ca}}\sigma_{\mathbf{bc}}$. Here, we focus on the first line, since it includes all terms which are relevant for two-particle scattering processes. The second line leads to a many-particle screening of the Coulomb-potential in the Hartree-Fock equations (4.44), for details see Ref. [44]. The contribution of the last three lines is supposed to be small and is neglect in following. Since, higher-order correlations, beyond second-order Born approximation, are also expected to damp the dynamics of $\Lambda^{\mathbf{12}c}_{\mathbf{34}}$, these terms can be summarized in a small damping constant γ. Now, Eq. (4.51) can be rewritten as

$$
\frac{d}{dt}\Lambda^{\mathbf{12}c}_{\mathbf{34}} = \left(\frac{i}{\hbar}\Delta\tilde{\varepsilon} - \gamma\right)\Lambda^{\mathbf{12}c}_{\mathbf{34}} + \frac{i}{\hbar}Q(t), \qquad (4.56)
$$

with the scattering kernel

$$
Q(t) = \sum_{\mathbf{abcd}} \left(V^{\mathbf{ab}}_{\mathbf{dc}} - V^{\mathbf{ba}}_{\mathbf{dc}}\right)\left[\sigma^{\dagger}_{\mathbf{1d}}\sigma^{\dagger}_{\mathbf{2c}}\sigma_{\mathbf{b3}}\sigma_{\mathbf{a4}} - \sigma_{\mathbf{1d}}\sigma_{\mathbf{2c}}\sigma^{\dagger}_{\mathbf{b3}}\sigma^{\dagger}_{\mathbf{a4}}\right]. \qquad (4.57)
$$

At this point, Eqs. (4.45) and (4.56) form a closed set of equations. Treating $\Lambda^{\mathbf{12}c}_{\mathbf{34}}$ as an independent variable, the equations can be solved numerically resulting in non-Markovian dynamics, as described in Ref. [6] for carbon nanotubes. However, in a two-dimensional system a non-Markovian treatment numerically extremely extensive, since $\Lambda^{\mathbf{12}c}_{\mathbf{34}}$ depends at least on three two-dimensional vectors. In the case of graphene, Eq. (4.56) will be solved analytically by applying the Markov approximation, as described in section "Markov-Approximation":

$$
\Lambda^{\mathbf{34}c}_{\mathbf{12}}(t) = \frac{1}{\hbar}Q(t)\left[i\frac{\gamma}{\Delta\omega^2 + \gamma^2} - \mathscr{P}\left(\frac{\Delta\omega}{\Delta\omega^2 + \gamma^2}\right)\right], \qquad (4.58)
$$

with $\Delta\omega = (\varepsilon_{\mathbf{d}} + \varepsilon_{\mathbf{c}} - \varepsilon_{\mathbf{b}} - \varepsilon_{\mathbf{a}})/\hbar \equiv \Delta\varepsilon/\hbar$. It can be shown, that the higher-order correlations γ are directly related to Boltzmann scattering rates [48]. In the limit of second-order Born-Markov approximation $\gamma \to 0$ Eq. (4.56) yields:

$$\Lambda_{\mathbf{12}}^{\mathbf{34}c}(t) = Q(t)\left[i\pi\delta(\Delta\varepsilon) - \mathscr{P}\left(\frac{1}{\Delta\omega}\right)/\hbar\right]. \tag{4.59}$$

The δ-function ensures the conservation of energy, whereas a finite γ in Eq. (4.58) leads to Lorentzian-like broadening of the energy conservation. The principal value $\mathscr{P}(\frac{1}{\Delta\omega})$ in Eq. (4.59) contains renormalization terms and is neglect in the following [49]. Now, the number of dynamic equations can be drastically reduced by inserting the analytic solution for $\Lambda_{\mathbf{12}}^{\mathbf{34}c}(t)$ into Eq. (4.45) yielding:

$$\begin{aligned}
&\frac{d}{dt}\sigma_{\mathbf{12}}\Big|_{H_{cc}} = \\
&\frac{\pi}{\hbar}\sum_{\mathbf{abc}} V_{\mathbf{bc}}^{\mathbf{2a}}\Big[\sum_{\mathbf{ABCD}} \tilde{V}_{\mathbf{DC}}^{\mathbf{AB}}\left[\sigma_{\mathbf{1D}}^{\dagger}\sigma_{\mathbf{aC}}^{\dagger}\sigma_{\mathbf{Bc}}\sigma_{\mathbf{Ab}} - \sigma_{\mathbf{1D}}\sigma_{\mathbf{aC}}\sigma_{\mathbf{Bc}}^{\dagger}\sigma_{\mathbf{Ab}}^{\dagger}\right]\delta(\Delta\varepsilon)\Big] \\
-\ &\frac{\pi}{\hbar}\sum_{\mathbf{abc}} V_{\mathbf{1c}}^{\mathbf{ab}}\Big[\sum_{\mathbf{ABCD}} \tilde{V}_{\mathbf{DC}}^{\mathbf{AB}}\left[\sigma_{\mathbf{aD}}^{\dagger}\sigma_{\mathbf{bC}}^{\dagger}\sigma_{\mathbf{Bc}}\sigma_{\mathbf{A2}} - \sigma_{\mathbf{aD}}\sigma_{\mathbf{bC}}\sigma_{\mathbf{Bc}}^{\dagger}\sigma_{\mathbf{A2}}^{\dagger}\right]\delta(\Delta\varepsilon)\Big],
\end{aligned} \tag{4.60}$$

with $\tilde{V}_{\mathbf{DC}}^{\mathbf{AB}} = V_{\mathbf{DC}}^{\mathbf{AB}} - V_{\mathbf{DC}}^{\mathbf{BA}}$ and $\Delta\varepsilon = \varepsilon_{\mathbf{D}} + \varepsilon_{\mathbf{C}} - \varepsilon_{\mathbf{B}} - \varepsilon_{\mathbf{A}}$.

Applying spatial homogeneity ($\sigma_{\mathbf{12}} = \sigma_{\mathbf{1}}^{12}\delta_{\mathbf{k}_1,\mathbf{k}_2}$, $1 \hat{=} \mathbf{k}_1$) the Boltzmann-like scattering equation for the carrier occupation can be obtained by collecting all terms in Eq. (4.60) containing only band-diagonal density matrix elements $\sigma_{\mathbf{1}}^{11} = \rho_{\mathbf{1}}$ ($\mathbf{1} = \mathbf{k}_1, \lambda_1$). The result reads:

$$\frac{d}{dt}\rho_{\mathbf{1}} = \Gamma_{\mathbf{1}}^{in(cc)}\left[1 - \rho_{\mathbf{1}}\right] - \Gamma_{\mathbf{1}}^{out(cc)}(t)\rho_{\mathbf{1}}, \tag{4.61}$$

with the in- and out-scattering rates:

$$\Gamma_{\mathbf{1}}^{in(cc)} = \frac{2\pi}{\hbar}\sum_{\mathbf{abc}} V_{\mathbf{bc}}^{\mathbf{1a}}\tilde{V}_{\mathbf{1a}}^{\mathbf{bc}}\left[1 - \rho_{\mathbf{a}}\right]\rho_{\mathbf{b}}\rho_{\mathbf{c}}\delta(\varepsilon_{\mathbf{1}} + \varepsilon_{\mathbf{a}} - \varepsilon_{\mathbf{b}} - \varepsilon_{\mathbf{c}}) \tag{4.62}$$

and

$$\Gamma_{\mathbf{1}}^{out(cc)} = \frac{2\pi}{\hbar}\sum_{\mathbf{abc}} V_{\mathbf{bc}}^{\mathbf{1a}}\tilde{V}_{\mathbf{1a}}^{\mathbf{bc}}\rho_{\mathbf{a}}\left[1 - \rho_{\mathbf{b}}\right]\left[1 - \rho_{\mathbf{c}}\right]\delta(\varepsilon_{\mathbf{1}} + \varepsilon_{\mathbf{a}} - \varepsilon_{\mathbf{b}} - \varepsilon_{\mathbf{c}}). \tag{4.63}$$

Overall, the Eqs. (4.61–4.63) describe the Coulomb-induced carrier dynamics in second-order Born-Markov approximation. The raise of occupation in a specific state $\mathbf{1} = (\mathbf{k}_1, \lambda_1)$ is proportional to the product of the corresponding Pauli blocking term and in-scattering rate, whereas decrease of occupation is given the occupation and the out-scattering rate. These scattering rates, which are explicitly time and

momentum dependent, fulfill the energy as well as momentum conservation. The sum in Eqs. (4.62) and (4.63) contains all possible processes to scatter from the **1** into the final state **b**. The probability therefore is determined by the sum over all secondary processes $\mathbf{a} \rightarrow \mathbf{c}$ matching in energy and momentum.

The Coulomb-induced scattering, described by Eqs. (4.61–4.63), is responsible for an ultrafast equilibration within the first tens of femtoseconds after an optical excitation [10, 16]. In particular, in graphene Auger-type processes have to be considered as discussed in Refs. [12, 21, 27].

For the dynamics of $p_{\mathbf{k}}$ all terms in Eq. (4.60), which are in first order proportional to a microscopic polarization, are here considered resulting in

$$\frac{d}{dt}p_{\mathbf{k}} = -\gamma_{\mathbf{k}}^{(cc)} p_{\mathbf{k}} + \sum_{\mathbf{k}_a} \left[\mathscr{U}^{vc}_{\mathbf{k}\mathbf{k}_a} p_{\mathbf{k}_a} + \mathscr{U}^{cv}_{\mathbf{k}\mathbf{k}_a} p^*_{\mathbf{k}_a} \right], \tag{4.64}$$

where

$$\gamma_{\mathbf{k}}^{(cc)} = \frac{1}{2} \sum_{\lambda} \left[\Gamma^{in(cc)}_{\lambda\mathbf{k}} + \Gamma^{out(cc)}_{\lambda\mathbf{k}} \right] \tag{4.65}$$

is the diagonal dephasing and the second term is the off-diagonal dephasing:

$$\begin{aligned} \mathscr{U}^{\lambda_1\lambda_2}_{\mathbf{k}\mathbf{k}_a} = \frac{\pi}{\hbar} \sum_{\mathbf{bc}} \sum_{\lambda} & \\ \times \Big[\tilde{V}^{\mathbf{k}\ \mathbf{k}_c\ c\ \lambda_c}_{\mathbf{k}_a\ \mathbf{k}_b\ \lambda_2\ \lambda_b} \tilde{V}^{\mathbf{k}_a\ \mathbf{k}_b\ \lambda_1\ \lambda_b}_{\mathbf{k}\ \mathbf{k}_c\ v\ \lambda_c} \left(\rho^{\lambda}_{\mathbf{k}} [1-\rho_{\mathbf{b}}] \rho_{\mathbf{c}} + [1-\rho^{\lambda}_{\mathbf{k}}] \rho_{\mathbf{b}} [1-\rho_{\mathbf{c}}] \right) \delta^{+} & \\ - V^{\mathbf{k}\ \mathbf{k}_a\ c\ \lambda_1}_{\mathbf{k}_b\ \mathbf{k}_c\ \lambda_b\ \lambda_c} \tilde{V}^{\mathbf{k}_b\ \mathbf{k}_c\ \lambda_b\ \lambda_c}_{\mathbf{k}\ \mathbf{k}_a\ v\ \lambda_2} \left([1-\rho^{\lambda}_{\mathbf{k}}] \rho_{\mathbf{b}} \rho_{\mathbf{c}} + \rho^{\lambda}_{\mathbf{k}} [1-\rho_{\mathbf{b}}] [1-\rho_{\mathbf{c}}] \right) \delta^{-} \Big] & \end{aligned} \tag{4.66}$$

with $\delta^{\pm} = \delta\left(\varepsilon^{\lambda}_{k} + \sigma_{\lambda_1}\varepsilon^{\lambda}_{k_a} - \varepsilon_{\mathbf{b}} \pm \varepsilon_{\mathbf{c}}\right)$ and $\sigma_{\lambda} = sgn(\varepsilon^{\lambda})$. The dephasing damps the free energy coherent oscillations of $p_{\mathbf{k}}$ after an optical excitation on a femtosecond timescale. The role of the diagonal and off-diagonal dephasing is discussed in Ref. [13].

Carrier-Phonon Coupling

Next to carrier-carrier scattering the phonon-induced dynamics is an efficient relaxation channel. In the following the scattering equations for coupled electron-phonon system are derived. The treatment is partially analog to derivation of the carrier-carrier scattering equation and leads to the same structure of electronic equations in terms of in- and out scattering rates as well as diagonal and off-diagonal dephasing. Additionally, the equations of motion for the phonon population have to be derived.

From the Heisenberg equation and the Hamilton operator for the electron-phonon interaction (Eq. 4.7) the dynamics for a momentum-diagonal[4] density matrix element is determined by

$$i\hbar\frac{d}{dt}\sigma_{\mathbf{k}}^{1,2}\Big|_{H_{cp}} = \sum_{\lambda_3}\sum_{j\mathbf{q}} g_{\mathbf{k},\mathbf{q}}^{\lambda_2\lambda_3 j} S_{\mathbf{k},\mathbf{q}}^{\lambda_1\lambda_3 j} - g_{\mathbf{k}+\mathbf{q},\mathbf{q}}^{\lambda_3\lambda_1 j} S_{\mathbf{k}+\mathbf{q},\mathbf{q}}^{\lambda_3\lambda_2 j} + \sum_{\lambda_3}\sum_{j\mathbf{q}} g_{\mathbf{k}+\mathbf{q},\mathbf{q}}^{\lambda_3\lambda_2 j*} T_{\mathbf{k}+\mathbf{q},\mathbf{q}}^{\lambda_1\lambda_3 j} - g_{\mathbf{k},\mathbf{q}}^{\lambda_1\lambda_3 j*} T_{\mathbf{k},\mathbf{q}}^{\lambda_3\lambda_2 j}, \tag{4.67}$$

where

$$S_{\mathbf{k},\mathbf{q}}^{\lambda_1\lambda_2 j} = \langle a_{\mathbf{k}}^{\lambda_1\dagger} a_{\mathbf{k}-\mathbf{q}}^{\lambda_2} b_{\mathbf{q}}^{j}\rangle \quad \text{and} \quad T_{\mathbf{k},\mathbf{q}}^{\lambda_1\lambda_2 j} = \langle a_{\mathbf{k}-\mathbf{q}}^{\lambda_1\dagger} a_{\mathbf{k}}^{\lambda_2} b_{\mathbf{q}}^{j\dagger}\rangle \tag{4.68}$$

are the phonon-assisted quantities, which also determine the temporal evolution of the phonon-occupation, given by

$$i\hbar\frac{d}{dt}n_{\mathbf{q}}^{j}\Big|_{H_{cp}} = -\sum_{\lambda_1\lambda_2\mathbf{k}} g_{\mathbf{k},\mathbf{q}}^{\lambda_1\lambda_2 j} S_{\mathbf{k},\mathbf{q}}^{\lambda_1\lambda_2 j} - g_{\mathbf{k},\mathbf{q}}^{\lambda_1\lambda_2 j*} T_{\mathbf{k},\mathbf{q}}^{\lambda_2\lambda_1 j}. \tag{4.69}$$

Analog to the previous section, the correlation expansion is applied for the two-particle EVs, which are here the phonon-assisted quantities, e.g.

$$S_{\mathbf{k},\mathbf{q}}^{\lambda_1\lambda_2 j} = \langle a_{\mathbf{k}}^{\lambda_1\dagger} a_{\mathbf{k}-\mathbf{q}}^{\lambda_2}\rangle\langle b_{\mathbf{q}}^{j}\rangle + S_{\mathbf{k},\mathbf{q}}^{\lambda_1\lambda_2 j,c}. \tag{4.70}$$

The first term contains coherent phonons $\langle b_{\mathbf{q}}^{j}\rangle$, which are known to induce signatures in differential reflectivity spectra [50]. However, their influence on relaxations dynamics plays a minor role and will be neglect in the following. As a consequence the phonon-assisted quantities are equal to their correlations and a further differentiation between both is redundant. To close the set of equations on the second order level, the equation of motions of the phonon-assisted quantities are set up. The contribution from free particle Hamilton operator is

$$i\hbar\frac{d}{dt}S_{\mathbf{k},\mathbf{q}}^{\lambda_1\lambda_2 j}\Big|_{H_0} = -\left(\varepsilon_{\mathbf{k}}^{\lambda_1} - \varepsilon_{\mathbf{k}-\mathbf{q}}^{\lambda_2} - \hbar\omega_{\mathbf{q}}^{j}\right) S_{\mathbf{k},\mathbf{q}}^{\lambda_1\lambda_2 j}, \tag{4.71}$$

$$i\hbar\frac{d}{dt}T_{\mathbf{k},\mathbf{q}}^{\lambda_1\lambda_2 j}\Big|_{H_0} = -\left(\varepsilon_{\mathbf{k}-\mathbf{q}}^{\lambda_1} - \varepsilon_{\mathbf{k}}^{\lambda_2} + \hbar\omega_{\mathbf{q}}^{j}\right) T_{\mathbf{k},\mathbf{q}}^{\lambda_1\lambda_2 j}. \tag{4.72}$$

and the commutation with the electron-phonon Hamiltonian yields

$$i\hbar\frac{d}{dt}S_{\mathbf{k},\mathbf{q}}^{\lambda_1\lambda_2 j}\Big|_{H_{cp}} = -\sum_{\lambda_3\lambda_4} g_{\mathbf{k},\mathbf{q}}^{\lambda_3\lambda_4 j*} Q_{\mathbf{k},\mathbf{q}}^{\lambda_1\lambda_3\lambda_4\lambda_2 j}, \tag{4.73}$$

[4] In this derivation the spatial homogeneity applied form the beginning.

$$i\hbar\frac{d}{dt}T^{\lambda_1\lambda_2 j}_{\mathbf{k},\mathbf{q}}\Big|_{Hcp} = \sum_{\lambda_3\lambda_4} g^{\lambda_3\lambda_4 j}_{\mathbf{k},\mathbf{q}} Q^{\lambda_3\lambda_2\lambda_1\lambda_4 j}_{\mathbf{k},\mathbf{q}} \tag{4.74}$$

with the scattering kernel

$$Q^{\lambda_1\lambda_2\lambda_3\lambda_4 j}_{\mathbf{k},\mathbf{q}} = \left(\delta_{\lambda_1,\lambda_2} - \sigma^{\lambda_1\lambda_2}_{\mathbf{k}}\right)\sigma^{\lambda_3\lambda_4}_{\mathbf{k}-\mathbf{q}} n^j_{\mathbf{q}} - \sigma^{\lambda_1\lambda_2}_{\mathbf{k}}\left(\delta_{\lambda_3,\lambda_4} - \sigma^{\lambda_3\lambda_4}_{\mathbf{k}-\mathbf{q}}\right)\left(n^j_{\mathbf{q}}+1\right). \tag{4.75}$$

Thereby, appearing electronic four-operators EVs $\Lambda^{\mathbf{12}}_{\mathbf{34}}$ are treated within the Hartree-Fock approximation, c.f. Eq. (4.46). Within the Markov approximation Eqs. (4.71–4.74) can be solved analytically yielding:

$$S^{\lambda_1\lambda_2 j}_{\mathbf{k},\mathbf{q}}\Big|_{H_0+Hcp} = i\pi \sum_{\lambda_3\lambda_4} g^{\lambda_3\lambda_4 j*}_{\mathbf{k},\mathbf{q}} Q^{\lambda_1\lambda_3\lambda_4\lambda_2 j}_{\mathbf{k},\mathbf{q}} \delta\left(\varepsilon^{\lambda_3}_{\mathbf{k}} - \varepsilon^{\lambda_4}_{\mathbf{k}-\mathbf{q}} - \hbar\omega^j_{\mathbf{q}}\right), \tag{4.76}$$

$$T^{\lambda_1\lambda_2 j}_{\mathbf{k},\mathbf{q}}\Big|_{H_0+Hcp} = -i\pi \sum_{\lambda_3\lambda_4} g^{\lambda_3\lambda_4 j}_{\mathbf{k},\mathbf{q}} Q^{\lambda_3\lambda_2\lambda_1\lambda_4 j}_{\mathbf{k},\mathbf{q}} \delta\left(\varepsilon^{\lambda_4}_{\mathbf{k}-\mathbf{q}} - \varepsilon^{\lambda_3}_{\mathbf{k}} + \hbar\omega^j_{\mathbf{q}}\right). \tag{4.77}$$

With the knowledge about the dynamics of the phonon-assisted quantities the equations of motion for $\rho^{\lambda}_{\mathbf{k}}$, $p_{\mathbf{k}}$, and $n^j_{\mathbf{q}}$ can be determined.

Electron Dynamics

Inserting Eqs. (4.76) and (4.77) into Eq. (4.67) the equation of motion for an electronic density matrix element reads:

$$\begin{aligned}\frac{d}{dt}\sigma^{\lambda_1,\lambda_2}_{\mathbf{k}} = {} & \frac{\pi}{\hbar}\sum_{\lambda_3\lambda_4\lambda_5}\sum_{j\mathbf{q}} g^{\lambda_2\lambda_3 j}_{\mathbf{k},\mathbf{q}} g^{\lambda_4\lambda_5 j*}_{\mathbf{k},\mathbf{q}} Q^{\lambda_1\lambda_4\lambda_5\lambda_3 j}_{\mathbf{k},\mathbf{q}} \delta\left(\varepsilon^{\lambda_4}_{\mathbf{k}} - \varepsilon^{\lambda_5}_{\mathbf{k}-\mathbf{q}} - \hbar\omega^j_{\mathbf{q}}\right) \\ & - \frac{\pi}{\hbar}\sum_{\lambda_3\lambda_4\lambda_5}\sum_{j\mathbf{q}} g^{\lambda_3\lambda_1 j}_{\mathbf{k}+\mathbf{q},\mathbf{q}} g^{\lambda_4\lambda_5 j*}_{\mathbf{k}+\mathbf{q},\mathbf{q}} Q^{\lambda_3\lambda_4\lambda_5\lambda_2 j}_{\mathbf{k}+\mathbf{q},\mathbf{q}} \delta\left(\varepsilon^{\lambda_4}_{\mathbf{k}+\mathbf{q}} - \varepsilon^{\lambda_5}_{\mathbf{k}} - \hbar\omega^j_{\mathbf{q}}\right) \\ & - \frac{\pi}{\hbar}\sum_{\lambda_3\lambda_4\lambda_5}\sum_{j\mathbf{q}} g^{\lambda_3\lambda_2 j*}_{\mathbf{k}+\mathbf{q},\mathbf{q}} g^{\lambda_4\lambda_5 j}_{\mathbf{k}+\mathbf{q},\mathbf{q}} Q^{\lambda_4\lambda_3\lambda_1\lambda_5 j}_{\mathbf{k}+\mathbf{q},\mathbf{q}} \delta\left(\varepsilon^{\lambda_4}_{\mathbf{k}+\mathbf{q}} - \varepsilon^{\lambda_5}_{\mathbf{k}} - \hbar\omega^j_{\mathbf{q}}\right) \\ & + \frac{\pi}{\hbar}\sum_{\lambda_3\lambda_4\lambda_5}\sum_{j\mathbf{q}} g^{\lambda_1\lambda_3 j*}_{\mathbf{k},\mathbf{q}} g^{\lambda_4\lambda_5 j}_{\mathbf{k},\mathbf{q}} Q^{\lambda_4\lambda_2\lambda_3\lambda_5 j}_{\mathbf{k},\mathbf{q}} \delta\left(\varepsilon^{\lambda_4}_{\mathbf{k}} - \varepsilon^{\lambda_5}_{\mathbf{k}-\mathbf{q}} - \hbar\omega^j_{\mathbf{q}}\right)\end{aligned} \tag{4.78}$$

Analog to section “Carrier-Carrier Scattering” the phonon-induced scattering equation for the carrier occupation can be obtained:

$$\frac{d}{dt}\rho^{\lambda}_{\mathbf{k}}\Big|_{Hcp} = \Gamma^{in(cp)}_{\lambda,\mathbf{k}}[1-\rho^{\lambda}_{\mathbf{k}}] - \Gamma^{out(cp)}_{\lambda,\mathbf{k}}\rho^{\lambda}_{\mathbf{k}} \tag{4.79}$$

with the in-scattering rate

$$\Gamma^{in(cp)}_{\lambda,\mathbf{k}} = \frac{2\pi}{\hbar}\sum_{\lambda' j\mathbf{q}}\Big[|g^{\lambda'\lambda j}_{\mathbf{k}+\mathbf{q},\mathbf{q}}|^2\rho^{\lambda'}_{\mathbf{k}+\mathbf{q}}[n^j_{\mathbf{q}}+1]\delta(\varepsilon^{\lambda'}_{\mathbf{k}+\mathbf{q}}-\varepsilon^{\lambda}_{\mathbf{k}}-\hbar\omega^j_{\mathbf{q}}) + |g^{\lambda'\lambda j}_{\mathbf{k},\mathbf{q}}|^2\rho^{\lambda'}_{\mathbf{k}-\mathbf{q}}n^j_{\mathbf{q}}\delta(\varepsilon^{\lambda'}_{\mathbf{k}-\mathbf{q}}-\varepsilon^{\lambda}_{\mathbf{k}}+\hbar\omega^j_{\mathbf{q}})\Big] \tag{4.80}$$

and the out-scattering rate

$$\Gamma^{out(cp)}_{\lambda,\mathbf{k}} = \frac{2\pi}{\hbar}\sum_{\lambda' j\mathbf{q}}\Big[|g^{\lambda'\lambda j}_{\mathbf{k}+\mathbf{q},\mathbf{q}}|^2[1-\rho^{\lambda'}_{\mathbf{k}+\mathbf{q}}]n^j_{\mathbf{q}}\delta(\varepsilon^{\lambda'}_{\mathbf{k}+\mathbf{q}}-\varepsilon^{\lambda}_{\mathbf{k}}-\hbar\omega^j_{\mathbf{q}}) + |g^{\lambda'\lambda j}_{\mathbf{k},\mathbf{q}}|^2[1-\rho^{\lambda'}_{\mathbf{k}-\mathbf{q}}][n^j_{\mathbf{q}}+1]\delta(\varepsilon^{\lambda'}_{\mathbf{k}-\mathbf{q}}-\varepsilon^{\lambda}_{\mathbf{k}}+\hbar\omega^j_{\mathbf{q}})\Big]. \tag{4.81}$$

The interpretation of these equation is analogously to the Coulomb-induced Boltzmann equation, where here the secondary process is promoted by the emission or absorption of a phonon. While each scattering process conserves the total energy, an exchange between the electron and the phonon system takes place. Typically, after an optical excitation, energy dissipates from the electron to the phonon system being responsible for the second decay in differential pump-probe spectra [10, 16, 17].

The phonon-induced dynamics of the microscopic polarization reads:

$$\frac{d}{dt}p_{\mathbf{k}}\Big|_{H_{cp}} = -\gamma^{(cp)}_{\mathbf{k}}p_{\mathbf{k}} + \mathscr{U}^{(cp)}_{\mathbf{k}} \tag{4.82}$$

where the diagonal dephasing is given by

$$\gamma^{(cp)}_{\mathbf{k}} = \frac{1}{2}\sum_{\lambda}\left[\Gamma^{in(cp)}_{\lambda,\mathbf{k}} + \Gamma^{out(cp)}_{\lambda,\mathbf{k}}\right], \tag{4.83}$$

and for the off-diagonal dephasing is

$$\mathscr{U}^{(cp)}_{\mathbf{k}} = \frac{\pi}{\hbar}\sum_{\lambda j\mathbf{q}}|g^{\lambda\lambda j}_{\mathbf{k}+\mathbf{q},\mathbf{q}}|^2\left[(1-\rho^{\lambda}_{\mathbf{k}})(n^j_{\mathbf{q}}+1)+\rho^{\lambda}_{\mathbf{k}}n^j_{\mathbf{q}}\right]p_{\mathbf{k}+\mathbf{q}}\delta(\varepsilon^{\lambda}_{\mathbf{k}+\mathbf{q}}-\varepsilon^{\lambda}_{\mathbf{k}}-\hbar\omega^j_{\mathbf{q}}) + \frac{\pi}{\hbar}\sum_{\lambda j\mathbf{q}}|g^{\lambda\lambda j}_{\mathbf{k},\mathbf{q}}|^2\left[(1-\rho^{\lambda}_{\mathbf{k}})n^j_{\mathbf{q}}+\rho^{\lambda}_{\mathbf{k}}(n^j_{\mathbf{q}}+1)\right]p_{\mathbf{k}-\mathbf{q}}\delta(\varepsilon^{\lambda}_{\mathbf{k}}-\varepsilon^{\lambda}_{\mathbf{k}-\mathbf{q}}-\hbar\omega^j_{\mathbf{q}}) \tag{4.84}$$

obtained. Recent studies have shown that the phonon-induced dephasing is less efficient than the Coulomb-induced [19].

Phonon Dynamics

Applying Markovian dynamics for the phonon-assisted quantities, the equation of motion for the phonon occupation, cf. Eq. (4.69) directly leads to

$$\frac{d}{dt} n_{\mathbf{q}}^{j}\Big|_{H_{cp}} = \Gamma_{j\mathbf{q}}^{em}[n_{\mathbf{q}}^{j}+1] - \Gamma_{j\mathbf{q}}^{abs} n_{\mathbf{q}}^{j}, \tag{4.85}$$

with the phonon emission rate

$$\Gamma_{j\mathbf{q}}^{em} = \frac{2\pi}{\hbar} \sum_{\lambda_1\lambda_2\mathbf{k}} |g_{\mathbf{k},\mathbf{q}}^{\lambda_1\lambda_2 j}|^2 \rho_{\mathbf{k}}^{\lambda_1} [1-\rho_{\mathbf{k}-\mathbf{q}}^{\lambda_2}] \delta(\varepsilon_{\mathbf{k}}^{\lambda_1} - \varepsilon_{\mathbf{k}-\mathbf{q}}^{\lambda_2} - \hbar\omega_{\mathbf{q}}^{j}) \tag{4.86}$$

and the absorption rate

$$\Gamma_{j\mathbf{q}}^{abs} = \frac{2\pi}{\hbar} \sum_{\lambda_1\lambda_2\mathbf{k}} |g_{\mathbf{k},\mathbf{q}}^{\lambda_1\lambda_2 j}|^2 [1-\rho_{\mathbf{k}}^{\lambda_1}] \rho_{\mathbf{k}-\mathbf{q}}^{\lambda_2} \delta(\varepsilon_{\mathbf{k}}^{\lambda_1} - \varepsilon_{\mathbf{k}-\mathbf{q}}^{\lambda_2} - \hbar\omega_{\mathbf{q}}^{j}). \tag{4.87}$$

Note, the electron dynamics (Eqs. 4.79 and 4.80) and the phonon dynamics (Eqs. 4.85–4.87) form a consistent set of equations, i.e., for each process in Eq. (4.79) where an electron scatters to an energetically lower state the corresponding phonon is generated in Eq. (4.85).

This microscopic treatment of the phonon-electron dynamics, beyond the bath assumption, plays an important role also for the carrier dynamics, since the absorption of hot phonons through the electronic system decelerates the relaxation [10,14].

The microscopic description of the phonon-phonon interaction, being responsible for the decay of excited phonon populations, is beyond the scope of this work. The finite phonon lifetime is consider by a coupling to a phonon bath at the ambient temperature $n_{0,\mathbf{q}}^{j}$:

$$\frac{d}{dt} n_{\mathbf{q}}^{j}\Big|_{pp} = -\gamma_{ph}[n_{0,\mathbf{q}}^{j} - n_{\mathbf{q}}^{j}], \tag{4.88}$$

with the experimentally determined optical phonon lifetime of $\gamma_{ph}^{-1} \approx 1.2\,\mathrm{ps}$ [51]. The lifetime of the *LA*-mode is taken from Ref. [52].

4.5 Conclusions

Based on the density matrix formalism, we derived the graphene Bloch equations describing the dynamics of the coupled electron-phonon system under the influence of an external optical field. In particular, matrix elements as well as many-particle interactions are treated on a consistent microscopic footing. The obtained equations offer a microscopic access to the ultrafast non-equilibrium carrier dynamics in graphene.

Acknowledgements We acknowledge the financial support from the Deutsche Forschungsgemeinschaft through SPP 1459. Ermin Malić thanks the Einstein Foundation Berlin. We thank Faris Kadi (TU Berlin) for fruitful discussions.

4.A Appendix

4.A.1 Derivation of Optical Matrix Element

In this section the optical matrix element is derived, where the starting point is its definition in second quantization:

$$\mathbf{M}^{\lambda,\lambda'}_{\mathbf{k},\mathbf{k}'} = \langle \Psi^{\lambda}(\mathbf{k},\mathbf{r})|\nabla_{\mathbf{r}}|\Psi^{\lambda'}(\mathbf{k}',\mathbf{r})\rangle. \tag{4.89}$$

The optical matrix element can be determined analytically by applying the tight-binding wave functions:

$$\mathbf{M}^{\lambda,\lambda'}_{\mathbf{k},\mathbf{k}'} = \frac{1}{N}\sum_{l,\mathbf{R}_l}^{A,B}\sum_{l',\mathbf{R}_{l'}} c_l^{\lambda *}(\mathbf{k})c_{l'}^{\lambda'}(\mathbf{k}')e^{-i(\mathbf{k}\mathbf{R}_l-\mathbf{k}'\mathbf{R}_{l'})}\langle\phi(\mathbf{r}-\mathbf{R}_l)|\nabla_{\mathbf{r}}|\phi(\mathbf{r}-\mathbf{R}_{l'})\rangle. \tag{4.90}$$

For each summand of the first sum $\mathbf{R}_l$ the next-neighbor approximation is applied for the evaluation of the second sum consisting of $\mathbf{R}_l$ itself and the three neighbors from the other sublattice $l' \neq l$. Since the $2p_z$-orbital is symmetric in the x-y plane and antisymmetric in z direction, same-sided integrals vanish $\langle\phi(\mathbf{r}-\mathbf{R}_l)|\nabla_{\mathbf{r}}|\phi(\mathbf{r}-\mathbf{R}_l)\rangle = 0$. Therewith, Eq. (4.90) yields:

$$\begin{aligned}\mathbf{M}^{\lambda_i,\lambda_j}_{\mathbf{k},\mathbf{k}'} = \delta_{\mathbf{k},\mathbf{k}'}\Big[&c_A^{\lambda_i *}(\mathbf{k})c_B^{\lambda_j}(\mathbf{k})\sum_{i=1}^{3}e^{i\mathbf{k}\mathbf{b}_i}\langle\phi(\mathbf{r}+\mathbf{b}_i)|\nabla_{\mathbf{r}}|\phi(\mathbf{r})\rangle \\ &+c_B^{\lambda_i *}(\mathbf{k})c_A^{\lambda_j}(\mathbf{k})\sum_{i=1}^{3}e^{-i\mathbf{k}\mathbf{b}_i}\langle\phi(\mathbf{r})|\nabla_{\mathbf{r}}|\phi(\mathbf{r}+\mathbf{b}_i)\rangle\Big].\end{aligned} \tag{4.91}$$

It remains to determine the integral $\mathbf{I}_i = \langle\phi(\mathbf{r}+\mathbf{b}_i)|\nabla_{\mathbf{r}}|\phi(\mathbf{r})\rangle$. Regarding the next neighbor vectors in polar coordinates $\mathbf{b}_i = (b,\alpha_i)$ the integral reads:

$$\mathbf{I}_i = \left\langle \phi\begin{pmatrix} x+b\cos\alpha_i \\ y+b\sin\alpha_i \\ z\end{pmatrix}|\begin{pmatrix}\partial/\partial x \\ \partial/\partial y \\ \partial/\partial z\end{pmatrix}|\phi\begin{pmatrix}x\\y\\z\end{pmatrix}\right\rangle.$$

A rotation of the coordinates system $\Sigma(x,y,z)$ by the angle $-\alpha_i$ yields

$$\mathbf{I}_i = \begin{pmatrix}\cos\alpha_i \\ \sin\alpha_i \\ 0\end{pmatrix}\left\langle \phi\begin{pmatrix}(x'+b)\cos\alpha_i - y'\sin\alpha_i \\ (x'+b)\sin\alpha_i + y'\cos\alpha_i \\ z\end{pmatrix}|\frac{\partial}{\partial x'}|\phi\begin{pmatrix}x'\cos\alpha_i - y'\sin\alpha_i \\ x'\sin\alpha_i + y'\cos\alpha_i \\ z\end{pmatrix}\right\rangle.$$

Since the $2p_z$-orbital depends in the plane just on the modulus, the arguments can be rotated back by the angle α_i, finally resulting in

$$\mathbf{I}_i = M\frac{\mathbf{b}_i}{|\mathbf{b}_i|}. \tag{4.92}$$

The remaining integral $M = \left\langle \phi\begin{pmatrix} x+b \\ y \\ z \end{pmatrix} | \frac{\partial}{\partial x} | \phi\begin{pmatrix} x \\ y \\ z \end{pmatrix} \right\rangle$ can be evaluated numerically by applying $2p_z$-orbitals with the effective charge number Z. Therewith, M as well as Z are determined by the value of the overlap integral s_0, cf. Sect. 4.3.1. With Eqs. (4.91) and (4.92) the optical matrix elements can directly be obtained as denoted in the main text, cf. Eqs. (4.25) and (4.26):

$$\mathbf{M}^{v,c}_{\mathbf{k},\mathbf{k}'} = \delta_{\mathbf{k},\mathbf{k}'}\frac{1}{\sqrt{1-s_0^2|e(\mathbf{k})|^2}}\frac{M}{|e(\mathbf{k})|}\Re\left[e^*(\mathbf{k})\sum_{i=1}^{3}e^{i\mathbf{k}\mathbf{b}_i}\frac{\mathbf{b}_i}{|\mathbf{b}_i|}\right] \tag{4.93}$$

and

$$\mathbf{M}^{v,v}_{\mathbf{k},\mathbf{k}'} = \delta_{\mathbf{k},\mathbf{k}'}\frac{i}{\sqrt{1-s_0^2|e(\mathbf{k})|^2}}\frac{M}{|e(\mathbf{k})|}\Im\left[e^*(\mathbf{k})\sum_{i=1}^{3}e^{i\mathbf{k}\mathbf{b}_i}\frac{\mathbf{b}_i}{|\mathbf{b}_i|}\right], \tag{4.94}$$

with

$$\Re[\cdots]_x = \cos(a_0k_y) - \cos\left(\frac{\sqrt{3}a_0}{2}k_x\right)\cos\left(\frac{a_0}{2}k_y\right), \tag{4.95}$$

$$\Re[\cdots]_y = -\sqrt{3}\sin\left(\frac{a_0}{2}k_y\right)\sin\left(\frac{\sqrt{3}a_0}{2}k_x\right) \tag{4.96}$$

$$\Im[\cdots]_x = 3\cos\left(\frac{a_0}{2}k_y\right)\sin\left(\frac{\sqrt{3}a_0}{2}k_x\right) \tag{4.97}$$

$$\Im[\cdots]_y = \sqrt{3}\left[\sin(a_0k_y) + \sin\left(\frac{a_0}{2}k_y\right)\cos\left(\frac{\sqrt{3}a_0}{2}k_x\right)\right] \tag{4.98}$$

4.A.2 Derivation of Coulomb Matrix Element

The starting point for the derivation of the Coulomb matrix element is its description in second quantization:

$$V^{\mathbf{ab}}_{\mathbf{cd}} = \langle\Psi_{\mathbf{a}}(\mathbf{r})\Psi_{\mathbf{b}}(\mathbf{r}')|V(\mathbf{r}-\mathbf{r}')|\Psi_{\mathbf{d}}(\mathbf{r}')\Psi_{\mathbf{c}}(\mathbf{r})\rangle, \tag{4.99}$$

The Coulomb potential $V(\mathbf{r}-\mathbf{r}') = \frac{e_0^2}{4\pi\varepsilon_0}\frac{1}{|\mathbf{r}-\mathbf{r}'|}$ depends in principle a three-dimensional potential vectors. Since all electron wave vectors lies in the graphene plane, a two-dimensional Fourier transform is applied to decouple the integrals in Eq. (4.99):

$$V_{2d}(\mathbf{r}_\parallel) = \sum_{\mathbf{q}} V_{\mathbf{q}} e^{-i\mathbf{q}\mathbf{r}_\parallel}, \qquad \text{with} \qquad V_{\mathbf{q}} = \frac{e_0^2}{2\varepsilon_0 L^2}\frac{1}{q}. \tag{4.100}$$

Extended into the third dimension the entire Coulomb potential reads

$$V(\mathbf{r}) = \frac{e_0^2}{2\varepsilon_0 L^2}\sum_{\mathbf{q}}\frac{1}{q}e^{i\mathbf{q}\mathbf{r}} \qquad \text{with} \qquad q_z \equiv 0. \tag{4.101}$$

Therewith, the decoupling of Eq. (4.99) yields:

$$V_{\mathbf{cd}}^{\mathbf{ab}} = \sum_{\mathbf{q}} V_q \Gamma_{\mathbf{a},\mathbf{c}}(\mathbf{q})\Gamma_{\mathbf{d},\mathbf{b}}^*(\mathbf{q}) \quad \text{with} \quad \Gamma_{\mathbf{i},\mathbf{j}}(\mathbf{q}) = \int_V dr^3 \Psi_{\mathbf{i}}^*(\mathbf{r}) e^{i\mathbf{q}\mathbf{r}} \Psi_{\mathbf{j}}(\mathbf{r}). \tag{4.102}$$

The wave function Ψ can be represented by the components of the sublattices, cf. Eq. (4.8):

$$\Gamma_{\mathbf{i},\mathbf{j}}(\mathbf{q}) = \int_V dr^3 \sum_{l,l'} c_l^{\mathbf{i}*} c_{l'}^{\mathbf{j}} \Phi_l^{\mathbf{i}*}(\mathbf{r}) e^{i\mathbf{q}\mathbf{r}} \Phi_{l'}^{\mathbf{j}}(\mathbf{r}). \tag{4.103}$$

Neglecting the hoping integrals between different sublattices and exploiting their equivalence, Eq. (4.103) reads:

$$\Gamma_{\mathbf{i},\mathbf{j}} = f(\mathbf{i},\mathbf{j}) I_A^{\mathbf{ij}}(\mathbf{q}) \tag{4.104}$$

$$\text{with} \qquad I_A^{\mathbf{ij}}(\mathbf{q}) = \int_V dr^3 \Phi_A^{\mathbf{i}*}(\mathbf{r}) e^{i\mathbf{q}\mathbf{r}} \Phi_A^{\mathbf{j}}(\mathbf{r}) \tag{4.105}$$

$$\text{and} \qquad f(\mathbf{i},\mathbf{j}) = \left[c_A^{\mathbf{i}*} c_A^{\mathbf{j}} + c_B^{\mathbf{i}*} c_B^{\mathbf{j}}\right] = \frac{1}{2}\left[1 + \sigma_i \sigma_j \frac{e^*(\mathbf{k}_i) e(\mathbf{k}_j)}{|e(\mathbf{k}_i)||e(\mathbf{k}_j)|}\right] \tag{4.106}$$

With the Bloch functions (Eq. 4.9) and the neglect of overlaps between different unit cells, the integral in Eq. (4.105) can be simplified to:

$$I_A^{\mathbf{ij}}(\mathbf{q}) = \delta_{\mathbf{q},\mathbf{k_i}-\mathbf{k_j}} \int_V dr^3 \phi^*(\mathbf{r}) e^{i\mathbf{q}\mathbf{r}} \phi(\mathbf{r}). \tag{4.107}$$

The remaining integral can be evaluated analytically by applying the $2p_z$-orbital with the effect charge Z [53]:

$$\mathscr{V}_q = \int_V dr^3 \phi^*(\mathbf{r}) e^{i\mathbf{q}\mathbf{r}} \phi(\mathbf{r}) = \left[(qa_B/Z)^2 + 1\right]^{-3}. \tag{4.108}$$

Overall, the Coulomb matrix element reads:

$$V_{\mathbf{cd}}^{\mathbf{ab}} = V_q \mathscr{V}_q^2 f(\mathbf{a},\mathbf{c}) f(\mathbf{b},\mathbf{d}) \delta_{\mathbf{k}_a+\mathbf{k}_b,\mathbf{k}_c+\mathbf{k}_d}, \tag{4.109}$$

where the Kronecker ensures the conservation of momentum.

References

1. Xia YN, Yang PD, Sun YG, Wu YY, Mayers B, Gates B, Yin YD, Kim F, Yan YQ (2003) Adv Mater 15(5):353
2. Geim AK, Novoselov KS (2007) Nat Mater 6(3):183
3. Bonaccorso F, Sun Z, Hasan T, Ferrari AC (2010) Nat Photonics 4(9):611
4. Haug H, Koch SW (2004) Quantum theory of the optical and electronic properties of semiconductors. World Scientific, Singapore
5. Kira M, Koch S (2006) Prog Quantum Electron 30(5):155
6. Hirtschulz M, Malic E, Milde F, Knorr A (2009) Phys Rev B 80(8):085405
7. Malić E, Hirtschulz M, Milde F, Wu Y, Maultzsch J, Heinz TF, Knorr A, Reich S (2008) Phys Rev B 77(4):045432
8. Malic E, Maultzsch J, Reich S, Knorr A (2010) Phys Rev B 82(3):035433
9. Malic E, Maultzsch J, Reich S, Knorr A (2010) Phys Rev B 82(11):115439
10. Malic E, Winzer T, Bobkin E, Knorr A (2011) Phys Rev B 84(20):205406
11. Bobkin E, Knorr A, Malic E (2012) Phys Rev B 85(3):033409
12. Winzer T, Knorr A, Malic E (2010) Nano Lett 10(12):4839
13. Malic E, Weber C, Richter M, Atalla V, Klamroth T, Saalfrank P, Reich S, Knorr A (2011) Phys Rev Lett 106(9):097401
14. Butscher S, Milde F, Hirtschulz M, Malić E, Knorr A (2007) Appl Phys Lett 91(20):203103
15. Winzer T, Malić E (2011) Phys Status Solidi B 248(11):2615–2618
16. Breusing M, Kuehn S, Winzer T, Malić E, Milde F, Severin N, Rabe JP, Ropers C, Knorr A, Elsaesser T (2011) Phys Rev B 83(15):153410
17. Winnerl S, Orlita M, Plochocka P, Kossacki P, Potemski M, Winzer T, Malic E, Knorr A, Sprinkle M, Berger C, de Heer WA, Schneider H, Helm M (2011) Phys Rev Lett 107(23):237401
18. Malic E, Winzer T, Knorr A (2012) Appl Phys Lett 101(21):213110
19. Winzer T, Malic E (2013) J Phys Condens Matter 25:054201
20. Winzer T, Knorr A, Mittendorff M, Winnerl S, Lien MB, Sun D, Norris TB, Helm M, Malic E (2012) Appl Phys Lett 101(22):221115
21. Winzer T, Malić E (2012) Phys Rev B 85(24):241404
22. Gabor NM, Song JCW, Ma Q, Nair NL, Taychatanapat T, Watanabe K, Taniguchi T, Levitov LS, Jarillo-Herrero P (2011) Science 334(6056):648
23. Tani S, Blanchard F, Tanaka K (2012) Phys Rev Lett 109(16):166603
24. Sun D, Aivazian G, Jones AM, Ross JS, Yao W, Cobden D, Xu X (2012) Nat Nanotechnol 7(2):114
25. Brida D, Tomadin A, Manzoni C, Kim YJ, Lombardo A, Milana S, Nair RR, Novoselov KS, Ferrari AC, Cerullo G, Polini M (2012) arXiv:1209.5729
26. Li T, Luo L, Hupalo M, Zhang J, Tringides MC, Schmalian J, Wang J (2012) Phys Rev Lett 108(16):167401
27. Winzer T, Malic E, Knorr A (2013) Phys Rev B 87:165413
28. Sun D, Divin C, Mihnev M, Winzer T, Malic E, Knorr A, Sipe JE, Berger C, de Heer WA, First PN, Norris TB (2012) New J Phys 14(10):105012

29. Scully MO, Zubairy MS (1997) Quantum optics, 1st edn. Cambridge University Press, Cambridge
30. Piscanec S, Lazzeri M, Mauri F, Ferrari AC, Robertson J (2004) Phys Rev Lett 93(18):185503
31. Hwang EH, Das Sarma S (2008) Phys Rev B 77(11):115449
32. Lee C, Wei X, Kysar JW, Hone J (2008) Science 321(5887):385
33. Machón M, Reich S, Thomsen C, Sánchez-Portal D, Ordejón P (2002) Phys Rev B 66(15):155410
34. Ashcroft NW, Mermin ND (1976) Solid state physics, 1st edn. Brooks Cole, Oxford
35. Reich S, Maultzsch J, Thomsen C, Ordejón P (2002) Phys Rev B 66(3):035412
36. Reich S, Thomsen C, Maultzsch J (2004) Carbon nanotubes, 1st edn. Wiley-VCH, Weinheim
37. Yang L, Deslippe J, Park CH, Cohen ML, Louie SG (2009) Phys Rev Lett 103(18):186802
38. Saito R, Dresselhaus G, Dresselhaus MS (1998) Physical properties of carbon nanotubes. Imperial College Press, London
39. Grüneis A, Saito R, Samsonidze GG, Kimura T, Pimenta MA, Jorio A, Filho AGS, Dresselhaus G, Dresselhaus MS (2003) Phys Rev B 67:165402
40. Malić E, Hirtschulz M, Milde F, Knorr A, Reich S (2006) Phys Rev B 74(19):195431
41. Stroucken T, Grönqvist JH, Koch SW (2011) Phys Rev B 84(20):205445
42. Ando T (2006) J Physical Soc Japan 75(7):074716
43. Jiang J, Saito R, Samsonidze GG, Jorio A, Chou SG, Dresselhaus G, Dresselhaus MS (2007) Phys Rev B 75(3):035407
44. Verdenhalven E, Binder R, Knorr A, Malić E (2013) J Chem Phys 413:3
45. Fricke J (1996) Ann Phys 252(2):479
46. Heitler W (1954) The quantum theory of radiation, 3rd edn. Courier Dover Publications, New York
47. Fick E, Sauermann G (1990) The quantum statistics of dynamic processes. Springer, New York
48. Schilp J, Kuhn T, Mahler G (1994) Phys Rev B 50(8):5435
49. Rossi F, Kuhn T (2002) Rev Mod Phys 74(3):895
50. Koga S, Katayama I, Abe S, Fukidome H, Suemitsu M, Kitajima M, Takeda J (2011) Appl Phys Express 4(4):045101
51. Kang K, Abdula D, Cahill DG, Shim M (2010) Phys Rev B 81(16):165405
52. Bonini N, Lazzeri M, Marzari N, Mauri F (2007) Phys Rev Lett 99(17):176802
53. Straton JC (1987) Phys Rev A 35(6):2729

Chapter 5
Transport Through a Coulomb Blockaded Majorana Nanowire

Alex Zazunov, Reinhold Egger, Alfredo Levy Yeyati, Roland Hützen, and Bernd Braunecker

Abstract In one-dimensional (1D) quantum wires with strong spin-orbit coupling and a Zeeman field, a superconducting substrate can induce zero-energy Majorana bound states located near the ends of the wire. We study electronic properties when such a wire is contacted by normal metallic or superconducting electrodes. A special attention is devoted to Coulomb blockade effects. We analyze the "Majorana single-charge transistor" (MSCT), i.e., a floating Majorana wire contacted by normal metallic source and drain contacts, where charging effects are important. We describe Coulomb oscillations in this system and predict that Majorana fermions could be unambiguously detected by the emergence of sideband peaks in the nonlinear differential conductance. We also study a superconducting variant of the MSCT setup with *s*-wave superconducting (instead of normal-conducting) leads. In the noninteracting case, we derive the exact current-phase relation (CPR) and find π-periodic behavior with negative critical current for weak tunnel couplings. Charging effects then cause the anomalous CPR $I(\varphi) = I_c \cos\varphi$, where the parity-sensitive critical current I_c provides a signature for Majorana states.

A. Zazunov (✉) • R. Egger • R. Hützen
Institut für Theoretische Physik, Heinrich-Heine-Universit, D-40225 Düsseldorf, Germany
e-mail: zazu@thphy.uni-duesseldorf.de; egger@thphy.uni-duesseldorf.de; huetzen@thphy.uni-duesseldorf.de

A. Levy Yeyati • B. Braunecker
Departamento de Física Teórica de la Materia Condensada, Universidad Autónoma de Madrid, E-28049 Madrid, Spain
e-mail: a.l.yeyati@uam.es; bernd.braunecker@uam.es

R. Egger et al. (eds.), *Low-Dimensional Functional Materials*, NATO Science for Peace and Security Series B: Physics and Biophysics, DOI 10.1007/978-94-007-6618-1_5,

5.1 Introduction

Charge transport through topologically nontrivial materials is of great current interest, offering novel fundamental insights as well as potential applications in topological quantum computing [1]. The recently discovered topological insulators as well as topological superconductors (TSs) [7] are predicted to exhibit spectacular nonlocal transport phenomena and have consequently attracted a lot of attention. In particular, for 1D TS quantum wires, the crucial role of Majorana bound states (MBSs) located near the interface to topologically trivial regions has been emphasized [5, 9]. Majorana fermions are special in that they are their own antiparticles, i.e., the fermion creation operator is equal to the annihilation operator, and the condensed-matter setup discussed below could offer experimental signatures for these elusive and hitherto unobserved particles.

When a grounded TS is weakly contacted by a normal metal, the MBS is expected to produce a characteristic zero-bias anomaly peak in the tunnel conductance. Very recently, such a feature has been experimentally observed in tunnel spectroscopy using InSb or InAs nanowires [13], where Majorana fermions are theoretically expected due to the interplay of strong spin-orbit coupling, Zeeman field, and proximity-induced superconducting pairing. We here discuss an interacting variant of previously studied Majorana wire setups, the floating "Majorana single-charge transistor" (MSCT) schematically shown in Fig. 5.1. A comprehensive picture of its transport properties in the presence of interactions emerges from our analysis [8, 16]. Noting that the experimentally observed peak features could be related to a disorder-induced spectral peak [2, 11], our results should help to distinguish the Majorana state from alternative explanations in future experiments.

Previous works have studied electron-electron interactions in an isolated TS wire and found that Majoranas still exist under rather general conditions. As sketched in Fig. 5.1, here we instead study a generalization of the setup in Ref. [13], where source and drain metallic electrodes contact the TS wire. We stress that the MSCT could be realized not only with nanowires but using most other Majorana proposals as well. In such a geometry, Coulomb blockade effects due to the finite charging energy E_c of the TS can play a decisive role. For instance, one expects Coulomb

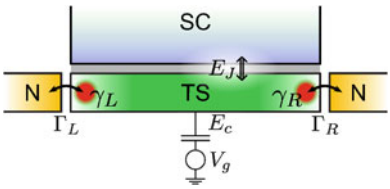

Fig. 5.1 Majorana single-charge transistor (MSCT): the TS wire with Majorana end states is tunnel-coupled (Γ_L, Γ_R) to normal metal electrodes and Josephson coupled (E_J) to another bulk superconductor. Capacitive charging effects are encoded by E_c and can be tuned by a gate voltage parameter $n_g \propto V_g$

oscillations of the conductance as a function of a gate voltage parameter n_g, with peaks (valleys) near half-integer (integer) n_g, while in the noninteracting ($E_c = 0$) limit, the MBSs pinned to zero energy cause resonant Andreev reflection (AR) [3, 10, 14], with n_g-independent linear conductance $G = 2e^2/h$ at temperature $T = 0$. Resonant AR also survives for $E_c < \Gamma = \Gamma_L + \Gamma_R$, albeit with reduced conductance [16]. For $E_c \gg \Gamma$, Coulomb blockade is firmly established, and the peak conductance approaches the (spinless) resonant tunneling value $G = e^2/h$, which has been pointed out as a signature of electron teleportation [4].

Below we consider Coulomb blockaded charge transport through the MSCT [8]. We provide an exact expression for the current in this interacting system, and develop three different approximation schemes to study Coulomb oscillations in the MSCT both for $T = 0$ and finite T. We quantitatively describe the $T = 0$ crossover of the peak conductance from $G = 2e^2/h$ to e^2/h as E_c/Γ increases, which constitutes a characteristic signature of Majoranas. Remarkably, this "halving" of the peak conductance is universal and found to hold for arbitrary T. For the valley conductance, we find that elastic cotunneling dominates while AR is subleading. We predict finite-voltage sidebands in the nonlinear differential conductance which are directly related to anomalous tunneling processes where the Majorana state and the Cooper pair number change simultaneously. The presence of Majoranas can be unambiguously identified in experiments by the magnetic field dependence of the sideband location.

We have also studied the Josephson effect for a TS wire with Majorana end states tunnel-coupled to s-wave BCS superconducting (S) electrodes [15]. We show that under generic conditions, a supercurrent blockade occurs in S-TS Josephson junctions. In the S-TS-S junction, this blockade imposes severe restrictions; in particular, quasiparticle excitations are necessary to have a Josephson effect. For the noninteracting case, the analytical solution for the current-phase relation (CPR) has been obtained. It shows that the 4π-periodic Josephson effect is absent in S-TS-S junctions. For weak tunneling, the CPR is π-periodic with a negative critical current, while a finite charging energy results in the anomalous CPR $I(\varphi) = I_c \cos\varphi$. The parity sensitivity of I_c could then be used to detect the Majorana states in supercurrent measurements. We hope that our predictions will soon be tested experimentally.

5.2 Model and Approaches

The MSCT Hamiltonian, $H = H_c + H_t + H_l$, contains a piece H_c describing the TS wire, a tunnel Hamiltonian H_t connecting the TS to the left ($j = L$) and right ($j = R$) electrode, and a term H_l describing the leads (we often use units with $e = \hbar = k_B = 1$). Topological arguments warrant that the TS wire holds a single unpaired MBS near each end described by the Majorana operator $\gamma_j = \gamma_j^\dagger$ with anticommutator $\{\gamma_j, \gamma_{j'}\} = \delta_{jj'}$. We introduce the non-local fermion operator $d = (\gamma_L + i\gamma_R)/\sqrt{2}$ such that $\gamma_L = (d + d^\dagger)/\sqrt{2}$ and $\gamma_R = -i(d - d^\dagger)/\sqrt{2}$. With

$\hat{n}_d = d^\dagger d$ and the number operator $\hat{N}$ for Cooper pairs in the TS, the instantaneous charge state of the wire is described by (N, n_d), where the integer N and $n_d = 0, 1$ are eigenvalues of $\hat{N}$ and $\hat{n}_d$, respectively. With the phase χ conjugate to $\hat{N}$, where $[\chi, \hat{N}] = i$ and $e^{-i\chi}$ ($e^{i\chi}$) lowers (raises) N by one unit, we have

$$H_c = E_c(2\hat{N} + \hat{n}_d - n_g)^2 - E_J \cos(\chi - \phi_S). \tag{5.1}$$

The TS wire is assumed sufficiently long to exclude a direct tunnel coupling between γ_L and γ_R. However, note that E_c introduces a dynamical coupling between the Majoranas. Proximity-induced pairing correlations are required for MBS formation, and in Eq. (5.1) we include Cooper pair exchange (with Josephson coupling E_J) between the TS condensate and another bulk superconductor (with fixed phase ϕ_S). We focus on the most interesting case of a large proximity gap $\Delta_{\rm TS} > \max(E_c, \Gamma, T)$, where charge transport involves MBSs and the contribution of quasi-particles above the gap can be neglected. Next, electrons in lead j correspond to free fermions with chemical potential μ_j and (effectively spinless) fermionic operators $c_{j,k}$ for momentum k. H_l is treated within the usual wide-band approximation and the bias voltage is $eV = \mu_L - \mu_R$. Taking into account charge conservation and expressing the Majoranas in terms of the non-local d fermion, the tunnel Hamiltonian reads [16]

$$H_t = \sum_j \lambda_j c_j^\dagger \eta_j + \text{h.c.}, \quad \eta_j = \frac{1}{\sqrt{2}}(d + s_j e^{-i\chi} d^\dagger), \tag{5.2}$$

where $c_j = \sum_k c_{j,k}$, $s_L = +1$ and $s_R = -1$, and $\lambda_{L,R}$ denotes the respective tunnel matrix elements. Tunneling from the TS to lead j thus proceeds either by destroying the d state without changing N ("normal" tunneling) or by occupying the d state and simultaneously splitting a Cooper pair ("anomalous" tunneling), plus the conjugate processes. Below we use the hybridization scales $\Gamma_j = 2\pi\nu_j|\lambda_j|^2$, where ν_j is the density of states in lead j. Experimentally, the Γ_j (and n_g) can be changed via gate voltages [13].

5.2.1 Exact Expression for Current

Using non-equilibrium Green's function (GF) techniques, the current I_j flowing from lead j to the TS can be expressed in terms of the Keldysh GF $\check{G}_{\eta_j}(t,t') = -i\langle \mathscr{T}_C \eta_j(t)\eta_j(t')\rangle$, where $\mathscr{T}_C$ denotes Keldysh time ordering. With the Fourier-transformed retarded, $G^R_{\eta_j}(\varepsilon)$, and Keldysh, $G^K_{\eta_j}(\varepsilon)$, components of $\check{G}_{\eta_j}$, we obtain $I_j = (e\Gamma_j/h)\int d\varepsilon [F(\varepsilon - \mu_j)\ \mathrm{Im}G^R_{\eta_j}(\varepsilon) + (i/2)G^K_{\eta_j}(\varepsilon)]$, where $F(\varepsilon) = 1 - 2f = \tanh(\varepsilon/2T)$ encodes the Fermi function $f(\varepsilon)$ in the leads. Next we note that $G^K_{\eta_j}(t,t) = 0$ as a consequence of $\eta_j^\dagger \eta_j = \eta_j \eta_j^\dagger = 1/2$. Hence we find the exact result

$$I_j = \frac{e\Gamma_j}{h} \int d\varepsilon F(\varepsilon - \mu_j)\, \mathrm{Im} G^R_{\eta_j}(\varepsilon), \tag{5.3}$$

stating that the current can be computed from the spectral function $\propto \mathrm{Im} G^R_{\eta_j}$. The well-known expression for interacting quantum dots [12] has thereby been extended to the interacting Majorana wire, where there are two spectral functions associated to the currents I_L and I_R. Eq. (5.3) should be useful for numerically exact calculations, e.g., using the numerical or density-matrix renormalization group. For $E_c = 0$, the pseudo-fermions η_j reduce to Majorana fermions γ_j, and the Lorentzian spectral function, $-\mathrm{Im} G^R_{\gamma_j}(\varepsilon) = \Gamma_j/(\varepsilon^2 + \Gamma_j^2)$, implies resonant AR with $G = 2e^2/h$.

5.2.2 *Approaches*

For finite E_c, we present several complementary approximations in order to achieve a broad physical understanding of the MSCT transport properties. Current conservation implies $I_L + I_R + I_S = 0$, with the supercurrent I_S flowing through the interface to the bulk superconductor. Below we define the conductance $G = dI/dV$ using the symmetrized current $I = (I_L - I_R)/2$.

5.2.2.1 Equation-of-Motion (EOM) Approach

We constructed an EOM approach for $G^R_{\eta_j}$ to access the linear conductance near a peak. Within this method, we introduce the Nambu spinors $\Psi_d = \left(d, e^{-i\chi} d^\dagger\right)^T$ and the corresponding retarded GF, $G^R_{dd} = -i\Theta(t-t')\langle\{\Psi_d(t), \Psi_d^\dagger(t')\}\rangle$. The EOM for G^R_{dd} generates higher-order GFs, $\Gamma^R_{N^m dd} = -i\Theta(t-t')\langle\{\hat{N}^m(t)\Psi_d(t), \Psi_d^\dagger(t')\}\rangle$, which we truncate at the level $m = 2$ and solve in a self-consistent way. The resulting GF G^R_{dd} then yields $G^R_{\eta_j} = \frac{1}{2}\mathrm{Tr}\left[(1 + s_j\sigma_x) G^R_{dd}\right]$ with Pauli matrix σ_x. Finally, we obtain the conductance from Eq. (5.3). This approximation is valid by construction for $E_c > \Gamma$, but the imposed self-consistency allows us to extend it to $E_c < \Gamma$, where the resulting conductance (being determined by truncated fluctuations) gives a lower bound for the exact result.

5.2.2.2 Zero-Bandwidth Model (ZBWM)

Next we study the ZBWM where each lead is represented by just a single fermion site and only a finite number of TS Cooper pairs ($N < N_{\max}$) is included. The Hilbert space then has the finite dimension $8N_{\max}$, which allows us to numerically calculate the spectral density $\propto \mathrm{Im} G^R_{\eta_j}(\varepsilon)$ via its Lehmann representation, with poles phenomenologically broadened by Γ. With this spectral function, Eq. (5.3) yields the conductance within the ZBWM.

5.2.2.3 Master Equation and Cotunneling Processes

For $T > \Gamma$, the GF formulation reduces to a master equation description including sequential tunneling and cotunneling processes (for simplicity, $E_J = 0$ here). The stationary probability distribution P_Q for having $Q = 2N + n_d$ particles on the TS then obeys $\sum_{Q' \neq Q}[P_{Q'} W_{Q' \to Q} - P_Q W_{Q \to Q'}] = 0$. All non-vanishing transition rates $W_{Q \to Q'}$ are specified in terms of rates obtained under a systematic second-order T-matrix expansion in $\Gamma_{L,R}$. With the electrostatic energy $E_Q = E_c(Q - n_g)^2$, sequential tunneling yields the rate $\Gamma^{(\mathrm{seq})}_{j,Q \to Q\pm 1} = (\Gamma_j/2) f(E_{Q\pm 1} - E_Q \mp \mu_j)$ for one particle tunneling into (out of) the TS from (to) lead $j = L, R$. Next, elastic cotunneling transfers a particle from lead j to the opposite lead $-j$ with virtual excitation of the TS states $Q \pm 1$. The elastic cotunneling rate is

$$\Gamma^{(\mathrm{EC})}_{j,Q} = \frac{\Gamma_L \Gamma_R}{8\pi} \int d\varepsilon f(\varepsilon - \mu_j)[1 - f(\varepsilon - \mu_{-j})] \times \left| \frac{1}{\varepsilon - (E_{Q+1} - E_Q) + i0} - \frac{1}{\varepsilon - (E_Q - E_{Q-1}) - i0} \right|^2, \tag{5.4}$$

where the two terms come from the interference of normal and anomalous tunneling. We note in passing that for large Δ_{TS}, inelastic cotunneling does not contribute at all, while the conventional elastic cotunneling rate due to quasi-particle states above the gap (and without MBSs) would be much smaller, $\Gamma^{(\mathrm{EC})} \propto \Gamma_L \Gamma_R / \Delta_{\mathrm{TS}}$. To the same order in $\Gamma_{L,R}$, we also have local (and crossed) AR processes, where an electron and a hole from the same (different) lead(s) are combined to form a Cooper pair, $Q \to Q + 2$; the reverse process describes Cooper pair splitting, $Q \to Q - 2$. Some algebra yields the AR rates

$$\begin{aligned} \Gamma^{(\mathrm{AR})}_{j,j',Q \to Q\pm 2} = {} & \frac{1 + \delta_{j,-j'}}{2} \frac{\Gamma_j \Gamma_{j'}}{8\pi} \int d\varepsilon \int d\varepsilon' \\ & \times f(\pm(\varepsilon - \mu_j)) f(\pm(\varepsilon' - \mu_{j'})) \delta(\varepsilon + \varepsilon' \mp (E_{Q\pm 2} - E_Q)) \\ & \times \left| \frac{1}{\varepsilon \mp (E_{Q\pm 1} - E_Q) + i0} - \frac{s_j s_{j'}}{\varepsilon' \mp (E_{Q\pm 1} - E_Q) + i0} \right|^2, \end{aligned} \tag{5.5}$$

where $j = j'$ ($j \neq j'$) corresponds to local (crossed) AR. The $i0$ terms indicate that regularization of the integrals in Eqs. (5.4) and (5.5) is necessary. Application of the general regularization scheme then implies that the principal value of these integrals needs to be taken. Given these rates and the (numerical) solution P_Q of the master equation, the currents I_j then readily follow.

5.3 Transport Signatures of Majorana Bound States

We now present results for the conductance $G = dI/dV$ to quantify the effect of Coulomb interactions on the transport properties in the Majorana-wire setup.

5.3.1 Coulomb Oscillations

Let us first address the n_g-dependence of the linear ($V \to 0$) conductance, see Fig. 5.2; we take $\Gamma_L = \Gamma_R = \Gamma/2$ in all figures. Both the master equation (main panel, finite T) and the ZBWM (inset, $T = 0$) reveal clear conductance oscillations in the MSCT for $E_c \gg \Gamma$, with peaks (valleys) for half-integer (integer) gate voltage parameter n_g. The main panel shows that the peak (valley) conductance is halved (strongly suppressed) when going from the noninteracting to the deep Coulomb blockade limit. For $E_J = 0$ and $(\Gamma, T) \ll E_c$, the lineshape of the valley conductance is obtained in closed form,

$$G_{\text{valley}}(\delta) = \frac{e^2}{h} \frac{\Gamma_L \Gamma_R}{E_c^2} \frac{1}{(1-4\delta^2)^2}, \tag{5.6}$$

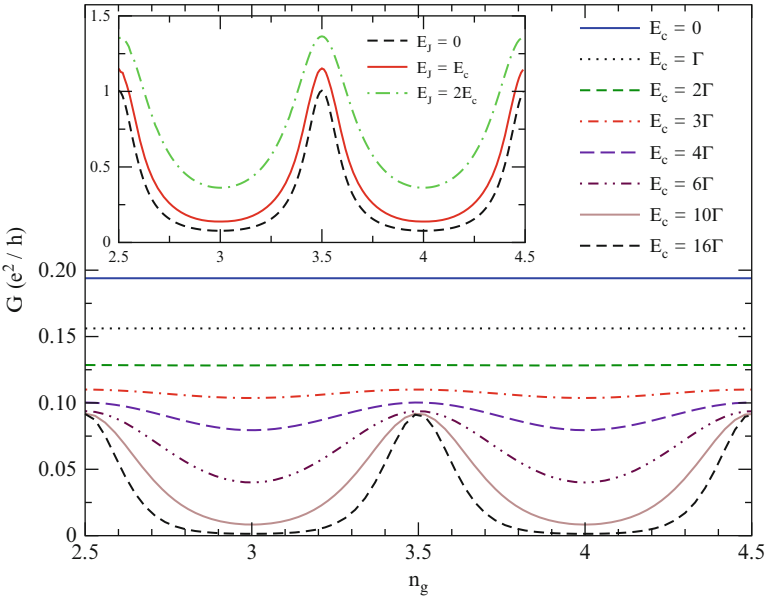

Fig. 5.2 Coulomb oscillations in the MSCT. *Main panel:* Conductance G vs. n_g from master equation for $E_J = 0, T = 2\Gamma$ and several E_c. *Inset:* Same but from ZBWM for $T = 0, E_c = 5\Gamma$ and several E_J

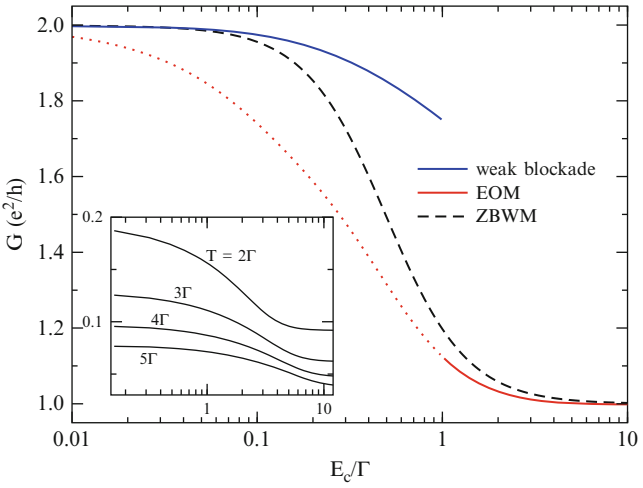

Fig. 5.3 Peak conductance G vs. E_c/Γ on a semi-logarithmic scale. *Main panel:* Comparison of $T = 0$ results using perturbation theory in E_c/Γ [16] (*blue solid curve*), the EOM approach (*red dotted-solid curve*), and the ZBWM (*black dashed curve*). The shown EOM results are quantitatively valid only for $E_c > \Gamma$ (*solid part*) but give a lower bound when $E_c < \Gamma$ (*dotted part*). Here $E_J = 0$ since G only weakly depends on E_J for $E_J < E_c$. *Inset:* Same but from master equation for several temperatures $T > \Gamma$ (color figure online)

where $\delta = n_g - [n_g]$ with $|\delta| \ll 1$ is the deviation from a valley center. Equation (5.6) comes from elastic cotunneling, with constructive interference of the normal and anomalous tunneling contributions, while AR is strongly suppressed in this limit. The inset of Fig. 5.2 shows that G increases when the Josephson coupling E_J grows. One can understand this by noting that for $E_J \gg E_c$, one ultimately reaches the resonant AR limit of a grounded TS, with the n_g-independent $T = 0$ conductance $G = 2e^2/h$. We find that AR yields significant conductance contributions for $E_J > E_c$, which are best detected through the non-local conductance $\partial I_L/\partial \mu_R$. However, we will discuss this quantity in detail elsewhere.

5.3.2 Peak Conductance

Results for the peak conductance are shown in Fig. 5.3. For $T = 0$ (main panel), we obtain the full crossover from $G = 2e^2/h$ to $G = e^2/h$ as E_c/Γ increases. The known small-E_c behavior [16] is nicely reproduced by the ZBWM calculation. In the opposite large-E_c limit, the EOM method is very accurate and Fig. 5.3 suggests that the simple ZBWM already captures the crossover from resonant AR to electron teleportation [4] surprisingly well. The inset of Fig. 5.3 again demonstrates the universal halving of the finite-T peak conductance, see also Fig. 5.2. Since

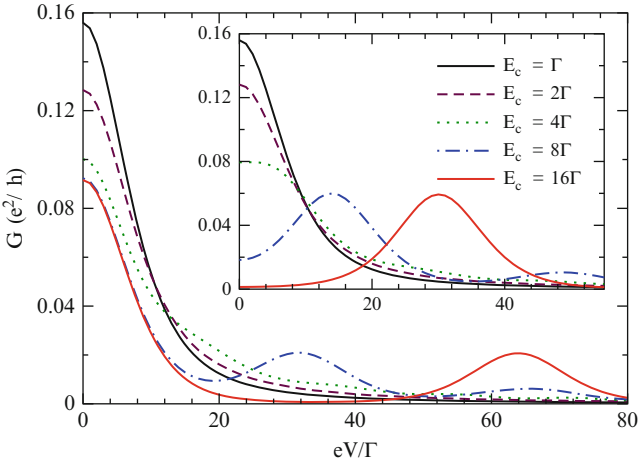

Fig. 5.4 $G = dI/dV$ vs. voltage V from the master equation for $T = 2\Gamma$, $E_J = 0$, and several E_c/Γ. The main panel (*inset*) is for half-integer (integer) n_g

experiments so far were conducted in the high-temperature regime $T > \Gamma$ [13], let us now specify the lineshape near a conductance peak for $E_c \gg \Gamma$. Using $\delta = n_g - [n_g] - 1/2$ with $|\delta| \ll 1$ for the deviation from a peak center, truncation of the master equation to two charge states gives

$$G_{\text{peak}}(\delta) = \frac{e^2}{h}\frac{\pi\Gamma}{16T}\frac{1}{\cosh^2(\delta E_c/T)}. \tag{5.7}$$

We stress that the peak conductance $[G_{\text{peak}}(\delta = 0)]$ is indeed halved compared to $E_c = 0$. Moreover, it exhibits both a thermal and an interaction-induced reduction.

5.3.3 *Finite-Voltage Sidebands*

Next we discuss the differential conductance at finite bias voltage V. Master equation results for $T = 2\Gamma$ are shown in Fig. 5.4. Starting with the main panel, we find sideband peaks when eV is equal to an integer multiple of $4E_c$. For these voltages, the chemical potentials $\mu_{L,R}$ are resonant with two (almost) degenerate higher-order charge states, implying additional sequential tunneling contributions beyond the resonant transition determining the linear conductance peak (Eq. 5.7). Note that the fluctuations in N needed to reach higher-order charge states can only be achieved through anomalous tunneling processes (see Eq. 5.2). Similar sideband peaks are also found for other n_g; the integer-n_g valley case is shown in the inset of Fig. 5.4. In Fig. 5.5 we show the evolution of the sideband peaks as E_J is changed, determined from the ZBWM at $T = 0$. For half-integer n_g, the

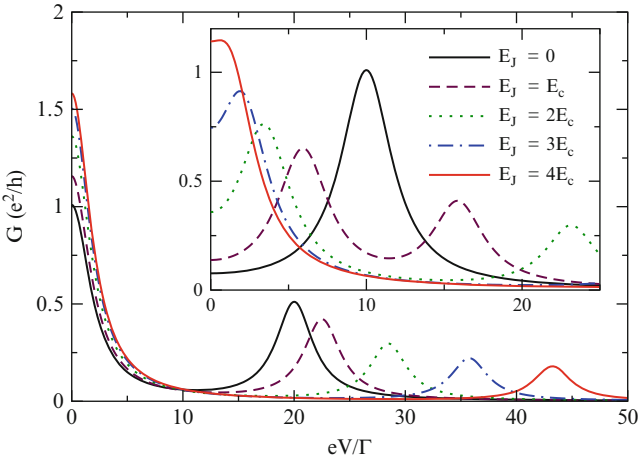

Fig. 5.5 Same as Fig. 5.4 but from ZBWM for $T = 0$, $E_c = 5\Gamma$ and several E_J

sideband peak position observed in the main panel of Fig. 5.5 is well described by $eV \simeq 4E_c\sqrt{1+(E_J/2E_c)^2}$, which comes from Josephson coupling between the two relevant charge states. Since E_J can be tuned by applying a small magnetic field parallel to the junction between the TS and the bulk superconductor, an experimental observation of the sideband peak and its shift with magnetic field (cf. the expression for the peak position above) would provide clear evidence for the anomalous tunneling mechanism, and thereby for the presence of MBSs.

5.4 Josephson Junctions with a Majorana Wire

When two TS wires are contacted, one expects the fractional Josephson effect with 4π-periodic CPR, $I(\varphi)$, due to parity conservation [1]. If the junction also contains a topologically trivial superconductor (TS-S-TS), additional periodicities may occur [6]. Here we discuss the ground-state supercurrent flowing through the S-TS and S-TS-S junctions schematically shown in Fig. 5.6. The left/right ($j = L/R$) electrodes correspond to standard s-wave BCS superconductors with (for simplicity identical) gap Δ and fixed phase φ_j. The 1D Majorana wire contains a pair of decoupled MBSs at its ends. We consider a finite proximity-induced TS gap Δ_w and take into account the (p-wave type) TS quasiparticles. For the S-TS-S junction with a floating (not grounded) Majorana wire, we also include a capacitive Coulomb interaction via the charging energy E_c. In practice, depending on the experimental realization, there can also be a parallel channel for Cooper pair transfer involving only the superconducting substrate, and we here focus only on the Josephson current involving the TS wire. Our main results are as follows.

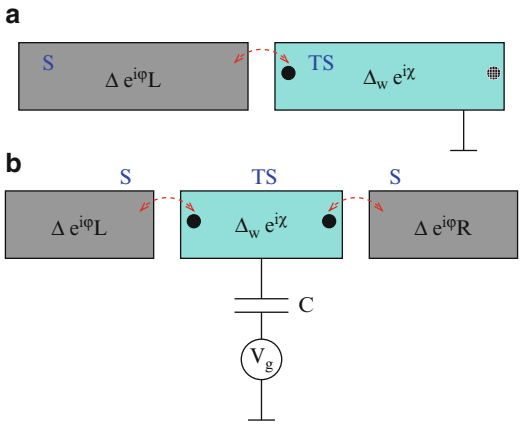

Fig. 5.6 Schematic Josephson junction setups involving a Majorana wire (TS) with proximity-induced gap Δ_w and phase χ. *Bold dots* stand for MBSs. The electrodes are *s*-wave BCS superconductors (S) with gap Δ and fixed phase $\varphi_{j=L/R}$. Tunneling processes between an S electrode and the respective MBS and/or TS quasiparticle states are indicated by *dashed arrows*. (**a**) S-TS junction. (**b**) S-TS-S junction with charging energy $E_c = e^2/(2C)$

5.4.1 S-TS Junction

For the S-TS junction (see Fig. 5.6(a)), the supercurrent is completely blocked for large Δ_w and/or for pointlike tunneling contacts. This has far-reaching consequences for the Josephson current through a Majorana wire whenever *s*-wave superconducting electrodes are involved. Below we provide a general condition explaining the supercurrent blockade.

The S-TS contact is modeled by the general tunneling Hamiltonian

$$H_t = \sum_{\mathbf{k},\sigma\sigma'} \int dx\, c^\dagger_{\mathbf{k},\sigma} \mathscr{T}_{\mathbf{k},\sigma\sigma'}(x) \psi_{\sigma'}(x) + \text{H.c.}$$

with the field operator $\psi_{\sigma(x)}$ for electrons with spin projection $\sigma = \uparrow, \downarrow$ in the TS wire. Note that the tunnel matrix elements encoded in the kernel $\mathscr{T}_{\mathbf{k},\sigma\sigma'}(x)$ may also describe spin-flip scattering at the interface. Expanding $\psi_{\sigma(x)}$ in terms of the TS quasiparticle operators f_α and the Majorana fermions γ_j, we obtain

$$H_t = \sum_{\mathbf{k}\sigma} c^\dagger_{\mathbf{k},\sigma} \psi_{\mathbf{k},\sigma} + \text{H.c.}\,, \quad \psi_{\mathbf{k},\sigma} = \lambda_{\mathbf{k},\sigma} \gamma_L + \sum_\alpha t_{\mathbf{k},\sigma;\alpha} f_\alpha. \tag{5.8}$$

The complex-valued tunnel couplings $\lambda_{\mathbf{k},\sigma}$ and $t_{\mathbf{k},\sigma;\alpha}$ now encapsulate the overlap integrals of the kernel $\mathscr{T}_{\mathbf{k},\sigma\sigma'}(x)$ with the Majorana and quasiparticle wavefunctions in the TS wire, respectively.

The exact CPR, $I(\varphi) = (2e/\hbar)\partial_\varphi F(\varphi)$, can be obtained from the partition function, $Z(\varphi) = \mathrm{Tr} e^{-\beta H} = e^{-\beta F}$, with inverse temperature β and phase difference $\varphi = \varphi_L - \chi$. After integration over the S electrons, the φ-dependent part of the free energy comes from the action piece

$$\beta \mathscr{F}_s = \int_0^\beta d\tau_1 d\tau_2 \sum_{\mathbf{k}} \Phi_{\mathbf{k}}^\dagger(\tau_1) G_k(\tau_1 - \tau_2) \Phi_{\mathbf{k}}(\tau_2), \tag{5.9}$$

where $\Phi_{\mathbf{k}} = (\psi_{\mathbf{k},\uparrow}, \psi_{-\mathbf{k},\downarrow}^\dagger)^T$ with Eq. (5.8). The (Fourier-transformed) anomalous Green's function is $G_k(\omega) = \frac{\Delta}{\omega^2 + \xi_k^2 + \Delta^2} \sigma_x e^{i\varphi\sigma_z}$. Using $G_k(\tau) = G_k(-\tau)$ and $G_k \sim \sigma_{x,y}$, we find $\mathscr{F}_s = 0$ whenever the time-reversed partners $\psi_{\mathbf{k},\uparrow}$ and $\psi_{-\mathbf{k},\downarrow}$ in Eq. (5.8) are collinear,

$$\psi_{-\mathbf{k},\downarrow} = \zeta_{\mathbf{k}} \psi_{\mathbf{k},\uparrow}, \tag{5.10}$$

with some complex parameter $\zeta_{\mathbf{k}}$. This is a sufficient (but not necessary) condition for supercurrent blockade in an S-TS junction. In simple terms, the S-TS Josephson effect will be strongly suppressed unless noncollinear time-reversed states are available in the TS wire. To give some examples, consider the limit $\Delta_w \to \infty$, where no TS quasiparticles are accessible. In that case, Eq. (5.8) yields $\psi_{\mathbf{k},\sigma} = \lambda_{\mathbf{k},\sigma}\gamma_L$, which always satisfies Eq. (5.10). In the absence of quasiparticles, an S-TS junction thus never carries a supercurrent. Similarly, Eq. (5.10) trivially holds for a spin-polarized TS wire, where $\zeta_{\mathbf{k}} = 0$. However, for a point-like tunneling contact with

$$\lambda_{\mathbf{k},\sigma} \to \lambda_\sigma, \quad t_{\mathbf{k},\sigma;\alpha} \to t_\sigma, \tag{5.11}$$

Equation (5.10) is generally not satisfied. Nonetheless, the supercurrent also vanishes in this limit [15].

5.4.2 S-TS-S Junction

In S-TS-S junctions (see Fig. 5.6(b)), as follows from Sect. 5.4.1, a finite supercurrent is only possible when quasiparticles (or other fermion excitations, e.g., a subgap impurity level) on the Majorana wire are accessible, at least for virtual transitions. In our work [15], the wire Hamiltonian H_w describes bulk TS quasiparticles f_α, and is supplemented by the Coulomb interaction term (cf. Eq. 5.1),

$$H_w = \sum_\alpha E_\alpha f_\alpha^\dagger f_\alpha + E_c \left(2\hat{N} + \hat{n}_d + \hat{n}^{(qp)} - n_g\right)^2, \tag{5.12}$$

where $\hat{n}^{(qp)} = \sum_\alpha f_\alpha^\dagger f_\alpha$ describes the occupation of TS quasiparticle states.

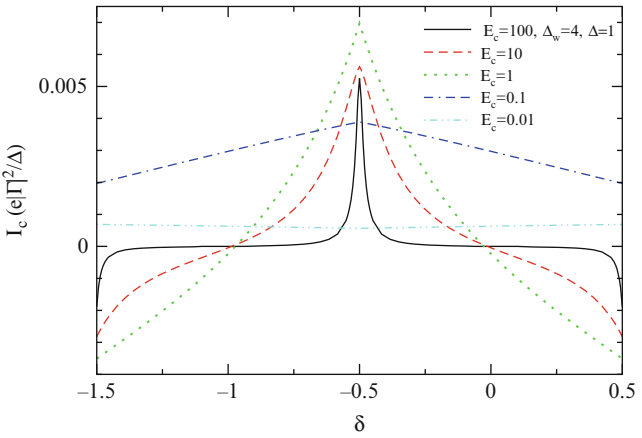

Fig. 5.7 Anomalous current I_c in Eq. (5.14) vs. $\delta = 2N - n_g$ in the cotunneling regime of an S-TS-S junction. I_c is computed for $\Delta_w/\Delta = 4$ and several E_c/Δ. Note that δ can be changed by varying a backgate, see Fig. 5.6(b). $I_c(\delta)$ is periodic; we show one fundamental interval only

For the noninteracting ($E_c = 0$) S-TS-S junction, the analytical solution for the CPR can be obtained. Some algebra reveals the periodicity $I(\varphi + n\pi) = I(\varphi)$, with $n = 2$ or even 1. In particular, the S-TS-S junction does not allow for the fractional 4π-periodic Josephson effect omnipresent in TS-TS junctions. For a symmetric junction with $\Gamma_{j=L/R} = 2\pi\nu_j \sum_\sigma \sigma\lambda_{j,\sigma} t^*_{j,-\sigma} = \Gamma$, expanding the free energy to lowest nontrivial order in the tunnel couplings yields:

$$I(\varphi) = -\frac{e\Delta}{\hbar} \left|\pi \nu_w \Gamma^2/\Delta_w\right|^2 \mathscr{G}(\Delta_w/\Delta) \sin(2\varphi) \tag{5.13}$$

with $\mathscr{G}(x) = x(2+x)/[4(1+x)^2]$ and the density of states $\nu_w = L/(2\pi v_F)$ in a wire of length L. Equation (5.13) describes a π-periodic CPR with negative critical current, $I_c \sim -|\Gamma/\Delta_w|^4$. It is worth mentioning that I_c is suppressed by the factor $|\Gamma/\Delta_w|^2$ compared to the usual cotunneling limit. This suppression can be traced back to the destructive interference of different contributions of order Γ^2.

For finite $E_c \neq 0$, this cancellation is incomplete and we recover $I_c \sim |\Gamma/\Delta_w|^2$ [15]. Moreover, we find the anomalous CPR

$$I(\varphi) = I_c \cos\varphi, \tag{5.14}$$

with the critical current I_c shown in Fig. 5.7 as a function of $\delta = 2N - n_g$. For half-integer δ, two charge states become degenerate and $|I_c|$ shows resonance enhancement. While for small E_c, we find a small positive and δ-independent I_c, these resonances become very narrow for large E_c, with I_c close to zero unless δ is nearly half-integer. The parity-sensitivity of I_c, i.e., the sign change of I_c between $\delta \approx -1/2$ and $\delta \approx 1/2$ (mod 2), see Fig. 5.7, may then provide an experimentally detectable signature for MBSs.

References

1. Alicea J (2012) Rep Prog Phys 75:076501
2. Bagrets D, Altland A (2012) Class D spectral peak in Majorana quantum wires. Phys Rev Lett 109:227005
3. Bolech CJ, Demler E (2007) Phys Rev Lett 98:237002
4. Fu L (2010) Phys Rev Lett 104:056402
5. Fu L, Kane CL (2008) Phys Rev Lett 100:096407
6. Jiang L, Pekker D, Alicea J, Refael G, Oreg Y, von Oppen F (2011) Phys Rev Lett 107:236401
7. Hasan MZ, Kane CL (2010) Rev Mod Phys 82:3045
8. Hützen R, Zazunov A, Braunecker B, Levy Yeyati A, Egger R (2012) Phys Rev Lett 109:166403
9. Kitaev AY (2001) Phys Usp 44:131
10. Law KT, Lee PA, Ng TK (2009) Phys Rev Lett 103:237001
11. Liu J, Potter AC, Law KT, Lee PA (2012) Zero-bias peaks in the tunneling conductance of spin-orbit-coupled superconducting wires with and without Majorana end-states. Phys Rev Lett 109:267002
12. Meir Y, Wingreen NS (1992) Phys Rev Lett 68:2512
13. Mourik V, Zuo K, Frolov SM, Plissard SR, Bakkers EPAM, Kouwenhoven LP (2012) Science 336:1003
14. Nilsson J, Akhmerov AR, Beenakker CWJ (2008) Phys Rev Lett 101:120403
15. Zazunov A, Egger R (2012) Phys Rev B 85:104514
16. Zazunov A, Levy Yeyati A, Egger R (2011) Phys Rev B 84:165440

Chapter 6
On the Electron-Phonon Interactions in Graphene

Bekir Kandemir

Abstract Chiral polaron formation arising from the electron-E_{2g} phonon coupling and the mini band gap formation due to electron-A_{1g} phonon coupling are investigated in pristine graphene. We present an analytical method to calculate the ground-state of the electron-phonon system within the framework of the Lee-Low-Pines theory. We show that the degenerate band structure of the graphene promotes the chiral polaron formation. Within our theoretical analysis, we also show that the interaction of charge carriers with the highest frequency zone-boundary phonon mode with A_{1g}-symmetry induces a mini band gap at the corners of the two-dimensional Brillouin zone of the graphene.

6.1 Introduction

Since the discovery of graphene [34,35] the investigation of its electronic properties have become one of the active areas in condensed matter physics both experimentally and theoretically, in past few years. From the theoretical point of view, in the low-energy limit, charge carries of graphene have linear dispersion relation around so-called Dirac points [43] having Fermi velocity [49] $v_F \simeq 10^6$ m/s, and Dirac-Weyl equation can be safely used within the framework of continuum description of the electronic band structure of the graphene [36]. Moreover, it is a well-known fact that both in-plane and out-of-plane phonon modes play an important role in charge carriers dynamics of the graphene [4–10, 13–15, 19, 22, 23, 25–27, 30–32, 37, 39, 40, 44–46, 50].

On the one hand, even though the interaction of electron with doubly degenerate optical phonon modes of E_{2g} symmetry near the zone center Γ does not open a

B. Kandemir (✉)
Faculty of Sciences, Department of Physics, Ankara University, 06100 Tandoğan, Ankara, Turkey
e-mail: kandemir@science.ankara.edu.tr

R. Egger et al. (eds.), *Low-Dimensional Functional Materials*, NATO Science for Peace and Security Series B: Physics and Biophysics, DOI 10.1007/978-94-007-6618-1_6,

gap [11, 22], they contribute significantly to intravalley-intraband and intravalley-interband scattering [41]. On the other hand, though the electron-highest frequency zone-boundary (K) phonon interaction, i.e., Kekulé-type distortion of the graphene lattice is one of the possible mechanisms among the gap generations. This first theoretical prediction of dynamical mini band gap formation in graphene due to the highest frequency phonon mode with A_{1g}-symmetry is reported by Samsonidze et al. [42]. The Kekulé structure consists of a network of hexagons with the alternating short and long bonds like in the classical benzene molecule. This pattern was studied for 1D simple model, finite size carbon nanotubes [17,18]. Investigation of the gap formation, in particular, its control, in both graphene and graphene based nanostructures is itself one of the hot topics of the current research in graphene, and such a gap generation can be created by strain [12, 28, 33] or by substrate induced effects [9, 51, 52].

In this talk, firstly, I present a theoretical model to investigate the effect of chirality dependent electron-E_{2g} phonon interactions on electronic spectrum of the pristine graphene, based on Lee-Low and Pines (LLP) theory [29]. Therefore, I address the question whether polaron formation is possible in graphene. Secondly, I will use the same procedure to investigate the effect of interaction of graphene charge carriers with the highest frequency optical phonon mode of A_{1g} symmetry near the zone boundary K (K′). The carrier-phonon interaction is described through a Kekulé-type distortion giving rise to inter-valley scattering between K and K′ points in graphene [1–3, 47, 48].

6.2 Interaction with E_{2g} Phonon

I will first construct the continuum Fröhlich type model to treat the interaction of electron with long wavelength E_{2g}-phonon [22]. A diagonalization procedure based on LLP like transformations to investigate the properties of both valence and conduction band polarons in graphene is introduced. Within the framework of low-energy continuum model of graphene, the Hamiltonian of an electron interacting with optical Γ-phonon can be written as

$$\mathscr{H} = \mathscr{H}_0 + \sum_{\mu}\sum_{\mathbf{q}} \hbar\omega_{\mu}(\mathbf{q}) b^{\dagger}_{q\mu} b_{q\mu} + \mathscr{H}_{e-p}, \tag{6.1}$$

where $\mathscr{H}_0 = v_F\ \boldsymbol{\sigma}.\mathbf{p}$ is the unperturbed bare Hamiltonian, whose spectrum describes cone like behavior with eigenvalues $\varepsilon_{k\lambda} = \lambda\varepsilon_k$ wherein $\varepsilon_k = \hbar v_F k$ and $\lambda = \pm$ is the chirality index, together with the corresponding bare eigenkets

$$\langle \mathbf{r} \,|\mathbf{k}\lambda\rangle = \frac{1}{\sqrt{2}L}\begin{pmatrix} \lambda \\ e^{i\theta(\mathbf{k})} \end{pmatrix} e^{i\mathbf{k}.\mathbf{r}}.$$

In Eq. (6.1), $\mathscr{H}_{e-p}$ is the electron-optical phonon interaction Hamiltonian [20], and can be described by the Hamiltonian

$$\mathscr{H}_{e-p} = -\sqrt{2}\frac{\beta\gamma}{a^2}\sum_{\mu}\left[\sigma \times \mathbf{u}_{\mu}(\mathbf{r})\right]_3,$$

together with the relative displacement of two sublattice atoms A and B of the graphene

$$\mathbf{u}_{\mu}(\mathbf{r}) = \sum_{\mathbf{q}}\left[\frac{\hbar}{2NM_C\omega_{\mu}(q)}\right]^{1/2}\left(\mathbf{b}_{\mathbf{q}\mu} + \mathbf{b}^{\dagger}_{-\mathbf{q}\mu}\right)\varepsilon_{\mu}(\mathbf{q})\, e^{i\mathbf{q}.\mathbf{r}}, \tag{6.2}$$

where $b^{\dagger}_{\mathbf{q}\mu}\left(b_{\mathbf{q}\mu}\right)$ is the optical phonon creation (annihilation) operator with longitudinal and transverse optical phonon branch index $\mu = 1$ (LO) and 2 (TO), respectively. Their dispersion have the form $\omega_{\mu}(\mathbf{q}) = \omega_{\Gamma}(0) R_{\mu}(qa)$ with dimensionless part $R_{\mu}(qa) = \left[1 - r_{\mu}(qa)\right]^{1/2}$, and with $\hbar\omega_{\Gamma}(0) = 0.196$ eV, where r_1 and r_2 are given by 0.1138 and 0.01979, respectively [45].

In Eq. (6.2), N is the number of unit cells, M_C is the mass of a carbon atom, a is the equilibrium bond length, and $\beta = -d\ln J_0/d\ln a$, $\gamma = (3a/2)J_0$. Here, J_0 is the resonance integral between nearest neighbor carbon atoms, and is of order of 2.7 eV. The polarization vectors of the relevant phonon modes in Eq. (6.2) are given by $\varepsilon_1(\mathbf{q}) = i(q_x, q_y)/q$ and $\varepsilon_2(q) = i(-q_y, q_x)/q$, respectively. To solve Eq. (6.1), we propose a diagonalization procedure based on the LLP method, which includes two successive unitary transformations. Eventually, to be compatible with this gapless band structure of the graphene, I will make an ansatz for the chiral polaron ground-state vector

$$|\Phi\rangle^{\lambda}_{pol} = \sum_{\lambda'}\alpha^{\lambda'}_{\lambda}\left|\mathbf{k}\lambda'\right\rangle \otimes U_1 U_2^{\lambda\lambda'}\left|\mathbf{0}\right\rangle_{ph} \tag{6.3}$$

such that $\mathscr{H}|\Phi\rangle^{\lambda}_{pol} = E_{\lambda}|\Phi\rangle^{\lambda}_{pol}$. In Eq. (6.3), while $|\mathbf{0}\rangle_{ph}$ stands for the phonon vacuum, $\alpha^{\lambda'}_{\lambda}|\mathbf{k}\lambda'\rangle$ corresponds to electronic state vector defined through the appropriate fractional amplitudes, $\alpha^{\lambda'}_{\lambda}$, due to the fact that polaronic wave function must be the linear combination of $|\mathbf{k}+\rangle$ and $|\mathbf{k}-\rangle$, respectively. The first unitary transformation [29] we apply to Eq. (6.1)

$$U_1 = \exp\left[-i\mathbf{r}.\sum_{\mu}\sum_{\mathbf{q}}\mathbf{q}\mathbf{b}^{\dagger}_{\mathbf{q}\mu}\mathbf{b}_{\mathbf{q}\mu}\right]$$

eliminates the electron coordinates, since the transformed operators are given by the relations, $\tilde{b}_{\mathbf{q}\mu} = b_{\mathbf{q}\mu}\exp[-i\mathbf{q}.\mathbf{r}]$ and $\tilde{\mathbf{p}} = \mathbf{p} - \sum_{\mu}\sum_{\mathbf{q}}\hbar\mathbf{q}\mathbf{b}^{\dagger}_{\mathbf{q}\mu}\mathbf{b}_{\mathbf{q}\mu}$. Hence, the transformed form of Eq. (6.1) under U_1 takes the form

$$\tilde{\mathscr{H}} = v_F \boldsymbol{\sigma}.\left(\mathbf{p}-\hbar\sum_{\mu}\sum_{\mathbf{q}}\mathbf{q}\mathbf{b}^{\dagger}_{\mathbf{q}\mu}\mathbf{b}_{\mathbf{q}\mu}\right) + \sum_{\mu}\sum_{\mathbf{q}}\hbar\omega_{\mu}(\mathbf{q})\mathbf{b}^{\dagger}_{\mathbf{q}\mu}\mathbf{b}_{\mathbf{q}\mu} - \sum_{\mu}\sum_{\mathbf{q}}\left[\tilde{\mathrm{M}}^{\mathbf{K}}_{\mu}(\mathbf{q})\mathbf{b}_{\mathbf{q}\mu} + \mathrm{H.c.}\right]. \tag{6.4}$$

Equations (6.4) still needs to be diagonalized in phonon coordinates. To do this, I will apply the second unitary LLP transformation [29]

$$U_2^{\lambda\lambda'} = \exp\left\{\sum_{\mathbf{q}}\left[\overline{\mathrm{M}}^{*}_{0\mu}(\mathbf{q})\left\langle\mathbf{k}\lambda'\right|\mathrm{M}^{\dagger}_{\mu}(\mathbf{q})\left|\mathbf{k}\lambda\right\rangle b^{\dagger}_{\mathbf{q}\mu} - \mathrm{H.c.}\right]\right\}$$

which is the displaced oscillator transformation with amplitude $\overline{\mathrm{M}}_{0\mu}(\mathbf{q}) = \overline{\mathrm{M}}^{\mathbf{K}}_{\mu}(\mathbf{q})/\hbar\omega_{\mu}(\mathbf{q})$. It just shifts the phonon coordinates, since it generates the coherent states for the phonon subsystem such that optical phonon operators transform according to the rule $\tilde{b}_{\mathbf{q}\mu} = b_{\mathbf{q}\mu} + \overline{\mathrm{M}}^{*}_{0\mu}(\mathbf{q})\left\langle\mathbf{k}\lambda'\right|\mathrm{M}^{\dagger}_{\mu}(\mathbf{q})\left|\mathbf{k}\lambda\right\rangle$. Finally, two simultaneous equations for $\alpha^{+}_{\pm}$ and $\alpha^{-}_{\pm}$ which can be rewritten in the following matrix equation:

$$\begin{bmatrix} E_{\pm} - \hbar v_F k + \hbar v_F \Sigma_{++}(\mathbf{k}) + \Sigma^{0}_{++}(\mathbf{k}) & \hbar v_F \Sigma_{+-}(\mathbf{k}) + 2\Sigma^{0}_{+-}(\mathbf{k}) \\ \hbar v_F \Sigma_{-+}(\mathbf{k}) + 2\Sigma^{0}_{-+}(\mathbf{k}) & E_{\pm} + \hbar v_F k + \hbar v_F \Sigma_{--}(\mathbf{k}) + \Sigma^{0}_{--}(\mathbf{k}) \end{bmatrix} \begin{bmatrix} \alpha^{+}_{\pm} \\ \alpha^{-}_{\pm} \end{bmatrix} = 0$$

where $\Sigma_{\pm\pm}$, $\Sigma_{\pm\mp}$, $\Sigma^{0}_{\mp\mp}$, and $\Sigma^{0}_{\pm\mp}$ are the relevant matrix elements. The above equation can be solved analytically as a function of k in closed form,

$$E_{\pm} = \pm\left\{(\hbar v_F k)^2 + 4\left[\Sigma^{0}_{\pm\mp}(\mathbf{k})\right]^2\right\}^{1/2} \mp \left|\Sigma^{0}_{\pm\pm}(\mathbf{k})\right|. \tag{6.5}$$

In Eq. (6.5), while the last term is due to the intraband transitions, second one in the parenthesis is contribution due to the coupling between valence and conduction bands, i.e. it corresponds to interband transitions. Taking the integrals in the associated matrix elements, one obtains k-dependent contributions as

$$\Sigma^{0}_{\lambda\lambda'}(\mathbf{k}) = \sum_{\mu}\frac{3\sqrt{3}}{4\pi\mathbf{r}_{\mu}}J_0\alpha(0)\ln\left[\frac{1}{1-\mathbf{r}_{\mu}\left(2\bar{k}_0\right)^2}\right], \tag{6.6}$$

where I have defined $\alpha(0) = \left|\overline{\mathrm{M}}\right|^2/4J_0\hbar\omega_{\Gamma}(0)$ and new dimensionless wave vector, $\bar{k}_o = ka$. $\alpha(0)$ is of order of $0.054\,(0.089)$ depending on the choice of $q_0 = 2\,(2.5)\ \mathring{A}^{-1}$.

It is convenient to rewrite Eq. (6.5) for small k's, which corresponds to neglect phonon dispersions, i.e., it results with polaron dispersion independent on r_{μ}. To do this, we first expand the logarithm in Eq. (6.6), in power series of k, and then replace the resultant back into Eq. (6.6) so that Eq. (6.5) reduces to the simple form

$$\overline{E}_{\pm} = \pm\overline{k}_o \left\{ 1 + 4 \left[\frac{4\sqrt{3}}{\pi} \alpha(0) \overline{k}_0 \right]^2 \right\}^{1/2} \mp \frac{4\sqrt{3}}{\pi} \alpha(0) \overline{k}_0^2, \tag{6.7}$$

where $\overline{E}_{\pm} = aE_{\pm}/\hbar v_F$ is the dimensionless energy. The existence of the inter-chirality band term, second term in the square root in Eq. (6.7), is the main difference from the standard electron self energy calculations taking into account only the intra-chirality transitions through the degenerate optical phonon modes with E_{2g} symmetry. Since Eq. (6.7) can easily be rearranged into the form $\overline{E}_{\lambda} = \lambda \hbar \tilde{v}_F \left(\overline{k}_0\right) \overline{k}_0$, we can thus define the renormalized Fermi velocity as

$$\tilde{v}_F \left(\overline{k}_0\right) = v_F \left[\sqrt{1 + 4\tilde{\alpha}^2 \left(\overline{k}_0\right)} - \tilde{\alpha} \left(\overline{k}_0\right) \right],$$

wherein, in analogy with quantum chromodynamics [16], we also define a new coupling constant, running coupling constant, as a function of k, i.e., energy,

$$\tilde{\alpha} \left(\overline{k}_0\right) = \frac{4\sqrt{3}}{\pi} \alpha(0) \overline{k}_0.$$

It is easy to show that, from the size of the renormalization of the Fermi velocity, i.e., from depending on the energy, for $\overline{k}_0 = 0.05$ and $\overline{k}_0 = 0.1$, respectively. In the graphene literature, except a few theoretical calculations and an experimental study, there are no works devoted to the investigation of the velocity renormalization through many-body techniques or to its direct/indirect experimental observations. While in Ref. [37] it was found to be reduced by 4–8 % depending for an electron doping $4 \times 10^{13}\,\mathrm{cm}^{-2}$, in Ref. [24] for a plasmoronic band it was estimated around 1–3 % depending on electron concentrations. The discrepancy between our results and that of Ref. [27] is due to the fact that, while $\overline{k}_0 = 0.05$ (0.1) corresponds to 200 meV (400 meV), for an electron doping $4 \times 10^{13}\mathrm{cm}^{-2}$ corresponding the Fermi level is 600 meV. This energy region lies out of the range of validity of our results, since our calculations based on the LLP theory are valid only below the phonon resonance, i.e. $E < \hbar\omega_{\Gamma}(0) = 196$ meV.

6.3 Interaction with A_{1g} Phonon

In the long-wave length regime, the Hamiltonian of the graphene electron (hole) interacting with A_{1g}-phonon mode can be written as

$$\mathscr{H} = \mathscr{H}_0 + \sum_{\mu \neq \nu} \sum_{\mathbf{q}} \hbar\omega_{\mu}(\mathbf{q}) b^{\dagger}_{\mu,\mathbf{q}} b_{\mu,\mathbf{q}} + \mathscr{H}_{e-p} \tag{6.8}$$

where $\mathscr{H}_0 = v_F \boldsymbol{\alpha}.\mathbf{p}$ is the unperturbed part of the Hamiltonian. I have labeled the well-known K and K′ points of graphene in Eq. (6.8) by the valley index μ. Here,

α are the four component Dirac matrices. Thus, the corresponding eigenfunctions of the unperturbed part $\mathscr{H}_0$ can easily be constructed in terms of four component pseudospinor

$$\langle r|\,\mathrm{K}\lambda\mathbf{k}\rangle = \frac{\exp(i\mathbf{k}.\mathbf{r})}{\sqrt{2}L}\begin{pmatrix}\lambda\\ e^{i\theta(\mathbf{k})}\\ 0\\ 0\end{pmatrix}$$

$$\langle r|\,\mathrm{K}'\lambda\mathbf{k}\rangle = \frac{\exp(i\mathbf{k}.\mathbf{r})}{\sqrt{2}L}\begin{pmatrix}0\\ 0\\ e^{i\theta(\mathbf{k})}\\ \lambda\end{pmatrix},$$

In Eq. (6.8), the last term represents the electron-phonon couplings [47], and is given by

$$\mathscr{H}_{e-p} = 2\frac{\beta_{\mathrm{K}}\gamma}{a^2}\begin{pmatrix}0 & \omega^{-1}\Delta_{\mathrm{K}'}(\mathbf{r})\sigma_y\\ \omega\Delta_{\mathrm{K}}(\mathbf{r})\Sigma_y & 0\end{pmatrix} \tag{6.9}$$

where $\beta_{\mathrm{K}} = -d\ln J_0/d\ln a$, σ_y is the 2×2 Pauli matrix. In Eq. (6.9), the amplitude of distortions at K and K$'$ points are defined by

$$\Delta_K(\mathbf{r}) = \sum_{\mathbf{q}}\sqrt{\frac{\hbar}{2NM_C\omega_K(\mathbf{q})}}\left(b_{K,\mathbf{q}} + b^{\dagger}_{K,'-\mathbf{q}}\right)e^{i\mathbf{q}.\mathbf{r}}$$

$$\Delta_{K'}(\mathbf{r}) = \sum_{\mathbf{q}}\sqrt{\frac{\hbar}{2NM_C\omega_K(\mathbf{q})}}\left(b_{K',\mathbf{q}} + b^{\dagger}_{K,-\mathbf{q}}\right)e^{i\mathbf{q}.\mathbf{r}}, \tag{6.10}$$

respectively. In Eq. (6.10), $b_{K,\mathbf{q}}$ ($b_{\mathrm{K}',\mathbf{q}}$) and $b^{\dagger}_{\mathrm{K},\mathbf{q}}$ ($b^{\dagger}_{\mathrm{K},'\mathbf{q}}$) are again the phonon creation and annihilation operators but at points K (K$'$) with phonon wave vector $\mathbf{q}$ and frequency $\omega_{\mathrm{K}}(\mathbf{q})$. The corresponding highest zone-boundary phonon energy is $\hbar\omega_{\mathrm{K}}(0) = 161.2$ meV. Therefore, the electron-phonon interaction Hamiltonian given by Eq. (6.9) can be rewritten in the following form:

$$\mathscr{H}_{e-p} = -\sum_{\mu\neq\nu}\sum_{\mathbf{q}}\left[\tilde{\mathrm{M}}_{\mu\nu}(\mathbf{q})\,b_{\mu,\mathbf{q}}e^{i\mathbf{q}.\mathbf{r}} + h.c.\right]. \tag{6.11}$$

where have defined $\tilde{\mathrm{M}}_{\mu\nu}(\mathbf{q})$ as $\mathrm{M}_0\mathrm{M}_{\mu\nu}(\mathbf{q})$ such that

$$\mathrm{M}_{\mathrm{KK}'}(\mathbf{q}) = \frac{\omega}{\sqrt{N}}\begin{pmatrix}\mathbf{0} & \mathbf{0}\\ \Sigma_y & \mathbf{0}\end{pmatrix},$$

$$\mathrm{M}_{\mathrm{K}'\mathrm{K}}(\mathbf{q}) = \frac{\omega^{-1}}{\sqrt{N}}\begin{pmatrix}\mathbf{0} & \Sigma_y\\ \mathbf{0} & \mathbf{0}\end{pmatrix},$$

together with $\mathrm{M}_0 = 3a_0 q_0 J_0$. Here, $a_0 = (\hbar/2M_C\omega_{\mathrm{K}}(0))^{1/2}$, and $q_0 = (\partial J_0/\partial a)/J_0$ is predicted [21, 38] around 2.0 and 2.5 $\mathring{A}^{-1}$.

To diagonalize the phonon subsystem of Eqs. (6.11) through (6.10) we employ a similar unitary transformation scheme, as in the previous section. But now, It should be considered that the zone boundary phonon gives rise to inter-valley scattering between K and K′. Therefore, to be compatible with this property of the problem, we make an ansatz for the ground-state of the whole system

$$\mid \Phi\rangle = \sum_{\mu' \neq \nu'} \sum_{\lambda'} \alpha_{\pm}^{\mu'\lambda'} \mid \mu'\lambda'\mathbf{k}\rangle \otimes U_1 U_2 \mid \mathbf{0}\rangle_{\mathrm{ph}} \tag{6.12}$$

such that $\mathscr{H} \mid \Phi\rangle = E_{\pm} \mid \Phi\rangle$. Here, $\mid \mathbf{0}\rangle_{\mathrm{ph}}$ stands for the phonon vacuum, and $\alpha_{\pm}^{\mu'\lambda'} \mid \mu'\lambda\mathbf{k}\rangle$ corresponds to electronic state vector defined through the appropriate fractional amplitudes, $\alpha_{\pm}^{\mu'\lambda}$, due to the fact that total wave function of the system must be the linear combination of $\mid \mu' + \mathbf{k}\rangle$ and $\mid \mu' - \mathbf{k}\rangle$, respectively.

On the one hand, the first unitary transformation

$$U_1 = \exp\left[-i\mathbf{r}.\sum_{\mathbf{q}} \mathbf{q} b_{\mu,\mathbf{q}}^{\dagger} b_{\mu,\mathbf{q}}\right]$$

eliminates electron coordinates from Eq. (6.11), since the transformed operators are given by the relations, $\tilde{b}_{\mu,\mathbf{q}} = b_{\mu,\mathbf{q}} \exp[-i\mathbf{q}.\mathbf{r}]$ and $\tilde{\mathbf{p}} = \mathbf{p} - \sum_{\mathbf{q}} \sum_{\mu \neq \nu} \hbar\mathbf{q} b_{\mu,\mathbf{q}}^{\dagger} b_{\mu,\mathbf{q}}$. Therefore, the transformed Hamiltonian takes the form,

$$\begin{aligned} \tilde{\mathscr{H}} = v_F \alpha.\left(\mathbf{p} - \hbar \sum_{\mathbf{q}} \sum_{\mu \neq \nu} \mathbf{q} b_{\mu,\mathbf{q}}^{\dagger} b_{\mu,\mathbf{q}}\right) \\ + \sum_{\mathbf{q}} \sum_{\mu \neq \nu} \hbar\omega_{\mathrm{K}} b_{\mu,\mathbf{q}}^{\dagger} b_{\mu,\mathbf{q}} - \sum_{\mathbf{q}} \sum_{\mu \neq \nu} \left(\tilde{M}_{\mu\nu} b_{\mu,\mathbf{q}} + h.c.\right). \end{aligned} \tag{6.13}$$

On the other hand, second unitary transformation

$$U_2 = \exp\left[\sum_{\mathbf{q}} \tilde{\mathrm{M}}_0 \langle \mu'\lambda'\mathbf{k} \mid \mathrm{M}_{\mu\nu}^{\dagger}(\mathbf{q}) \mid \nu'\lambda\mathbf{k}\rangle b_{\mathbf{q}\mu}^{\dagger} - \mathbf{h}.\mathbf{c}.\right]$$

is the well-known displaced oscillator transformation which shifts phonon coordinates by an amount of the interaction amplitude, $\tilde{M}_0 = \mathrm{M}_0/\hbar\omega_K(0)$. It just shifts the phonon coordinates, since it generates the coherent states for the phonon subsystem such that optical phonon operators transform according to the rule $\tilde{b}_{\mu,\mathbf{q}} = b_{\mu,\mathbf{q}} + \tilde{\mathrm{M}}_0 \langle \mu'\lambda'\mathbf{k} \mid \mathrm{M}_{\mu\nu}^{\dagger}(\mathbf{q}) \mid \nu'\lambda\mathbf{k}\rangle$. As a result, under the transformation U_2, Eq. (6.13) can then be rewritten as $\tilde{\mathscr{H}} = \mathscr{H}^0 + \mathscr{H}_1$. By using the ansatz given by Eq. (6.12) , one first applies Eq. (6.13) to the term $\alpha_{\pm}^{\mu'\lambda'} \mid \mu'\lambda'\mathbf{k}\rangle$, and then sums

over λ' to construct the eigenvalue equation $\mathscr{H} \mid \Phi\rangle^{\mu\nu\lambda} = E_{\pm} \mid \Phi\rangle^{\mu\nu\lambda}$. Finally, by taking inner products to compare the related coefficients of the states$\mid \mu'\lambda'\mathbf{k}\rangle$ we arrive four simultaneous equations for $\alpha_{\pm}^{\mathbf{K}\pm}$ and $\alpha_{\pm}^{\mathbf{K}'\pm}$ which can be rewritten in the following matrix equation:

$$\begin{bmatrix} E_{\pm}+\Sigma_{++}^{(0)KK} & \Sigma_{--}^{(1)KK} & \Sigma_{++}^{(2)KK'} & \Sigma_{+-}^{(2)KK'} \\ \Sigma_{++}^{(1)\mathrm{KK}} & E_{\pm}+\Sigma_{--}^{(0)KK} & \Sigma_{-+}^{(2)KK'} & \Sigma_{++}^{(2)KK'} \\ \Sigma_{++}^{(2)K'K} & \Sigma_{+-}^{(2)K'K} & E_{\pm}+\Sigma_{++}^{(0)K'K'} & \Sigma_{--}^{(1)K'K'} \\ \Sigma_{-+}^{(2)K'K} & \Sigma_{--}^{(2)K'K} & \Sigma_{++}^{(1)K'K'} & E_{\pm}+\Sigma_{--}^{(0)K'K'} \end{bmatrix} \begin{bmatrix} \alpha_{\pm}^{K+} \\ \alpha_{\pm}^{K-} \\ \alpha_{\pm}^{K'+} \\ \alpha_{\pm}^{K'-} \end{bmatrix} = 0$$

where $\Sigma_{\mp\mp}^{(0)KK}$, $\Sigma_{\mp\mp}^{(1)KK}$, and $\Sigma_{\lambda\lambda'}^{(2)KK'}$ are relevant matrix elements. This show that only inter-valley scattering having different chiralities are allowed due to the conservation of the chiral symmetry. After converting the associated sums into integrals over $\mathbf{q}$, except for $\Sigma_{\mp\pm}^{(2)KK'}$ and $\Sigma_{\mp\pm}^{(2)K'}$ terms, all the terms with $\Sigma_{\mp\mp}^{(0)KK}$, $\Sigma_{\mp\mp}^{(1)KK}$ and their corresponding K′ partners vanish. The non-vanishing terms can easily be calculated as

$$\Sigma_{\mp\pm}^{(2)KK'} = \Sigma_{\mp\pm}^{(2)K'K} = \frac{3\sqrt{3}}{\pi} J_0 \alpha_0 \overline{q}_c^2$$

where we have defined that $\alpha_0 = |\mathrm{M}_0|^2/4J_0\hbar\omega_K(0)$ which takes values 0.305 or 0.477 depending on whether q_0 is 2.0 $\mathring{A}^{-1}$ or 2.5 $\mathring{A}^{-1}$, respectively [21,38]. We must introduce an upper cut-off frequency $\overline{q}_c = q_c a$, while taking the relevant integrals, since they diverge at upper limit of the integrations. By solving the determinant of the above matrix the eigenvalues $E_{\pm}$ can be solved analytically in the following form:

$$E_{\pm} = \pm\left[(\hbar v_F k)^2 + \left(\Sigma_{\mp\pm}^{(2)KK'}\right)^2\right]^{1/2},$$

which is modified electronic band dispersion of the pristine graphene due to the Kekulé-type distortion of the lattice. As is seen above, Kekulé-type distortion preserves the chirality of the sublattice, i.e., the valley degeneracy is not lifted. ω_K, we can choose $q_c = \omega_K/v_F = 0.027\ \mathring{A}^{-1}$ such that $\overline{q}_c = q_c a = 0.039$. This suggest that the magnitude of the half-band gap is of order of 2.12 meV ($q_0 = 2.0\ \mathring{A}^{-1}$) or 3.34 meV ($q_0 = 2.5\ \mathring{A}^{-1}$), so that the induced gap, of 4.24 meV or 6.68 meV. This is smaller than that those previously found in the literature [42], where a mini band gap occurs 10 meV in their room temperature calculations.

6.4 Conclusion

In conclusion, a new type of polaronic formation in pristine graphene with respect to electron-E_{2g} phonon interactions and mini band gap opening at zero temperature with related to electron (hole) interacting with A_{1g}-phonon interaction is predicted. We show that chiral polaron band dispersions consist of k dependent terms besides the free undressed one. In addition to free undressed ones, both intraband and interband interactions coexist in a one polaron dispersion. Secondly, we investigate the first theoretical justification of a mini band gap formation in pristine graphene at absolute zero temperature, due to the interaction of electron (hole) with highest frequency optical phonon mode with A_{1g} symmetry near the zone boundary yielding Kekulé type distortion. We have shown that such an interaction opens a gap without breaking the chiral symmetry of the lattice.

References

1. Ajiki H, Ando T (1995) Lattice distortion of metallic carbon nanotubes induced by magnetic fields. J Phys Soc Jpn 64:260–267
2. Ajiki H, Ando T (1996) Lattice distortion with spatial variation of carbon nanotubes in magnetic fields. J Phys Soc Jpn 65:2976–2986
3. Araki Y (2011) Chiral symmetry restoration in monolayer graphene induced by Kekule distortion. Phys Rev B 84:113402
4. Araujo PT, Mafra DL, Sato K, Saito R, Kong J, Dresselhaus MS (2012) Phonon self-energy corrections to nonzero wave-vector phonon modes in single-layer graphene. Phys Rev Lett 109:046801
5. Badalyan SM, Peeters FM (2012) Electron-phonon bound state in graphene. Phys Rev B 85:205453
6. Basko DM (2007) Effect of inelastic collisions on multiphonon Raman scattering in graphene. Phys Rev B 76:081405(R)
7. Basko DM (2008) Theory of resonant multiphonon Raman scattering in graphene. Phys Rev B 78:125418
8. Basko DM, Aleiner IL (2008) Interplay of Coulomb and electron-phonon interactions in graphene. Phys Rev B 77:041409(R)
9. Calandra M, Mauri F (2007) Electron-phonon coupling and electron self-energy in electron-doped graphene: calculation of angular-resolved photoemission spectra. Phys Rev B 76:205411
10. Carbotte JP, Nicol EJ, Sharapov SG (2010) Effect of electron-phonon interaction on spectroscopies in graphene. Phys Rev B 81:045419
11. Dubay O, Kresse G (2003) Accurate density functional calculations for the phonon dispersion relations of graphite layer and carbon nanotubes. Phys Rev B 67:0354012003
12. Farjam M, Rafii-Tabar H (2010) Uniaxial strain on gapped graphene. Physica E 42:2109–2114
13. Faugeras C, Amado M, Kossacki P, Orlita M, Sprinkle M, Berger C, de Heer WA, Potemski M (2009) Tuning the electron-phonon coupling in multilayer graphene with magnetic fields. Phys Rev Lett 103:186803
14. Giuliani A, Mastropietro V, Porta M (2010) Lattice gauge theory model for graphene. Phys Rev B 82:121418(R)
15. Goerbig MO, Fuchs J-N, Kechedzhi K, Fal'ko VI (2007) Filling-factor-dependent magnetophonon resonance in graphene. Phys Rev Lett 99:087402
16. Griffiths D (1987) Introduction to elementary particles. Wiley, Singapore, p 249

17. Harigaya K (1992) From C60 to a fullerene tube: Systematic analysis of lattice and electronic structures by the extended Su-Schrieffer-Heeger model. Phys Rev B 45:12071
18. Harigaya K, Fujita M (1993) Dimerization structures of metallic and semiconducting fullerene tubules. Phys Rev B 47:16563
19. Hwang EH, Sensarma R, Das Sarma S (2010) Plasmon-phonon coupling in graphene. Phys Rev B 82:195406
20. Ishikawa K, Ando T (2006) Optical phonon interacting with electrons in carbon nanotubes. J Phys Soc Jpn 75:084713
21. Jishi RA, Dresselhaus MS, Dresselhaus G (1993) Electron-phonon coupling and the electrical conductivity of fullerene nanotubules. Phys Rev B 48:11385
22. Kandemir BS (2013) Possible formation of chiral polarons in graphene. J Phys Condens Matter 25:025302
23. Kandemir BS, Mogulkoc A (2012) Zone-boundary phonon induced mini band gap formation in graphene. arXiv:1211.3528
24. Krstajić PM, Peeters FM (2012) Energy-momentum dispersion relation of plasmarons in graphene. Phys Rev B 85:205454
25. Lazzeri M, Piscanec S, Mauri F, Ferrari AC, Robertson J (2005) Electron transport and hot phonons in carbon nanotubes. Phys Rev Lett 95:236802
26. Lazzeri M, Piscanec S, Mauri F, Ferrari AC, Robertson J (2006) Phonon linewidths and electron-phonon coupling in graphite and nanotubes. Phys Rev B 73:155426
27. Lazzeri M, Attaccalite C, Wirtz L, Mauri F (2008) Impact of the electron-electron correlation on phonon dispersion: failure of LDA and GGA DFT functionals in graphene and graphite. Phys Rev B 78:081406(R)
28. Lee S-H, Chung H-J, Heo J, Yang H, Shin J, Chung U-I, Seo S (2011) Band gap opening by two-dimensional manifestation of Peierls instability in graphene. ACS Nano 5:2964–2969
29. Lee TD, Low FE, Pines D (1953) The motion of slow electrons in a polar crystal. Phys Rev 90:297–302
30. Li WP, Wang ZW, Yin JW, Yu YF (2012) The effects of the magnetopolaron on the energy gap opening in graphene. J Phys Condens Matter 24:135301
31. Mariani E, von Oppen F (2008) Flexural phonons in free-standing graphene. Phys Rev Lett 100:076801
32. Mariani E, von Oppen F (2010) Temperature-dependent resistivity of suspended graphene. Phys Rev B 82:195403
33. Ni ZH, Yu T, Lu YH, Wang YY, Feng YP, Shen ZX (2008) Uniaxial strain on graphene: Raman spectroscopy study and band-gap opening. ACS Nano 2:2301–2305
34. Novoselov KS, Jiang D, Schedin F, Booth TJ, Khotkevich VV, Morozov SV, Geim AK (2005) Two-dimensional atomic crystals. Proc Nat Acad Sci USA 102:10451
35. Novoselov KS, Geim AK, Morozov SV, Jiang D, Zhang Y, Dubonos SV, Grigorieva IV, Firsov AA (2004) Electric field effect in atomically thin carbon films. Science 306:666
36. Novoselov KS, Geim AK, Morozov SV, Jiang D, Zhang Y, Dubonos SV, Grigorieva IV, Firsov A (2005) Two-dimensional gas of massless Dirac fermions in graphene. Nature 438:197–200
37. Park CH, Giustino F, Cohen ML, Louie SG (2007) velocity renormalization and carrier lifetime in graphene from the electron–phonon interaction. Phys Rev Lett 99:086804
38. Pietronero L, Strässler S, Zeller HR, Rice MJ (1980) Electrical conductivity of a graphite layer. Phys Rev B 22:904
39. Pisana S, Lazzeri M, Casiraghi C, Novoselov KS, Geim AK, Ferrari AC, Mauri F (2007) Breakdown of the adiabatic Born-Oppenheimer approximation in graphene. Nat Mater 3:198
40. Piscanec S, Lazzeri M, Mauri F, Ferrari AC, Robertson J (2004) Kohn anomalies and electron-phonon interactions in graphite. Phys Rev Lett 93:185503
41. Rana F, George PA, Strait JH, Dawlaty J, Shivaraman S, Chandrashekhar M, Spencer MG (2009) Carrier recombination and generation rates for intravalley and intervalley phonon scattering in graphene. Phys Rev B 79:115447

42. Samsonidze GG, Barros EB, Saito R, Jiang J, Dresselhaus G, Dresselhaus MS (2007) Electron-phonon coupling mechanism in two-dimensional graphite and single-wall carbon nanotubes. Phys Rev B 75:155420
43. Semenoff GW (1984) Condensed-matter simulation of a three-dimensional anomaly. Phys Rev Lett 53:2449
44. Stauber T, Peres NMR (2008) Effect of Holstein phonons on the electronic properties of graphene. J Phys Condens Matter 20:055002
45. Stauber T, Peres NMR, Castro Neto AH (2008) Conductivity of suspended and non-suspended graphene at finite gate voltage. Phys Rev B 78:085418
46. Stojanović VM, Vukmirovic N, Bruder C (2010) Polaronic signatures and spectral properties of graphene antidot lattices. Phys Rev B 82:165410
47. Suzuura H, Ando T (2008) Zone-boundary phonon in graphene and nanotube. J Phys Soc Jpn 77:044703
48. Viet NA, Ajiki H, Ando T (1994) Lattice instability in metallic carbon nanotubes. J Phys Soc Jpn 63:3036–3047
49. Wallace PR (1947) The band theory of graphite. Phys Rev 71:622
50. Yan J, Zhang Y, Kim P, Pinczuk A (2007) Electric field effect tuning of electron-phonon coupling in graphene. Phys Rev Lett 98:166802
51. Zhou SY, Gweon GH, Federov AV, First PN, De Heer WA, Lee D-H, Guinea F, Castro Neto AH, Lanzara A (2007) Substrate-induced bandgap opening in epitaxial graphene. Nature 6:770
52. Zhou SY, Siegel DA, Fedorov AV, Lanzara A (2008) Kohn anomaly and interplay of electron-electron and electron-phonon interactions in epitaxial graphene. Phys Rev B 78:193404

Chapter 7
Tunneling Conductance in Correlated Graphenes

Jongbae Hong

Abstract Line shape of tunneling conductance observed for a correlated graphene is studied theoretically. We focus on the line shape of scanning tunneling spectroscopy (STS) for a doped graphene flake. We obtain the STS line shape in terms of elastic tunneling of a Kondo singlet through the coherent tunneling levels that are formed due to two reservoirs within coherent regime. The resonant tunneling of a singlet through this coherent tunneling level causes the abrupt increase in tunneling conductance at a finite bias. The shifted position of Dirac point from the Fermi level is responsible for making the line shape of tunneling conductance asymmetric.

A number of tunneling experiments have been carried out to study their basic transport properties [1–6]. Among them, we focus our interest on the doped single-layer graphene [1, 2] because its peculiar line shape of differential conductance, dI/dV vs. V, where I and V denote the current and the bias voltage, respectively, is not fully understood. We conjecture that the peculiar dI/dV line shapes are attributable to the strongly correlated feature of the system [7]. Doping electrons or holes results in a nonvanishing density of states at the Fermi level. As a result, the π electrons of the graphene have a strong on-site Coulomb repulsion [7, 8]. Interestingly, the line shape of scanning tunneling spectroscopy (STS) for a doped graphene flake [1, 2] shows suppression at zero bias and an abrupt increase at a finite bias. The purpose of this study is to reveal the origin of the abrupt increase and the reason of suppression at zero-bias in the dI/dV line shapes. To understand the peculiar dI/dV line shapes observed for the doped graphene flake, we employ elastic resonant tunneling of a singlet through the coherent tunneling levels that are formed in a two-reservoir quantum impurity system with strong electron correlation.

J. Hong (✉)
Department of Physics, Pohang University of Science and Technology and Asia Pacific Center for Theoretical Physics, Pohang, Gyeongbuk 790-784, Korea
e-mail: jbhong@postech.ac.kr

R. Egger et al. (eds.), *Low-Dimensional Functional Materials*, NATO Science for Peace and Security Series B: Physics and Biophysics, DOI 10.1007/978-94-007-6618-1_7,

The position of Dirac point is attributable to the asymmetric form of the line shape [1]. A notable point is that the Dirac point is shifted from the Fermi level even at zero gate voltage if the sample is not intrinsic [1].

The characteristic features of the dI/dV line shapes of the doped graphene flake, i.e. abrupt increase at a finite bias and the suppression at zero bias, may not be explained by inelastic tunneling via quasiparticle excitations. According to the studies by Ohta et al. [9], Calandra and Mauri [10], and Park et al. [11], phonons may not play a role in low-energy tunneling in a graphene. In addition, both electron-plasmon interaction and electron-hole pair creation may contribute to the inelastic tunneling at a comparatively high bias [12, 13].

The graphene system under consideration comprises scanning tunneling microscope (STM) tip, graphene sample, and the metallic lead. At low energy, electrons cannot enter the graphene sample because of strong on-site Coulomb repulsion at the mediating atom. It can enter the sample by forming an entangled Kondo singlet connecting tip and sample. Under steady-state, coming one electron into sample requires going one electron out. Therefore, considering the process of electron entering sample is enough to study the tunneling conductance. Hence, the Hamiltonian is written as

$$\mathscr{H} = \mathscr{H}_0^t + \mathscr{H}_0^s + \sum_\sigma \varepsilon_m c_{m\sigma}^\dagger c_{m\sigma} + U n_{m\uparrow} n_{m\downarrow} + \sum_{k,\sigma,\nu=t,s} (V_{km}^\nu c_{m\sigma}^\dagger c_{k\sigma} + V_{km}^{\nu *} c_{k\sigma}^\dagger c_{m\sigma}), \tag{7.1}$$

where $\mathscr{H}_0^{t,s} = \sum_{k,\sigma} (\varepsilon_k - \mu^{t,s}) c_{k\sigma}^\dagger c_{k\sigma}$, and σ, ε_k, ε_m, V_{km}, U, and μ indicate the electron spin, the kinetic energy, the energy level of the mediating atom, the hybridization strength, on-site Coulomb repulsion, and the chemical potential, respectively. The superscripts s and t denote the sample and tip, respectively. In this study, the sample is characterized only by its density of states.

Considering resonant tunneling from the tip to the sample gives the formula of tunneling conductance at zero temperature as

$$dI/dV = (e/\hbar) \tilde{\Gamma}(\omega) \rho_m^{ss}(\omega)|_{\hbar\omega = eV}, \tag{7.2}$$

where $\tilde{\Gamma}(\omega) = \Gamma^t(\omega)\Gamma^s(\omega)/[\Gamma^t(\omega) + \Gamma^s(\omega)]$, and $\rho_m^{ss}(\omega)$ is the steady-state LDOS at the mediating atom. The coupling function is given by $\Gamma^{t(s)}(\omega) = 2\pi \sum_k |V_{km}^{t(s)}|^2 \delta(\omega - \omega_k)$. We use a constant for $\Gamma^t(\omega)$. Both $\Gamma^s(\omega)$ and $\Gamma^t(\omega)$ appear in the self-energy part of $\rho_m^{ss}(\omega)$. Equation (7.2) is derived from the well-known Meir–Wingreen current formula [14, 15] with proportionate coupling function [16], $\Gamma^t(\omega) \propto \Gamma^s(\omega)$, and the bias-independence condition, $\partial \rho_m^{ss}(\omega)/\partial V = 0$. The proportionate relation can be used for elastic resonant tunneling, which gives the condition $I(\omega) = I^t(\omega) = -I^s(\omega)$, and the bias-independence condition results from the effect of bias in coherent tunneling. Therefore, Eq. (7.2) is valid in this study.

In a Kondo system, one Kondo impurity has one Kondo singlet. The Hamiltonian in Eq. (7.1) has one Kondo impurity and two reservoirs. Therefore, the left and right Kondo singlets coupled by the mediating atom to the tip and sample, respectively, can be formed. The equilibrium ground state is an entangled Kondo singlet that

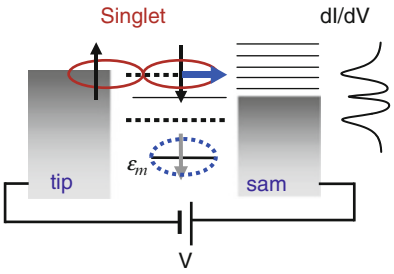

Fig. 7.1 Singlet tunneling under bias: resonant tunneling of a singlet via the coherent tunneling level (*dotted line*) yields a side peak. The down-spin at ε_m indicates the real spin that forms a singlet with the up-spin at the tip. The side peak of tunneling conductance curve (dI/dV) on the *right-hand side* matches the coherent tunneling level

is represented by a linear combination of the left and right Kondo singlets. The dynamical description of the entangled Kondo singlet is back and forth movements of a Kondo singlet along with exchange and singlet partner change. However, when a bias is applied, only unidirectional movement of Kondo singlet along the reverse direction of the electric field, as shown in Fig. 7.1. Backward movement of a singlet is prohibited no matter how small the bias. Therefore, $\rho^{ss}_m(\omega)$ indicating the probability of coherent dynamics is bias-independent until the quasiparticle excitations created by bias are involved in tunneling. Neglecting $\partial\rho^{ss}_m(\omega)/\partial V$ has been adopted in studying the dynamics of Kondo-involved mesoscopic systems [17–19]. Previous studies [20–23] on the two-reservoir Anderson impurity model obtained bias-dependent spectral functions. They encounter difficulties in explaining the experimental dI/dV line shapes observed for mesoscopic Kondo systems. We understand that one of the reasons for having bias-dependent spectral functions is attributable to not taking the unidirectional motion of the entangled Kondo singlet under bias.

We have obtained a complete set of basis vectors spanning the Liouville space of the two-reservoir Anderson impurity model at equilibrium [24, 25] in which the basis vectors describing multiple back and forth tunnelings are included. However, when a bias is applied, these basis vectors do not play a role and the degrees of freedom is significantly reduced. Hence, the LDOS $\rho^{ss}_{m\uparrow}(\omega)$ is given by a 5×5 matrix such as $\rho^{ss}_{m\uparrow}(\omega) = (1/\pi)\mathrm{Re}[(\mathbf{M}^r_{5\times 5})^{-1}]_{33}$, where

$$\mathbf{M}^r_{5\times 5} = \begin{pmatrix} -i\omega' & \gamma_{tt} & -U^t_{j-} & \gamma_{ts} & \gamma_j \\ -\gamma_{tt} & -i\omega' & -U^t_{j+} & \gamma_j & \gamma_{ts} \\ U^{t*}_{j-} & U^{t*}_{j+} & -i\omega' & U^{s*}_{j+} & U^{s*}_{j-} \\ -\gamma_{ts} & -\gamma_j & -U^s_{j+} & -i\omega' & -\gamma_{ss} \\ -\gamma_j & -\gamma_{ts} & -U^s_{j-} & \gamma_{ss} & -i\omega' \end{pmatrix}, \tag{7.3}$$

$\omega' \equiv \omega - \varepsilon_m - U\langle n_{m\downarrow}\rangle$, and $\langle n_{m\downarrow}\rangle$ denotes the average number of down-spin electrons occupying the mediating atom [24]. All the matrix elements, except $U^{t,s}_{j^\pm}$, have additional self-energy terms $i\Sigma_{mn} = \beta_{mn}[i\Sigma^t_0(\omega) + i\Sigma^s_0(\omega)]$, where $\Sigma^{t(s)}_0(\omega)$ denotes the self-energy of $\mathscr{H}^{t(s)}_0$. Hence, $i\Sigma_{mn}$ is written as $i\Sigma_{mn} = \mathrm{Re}[\beta_{mn}]\langle\Gamma(\omega)\rangle$, where $\langle\Gamma(\omega)\rangle = [\Gamma^t + \Gamma^s(\omega)]/2$. We discuss the coefficients β_{mn} below.

The matrix $\mathbf{M}_r$ in Eq. (7.3) consists of two 3×3 blocks that share the central element representing the localized spin and two 2×2 blocks at the corners. The three off-diagonal elements of the 3×3 block represent the degrees of singlet coupling ($\gamma_{tt(ss)}$) and incoherent double occupancy parameters ($U^{t(s)}_{j^\pm}$). Singlet tunneling is described by 2×2 corner blocks. Operator expressions of γ are given by [24]

$$\gamma_{tt(ss)} = \frac{\langle\sum_k i(V^*_{km}c^t_{k\uparrow} + V^*_{km}c^s_{k\uparrow})c^\dagger_{m\uparrow}[j^{-t(s)}_{m\downarrow}, j^{+t(s)}_{m\downarrow}]\rangle}{[\langle(\delta j^{-t(s)}_{m\downarrow})^2\rangle\langle(\delta j^{+t(s)}_{m\downarrow})^2\rangle]^{-1/2}},$$

$$\gamma_{ts} = \frac{\langle\sum_k i(V^*_{km}c^t_{k\uparrow} + V^*_{km}c^s_{k\uparrow})c^\dagger_{m\uparrow}[j^{-t}_{m\downarrow}, j^{+s}_{m\downarrow}]\rangle}{[\langle(\delta j^{-t}_{m\downarrow})^2\rangle\langle(\delta j^{+s}_{m\downarrow})^2\rangle]^{-1/2}},$$

and $\gamma_j = \gamma_{j^\mp}$, where

$$\gamma_{j^\mp} = \frac{\langle\sum_k i(V^*_{km}c^t_{k\uparrow} + V^*_{km}c^s_{k\uparrow})c^\dagger_{m\uparrow}[j^{\mp t}_{m\downarrow}, j^{\mp s}_{m\downarrow}]\rangle}{[\langle(\delta j^{\mp t}_{m\downarrow})^2\rangle\langle(\delta j^{\mp s}_{m\downarrow})^2\rangle]^{-1/2}},$$

where $j^+_{m\downarrow} = \sum_k(V_{km}c^\dagger_{m\downarrow}c_{k\downarrow} + V^*_{km}c^\dagger_{k\downarrow}c_{m\downarrow})$, $j^-_{m\downarrow} = i\sum_k(V_{km}c^\dagger_{m\downarrow}c_{k\downarrow} - V^*_{km}c^\dagger_{k\downarrow}c_{m\downarrow})$, and $\delta j \equiv j - \langle j\rangle$ [24]. $\gamma_{ss(tt)}$ represents the degree of exchange process between the mediating atom and the electron in sample (tip). γ_{ts} and γ_j represent symmetric and antisymmetric combinations of left and rightward tunnelings, respectively, i.e., $\langle\rightarrow\rangle \pm \langle\leftarrow\rangle$. Hence, in equilibrium, $\gamma_j = 0$. As discussed in Fig. 7.1, the tunneling of Kondo singlet is unidirectional under bias. This fact gives $\gamma_{ts} = \gamma_j$, which is the condition of steady-state nonequilibrium. Two different conditions for γ certify that $\rho^{ss}_{m\uparrow}(\omega)|_{V\to 0} \neq \rho^{eq}_{m\uparrow}(\omega)$. In addition, probability one for moving toward a specific direction implies the bias-independence of $\rho^{ss}_{m\uparrow}(\omega)$.

The 5×5 matrix $\mathbf{M}_r$ of Eq. (7.3) gives three coherent and two incoherent poles. The three coherent poles provide two different types of coherent tunneling channels: one at the Fermi level and the other at $\pm\hbar\omega_{rt\ell}$. The subscript $rt\ell$ denotes the resonant tunneling level. Hence, a singlet performs resonant tunneling and the tunneling current abruptly increases when the bias voltage reaches $\hbar\omega_{rt\ell}/e$. The simple atomic limit analysis for the same $U^{t,s}_{j^\pm}$ gives $\hbar\omega_{rt\ell} \approx \pm[(\gamma^2_{tt} + \gamma^2_{ss})/2]^{1/2}$ for large U. The zero-bias peak is formed by coherent tunneling through the Fermi level. However, the zero-bias peak is suppressed in the STS measurement for a doped graphene because of imbalance in Kondo coupling strength between tip and sample, i.e. $\gamma_{tt} \ll \gamma_{ss}$ and active double occupancy at the mediating atom. In summary, Eq. (7.3)

Table 7.1 Matrix elements for Fig. 7.2

	γ_{tt}	γ_{ss}	γ_{ts}	γ_j	$\mathrm{Re}U^{t}_{j+}$	$\mathrm{Re}U^{s}_{j+}$	$\mathrm{Re}U^{t,s}_{j-}$	$\lvert\mathrm{Im}U^{t,s}_{j\pm}\rvert$
DS	0.002	0.15	0.35	0.35	2.8/3	7/3	2.1/3	0.028

$\mathrm{Im}U^{s}_{j-} > 0, \mathrm{Im}U^{t}_{j-} < 0, \mathrm{Im}U^{t,s}_{j+} < 0$

with bias-independent matrix elements and the γ relations is suitable for describing coherent tunneling under bias in a mesoscopic quantum impurity system.

Now, we obtain the dI/dV line shape of the doped single-layer graphene. We first determine the matrix elements of Eq. (7.3). The STS setup requires the relation $\gamma_{tt} \ll \gamma_{ss}$ and we use the steady-state condition $\gamma_{ts} = \gamma_j$ discussed above. The double-occupancy parameters are given by Refs. [24, 25]

$$U^{t,s}_{j^{\pm}} = (U/2)[\langle D^{\pm t,s}_{m\uparrow\downarrow}\rangle + i(1 - 2\langle n_{m\downarrow}\rangle)]\langle j^{\pm t,s}_{m\downarrow}\rangle\langle(\delta j^{\pm t,s}_{m\downarrow})^2\rangle^{-1/2}, \tag{7.4}$$

where $\langle D^{\pm t,s}_{m\uparrow\downarrow}\rangle = \alpha^{\pm}\langle(1 - 2n_{m\uparrow})n_{m\downarrow}\rangle^{t,s}_{\pm}$, which indicates the probability of double occupancy described by the operators $j^{+}_{m\downarrow}$ or $j^{-}_{m\downarrow}$ on the tip or sample side. We assume the same relative fluctuations $\langle(\delta j^{\pm t,s}_{m\downarrow})^2\rangle^{1/2}/\langle j^{\pm t,s}_{m\downarrow}\rangle$ in steady-state nonequilibrium. The factor $\alpha^{\pm}$ denotes the parameter correcting decoupling mean-field approximation. In a left-right symmetric system such as a quantum dot single-electron transistor [26], the roles of symmetric ($j^{+}_{m\downarrow}$) and antisymmetric ($j^{-}_{m\downarrow}$) operators are the same, which gives $\langle D^{+t,s}_{m\uparrow\downarrow}\rangle = \langle D^{-t,s}_{m\uparrow\downarrow}\rangle$, i.e. $\mathrm{Re}[U^{t,s}_{J^+}] = \mathrm{Re}[U^{t,s}_{J^-}]$, and yields a prominent zero-bias peak. However, in such a heterogeneous junction like a tip and sample system, $\langle D^{+t,s}_{m\uparrow\downarrow}\rangle > \langle D^{-t,s}_{m\uparrow\downarrow}\rangle$. This imbalance also causes suppression of the zero-bias peak. In the STS setup for a doped graphene, we consider $\langle D^{+s}_{m\uparrow\downarrow}\rangle > \langle D^{+t}_{m\uparrow\downarrow}\rangle$ based on the stronger particle activity on the sample side than on tip side and $\langle D^{-t}_{m\uparrow\downarrow}\rangle = \langle D^{-s}_{m\uparrow\downarrow}\rangle$ based on the steady current. Hence, we adopt the relations $\mathrm{Re}[U^{s}_{J^+}] > \mathrm{Re}[U^{t}_{J^+}] > \mathrm{Re}[U^{s}_{J^-}] = \mathrm{Re}[U^{t}_{J^-}]$. We construct Table 7.1 based on these relations and the condition $\gamma_{ts} = \gamma_j$. In Table 7.1, DS means doped single-layer graphene. On the other hand, doping causes deviation from the charge neutrality point and nonvanishing of the imaginary part of $U^{t,s}_{J^{\pm}}$ which minutely controls the relative heights and the positions of the two side peaks. We allocate small values of $\mathrm{Im}[U^{t,s}_{J^{\pm}}]$ for the doped graphene. The absolute values of $\mathrm{Im}[U^{t,s}_{J^{\pm}}]$ are given in Table I. The sign of $\mathrm{Im}[U^{t,s}_{J^{\pm}}]$ depends on the signs of $\langle j^{\pm t,s}_{m\downarrow}\rangle$ and $1 - 2\langle n_{m\downarrow}\rangle$, as shown in Eq. (7.4).

Next, we determine the coupling function on the sample side, $\Gamma^{s}(\omega)$. We write $\Gamma^{s}(\omega) = \phi_0 + 2A|\omega + \omega_D|$ representing a shifted linear graphene density of states, where ϕ_0 results from defects, A is constant, and ω_D is the Dirac point. Then, $\langle\Gamma(\omega)\rangle = \phi + A|\omega + \omega_D|$, where $\phi = (\phi_0 + \Gamma^{t})/2$. The values of ϕ, A, and ω_D are determined phenomenologically. Finally, we decide the coefficients β_{mn}. Considering the same relative fluctuations gives vanishing $\mathrm{Im}[\beta_{mn}]$ because they are given by the difference of relative fluctuations [24]. In contrast, the real parts

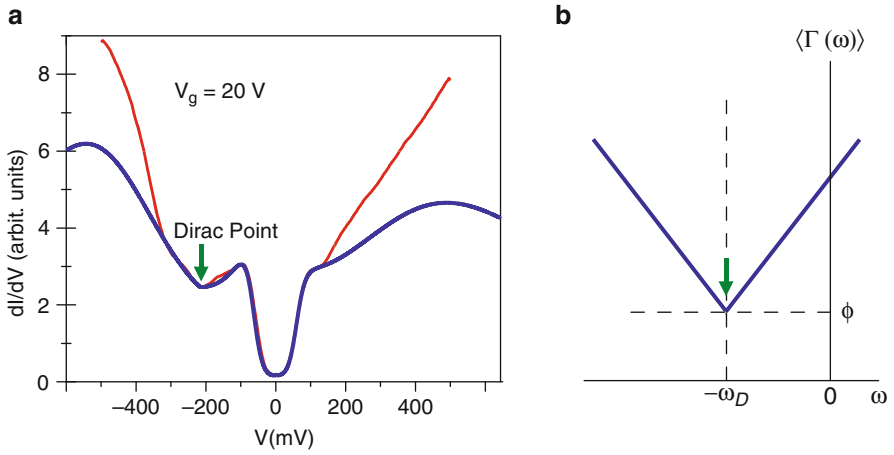

Fig. 7.2 (**a**) Comparison of the theoretical dI/dV line shape with the experimental data (*red*) for a doped graphene at the gate voltage $V_g = 20$ V given in Ref. [2]. We choose $\phi = 1.1\Delta_0$, $A = 0.43$, $\omega_D = 1.02\Delta_0$, and $\Gamma^t = 0.18\Delta_0$. The *green arrows* indicate the positions of Dirac point. (**b**) Plot of $\langle\Gamma(\omega)\rangle$ (color figure online)

$\mathrm{Re}[\beta_{mn}]$ are symmetric and have the following mutual relations due to $\langle j^{-t}_{m\downarrow}\rangle = -\langle j^{-s}_{m\downarrow}\rangle$ and the same relative fluctuations: $\mathrm{Re}[\beta_{12}] = \mathrm{Re}[\beta_{14}] = \mathrm{Re}[\beta_{15}] < \mathrm{Re}[\beta_{11}] = \mathrm{Re}[\beta_{22}] = \mathrm{Re}[\beta_{44}] = \mathrm{Re}[\beta_{55}] = \mathrm{Re}[\beta_{24}] = \mathrm{Re}[\beta_{25}] = \mathrm{Re}[\beta_{45}]$ and $\mathrm{Re}[\beta_{33}] = 1$. For example, $\mathrm{Re}[\beta_{25}]$ is given by $\mathrm{Re}[\beta_{25}] = \{\langle j^{-s}_{m\downarrow}(1-2n_{m\uparrow})\rangle\langle j^{+t}_{m\downarrow}(1-2n_{m\uparrow})\rangle + (1-2\langle n_{m\downarrow}\rangle)^2\langle j^{+s}_{m\downarrow}\rangle\langle j^{-t}_{m\downarrow}\rangle\}/\sqrt{\langle(\delta j^{+s}_{m\downarrow})^2\rangle}\sqrt{\langle(\delta j^{-t}_{m\downarrow})^2\rangle}$ [24]. To obtain the line shapes given in Fig. 7.2 (a), we choose $\mathrm{Re}[\beta_{12}] = 0.245$ and $\mathrm{Re}[\beta_{11}] = 0.255$ based on the standard value $\mathrm{Re}[\beta_{pq}] = 0.25$ that is obtained at the atomic limit [24] and use the values of Table 7.1 along with $\langle\Gamma(\omega)\rangle$ in Fig. 7.2 (b). Satisfying the inequalities of $\mathrm{Re}[\beta_{mn}]$ is crucial to obtain the well-fitting line shapes.

We superimpose our theoretical results on data panels presented by Brar et al. [2] for a doped graphene in Fig. 7.2 (a), and energy units are chosen as $\Delta_0 = 210$ meV. The fit shown in Fig. 7.2 (a) are remarkable in the low-bias region including the two abrupt increases. The difference in the high-bias region of Fig. 7.2 (a) could be explained by inelastic tunneling processes such as electron-phonon interactions [10–12], electron-hole pair creation [12], and electron-plasmon interactions [13]. These inelastic tunneling mechanisms operate at energies higher than 200 meV. One can revive the zero-bias peak by choosing $\mathrm{Re}[U^{t,s}_{j^+}] \approx \mathrm{Re}[U^{t,s}_{j^-}]$. The dI/dV line shape is changed into a mirror symmetric one for the axis of zero bias if electron doping is changed to hole doping, i.e. negative gate voltage [1]. This is achieved by changing the signs of ω_D.

In conclusion, we clarified that the characteristic structures of the dI/dV line shapes observed for the doped single-layer. The elastic resonant tunneling of a singlet through the coherent tunneling level results in abrupt increases in dI/dV

and the asymmetry of the line shape shown in Fig. 7.2 (a) is attributed to the shifted Dirac point. Further, the zero-bias peak is suppressed in this system, which results from both strong asymmetry in the degrees of Kondo coupling to tip and sample sides and the different contributions of the operators $j^{+}_{m\sigma}$ and $j^{-}_{m\sigma}$ describing the double occupancy at the mediating atom.

Acknowledgements This research was supported by Basic Science Research Program through the NRF, Korea (2012R1A1A2005220) and partially supported by KIAS grant funded by MEST.

References

1. Zhang Y et al (2008) Giant phonon-induced conductance in scanning tunnelling spectroscopy of gate-tunable graphene. Nat Phys 4:627
2. Brar VW et al (2010) Observation of carrier-density-dependent many-body effects in graphene via tunneling spectroscopy. Phys Rev Lett 104:036805
3. Bao W et al (2011) Stacking-dependent band gap and quantum transport in trilayer graphene. Nat Phys 7:948
4. Freitag F, Trbovic J, Weiss M, Schönenberger C (2012) Spontaneously gapped ground state in suspended bilayer graphene. Phys Rev Lett 108:076602
5. Li G et al (2010) Observation of Van Hove singularities in twisted graphene layers. Nat Phys 6:109
6. Velasco J Jr et al (2012) Transport spectroscopy of symmetry-broken insulating states in bilayer graphene. Nat Nanotech 7:156
7. Wehling TO et al (2011) Strength of effective coulomb interactions in graphene and graphite. Phys Rev Lett 106:236805
8. Castro Neto AH, Guinea F, Peres NMR, Novoselov KS, Geim AK (2009) The electronic properties of graphene. Rev Mod Phys 81:109
9. Ohta T, Bostwick A, Seyller T, Horn K, Rotenberg E (2006) Controlling the electronic structure of bilayer graphene. Science 313:951
10. Calandra M, Mauri F (2007) Electron-phonon coupling and electron self-energy in electron-doped graphene: calculation of angular-resolved photoemission spectra. Phys Rev B 76:205411
11. Park C-H, Giustino F, Cohen ML, Louie SG (2007) Velocity renormalization and carrier lifetime in graphene from the electron-phonon interaction. Phys Rev Lett 99:086804
12. Bostwick A, Ohta T, Seyller T, Horn K, Rotenberg E (2007) Nat Phys 3:36
13. Bostwick A et al (2010) Observation of plasmarons in quasi-freestanding doped graphene. Science 328:999
14. Meir Y, Wingreen NS (1992) Landauer formula for the current through an interacting electron region. Phys Rev Lett 68:2512
15. Hershfield S, Davies JH, Wilkins JW (1992) Resonant tunneling through an Anderson impurity. I. Current in the symmetric model. Phys Rev B 46:7046
16. Haug H, Jauho A-P (1996) Quantum kinetics in transport and optics of semiconductors. Berlin: Springer Chap. 12
17. Madhavan V, Chen W, Jamneala T, Crommie MF, Wingreen NS (2001) Local spectroscopy of a Kondo impurity: Co on Au(111). Phys Rev B 64:165412
18. Schiller A, Hershfield S (2000) Theory of scanning tunneling spectroscopy of a magnetic adatom on a metallic surface. Phys Rev B 61:9036
19. Plihal M, Gadzuk JW (2001) Nonequilibrium theory of scanning tunneling spectroscopy via adsorbate resonances: nonmagnetic and Kondo impurities. Phys Rev B 63:085404

20. Wingreen NS, Meir Y (1994) Anderson model out of equilibrium: noncrossing-approximation approach to transport through a quantum dot. Phys Rev B 49:11040
21. Fujii T, Ueda K (2003) Perturbative approach to the nonequilibrium Kondo effect in a quantum dot. Phys Rev B 68:155310
22. Han JE, Heary RJ (2007) Imaginary-time formulation of steady-state nonequilibrium: application to strongly correlated transport. Phys Rev Lett 99:236808
23. Anders FB (2008) Steady-state currents through nanodevices: a scattering-states numerical renormalization group approach to open quantum systems. Phys Rev Lett 101:066804
24. Hong J (2011) Kondo dynamics of quasiparticle tunneling in a two-reservoir Anderson model. Phys J Phys Condens Matter 23:275602
25. Hong J (2011) A complete set of basis vectors of the Anderson model and its Kondo dynamics. J Phys Condens Matter 23:225601
26. van der Wiel WG et al (2000) The Kondo effect in the unitary limit. Science 289:2105

Chapter 8
Landau Levels and Edge States in Graphene with Strong Spin-Orbit Coupling

Alessandro De Martino, Artur Hütten, and Reinhold Egger

Abstract We investigate the electronic properties of graphene in a magnetic and a strain-induced pseudo-magnetic field in the presence of strong spin-orbit interactions (SOI). For a homogeneous field we provide analytical results for the Landau level eigenstates for arbitrary intrinsic and Rashba SOI, including also the effect of a Zeeman field. We then study the edge states in a semi-infinite geometry in the absence of the Rashba term. We find that, for a critical value of the magnetic field, a quantum phase transition occurs, which separates two phases both with spin-filtered helical edge states but with opposite direction of the spin current. Finally,we discuss magnetic waveguides with inhomogeneous field profiles that allow for chiral snake orbits. Such waveguides are practically immune to disorder-induced backscattering, and the SOI provides non-trivial spin texture to these modes.

8.1 Introduction

The physics of graphene continues to attract a great deal of attention and to provide a rich source of interesting phenomena [1–3]. By studying the effects of the spin-orbit interaction (SOI) in a graphene monolayer, where symmetry allows for an "intrinsic" (Δ) and a "Rashba" (λ) term in the SOI, Kane and Mele [4] made a remarkable discovery that sparked the exciting field of topological insulators [5]: For $\Delta > \lambda/2$, the system presents a bulk gap with topologically protected edge states near the boundary of the sample. This is similar to the quantum Hall (QH)

A. De Martino (✉)
Department of Mathematical Science, City University London, Northampton Square, London EC1V 0HB, UK
e-mail: ademarti@city.ac.uk

A. Hütten • R. Egger
Institut für Theoretische Physik, Heinrich-Heine-Universit, D-40225 Düsseldorf, Germany
e-mail: huetten@thphy.uni-duesseldorf.de; egger@thphy.uni-duesseldorf.de

R. Egger et al. (eds.), *Low-Dimensional Functional Materials*, NATO Science for Peace and Security Series B: Physics and Biophysics, DOI 10.1007/978-94-007-6618-1_8,

effect but happens in a time-reversal invariant system. The resulting "quantum spin Hall" (QSH) edge states form a one-dimensional (1D) helical liquid, where right- and left-movers have opposite spin polarization, and spin-independent impurity backscattering is strongly suppressed. The QSH state has been observed in HgTe quantum wells [6], but several works [7–9] showed that Δ is probably too small to allow for the experimental verification of this novel phase of matter in pristine graphene. Consequently, other material classes have been employed to demonstrate that topologically insulating behavior is indeed possible [5].

Recent graphene experiments, however, have demonstrated that the Rashba coupling λ can be increased significantly by depositing graphene on Ni surfaces [10, 11]. Moreover, very recent theoretical predictions [12] suggest that already moderate indium or thallium adatom deposition will dramatically enhance Δ by several orders of magnitude. By using suitable adatoms, it is then expected that in the near future both SOI parameters Δ and λ can be varied over a wide range of values in experimentally accessible setups.

In view of these developments, in this paper we study the electronic properties of a graphene monolayer with strong SOI. Besides the SOI, we include piecewise constant electrostatic potentials, orbital and Zeeman magnetic fields, and strain-induced vector potentials. The latter cause pseudo-magnetic fields but do not violate time reversal invariance. (See Ref. [13] for a review.) While the interplay of the Rashba term λ with (pseudo-)magnetic fields in graphene has been studied in several theory works before [14–16], the effects of the intrinsic SOI Δ did not receive much attention so far (apart from recent investigations of the transmission properties of graphene's Dirac-Weyl (DW) quasiparticles through barriers with arbitrary SOI but without (pseudo-)magnetic fields [17, 18].)

The present contribution reports results obtained by the authors in [19]. The structure is as follows. In Sect. 8.2 we formulate the model and construct the general solution for piecewise constant fields, where we allow for orbital magnetic field, arbitrary SOI parameters Δ and λ, and Zeeman energy b. The homogeneous case is addressed in Sect. 8.3, where we determine the Landau level states for this problem in closed and explicit form. In particular, the fate of the zero modes residing at the Dirac point (energy $E = 0$) is discussed in the presence of the SOI. Our results also apply to the case of a strain-induced homogeneous pseudo-magnetic field [20]. Next, in Sect. 8.4, we study the edge states near the boundary of a semi-infinite sample for vanishing Rashba coupling, $\lambda = 0$. For weak magnetic fields, one expects to have helical (spin-filtered) QSH edge states. Interestingly, upon increasing the magnetic field we find that a quantum phase transition takes place between the QSH phase and a second QSH-like phase with spin-filtered edge states, considered previously in [21], where the spin current direction is reversed. This spin current reversal should allow for an experimental detection of the transition, on top of the obvious consequences for QH quantization rules [21–24]. In Sect. 8.5, we turn to a waveguide geometry, defined by a suitable inhomogeneous magnetic field [25–34]. We show that the SOIs give rise to interesting spin textures of the chiral states propagating in the waveguides. Finally, we conclude in Sect. 8.6.

8.2 Model and General Solution

In this section we introduce the model for graphene with SOI in the presence of a magnetic field, and obtain the general form of the eigenstates for piecewise constant couplings.

8.2.1 Model

The low-energy electronic properties of graphene are well captured by two copies of a DW Hamiltonian supplemented with various terms describing SOI, (pseudo-)magnetic fields, and electrostatic potentials [3]. The wavefunction is a eight component spinor

$$\Psi(x,y) = e^{ik_x x}\begin{pmatrix}\phi^K(y)\\ \phi^{K'}(y)\end{pmatrix}, \qquad \phi^{K,K'} = \begin{pmatrix}\Psi_{A\uparrow K,K'}\\ \Psi_{B\uparrow K,K'}\\ \Psi_{A\downarrow K,K'}\\ \Psi_{B\downarrow K,K'}\end{pmatrix}. \tag{8.1}$$

The Pauli matrices $\sigma_{i=x,y,z}$ below act in sublattice space corresponding to the two carbon atoms (A/B) in the basis of the honeycomb lattice, while Pauli matrices s_i act in physical spin $(\uparrow,\downarrow)$ space. Finally, the valley degree of freedom (K,K') corresponds to the two K points [3] and Pauli matrices τ_i refer to that space. Here we consider models where the mentioned extra terms in the Hamiltonian are piecewise constant along the y-direction and uniform along the x-axis. Consequently, the momentum p_x is conserved, and we have an effectively 1D problem in terms of the four-spinors $\phi^{K,K'}(y)$. The orbital magnetic field $B_z = \varepsilon B$ (with $\varepsilon = \pm$ and $B \geq 0$) is expressed in terms of the vector potential $\mathbf{A}(x,y)$, where we choose the gauge

$$A_x = -\varepsilon B(y - c_0), \quad A_y = 0. \tag{8.2}$$

Inclusion of the constant c_0 is necessary when connecting regions with different magnetic fields in order to make A_x continuous. With the magnetic field perpendicular to the graphene sheet, the Zeeman effect determines the coupling constant $b = g_s\mu_B B/2$, where $g_s \approx 2$ is the Landé factor and μ_B denotes the Bohr magneton. The full Hamiltonian then reads [3] ($e > 0$)

$$\begin{aligned} H = {} & v_F\left[\sigma_x\tau_z\left(p_x + \frac{e}{c}(A_x + \tau_z\mathscr{A}_x)\right) + \sigma_y\left(\hat{p}_y + \frac{e}{c}\tau_z\mathscr{A}_y\right)\right] \\ & + V + \varepsilon b s_z + \frac{\lambda}{2}(\sigma_x s_y\tau_z - \sigma_y s_x) + \Delta\sigma_z s_z\tau_z. \end{aligned} \tag{8.3}$$

In Eq. (8.3) $p_x = \hbar k_x$ is the conserved momentum in the x-direction, while $\hat{p}_y = -i\hbar\partial_y$. The constant c_0 in Eq. (8.2) can be included by shifting p_x, and we suppose that this shift has been carried out in the remainder of this section. The Fermi velocity is $v_F \approx 10^6$ m/s, while the SOI couplings Δ and λ (both are assumed non-negative) correspond to the intrinsic and Rashba terms, respectively. A constant electrostatic potential, V, has been included in Eq. (8.3). Strain-induced forces [13] lead to a renormalization of V as well as to the appearance of an effective vector potential,

$$\begin{pmatrix} \mathscr{A}_x \\ \mathscr{A}_y \end{pmatrix} = \kappa \begin{pmatrix} u_{xx} - u_{yy} \\ -2u_{xy} \end{pmatrix},$$

expressed in terms of the in-plane strain tensor u_{ij}, see Ref. [35]. The constant κ can be found in Refs. [13, 36]. As discussed in Ref. [37] in many cases it is sufficient to consider a piecewise constant strain configuration. Assuming that the x-axis is oriented along the zig-zag direction, strain causes only a finite but constant $\mathscr{A}_x$ while $\mathscr{A}_y = 0$. This can be taken into account by simply shifting p_x in this region. Below we suppose that also this shift has already been done. Estimates for $\mathscr{A}_x$ in terms of physical quantities can be found in Refs. [13, 37]. The resulting pseudo-magnetic field then consists of δ-barriers at the interfaces between regions of different strain. An alternative situation captured by our model is given by a constant pseudo-magnetic field, whose practical realization has been described recently [20]. In that case, $\mathscr{A}_x$ is formally identical to A_x in Eq. (8.2). Unless specified explicitly, we consider the case of constant $\mathscr{A}_x$ below.

8.2.2 Symmetries

Let us briefly comment on the symmetries of this Hamiltonian. For H in Eq. (8.3) with $\varepsilon = \mathrm{sgn}(B_z)$, the time reversal symmetry implies the relation

$$\mathscr{T} H_\varepsilon(k_x) \mathscr{T}^{-1} = H_{-\varepsilon}(-k_x), \tag{8.4}$$

where $\mathscr{T} = \tau_x(-is_y)\mathscr{C}$ is an antiunitary operator[1] with complex conjugation operator $\mathscr{C}$. Since H is diagonal in valley space, Eq. (8.4) implies that the Hamiltonian $H^{K'}$ near the K' point is related to H^K by the relation

$$H^{K'}_{-\varepsilon}(-k_x) = s_y [H^K_\varepsilon(k_x)]^* s_y. \tag{8.5}$$

By solving the eigenvalue problem at the K point, we could thus obtain the eigenstates at K' via Eq. (8.5). A simpler way to achieve this goal is sketched at the end of this subsection.

[1] A different representation for $\mathscr{T}$ has been given in Ref. [2] because of a different arrangement of the sublattice components in the spinor (Eq. 8.1).

From now on we switch to dimensionless quantities by measuring all energies in units of the cyclotron energy $\hbar\omega_c$, where we define $\omega_c = v_F/\ell_B$. The magnetic length $\ell_B = (\hbar c/2eB)^{1/2}$ sets the unit of length. A field of 1 T corresponds to $\hbar\omega_c \approx 36$ meV and $\ell_B \approx 18$ nm. Measuring B in units of Tesla, we get for the Zeeman coupling $b = (g_s\mu_B B/2)/\hbar\omega_c \approx 1.6\times 10^{-3}\sqrt{B[\mathrm{T}]}$. With the dimensionless coordinate

$$\eta = y - 2\varepsilon k_x \tag{8.6}$$

and the auxiliary quantities

$$\mu_\pm = E - V + b \pm \Delta, \quad \nu_\pm = E - V - b \pm \Delta, \tag{8.7}$$

we find the representation

$$E - H^K_{\varepsilon=+1} = \begin{pmatrix} \nu_- & a & 0 & 0 \\ a^\dagger & \nu_+ & i\lambda & 0 \\ 0 & -i\lambda & \mu_+ & a \\ 0 & 0 & a^\dagger & \mu_- \end{pmatrix},$$

$$E - H^K_{\varepsilon=-1} = \begin{pmatrix} \mu_- & -a^\dagger & 0 & 0 \\ -a & \mu_+ & i\lambda & 0 \\ 0 & -i\lambda & \nu_+ & -a^\dagger \\ 0 & 0 & -a & \nu_- \end{pmatrix}, \tag{8.8}$$

where we have introduced the standard ladder operators

$$a = \frac{\eta}{2} + \partial_\eta, \quad a^\dagger = \frac{\eta}{2} - \partial_\eta, \quad [a, a^\dagger] = 1. \tag{8.9}$$

According to the above discussion, eigenstates at the K' point for $\varepsilon = \pm 1$ could be obtained from the corresponding solutions at the K point with $\varepsilon = \mp 1$. Alternatively, there is a simpler way to obtain the K' states as follows. The 1D Hamiltonians $H^{K,K'}$ (for given ε) can be written in dimensionless notation as

$$H^K = -\frac{\varepsilon\eta}{2}\sigma_x - i\sigma_y\partial_\eta + \Delta\sigma_z s_z + \frac{\lambda}{2}(\sigma_x s_y - \sigma_y s_x) + \mathscr{A}_x\sigma_x + \varepsilon b s_z,$$
$$H^{K'} = \frac{\varepsilon\eta}{2}\sigma_x - i\sigma_y\partial_\eta - \Delta\sigma_z s_z + \frac{\lambda}{2}(-\sigma_x s_y - \sigma_y s_x) + \mathscr{A}_x\sigma_x + \varepsilon b s_z.$$

Both Hamiltonians are therefore related by the transformation

$$H^{K'}(\mathscr{A}_x) = \sigma_y H^K(-\mathscr{A}_x)\sigma_y, \tag{8.10}$$

without the need to invert the real magnetic field, since this is not a time reversal transformation. As a consequence, the 1D eigenstates $\phi^{K'}(\eta)$ follow from the corresponding ϕ^K by multiplying with $-i\sigma_y$ and inverting the sign of $\mathscr{A}_x$,

$$\phi^{K'}(\eta, \mathscr{A}_x) = -i\sigma_y \phi^K(\eta, -\mathscr{A}_x). \tag{8.11}$$

8.2.3 General Solution

We now determine the spinors ϕ solving the DW equation for energy E,

$$(E - H^K)\phi(\eta) = 0, \tag{8.12}$$

with $E - H^K$ in Eq. (8.8). We construct the solution to Eq. (8.12) within a spatial region where all parameters (magnetic fields, strain, SOI, etc.) are constant but arbitrary. This general solution will be employed in later sections, where specific geometries are considered by matching wavefunctions in adjacent parts. Equation (8.12) is a system of four first-order linear differential equations that admits four linearly independent solutions. For energy E and positive magnetic field we find two states:

$$\phi_{\varepsilon=+1,p} = \begin{pmatrix} pD_{p-1}(-\eta) \\ \nu_- D_p(-\eta) \\ \frac{i(\nu-p)}{\lambda} D_p(-\eta) \\ \frac{i(\nu-p)}{\lambda\mu_-} D_{p+1}(-\eta) \end{pmatrix}, \quad \psi_{\varepsilon=+1,p} = \begin{pmatrix} -iD_{-p}(-i\eta) \\ \nu_- D_{-p-1}(-i\eta) \\ \frac{i(\nu-p)}{\lambda} D_{-p-1}(-i\eta) \\ -\frac{(\nu-p)(p+1)}{\lambda\mu_-} D_{-p-2}(-i\eta) \end{pmatrix}, \tag{8.13}$$

for each of the two values of the parameter p given by

$$p = \frac{1}{2}\left[\mu + \nu - 1 \pm \sqrt{(\mu+\nu-1)^2 + 4\lambda^2\mu_-\nu_-}\right], \tag{8.14}$$

where we define (cf. Eq. 8.7)

$$\begin{aligned} \mu &= \mu_+\mu_- = (E - V + b)^2 - \Delta^2, \\ \nu &= \nu_+\nu_- = (E - V - b)^2 - \Delta^2, \end{aligned} \tag{8.15}$$

and D_p is the parabolic cylinder function of order p [38, 39]. For details about the solutions and the solutions for a negative magnetic field (i.e., $\varepsilon = -1$), see Ref. [19].

Next, we analyze the spatially uniform case.

8.3 The Uniform Field Case

In this section we study an unstrained infinitely extended graphene monolayer where the magnetic field $B_z = B$ (i.e., we assume $\varepsilon = +1$) and the SOI parameters Δ and λ are constant everywhere. (The electrostatic potential V just shifts all states and is set to zero here.) We are thus concerned with the relativistic Landau level structure for graphene in the presence of arbitrary SOI parameters, including also the Zeeman field b. This problem was solved for the special case $\Delta = b = 0$ by Rashba [16], see also Ref. [15], and below we reproduce and generalize this solution. We focus on the K point only, since the spectrum and the eigenstates at the K' point follow from Eqs. (8.5) and (8.11). We also allow for a constant pseudo-magnetic field. When only an orbital or a strain-induced pseudo-magnetic field is present but not both, each energy level below has an additional twofold valley degeneracy.

In the homogeneous case, the spinors ϕ_p in Eq. (8.13) are normalizable only if the order p is constrained to integer values $p = -1, 0, 1, 2, \ldots$, while the spinors ψ_p in Eq. (8.13) are not normalizable. Solutions for the homogeneous problem thus have to be constructed using ϕ_p only. Expressing the energy E (we remind the reader that here all energy scales are measured in units of $\hbar\omega_c$) in terms of p (Eq. 8.14), the sought (valley-degenerate) Landau levels follow as the roots of the quartic equation

$$\left[(E+b)^2 - (p+1+\Delta^2)\right]\left[(E-b)^2 - (p+\Delta^2)\right] = \lambda^2\left[(E-\Delta)^2 - b^2\right]. \quad (8.16)$$

For $b = \lambda = \Delta = 0$ this recovers the standard relativistic spin-degenerate Landau levels [3], $E_{\pm,n} = \pm\sqrt{n}$ for $n = 1, 2, 3, \ldots$ (with $n = p$ for spin up and $n = p+1$ for spin down states), plus a spin-degenerate zero mode $E_0 = 0$ (for $p = 0, -1$). We notice from Eq. (8.16) that for $b = 0$, the combination of Δ and λ breaks particle-hole symmetry, while the two couplings separately do not. Furthermore, zero-energy solutions are generally not possible except for special fine-tuned parameters. The $\phi_p(\eta)$ thus represent Landau level states in the presence of SOI and Zeeman coupling. The normalization constant $1/\sqrt{\mathcal{N}_p}$, entering as a prefactor in Eq. (8.13), can be computed analytically since $D_p(z)$ can be expressed in terms of Hermite functions for integer p [39], see Ref. [19].

Remarkably, for $p = -1$, we find the *exact* normalized state,

$$\phi_{-1}(\eta) = \frac{1}{(2\pi)^{1/4}} \begin{pmatrix} 0 \\ 0 \\ 0 \\ D_0(-\eta) \end{pmatrix}, \quad (8.17)$$

with the eigenvalue

$$E_{p=-1} = \Delta - b. \quad (8.18)$$

This unique admissible eigenstate for $p = -1$ is endowed with full spin polarization in the $\downarrow$ direction. For $p = 0$, the secular Eq. (8.16) becomes effectively a cubic

equation: the solution $E = \Delta + b$ (i.e., $\nu_- = 0$) does not correspond to any admissible eigenstate. The three allowed states are described by

$$\phi_{p=0}(\eta) = \frac{1}{\sqrt{\mathcal{N}_0}} \begin{pmatrix} 0 \\ \lambda\mu_- \nu_- D_0(-\eta) \\ i\mu_- \nu D_0(-\eta) \\ i\nu D_1(-\eta) \end{pmatrix}. \tag{8.19}$$

This includes a "zero-mode" partner of the $p = -1$ state, plus a pair of states obtained by mixing the spin-up $n = 0$ and spin-down $n = \pm 1$ Landau orbitals via the Rashba SOI.

8.3.1 Rashba SOI Only

For $\Delta = b = 0$ but finite Rashba SOI parameter λ, Eq. (8.16) admits a simple solution, previously given in Ref. [16] and briefly summarized here for completeness. For $p = -1$ we have the solution (8.17), which now is a zero mode, while for $p = 0, 1, 2, \ldots$, the eigenenergies are given by

$$E_{p,\alpha,\beta} = \alpha \left[\frac{1+\lambda^2}{2} + p\beta \sqrt{\left(\frac{1+\lambda^2}{2} + p \right)^2 - p(p+1)} \right]^{1/2}, \tag{8.20}$$

with $\alpha, \beta = \pm$. According to our discussion above, here $E_{0,\pm,-} = 0$ should be counted only once, with eigenstate $\phi^T_{0,,-} \propto (0, D_0(-\eta), 0, -i\lambda D_1(-\eta))$, while $E_{0,\pm,+} = \pm\sqrt{1+\lambda^2}$ correspond to a particle/hole pair of first Landau levels modified by the Rashba SOI, with eigenstates $\phi^T_{0,\pm,+} \propto (0, \lambda D_0(-\eta), \pm i\sqrt{1+\lambda^2} D_0(-\eta), iD_1(-\eta))$. We thus get precisely two zero-energy states.

For small λ, we find the expansion

$$E_{p-1,\pm,+} = \pm(1+\lambda^2/2)\sqrt{p} + \mathcal{O}(\lambda^4),$$
$$E_{p,\pm,-} = \pm(1-\lambda^2/2)\sqrt{p} + \mathcal{O}(\lambda^4),$$

which shows that the states $E_{p,\pm,+}$ and $E_{p+1,\pm,-}$, which form a degenerate Landau level for $\lambda = 0$, are split by a finite λ.

8.3.2 Intrinsic SOI Only

Let us next consider the case $\lambda = 0$, where one has a QSH phase [4] for $B = 0$ and $\Delta \neq 0$. Now the Hamiltonian is block diagonal in spin space and the eigenstates

become quite simple even for finite Zeeman coupling, since we can effectively work with the bi-spinors $\phi^{K,K'}_{\uparrow,\downarrow}(y)$ for spin $s = \uparrow / \downarrow = \pm$. We easily obtain the (unnormalized) eigenstates with $p \in \mathbb{N}_0$ in the form[2]

$$\phi^{K}_{p,\pm,s}(\eta) = \begin{pmatrix} \nu_{p,\pm,s} D_{p-1}(-\eta) \\ D_p(-\eta) \end{pmatrix},$$
$$\phi^{K'}_{p,\pm,s}(y) = \begin{pmatrix} -D_p(-\eta) \\ \nu_{p,\pm,s} D_{p-1}(-\eta) \end{pmatrix}, \tag{8.21}$$

where the eigenenergies follow from Eq. (8.16),

$$E_{p,\pm,s} = sb \pm \sqrt{p + \Delta^2}. \tag{8.22}$$

We employ the notation

$$\nu_{p,\pm,s} \equiv E_{p,\pm,s} - E_{0,-s,s} = \pm\sqrt{p+\Delta^2} - s\Delta. \tag{8.23}$$

For $p = 0$, the second index in $\phi_{p,\pm,s}$ and $E_{p,\pm,s}$ should be replaced by $-s$, i.e., there is only one solution for given spin (and valley). Note that $E_{0,+,\downarrow}$ in the present notation corresponds[3] to the solution (8.17). When $b = 0$, interestingly enough, Δ does *not* lift the spin degeneracy of the Landau levels except for the zero mode ($p = 0$).[4] A Zeeman term with $b = \Delta$ restores a true doubly-degenerate zero-energy state for $p = 0$ again. In Sect. 8.4 we show that this implies a quantum phase transition.

8.3.3 General Case

Although the quartic Eq. (8.16) can be solved analytically when both SOI couplings are finite, the resulting expressions are not illuminating and too lengthy to be quoted here. Only the $p = -1$ state in Eq. (8.17) remains exact for arbitrary parameters. We here specify the leading perturbative corrections around the special cases above, and then show the generic behavior in two figures.

[2]For notational convenience, we shift $p + 1 \to p$ for $s = \downarrow$ in the discussion of the purely intrinsic SOI.

[3]See footnote 2.

[4]We note that we made a wrong statement in Ref. [32] in that direction: For the case $j < 0$ on page 3 therein, we stated that for $a' = 0$ there are two normalizable states with $E = \pm|M|$ which for $M \to 0$ coalesce into a single zero-energy Landau level. However, only the state $E = -|M|$ is allowed, and the other one is not normalizable.

Expanding around the Rashba limit of Sect. 8.3.1, which is justified for $b, \Delta \ll 1$, we get the lowest-order perturbative correction to the finite-energy (i.e., $p \neq 0, -1$) Landau levels (Eq. 8.20) in the form

$$\delta E_{p,\pm,+} = -\delta E_{p,\pm,-} = \frac{(\lambda^2 \Delta + b)}{\sqrt{(1+\lambda^2)^2 + 4p\lambda^2}}. \tag{8.24}$$

Expanding instead around the intrinsic SOI limit of Sect. 8.3.2, we find the following small-λ corrections to the Landau levels in Eq. (8.22)[5]: For $p = 0$, the state $E_{0,+,\downarrow}$ corresponding to the exact solution (8.17) is not changed by λ to any order, while $E_{0,-,\uparrow}$ gets the lowest-order correction

$$\delta E_{0,-,\uparrow} = \frac{2(\Delta - b)\lambda^2}{4b(b-\Delta)+1}.$$

The corresponding eigenstate is, however, not a spin-$\uparrow$ state anymore. For $p > 0$, the eigenenergy $E_{p,\pm,s}$ (Eq. 8.22) acquires the perturbative correction

$$\delta E_{p,\pm,s} = \pm \frac{s\lambda^2}{2\sqrt{p+\Delta^2}} \frac{p + 2(\Delta - sb)(\Delta \mp \sqrt{p+\Delta^2})}{1 + 4b\left(sb \pm \sqrt{p+\Delta^2}\right)}. \tag{8.25}$$

We now consider two different SOI parameter sets consistent with the estimates in Ref. [12], and show the complete evolution of the Landau levels from the weak- to the strong-field limit. In Fig. 8.1, numerical results for the few lowest-energy Landau levels are depicted for $\Delta > \lambda/2$, corresponding to a QSH phase for $B = 0$. The (valley-degenerate) spin-split levels corresponding to the $\Delta = \lambda = b = 0$ zero mode exhibit a zero-energy crossing at $B \approx 11$ T for the chosen SOI parameters. This crossing signals a quantum phase transition from the QSH phase, which survives for sufficiently small B and $\Delta > \lambda/2$, to a peculiar QH phase for large B. As we discuss in Sect. 8.4, one then again has helical edge states [21] but with reversed spin current. Similar crossings can occur for higher Landau states as well, as is shown in Fig. 8.2 for a parameter set with $\Delta < \lambda/2$ where no QSH physics is expected. For even larger B, not displayed in Fig. 8.2, we find an $E = 0$ crossing where the Rashba-dominated small-B phase turns into the helical QH phase.

8.3.4 Spin Polarization

Given the Landau level eigenstates, it is straightforward to compute the spin-polarization densities $S_i(y) = \Psi^\dagger \frac{s_i}{2} \Psi$ ($i = x, y, z$). We find $S_x(y) = 0$, while

[5] See footnote 2.

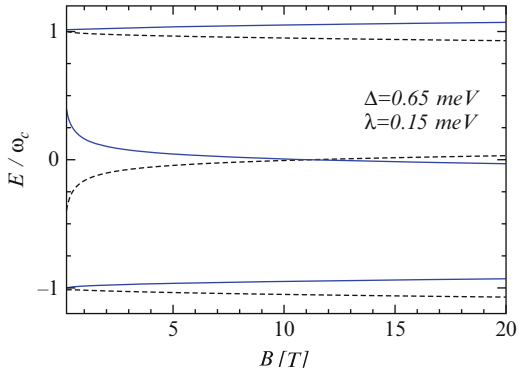

Fig. 8.1 Low-lying Landau level energies (in units of the cyclotron energy $\hbar\omega_c$) vs. magnetic field B (in Tesla) for the SOI parameters $\Delta = 0.65$ meV and $\lambda = 0.15$ meV. For small B, this corresponds to the QSH phase, $\Delta > \lambda/2$. For better visibility, the deviation from the respective $\Delta = \lambda = b = 0$ level has been magnified by a factor 10 for each curve

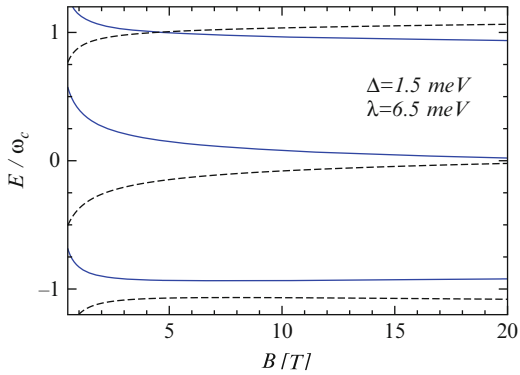

Fig. 8.2 Same as in Fig. 8.1 but for $\Delta = 1.5$ meV and $\lambda = 6.5$ meV

$$S_y(y) = \frac{\nu - p}{\lambda \mathcal{N}_p}\left(pD_{p-1}D_p + \frac{\nu_-}{\mu_-}D_pD_{p+1}\right),$$
$$S_z(y) = \frac{1}{2\mathcal{N}_p}\left[p^2D_{p-1}^2 + \left(\nu_-^2 - \frac{(\nu-p)^2}{\lambda^2}\right)D_p^2 - \frac{(\nu-p)^2}{\lambda^2\mu_-^2}D_{p+1}^2\right], \quad (8.26)$$

where $D_p \equiv D_p(-\eta)$. In the absence of the Rashba term ($\lambda = 0$), the in-plane component S_y vanishes identically, since then the eigenstates are simultaneously eigenstates of s_z. For finite λ, integration over y yields a vanishing expectation value for the overall in-plane polarization, but the Rashba coupling still induces *local* in-plane spin polarization. The case $\Delta = b = 0$ has been discussed in detail by Rashba [16].

8.4 QH Edge States for Intrinsic SOI

In this section, we consider the edge states corresponding to the relativistic Landau level problem in Sect. 8.3 when a boundary at $y = 0$ is present. We focus on the case of purely intrinsic SOI, $\lambda = 0$, but the physics should be qualitatively unchanged for $\lambda \ll \Delta$. In the region $y < 0$ we then have a homogeneous magnetic field $B_z = +B$, i.e., $\varepsilon = +1$. (For a pseudo-magnetic field, this holds at the K point while at the K' point, $B_z \to -B_z$.)

Since the problem of edge states in graphene has been studied extensively before, some remarks are in order at this point. In fact, putting $\Delta = b = \lambda = 0$, our results are consistent with those of Refs. [23, 24, 40–42] reporting chiral QH edge states in graphene. On the other hand, the $B = 0$ model is equivalent to the continuum limit of the Kane–Mele model [4] and thus exhibits helical QSH edge states [6]. (The helical state has a pair of counterpropagating 1D modes with opposite spin polarization.) The Kane–Mele model with $(\Delta, b) \neq 0$ but without orbital magnetic field has recently been studied [43], and a quantum phase transition from a (generalized) QSH phase for $b < \Delta$ to a quantum anomalous Hall (QAH) phase for $b > \Delta$ has been predicted. It is worthwhile to stress that the QSH effect survives even when time-reversal symmetry is broken. In the QAH phase, one has chiral edge states moving in the same direction for both spin polarizations [44]. The valley analogue of this quantum phase transition has also been studied [45]. Furthermore, for the 2D topological insulator realized in HgTe quantum well structures, a related transition has been predicted [46] by including the orbital field but omitting the Zeeman term.

However, the Zeeman term is crucial in graphene near the Dirac point: for $\Delta = 0$ and $b \neq 0$, spin-filtered helical edge states (similar to the QSH case) emerge again [21, 47]. Our results below show that this QSH-like phase is separated from the "true" QSH phase by a *quantum phase transition* at $b = \Delta$. Albeit both phases have spin-filtered edge states, they differ in the *direction* of the spin current. This feature should allow to experimentally distinguish both phases and to identify the quantum phase transition separating them. In practice, one may reach this transition simply by changing the magnetic field.

Normalizability of the wavefunctions for $y \to -\infty$ implies [38] that the only allowed solutions follow from the ϕ_p spinors in Eq. (8.13), while the ψ_p solutions in Eq. (8.13) have to be discarded. Since we do not have to impose normalizability at $y \to \infty$, the order p is not constrained to integer values and can now take any real value consistent with suitable boundary conditions at $y = 0$. For given conserved momentum k_x and spin s, the solutions for p yield the edge state spectrum, $E_s(k_x)$. Note that for finite magnetic field and $k_x < 0$, the distance from the boundary is set by $|k_x|$. Putting $\lambda = 0$, possible solutions $\phi^{K,K'}_{p,\pm,s}(y)$ must be of the form in Eq. (8.21), with energy $E_{p,\pm,s}$ given by Eq. (8.22). While $p \in \mathbb{N}_0$ in Sect. 8.3.2, we now consider arbitrary real p. To make progress, we have to specify boundary conditions at $y = 0$. We investigate two widely used boundary conditions, namely the zig-zag edge and the armchair edge [3, 21, 48, 49].

8.4.1 Zig-Zag Edge

For a zig-zag edge with the last row of carbon atoms residing on, say, sublattice A, the microscopic wavefunction must vanish on the next row outside the sample, belonging to sublattice B. In the continuum limit, since the x-axis here points in the zig-zag direction, the lower component of the spinor $\phi^K_{p,\pm,s}$ (Eq. 8.21) has to vanish at $y = 0$ [21, 23]. For both spin directions $s = \pm$, this yields the condition

$$D_p(2k_x) = 0, \tag{8.27}$$

which has to be solved for the energy, expressed in terms of p as $E_s = sb \pm \sqrt{p + \Delta^2}$. At the other Dirac point, the lower component of the spinor $\phi^{K'}_{p,\pm,s}$ should vanish at $y = 0$, where Eq. (8.11) implies the condition

$$\nu_{p,\pm,s} D_{p-1}(2k_x) = 0, \tag{8.28}$$

with $\nu_{p,\pm,s}$ in Eq. (8.23). It is not possible to find simultaneous solutions to both Eqs. (8.27) and (8.28). Possible states are thus confined to a single valley: the boundary condition does not mix the valleys but lifts the KK' degeneracy. Remarkably, for $s = \pm$ and arbitrary k_x, Eq. (8.28) is satisfied by the K' solution for $p = 0$ in Sect. 8.3.2, with $E_s(k_x) = s(b - \Delta)$, i.e., we find a pair of "flat" states. For all other states, Eq. (8.28) simplifies to condition (8.27) with $p \to p - 1$ (and $K \to K'$). We mention in passing that for $\Delta = 0$ this condition reduces to Eq. 9 in Ref. [42]. Equation (8.27) can be solved in closed form for $k_x \to -\infty$ using asymptotic properties of the parabolic cylinder function. To exponential accuracy, with $n \in \mathbb{N}_0$ we find

$$p = n + \frac{|2k_x|^{2n+1}}{\sqrt{2\pi} n!} e^{-2k_x^2}. \tag{8.29}$$

Numerical analysis of the above equations recovers the expected spin-filtered helical edge states [21] for $b > \Delta$, but the continuum approach used in this paper fails to give clear evidence for the helical QSH edge states for $b < \Delta$. As pointed out in Ref. [47], under the zig-zag boundary condition one needs a more microscopic description in order to capture these states. The "flat" states above are remnants of the sought QSH edge states, but the continuum model is not sufficient to describe their proper dispersion relation. We therefore turn to the armchair boundary condition.

8.4.2 Armchair Edge

Under the armchair boundary condition, we instead impose $\Psi^K_A + \Psi^{K'}_A = 0$ and $\Psi^K_B + \Psi^{K'}_B = 0$ at the boundary, with Ψ in Eq. (8.1). This boundary condition mixes the valleys and involves both sublattices. Since in our coordinate system the x-axis is

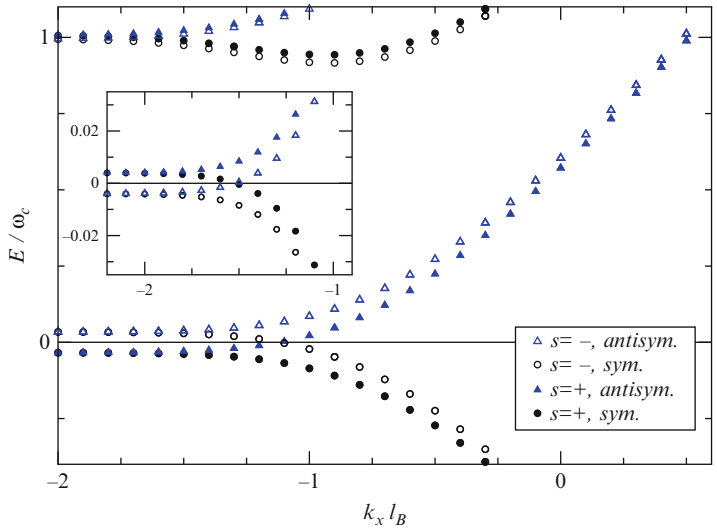

Fig. 8.3 Dispersion relation $E_{s,\pm}(k_x)$ of a semi-infinite graphene sheet with an armchair edge at $y = 0$, obtained numerically from Eq. (8.30). We use $\lambda = 0$, $B = 15$ T, $\Delta = 6$ meV, and the $+$ $(-)$ sign is for the symmetric (antisymmetric) valley combination in Eq. (8.30). *Inset:* Same for $\Delta = 0.3$ meV

parallel to the zig-zag direction, we first rotate the system by $\pi/2$ and then impose the boundary condition at $y = 0$. Written in the original coordinates, we find (for each spin direction s)

$$\nu_{p,\pm,s} D_{p-1}(2k_x) \pm D_p(2k_x) = 0. \tag{8.30}$$

We note that the relative phase between the K and K' components is not fixed by the Dirac equation, which is diagonal in valley space. However, the only relative phase compatible with the boundary condition imposed simultaneously on both sublattices is ± 1. Each of the two conditions in Eq. (8.30) may thus be imposed separately. We have checked that the numerical solution of Eq. (8.30) for $\Delta = 0$ recovers the known results for the QH edge state spectrum [21, 42]. In addition, for $B = 0$, the armchair edge is known [48, 50] to yield QSH edge states.

Our numerical results for the dispersion relation $E_{s,\pm}(k_x)$ for the armchair edge are shown in Fig. 8.3, where $\pm$ corresponds to the symmetric or antisymmetric linear combination in Eq. (8.30) and the magnetic field is $B = 15$ T. The main panel shows results for $\Delta = 6$ meV. Then $\Delta > b$, and we have the (generalized) QSH phase. Indeed, for $E = 0$ we find the helical edge state, where the right- (left-)mover has spin $s = \uparrow$ ($s = \downarrow$). The inset of Fig. 8.3 is for $\Delta = 0.3$ meV, where $\Delta < b$ and the spin-filtered helical QH phase [21] is found. Here we have spin $s = \downarrow$ ($s = \uparrow$) for the right- (left-)mover. Hence the *spin current* differs in sign for $\Delta > b$ and $\Delta < b$, with

a quantum phase transition at $\Delta = b$ separating both phases. This feature should allow for an experimentally observable signature of the transition.

8.5 Spin Structure in Magnetic Waveguides

In this section, we consider a spatially inhomogeneous situation, where a magnetic waveguide [27–29] along the x-direction can be realized. Since the problem remains homogeneous along the x-direction, $p_x = \hbar k_x$ is still conserved. For the physics described below, the Zeeman coupling b gives only tiny corrections [29] and will be neglected. Moreover, there are no valley-mixing terms, thus we can focus on a single valley.

We distinguish a central strip of width $2L$ (the "waveguide"), $-L < y < L$, and two outer regions $y < -L$ and $y > L$. In the central strip, we shall allow for arbitrary SOI parameters Δ and λ. In addition, strain may cause a constant contribution to the vector potential, $\mathscr{A}_x$, and a scalar potential, V. The magnetic field in the central strip is denoted by B_c. For $|y| > L$, we assume that all strain- or SOI-related effects can be neglected, $\Delta = \lambda = \mathscr{A}_x = V = 0$. In principle, by lithographic deposition of adatoms, one may realize this configuration experimentally. For $y < -L$, the magnetic field is $B_z = B > 0$, while for $y > L$, we set $B_z = \varepsilon B$, where $\varepsilon = 1$ ($\varepsilon = -1$) corresponds to the parallel (antiparallel) field orientation on both sides. For $\varepsilon = -1$, we take $B_c = 0$, while for $\varepsilon = +1$, we set $B_c = -B$.

The setup with $\varepsilon = -1$ could be realized by using a "folded" geometry [51, 52], cf. recent experimental studies [53]. Note that when the magnetic field changes sign, one encounters "snake orbits," which have been experimentally observed in graphene *pn* junctions [54]. For the $\varepsilon = -1$ configuration, we have uni-directional snake orbits mainly localized along the waveguide, while for $\varepsilon = +1$, we get two counterpropagating snake states centered near $y = \pm L$. For $\Delta = \lambda = \mathscr{A}_x = V = 0$, both cases ($\varepsilon = \pm 1$) have been studied in detail in Ref. [28]. Technically, one determines the eigenstates and the spectrum, $E(k_x)$, by matching the wavefunctions in the three different regions, which results in an energy quantization condition. This method can be straightforwardly extended to the more complex situation studied here by employing the general solution in Sect. 8.2 for the central strip.

Before turning to results, we briefly summarize the parameter values chosen in numerical calculations. We take a magnetic field value $B = 0.2$ T, and the waveguide width is $2L = \sqrt{8}\ell_B \approx 40$ nm. The strain-induced parameters in the central strip are taken as $\mathscr{A}_x = -16\,\mu\mathrm{m}^{-1}$ and $V = -20$ meV. These values have been estimated for a folded setup [52], where V comes from the deformation potential. We consider two different parameter choices for the SOI couplings: Set (A) has $\Delta = 13$ meV and $\lambda = 3$ meV, corresponding to the QSH phase. For set (B), we exchange both values, i.e., $\Delta = 3$ meV and $\lambda = 13$ meV.

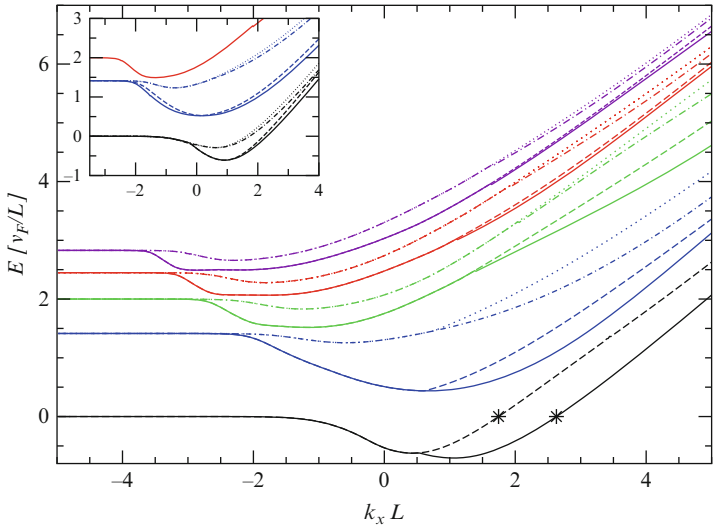

Fig. 8.4 Dispersion relation of the lowest few energy branches for a strained magnetic waveguide with $\varepsilon = -1$ and SOI in the central strip of width $2L$. Energies are given in units of $\hbar v_F/L$. The main panel is for parameter set (B). The *stars* refer to the states further studied in Fig. 8.5. *Inset:* Same for set (A) (See main text for details)

8.5.1 Antiparallel Case: Snake Orbit

Let us first discuss the $\varepsilon = -1$ configuration, where the magnetic field B_z differs in sign in the regions $y < -L$ and $y > L$. The dispersion relation of typical low-energy 1D waveguide modes is shown in Fig. 8.4. For $k_x \to -\infty$ the centers of the quantum states are located deep in the left and right magnetic regions, far from the waveguide. Thus one has doubly-degenerate dispersionless "bulk" Landau states. With increasing k_x these states are seen to split up. The dominant splitting, which is already present for $\Delta = \lambda = 0$, comes from the splitting of symmetric and anti-symmetric linear combinations of the Landau states for $y < -L$ and $y > L$ with increasing overlap in the waveguide region [28]. Asymptotically, the dispersion relation of all positive-energy snake states is $E(k_x \to +\infty) \simeq \hbar v_F k_x$ [28]. For intermediate k_x and $(\Delta, \lambda) \neq 0$, however, we get *spin-split snake states* out of the previously spin-degenerate states. The spin splitting is mainly caused by the Rashba coupling λ and disappears for $\lambda \to 0$, cf. the inset of Fig. 8.4.

The zero-energy bulk Landau state (for $k_x \to -\infty$) shows rich and interesting behavior in this setup. While for $k_x \to +\infty$, we expect one pair of snake states with positive slope and one pair with negative slope, for the studied parameter set and range of $k_x L$, there is just one state with negative slope while three branches first move down and then have a positive slope. Accordingly, at the Dirac point ($E = 0$), Fig. 8.4 shows that there are three right-movers with different Fermi momenta and different spin texture. Two of those states are indicated by stars (*) in the main

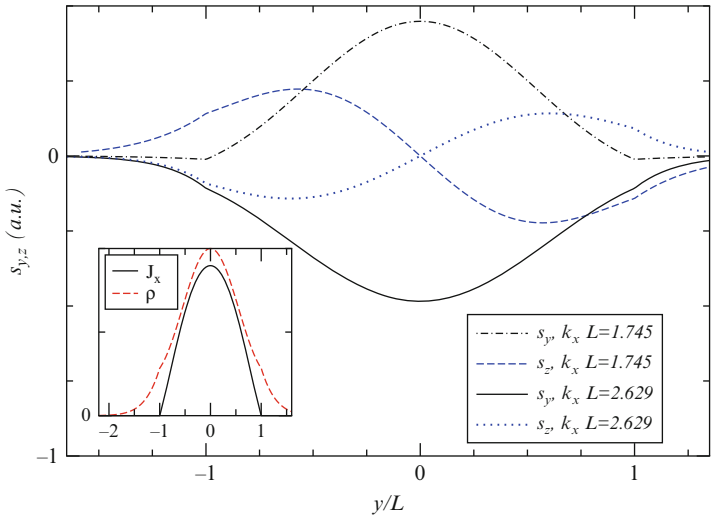

Fig. 8.5 Spin density profile $S_{y,z}$ (in arbitrary units) vs. y/L for the two $E = 0$ right-moving states indicated by stars in the main panel of Fig. 8.4. The left star corresponds to $k_xL = 1.745$, the right star to $k_xL = 2.629$. *Inset:* Particle density, ρ, and current density, J_x (which is the only non-vanishing component), in arbitrary units vs. y/L. We show the result only for $k_xL = 1.745$, since $k_xL = 2.629$ yields practically the same (color figure online)

panel of Fig. 8.4 and their local spin texture is shown in Fig. 8.5. Evidently, they are mainly localized inside the waveguide and have antiparallel spin polarization. We find spin densities with $S_x = 0$ for both states. For the Rashba-dominated situation in Fig. 8.5, spin is polarized perpendicular to the current direction and has a rather complex spatial profile.

8.5.2 *Parallel Configuration*

Next we come to the $\varepsilon = +1$ configuration, where the magnetic field is $+B$ for $|y| > L$ and $-B$ for $|y| < L$. One therefore expects two counterpropagating snake states in the x-direction localized around $y = \pm L$. The corresponding spectrum is shown in Fig. 8.6. We focus on parameter set (B), since for set (A), the spin splitting is minimal and less interesting. The spectrum consists of two qualitatively different states, namely states of bulk Landau character for large $|k_x|L$, and a set of propagating waveguide modes [28]. The spectral asymmetry seen in Fig. 8.6 for all propagating modes, $E(-k_x) \neq E(k_x)$, is caused by the strain ($\mathscr{A}_x$)-induced shift of k_x. Such a spectral asymmetry may give rise to interesting chirality and magnetoasymmetry effects [55]. The spin texture is shown in Fig. 8.7 for a pair of right- and left-moving states with $E = 1.2\hbar v_F/L$, cf. the stars in Fig. 8.6. We observe from the main panel in Fig. 8.7 that the spin polarization of both states is

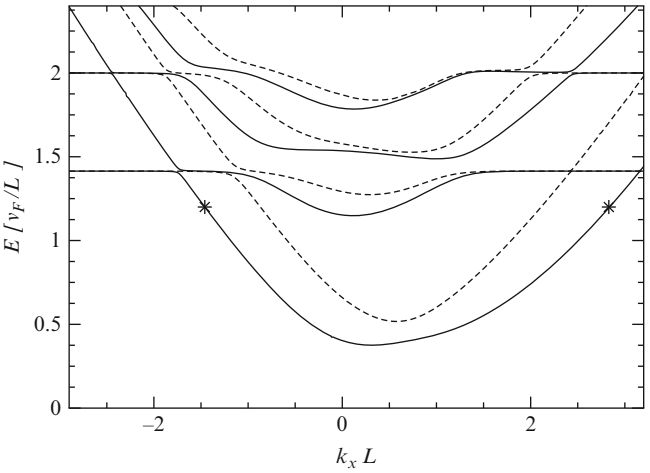

Fig. 8.6 Same as Fig. 8.4 but for the setup with $\varepsilon = +1$ and parameter set (B). *Solid* and *dashed curves* are for better visibility only. The two states indicated by *stars* are studied in Fig. 8.7

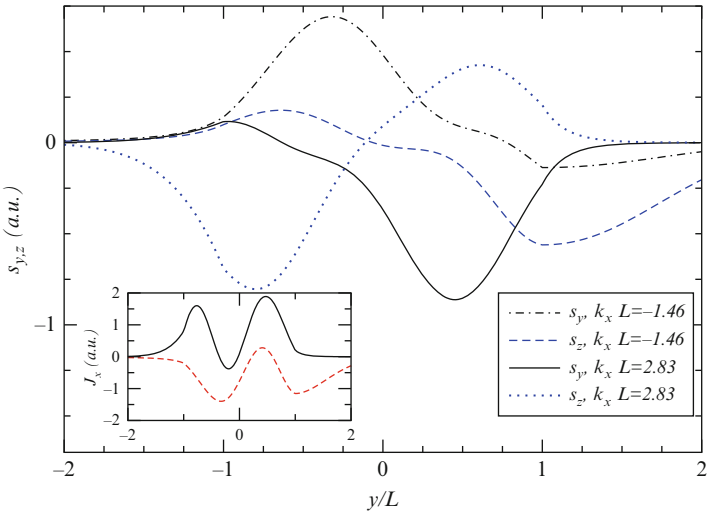

Fig. 8.7 Spin density $S_{y,z}$ (in arbitrary units) vs. y/L for the two states indicated by stars in Fig. 8.6. The left (right) star corresponds to a left- (right-)mover with $k_xL = -1.46$ ($k_xL = 2.83$). Note that the spin polarizations of both states are approximately antiparallel. *Inset:* Particle current profile J_x (in arbitrary units) vs. y/L for both states. *Black solid curve:* $k_xL = 2.83$. *Dashed red curve:* $k_xL = -1.46$ (color figure online)

approximately antiparallel. Because of their spatial separation and the opposite spin direction, elastic disorder backscattering between these counterpropagating snake modes should be very strongly suppressed. The inset of Fig. 8.7 shows the current density profile across the waveguide. Although the profile is quite complex, we observe that the current has opposite sign for both modes.

8.6 Concluding Remarks

In this work, we have studied the magnetoelectronic properties of graphene in the presence of strong intrinsic and Rashba-type spin-orbit couplings. According to a recent proposal [12], large intrinsic couplings may be realized by suitable adatom deposition on graphene. We have presented an exact solution for the Landau level states for arbitrary SOI parameters. When the intrinsic SOI dominates, by increasing the magnetic field, we predict a quantum phase transition from the quantum spin Hall phase to a helical quantum Hall phase at the Dirac point. In both phases, one has spin-filtered edge states but with opposite spin current direction. Thus the transition could be detected by measuring the spin current either in a transport experiment (e.g., along the lines of Ref. [56]) or via a magneto-optical experiment.

In inhomogeneous magnetic fields, especially when also strain-induced pseudo-magnetic fields are present, interesting waveguides can be envisioned. Such setups allow for snake states, where spin-orbit couplings result in a spin splitting. In a double-snake setup, there is a pair of counterpropagating snake states that carry (approximately) opposite spin polarization. This implies that scattering by elastic impurities is drastically suppressed. The resulting spin textures can in principle be detected by spin resolved ARPES (see, e.g., Refs. [10] and [57]) or spin-polarized STM measurements.

Acknowledgements We acknowledge financial support by the DFG programs SPP 1459 and SFB TR 12.

References

1. Geim AK (2009) Graphene: Status and prospects. Science 324:1530
2. Beenakker CWJ (2008) Colloquium: Andreev reflection and Klein tunneling in graphene. Rev Mod Phys 80:1337
3. Castro Neto AH, Guinea F, Peres NMR, Novoselov KS, Geim A (2009) The electronic properties of graphene. Rev Mod Phys 81:109
4. Kane CL, Mele EJ (2005) Quantum spin Hall effect in graphene. Phys Rev Lett 95:226801
5. Hasan MZ, Kane CL (2010) Colloquium: Topological insulators. Rev Mod Phys 82:3045
6. König M, Buhmann H, Molenkamp LW, Hughes T, Liu CX, Qi XL, Zhang SC (2008) The quantum spin Hall effect: Theory and experiment. J Phys Soc Jpn 77:031007
7. Huertas-Hernando D, Guinea F, Brataas A (2006) Spin-orbit coupling in curved graphene, fullerenes, nanotubes, and nanotubes caps. Phys Rev B 74:155426
8. Min H, Hill JE, Sinitsyn NA, Sahu BR, Kleinman L, MacDonald AH (2006) Intrinsic and Rashba spin-orbit interactions in graphene sheets. Phys Rev B 74:165310
9. Yao Y, Ye F, Qi XL, Zhang SC, Fang Z (2007) Spin-orbit of graphene: First-principle calculations. Phys Rev B 75:041401(R)
10. Dedkov YS, Fonin M, Rüdiger U, Laubschat C (2008) Rashba effect in the graphene/Ni(111) system. Phys Rev Lett 100:107602
11. Varykhalov A, Sánchez-Barriga J, Shikin AM, Biswas C, Vescovo E, Rybkin A, Marchenko D, Rader O (2008) Electronic and magnetic properties of quasifreestanding graphene on Ni. Phys Rev Lett 101:157601

12. Weeks C, Hu J, Alicea J, Franz M, Wu R (2011) Engineering a robust quantum spin Hall state in graphene via adatom deposition. Phys Rev X1:021001
13. Vozmediano MAH, Katsnelson MI, Guinea F (2010) Gauge fields in graphene. Phys Rep 496:109
14. Castro Neto AH, Guinea F (2009) Impurity-induced spin-orbit coupling in graphene. Phys Rev Lett 103:026804
15. Huertas-Hernando D, Guinea F, Brataas A (2009) Spin-orbit-mediated spin relaxation in graphene. Phys Rev Lett 103:146801
16. Rashba EI (2009) Graphene with structure-induced spin-orbit coupling: Spin-polarized states, spin zero modes, and quantum Hall effect. Phys Rev B 79:161409(R)
17. Bercioux D, De Martino A (2010) Spin-resolved scattering through spin-orbit nanostructures in graphene. Phys Rev B 81:165410
18. Lenz L, Bercioux D (2011) Dirac-Weyl electrons in a periodic spin-orbit potential. Europhys Lett 96:27006
19. De Martino A, Hütten A, Egger R (2011) Landau levels, edge states, and strained magnetic waveguides in graphene monolayers with enhanced spin-orbit interaction. Phys Rev B 84:155420
20. Guinea F, Katsnelson MI, Geim AK (2010) Energy gaps and a zero-field quantum Hall effect in graphene by strain engineering. Nat Phys 6:30
21. Abanin DA, Lee PA, Levitov LS (2007) Spin-filtered edge states and quantum Hall effect in graphene. Phys Rev Lett 96:176803; Abanin DA, Lee PA, Levitov LS (2007) Charge and spin transport at the quantum Hall edge of graphene. Solid State Commun 143:77
22. Gusynin VP, Sharapov SG (2005) Unconventional integer quantum Hall effect in graphene. Phys Rev Lett 95:146801
23. Brey L, Fertig HA (2006) Edge states and the quantized Hall effect in graphene. Phys Rev B 73:195408
24. Peres NMR, Castro Neto AH, Guinea F (2006) Dirac fermion confinement in graphene. Phys Rev B 73:241403
25. De Martino A, Dell'Anna L, Egger R (2007) Magnetic confinement of massless Dirac fermions in graphene. Phys Rev Lett 98:066802
26. Ramezani Masir M, Vasilopoulos P, Matulis A, Peeters FM (2008) Direction-dependent tunneling through nanostructured magnetic barriers in graphene. Phys Rev B 77:235443
27. Oroszlány L, Rakyta PK, Kormányos A, Lambert CJ, Cserti J (2008) Theory of snake states in graphene. Phys Rev B 77:081403(R)
28. Ghosh TK, De Martino A, Hüsler W, Dell'Anna L, Egger R (2008) Conductance quantization and snake states in graphene magnetic waveguide. Phys Rev B 77:081404(R)
29. Häusler W, De Martino A, Ghosh TK, Egger R (2008) Tomonaga-Luttinger liquid parameters of magnetic waveguides in graphene. Phys Rev B 78:165402
30. Dell'Anna L, De Martino A (2009) Multiple magnetic barriers in graphene. Phys Rev B 79:045420
31. Dell'Anna L, De Martino A (2009) Wave-vector-dependent spin filtering and spin transport through magnetic barriers in graphene. Phys Rev B 80:155416
32. De Martino A, Egger R (2010) On the spectrum of a magnetic quantum dot in graphene. Semicond Sci Technol 25:034006
33. Egger R, De Martino A, Siedentop H, Stockmeyer E (2010) Multiparticle equations for interacting Dirac fermions in magnetically confined graphene quantum dots. J Phys A 43:215202
34. Dell'Anna L, De Martino A (2011) Magnetic superlattice and finite-energy Dirac points in graphene. Phys Rev B 83:155449
35. Landau LD, Lifshitz EM (1986) Elasticity theory. Pergamon, New York
36. Suzuura H, Ando T (2002) Phonons and electron-phonon scattering in carbon nanotubes. Phys Rev B 65:235412
37. Fogler MM, Guinea F, Katsnelson MI (2008) Pseudomagnetic fields and ballistic transport in a suspended graphene sheet. Phys Rev Lett 101:226804

38. Abramowitz M, Stegun IA (1965) Handbook of mathematical functions with formulas, graphs and mathematical tables. Dover, New York (Ch. 19)
39. Gradshteyn IS, Ryzhik IM (1980) Table of integrals, series, and products. Academic Press, Inc., New York
40. Rakyta P, Kormányos A, Cserti J, Koskinen P (2010) Exploring the graphene edges with coherent electron focusing. Phys Rev B 81:115411
41. Delplace P, Montambaux G (2010) WKB analysis of edge states in graphene in a strong magnetic field. Phys Rev B 82:205412
42. Romanovsky I, Yannouleas C, Landman U (2011) Unique nature of the lowest Landau level in finite graphene samples with zigzag edges: Dirac electrons with mixed bulk-edge character. Phys Rev B 83:045421
43. Yang Y, Xu Z, Sheng L, Wang B, Xing DY, Sheng DN (2011) Time-reversal-symmetry-broken quantum spin Hall effect. Phys Rev Lett 107:066602
44. Qiao Z, Yang SA, Feng W, Tse WK, Ding J, Yao Y, Wang J, Niu Q (2010) Quantum anomalous Hall effect in graphene from Rashba and exchange effects. Phys Rev B 82:161414(R); Tse WK, Qiao Z, Yao Y, MacDonald AH, Niu Q (2011) Phys Rev B 83:155447
45. Yao W, Yang SA, Niu Q (2009) Edge states in graphene: From gapped flat-band to gapless chiral modes. Phys Rev Lett 102:096801
46. Tkachov G, Hankiewicz EM (2010) Ballistic quantum spin Hall state and enhanced edge backscattering in strong magnetic fields. Phys Rev Lett 104:166803; (2011) Transition between ordinary and topological insulator regimes in two-dimensional resonant magnetotransport. Phys Rev B 83:155412
47. Arikawa M, Hatsugai Y, Aoki H (2008) Edge states in graphene in magnetic fields: A specialty of the edge mode embedded in the n=0 Landau band. Phys Rev B 78:205401
48. Nakada K, Fujita M, Dresselhaus G, Dresselhaus MS (1996) Edge state in graphene ribbons: Nanometer size effect and edge shape dependence. Phys Rev B 54:17954; Brey L, Fertig HA (2006) Electronic states of graphene nanoribbons studied with the Dirac equation. Phys Rev B 73:235411
49. Akhmerov AR, Beenakker CWJ (2008) Boundary conditions for Dirac fermions on a terminated honeycomb lattice. Phys Rev B 77:085423
50. Tworzydlo J, Trauzettel B, Titov M, Rycerz A, Beenakker CWJ (2006) Sub-Poissonian shot noise in graphene. Phys Rev Lett 96:246802; Zarea M, Sandler N (2007) Electron-electron and spin-orbit interactions in armchair graphene ribbons. Phys Rev Lett 99:256804
51. Prada E, San-Jose P, Brey L (2010) Zero Landau level in folded graphene nanoribbons. Phys Rev Lett 105:106802
52. Rainis D, Taddei F, Polini M, León G, Guinea F, Fal'ko VI (2011) Gauge fields and interferometry in folded graphene. Phys Rev B 83:165403
53. Kim K, Lee Z, Malone BD, Chan KT, Alemán B, Regan W, Gannett W, Crommie MF, Cohen ML, Zettl A (2011) Multiply folded graphene. Phys Rev B 83:245433
54. Williams JR, Marcus CM (2011) Snake states along graphene p-n junctions. Phys Rev Lett 107:046602
55. De Martino A, Egger R, Tsvelik AM (2006) Nonlinear magnetotransport in interacting chiral nanotubes. Phys Rev Lett 97:076402
56. Tombros N, Josza C, Popinciuc M, Jonkman HT, van Wees BJ (2007) Electronic spin transport and spin precession in single graphene layers at room temperature. Nature 448:571
57. Bostwick A et al (2010) Observation of plasmarons in quasi-freestanding doped graphene. Science 328:999

Chapter 9
Wave Packet Propagation Through Randomly Distributed Scattering Centers in Graphene

Khamdam Yu. Rakhimov, Andrey Chaves, and Gil de Aquino Farias

Abstract We numerically investigate the wave packet propagation in graphene in the presence of randomly distributed circular potential steps. The calculations are performed within the continuum model, and the time propagation is made by a simple computational technique, based on the split-operator method. Our results show that, despite the Klein tunnelling effect, the presence of these potential steps significantly reduces the transmission probabilities, specially for higher concentration of scatterers and higher potential heights.

9.1 Introduction

In monolayer graphene, the energy spectrum is gapless in two inequivalent points of the first Brillouin zone, which are usually named as K and K'. In the vicinity of these points, low energy electrons exhibit a linear energy dispersion, so that, within a continuum model, they can be described as massless Dirac particles [1]. This has interesting consequences – for instance, such particles exhibit perfect transmission through potential barriers, due to the Klein tunnelling effect. Although this is quite interesting from the scientific point of view, since it allows one to use electrons in graphene to probe the Klein tunnelling effect in a lab, this is may be a problem for future technological applications of graphene, since it makes much harder to confine and manipulate electrons by electrostatic gates in these systems [2].

Kh.Yu. Rakhimov (✉)
Department of Physics, National University of Uzbekistan, 100174 Tashkent, Uzbekistan
e-mail: kh.rakhimov@gmail.com

A. Chaves • G. de Aquino Farias
Departamento de Física, Universidade Federal do Ceará, CP 6030, CEP 60455-900, Fortaleza-CE, Brazil
e-mail: andrey@fisica.ufc.br; gil@fisica.ufc.br

R. Egger et al. (eds.), *Low-Dimensional Functional Materials*, NATO Science for Peace and Security Series B: Physics and Biophysics, DOI 10.1007/978-94-007-6618-1_9,

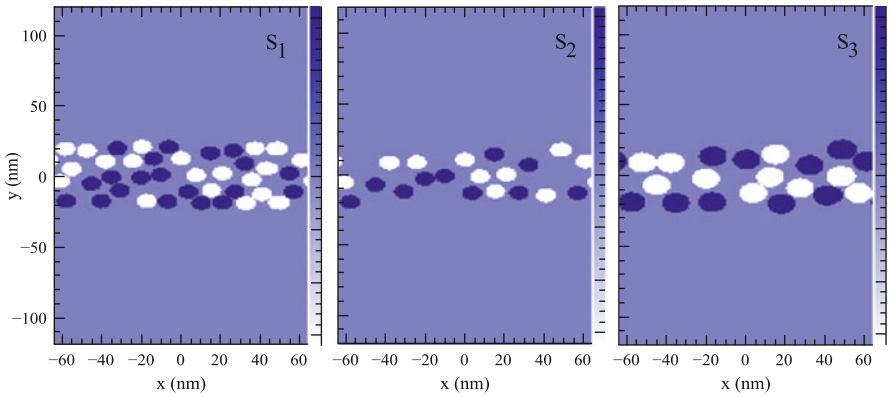

Fig. 9.1 Color map of the random potential landscape for the three sample cases investigated in this work: S_1, with 40 dots of radius $R = 5$ nm (D_s = 0.618), S_2, with 20 dots of radius $R = 5$ nm (D_s = 0.309), and S_3, with 20 dots of radius $R = 7$ nm (D_s = 0.606) (color figure online)

Recent studies have demonstrated the existence of charged regions, like electron-rich and hole-rich puddles, due to the inevitable disorder in graphene samples [3,4]. It is then interesting to understand how such a disorder affects the transmission of electrons through the graphene sheet.

In this work, we numerically solve the time-dependent Dirac equation for electrons in graphene, in order to investigate the propagation of a wave packet through a set of randomly distributed circular step potential barriers.[1] We assume that such a set of barriers might mimic the existence of electron and hole puddles in a real graphene sample, where these puddles appear with equal probability for electrons and holes [3]. Therefore, we assumed scattering centers that alternate between positive ($+V_0$) and negative ($-V_0$) potentials, representing that, locally, the electrons (holes) density is higher in negative (positive) potential regions, but the overall average potential in the whole scattering region is zero. This potential landscape is illustrated by the color maps in Fig. 9.1, for the three sample cases we will investigate in this work: S_1 (S_2) where 40 (20) scattering centers of radius $R = 5$ nm are considered, and S_3, with 20 scattering dots of radius $R = 7$ nm. Defining the density of scattering centers as $D_s = N_s \pi R^2 / A = 0.610$, where N_s is the number of circular scattering centers of (uniform) radius R, and A is the area of the scattering region, one obtains $D_s = 0.618, 0.309$ and 0.606 for S_1, S_2 and S_3, respectively. By comparing S_1 to S_2, we intend to analyze the effect of the density of scattering centers in the propagation behavior, whereas comparing S_1 to S_3, one observes only the effect of the reduction in the number of particles, since S_3 has a lower number of particles but with practically the same density D_s as S_1.

[1] A similar problem was studied recently by Palpacelli et al [5] arXiv:1202.6217, but with a different focus.

9.2 Theoretical Framework

As initial wave packet, we consider a Gaussian wave front, namely, a wave packet that is constant the x-direction, but which has a width a_y in the y-direction, multiplied by a pseudo-spinor $(1\ i)^T$ and by a plane wave

$$\Psi(x,y,0) = N \begin{pmatrix} 1 \\ i \end{pmatrix} e^{iky - \frac{y^2}{2a_y^2}} \tag{9.1}$$

where N is a normalization constant and k is the wave vector, which, in graphene, is related to the wave packet energy E by $k = E/\hbar v_F$, where v_F is the Fermi velocity. The choice of the pseudo-spinor is made so that $\langle \sigma_y \rangle = 1$ and $\langle \sigma_x \rangle = \langle \sigma_z \rangle = 0$, which guarantees a wave packet propagation towards the up direction [6]. Moreover, we choose to work with a wave front, instead of a circularly symmetric wave packet, in order to avoid *zitterbewegung* (a trembling motion of the wave packet) [6, 7] along the x-direction. All the results in the remainder of this paper are obtained for a wave packet with energy $E = 100$ meV and width $a_y = 20$ nm.

The propagation of the wave packet is performed by applying the time-evolution operator on the initial wave packet

$$\Psi(x,y,t+\Delta) = e^{-\frac{i}{\hbar}H\Delta t}\Psi(x,y,0) \tag{9.2}$$

where the Hamiltonian H, assumed to be time-independent, is the one for low energy electrons in graphene [1]

$$H = v_F \boldsymbol{\sigma} \cdot (\mathbf{p}) + V(x,y)\mathbf{I}, \tag{9.3}$$

where $\boldsymbol{\sigma}$ is the usual Pauli vector, $\mathbf{I}$ is the 2×2 identity matrix and the wave functions are written as pseudo-spinors $\Psi = (\Psi_A, \Psi_B)^T$, where Ψ_A (Ψ_B) is the probability of finding the electron in the sub-lattice A (B) of graphene. We separate the potential and kinetic energy terms of the time-evolution operator through the split-operator technique [8, 9],

$$\exp\left[-\frac{i}{\hbar}H\Delta t\right] = \exp\left[-\frac{i}{2\hbar}V(x,y)\mathbf{I}\Delta t\right] \exp\left[-\frac{i}{\hbar}v_F \mathbf{p}\cdot\boldsymbol{\sigma}\Delta t\right] \exp\left[-\frac{i}{2\hbar}V(x,y)\mathbf{I}\Delta t\right], \tag{9.4}$$

where terms of order higher than $O(\Delta t^3)$ are neglected as an approximation. The advantage of such separation is that it allows us to perform multiplications in real and reciprocal spaces separately, so that we avoid writing the momentum operator as a derivative just by making a Fourier transform of the functions and writing $\mathbf{p} = \hbar\mathbf{k}$. Furthermore, the exponentials of Pauli matrices terms can be re-written exactly as matrices [10], which simplifies even more the calculations. We perform wave packet propagations with a time step as small as $\Delta t = 0.1$ fs and keep track of

the probabilities of finding the electron before (P_1), inside (P_2), and after (P_3) the scattering region. The probability P_3 can also be seen as a transmission probability through the scattering region.

Notice that performing a Fourier transform while solving Eq. (9.4) necessarily imposes a periodic boundary condition to our system. Thus, in order to avoid spurious reduction (enhancement) of the transmission (reflection) probability P_3 (P_1) when the wave packet reaches the upper edge of the numerical grid, we consider a very long grid in the propagation direction, with an area $1,28$ nm $\times$ 1024 nm, whereas the scattering centers are distributed within an area of $A = 128$ nm $\times$ 40 nm around the $y = 0$ axis.

9.3 Results and Discussion

As a test case, we initially study the wave packet propagation in the absence of any potential, i.e. $V_0 = 0$. The results are shown in Fig. 9.2, where we see that the wave packet reaches the region 3 after ≈ 200 fs, when the probability P_3 saturates as 1.

In the presence of non-zero scattering potentials, the probability of finding the electron after the scattering region decreases significantly as the potential barrier enhances, as shown in Fig. 9.3, for a density of scattering centers $D_s = 0.618$ (S_1). This is a consequence of the non-normal incidence of a large part of the packet on

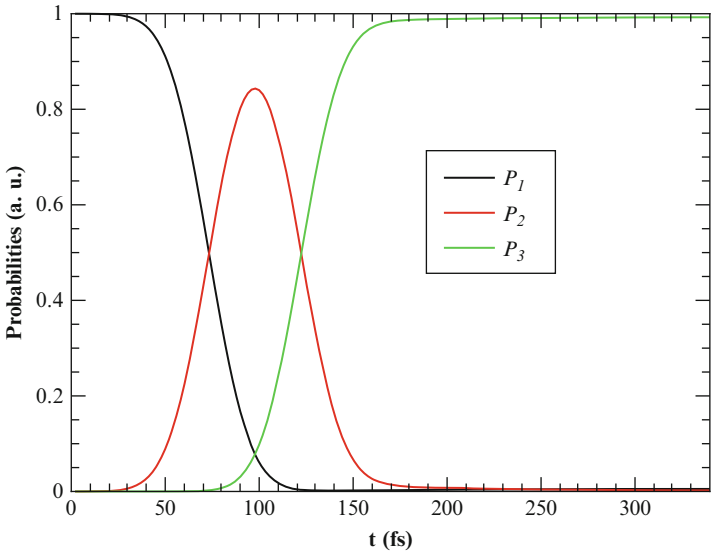

Fig. 9.2 Probabilities of finding the electron before (P_1), inside (P_2), and after (P_3) the scattering region, as a function of time, for a $E = 100$ meV wave packet propagating in a test case, where $V_0 = 0$

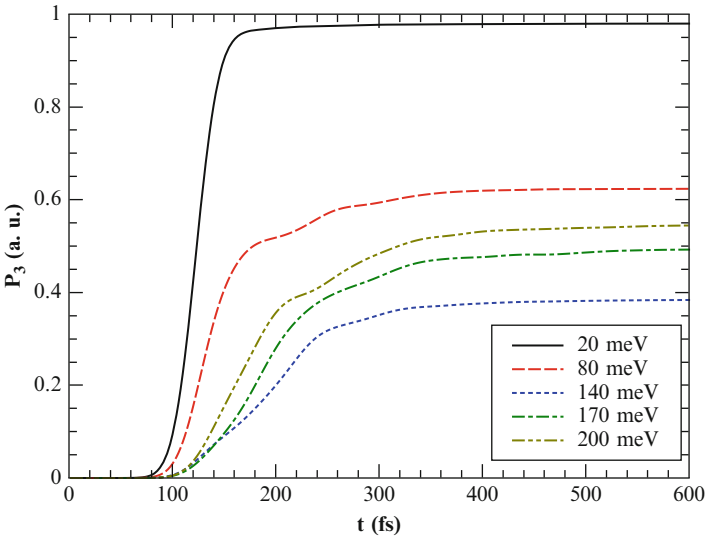

Fig. 9.3 Probability of finding the electron after the scattering region (P_3) as a function of time, for $E = 100$ meV and several values of barrier height V_0

the circular scattering potentials, so that the Klein tunnelling is not perfect in this case [2].

In Fig. 9.3, it can also be clearly observed that P_3 saturates faster for lower values of potential height V_0, which suggests that the dwell time of the wave packet inside the scattering region becomes longer as the potential height increases. This is indeed confirmed by the results in Fig. 9.4, which show the probability of finding the electron inside the scattering region (P_2) as a function of time, for different values of potential height V_0. We consider, for each value of V_0 and each sample S_i, a set of eight realizations of random distributions of scattering centers, so that we can take the average of the results and obtain the smooth curves shown in Fig. 9.4. The results for the three sample cases considered in this work are qualitatively the same: as the potential height increases, the decay of P_2 becomes much slower, which retards the saturation of the transmission probability P_3.

Notice that the saturation values of P_3 in Fig. 9.3 decrease with increasing V_0 until they reach a minimum for $V_0 = 140$ meV, as slightly larger transmission probabilities are observed for $V_0 = 170$ and 200 meV. This can be better visualized in Fig. 9.5, which shows the saturation values of P_3 as a function of the potential barrier V_0, for the three sample cases considered in this work. As in Fig. 9.4, the results in Fig. 9.5 were also obtained by taking the average of eight realizations. The standard deviations are shown as vertical bars in the figure. In all three cases, the transmission probabilities monotonically decrease with increasing the potential height until $V_0 \approx$ 100 meV, where the Klein tunneling of non-normal incident parts of the packet is minimal, since this value of V_0 is close to the wave packet energy $E = 100$

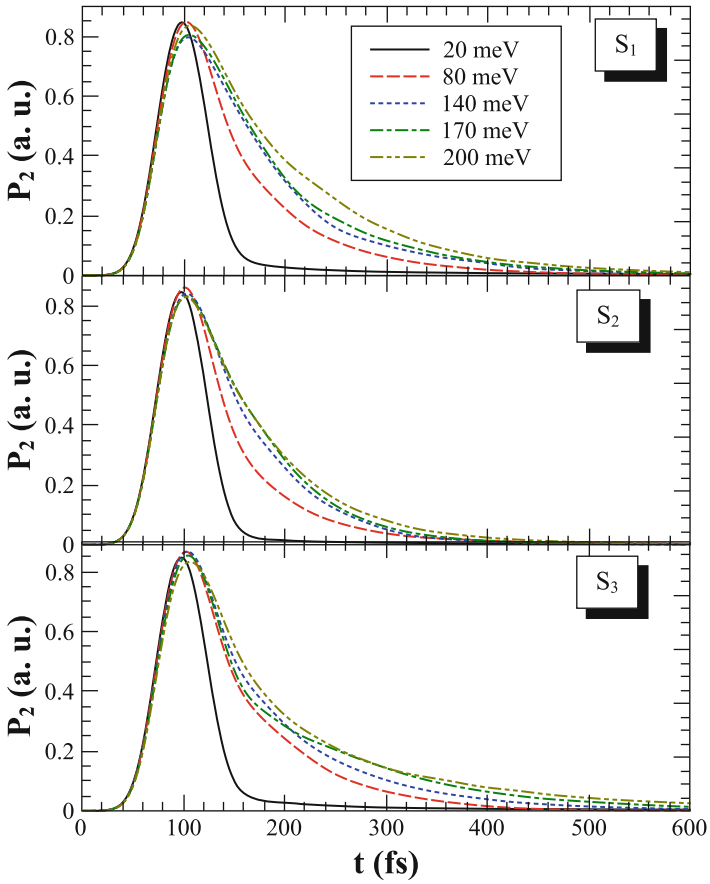

Fig. 9.4 Probability of finding the electron inside the scattering region (P_2) as a function of time, for several values of barrier height V_0 in the three sample cases considered in this work

meV [2, 10]. After this value, the transmission probabilities oscillate from ≈ 0.4 to ≈ 0.6. The S_1 and S_3 samples, which have similar scattering densities D_s, exhibit also similar oscillations of P_3, whereas S_2, with lower scattering density, exhibits a smoother reduction of the transmission probability as V_0 increases.

9.4 Conclusions

In summary, we have investigated the transmission of a wave packet through a set of randomly distributed circular potential steps. Our results demonstrate that the dwell time of the wave packet inside the scattering region is significantly enhanced

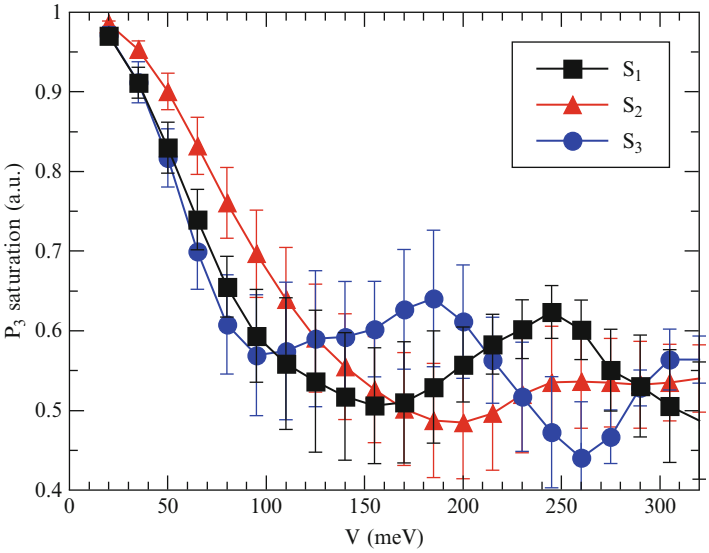

Fig. 9.5 Saturation values of the probabilities of finding the electron after the scattering region (P_3) for the three different sample cases considered in this work

by the presence of the scattering centers. Numerical results also show that the transmission probability decreases as the step barriers height increases, but only until a critical value is reached. After this critical value of potential height, the transmission probability starts to oscillate around ≈0.5. It is also demonstrated that, for lower densities of potential barriers, both the oscillations and the decay of the transmission probabilities with the potential height are smoother.

Acknowledgements The work of Kh. Rakhimov was supported by Matsumae International Foundation (Ref. Nr. Gno: 12G09) and partially supported by VolkswagenStiftung (Ref. Nr. Az.: 86 140). A. Chaves and G.A. Farias gratefully acknowledge financial support from the Brazilian Council for Research (CNPq).

References

1. Castro Neto AH, Guinea F, Peres NMR, Novoselov KS, Geim AK (2009) The electronic properties of graphene. Rev Mod Phys 81:109
2. Matulis A, Peeters FM (2008) Quasibound states of quantum dots in single and bilayer graphene. Phys Rev B 77:115423
3. Martin J, Akerman N, Ulbricht G, Lohmann T, Smet JH, von Klitzing K, Yacoby A (2008) Observation of electron-hole puddles in graphene using a scanning single-electron transistor. Nat Phys 4:144
4. Schubert G, Fehske H (2012) Metal-to-insulator transition and electron-hole puddle formation in disordered graphene nanoribbons. Phys Rev Lett 108:066402

5. Palpacelli S, Mendoza M, Herrmann HJ, Succi S (2012) Klein tunneling in the presence of random impurities. Int J Mod Phys C 23:1250080
6. Chaves A, Covaci L, Rakhimov KY, Farias GA, Peeters FM (2010) Wave-packet dynamics and valley filter in strained graphene. Phys Rev B 82:205430
7. Rusin TM, Zawadzki W (2010) Zitterbewegung of relativistic electrons in a magnetic field and its simulation by trapped ions. Phys Rev D 82:125031
8. Degani MH, Leburton JP (1991) Single-electron states and conductance in lateral-surface superlattices. Phys Rev B 44:10901
9. Suzuki M (1990) Fractal decomposition of exponential operators with applications to many-body theories and Monte Carlo simulations. Phys Lett A 146:319
10. Rakhimov KY, Chaves A, Farias GA, Peeters FM (2011) Wavepacket scattering of Dirac and Schrodinger particles on potential and magnetic barriers. J Phys Condens Matter 23:275801

Chapter 10
Are Scattering Properties of Networks Uniquely Connected to Their Shapes?

Oleh Hul, Michał Ławniczak, Szymon Bauch, Adam Sawicki, Marek Kuś, and Leszek Sirko

Abstract Are scattering properties of networks uniquely connected to their shapes? This is a modification of the famous question of Mark Kac "Can one hear the shape of a drum?" which can be asked in the case of scattering systems such as quantum graphs and microwave networks. We present the experimental approach to this problem (Hul et al., Phys Rev Lett 109:040402, 2012). Our experimental results indicate a negative answer to the above question. To demonstrate this we constructed a pair of isospectral microwave networks consisting of vertices connected by microwave coaxial cables and extended them to scattering systems by connecting leads to infinity to form isoscattering networks. We show that the amplitudes and phases of the determinants of the scattering matrices of such networks are the same within the experimental uncertainties. Additionally, we demonstrate that the scattering matrices of the networks are conjugated by the transplantation relation. The experimental results are in perfect agreement with the theoretical predictions.

In 1966 Marc Kac posed a famous question "Can one hear the shape of a drum?" [2]. It addressed the issue of uniqueness of the spectrum of the Laplace operator on the planar domain with Dirichlet boundary conditions. The answer was found in 1992 when Gordon, Webb, and Wolpert [3, 4] using the Sunada's theorem [5] found a way to construct pairs of isospectral domains in $\mathbb{R}^2$. An experimental confirmation that the shape of a drum can not be heard was presented by Sridhar and Kudrolli [6] and Dhar et al. [7] for a pair of isospectral microwave cavities.

O. Hul • M. Ławniczak • S. Bauch • L. Sirko (✉)
Institute of Physics, Polish Academy of Sciences, Aleja Lotników 32/46,
02-668 Warszawa, Poland
e-mail: sirko@ifpan.edu.pl

A. Sawicki • M. Kuś
Center for Theoretical Physics, Polish Academy of Sciences, Aleja Lotników 32/46,
02-668 Warszawa, Poland

R. Egger et al. (eds.), *Low-Dimensional Functional Materials*, NATO Science for Peace and Security Series B: Physics and Biophysics, DOI 10.1007/978-94-007-6618-1_10,

It is worth noting that basing on numerical simulations Okada et al. [8] conjectured that isospectral domains constructed by Gordon, Webb and Wolpert can be in fact discriminated in scattering experiments looking at poles of the scattering matrices.

Gutkin and Smilansky [9] extended the problem of isospectrality for quantum graphs. They proved that one can recover a graph from its spectrum if the lengths of its bonds are incommensurate. The method of construction of isospectral graphs [10, 11] uses the extended well known Sunada's approach. It is based on the elements of representation theory and its direct corollary ensures the existence of transplantation between isospectral graphs. In the process of transplantation one graph is divided into smaller building blocks which are then reassembled to form the second one of a different shape. The method provides also correct boundary conditions at vertices of the new graph. As a result of transplantation to every eigenfunction on the first graph an eigenfunction with the same eigenvalue on the second one is assigned. The procedure is reminiscent of the one used in designing isospectral planar domains where the 'drum' is cut into subdomains which are then rearranged into a new one with the same spectrum. Following the conjecture of Okada et al. [8] one can ask whether the geometry of a graph can be determined in scattering experiments.

The negative answer to the above question was given by Band, Sawicki and Smilansky [12, 13]. They extended the theory of isospectrality to scattering systems by considering isospectral quantum graphs with attached infinite leads and developed a method of constructing *isoscattering* pairs of graphs. According to the above authors two graphs are, by definition, isoscattering if their scattering matrices have the same poles – such graphs are called *isopolar*, or the amplitudes and phases of the determinants of their scattering matrices are equal – in this case the graphs are called isophasal. In this paper we will use the latter definition. They showed that any pair of isospectral quantum graphs obtained by the method described in [10, 11] is isoscattering if the infinite leads are attached in a way preserving the symmetry of the isospectral construction [12, 13].

Quantum graphs can be considered as idealizations of physical networks in the limit where the diameter of the wires are much smaller than their lengths. They were successfully applied to model variety of physical problems, see, e.g., [14] and references cited therein. They can also be realized experimentally. Recent developments in various epitaxy techniques allowed also for the fabrication and design of quantum nanowire networks [15, 16].

In 2004 Hul et al. [17] showed how quantum graphs could be successfully simulated by microwave networks. The experimental confirmation of the existence of isoscattering networks simulating isoscattering graphs was demonstrated in a recent paper by Hul et al. [1].

A general microwave network consists of n vertices connected by B bonds e.g., coaxial cables. The $n \times n$ connectivity matrix C_{ij} of a network takes the value 1 if the vertices i and j are connected and 0 otherwise. Each vertex i of a network is connected to the other vertices by v_i bonds, v_i is called the valency of the vertex i.

In this paper we consider networks with two most typical physical vertex boundary conditions, the Neumann and Dirichlet ones. The first one imposes the

continuity of waves propagating in bonds meeting at i and vanishing of the sum of their derivatives calculated at the vertex i. The latter demands vanishing of the waves at the vertex.

A coaxial cable consists of an inner conductor of radius r_1 surrounded by a concentric conductor of inner radius r_2. The space between the inner and the outer conductors is filled with a homogeneous material having the dielectric constant ε.

Below the onset of the next TE_{11} mode [18], inside a coaxial cable can propagate only the fundamental TEM mode, in the literature often called a Lecher wave.

We use the continuity equation for the charge and the current to find the propagation of a Lecher wave inside the coaxial cable joining the i–th and the j–th vertex of the microwave network [17, 19]

$$\frac{de_{ij}(x,t)}{dt} = -\frac{dJ_{ij}(x,t)}{dx}, \tag{10.1}$$

where $e_{ij}(x,t)$ and $J_{ij}(x,t)$ are the charge and the current per unit length on the surface of the inner conductor of a coaxial cable.

The potential difference $U_{ij}(x,t)$ between the conductors is given by

$$U_{ij}(x,t) = V_2^{ij}(x,t) - V_1^{ij}(x,t) = \frac{e_{ij}(x,t)}{\mathscr{C}}, \tag{10.2}$$

where $V_1^{ij}(x,t)$ and $V_2^{ij}(x,t)$ are the potentials of the inner and the outer conductors of a coaxial cable and $\mathscr{C}$ is the capacitance per unit length of a cable.

The spatial derivative of (10.2) gives [19]

$$\frac{d}{dx}U_{ij}(x,t) = -\mathscr{Z}J_{ij}(x,t), \tag{10.3}$$

where $\mathscr{Z}$ is the impedance per unit length. Calculation of the second spatial derivative of $U_{ij}(x,t)$ leads to the equation

$$\frac{d^2}{dx^2}U_{ij}(x,t) + \mathscr{Z}\frac{d}{dx}J_{ij}(x,t) = 0. \tag{10.4}$$

Using Eqs. (10.1) and (10.2) the Eq. (10.4) can be transformed to

$$\frac{d^2}{dx^2}U_{ij}(x,t) - \mathscr{Z}\mathscr{C}\frac{d}{dt}U_{ij}(x,t) = 0. \tag{10.5}$$

For a monochromatic wave propagating along the cable $e_{ij}(x,t)$ and $U_{ij}(x,t)$ are given by: $e_{ij}(x,t) = e^{-i\omega t}e_{ij}(x)$ and $U_{ij}(x,t) = e^{-i\omega t}U_{ij}(x)$, where the angular frequency $\omega = 2\pi\nu$ and ν is the microwave frequency. The impedance per unit length is then $\mathscr{Z} = \mathscr{R} - \frac{i\omega\mathscr{L}}{c^2}$ [19], where $\mathscr{R}$ and $\mathscr{L}$ denote the resistance and the inductance per unit length, respectively, and c stands here for the speed of light in a vacuum.

For an ideal lossless coaxial cable with the resistance $\mathscr{R} = 0$ the Eq. (10.5) leads to the telegraph equation on the microwave network

$$\frac{d^2}{dx^2}U_{ij}(x) + \frac{\omega^2\varepsilon}{c^2}U_{ij}(x) = 0, \tag{10.6}$$

where $\varepsilon = \mathscr{L}C$ [20].

The continuity equation for the potential difference requires that for every $i = 1, \ldots, N$

$$U_{ij}(x)|_{x=0} = \varphi_i, \quad U_{ij}(x)|_{x=L_{ij}} = \varphi_j, \quad i < j, \quad C_{ij} \neq 0. \tag{10.7}$$

The current conservation condition imposing the Neumann vertex boundary condition may be written in the form

$$-\sum_{j<i} C_{ij}\frac{d}{dx}U_{ji}(x)|_{x=L_{ij}} + \sum_{j>i} C_{ij}\frac{d}{dx}U_{ij}(x)|_{x=0} = 0, \tag{10.8}$$

where

$$\frac{dU_{ij}(x)}{dx} = -\mathscr{Z}J_{ij}(x). \tag{10.9}$$

L_{ij} represents the length of the bond joining the i–th and the j–th vertex of the network.

Assuming the correspondence: $\Psi_{ij}(x) \Leftrightarrow U_{ij}(x)$ and $k^2 \Leftrightarrow \frac{\omega^2\varepsilon}{c^2}$, Eq. (10.6) is formally equivalent to the one–dimensional Schrödinger equation (with $\hbar = 2m = 1$) on the graph possessing time reversal symmetry [21]

$$\frac{d^2}{dx^2}\Psi_{ij}(x) + k^2\Psi_{ij}(x) = 0. \tag{10.10}$$

Moreover, the Eqs. (10.7) and (10.8) are equivalent to the equations derived in [21] (see Eq. 10.3) for quantum graphs with Neumann boundary conditions and vanishing magnetic vector potential $A_{ij} = A_{ji} = 0$.

Various spectral and scattering properties of microwave networks simulating quantum graphs have been studied so far [17, 22–26]. The introduction of one-dimensional microwave networks simulating quantum graphs extended substantially the number of systems which are used to verify wave effects predicted on the basis of quantum physics [27–33]. To other systems used for this purpose one can include two-dimensional and three-dimensional microwave chaotic billiards and experiments with highly excited hydrogen and helium atoms. Experiments for two-dimensional microwave systems were pioneered by [34] and further developed by [35–47]. In the case of two dimensions the Schrödinger equation for quantum billiards is equivalent to the Helmholtz equation for microwave cavities of corresponding shape. Three-dimensional chaotic billiards have been also studied

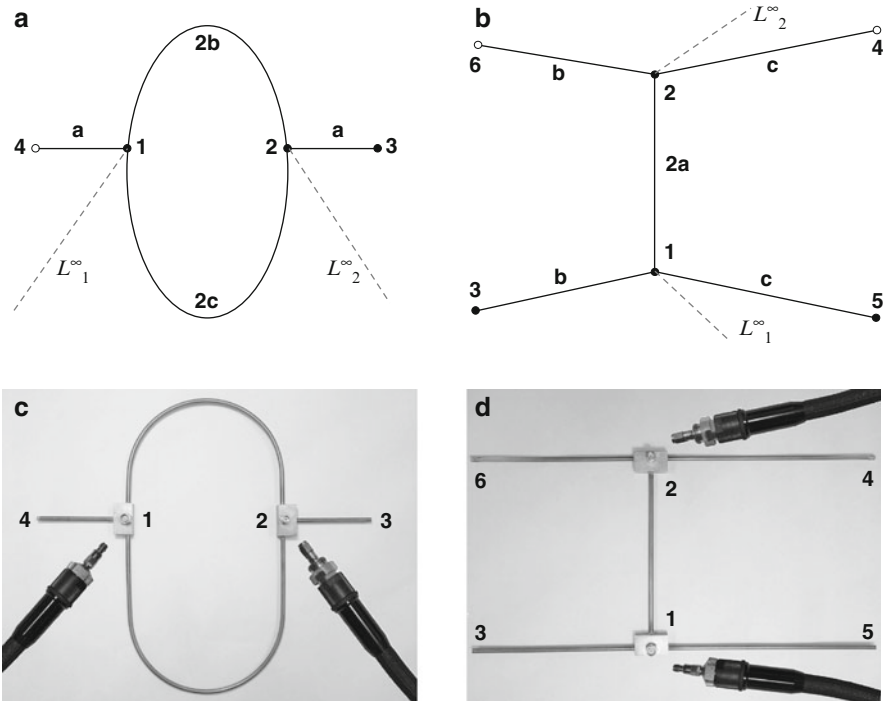

Fig. 10.1 A pair of isoscattering quantum graphs and the pictures of two isoscattering microwave networks are shown in the panels (**a**, **b**) and (**c**, **d**), respectively. Using the two isospectral graphs, (a) with $n = 4$ vertices and (b) with $n = 6$ vertices, isoscattering quantum graphs are formed by attaching the two infinite leads L_1^{∞} and L_2^{∞} (*dashed lines*). The vertices with Neumann boundary conditions are denoted by full circles while the vertices with Dirichlet boundary conditions by the open ones. The two isoscattering microwave networks with $n = 4$ and $n = 6$ vertices which simulate quantum graphs (a, b), respectively, are shown in the panels (c, d). The vertices of the both networks are numbered. To connect microwave networks to the Vector Network Analyzer (VNA) the two microwave coaxial cables were used. The connection of the VNA to a microwave network is equivalent to attaching of two infinite leads to quantum graphs

experimentally in the microwave frequency domain [48–51] but for these systems there is no direct analogy between the vectorial Helmholtz equation and the Schrödinger equation.

In order to verify experimentally a negative answer to the modified Mark Kac's question we consider the two microwave networks which simulate [17] the two isoscattering graphs shown in Fig. 10.1a, b. The isoscattering graphs are obtained from the two isospectral ones by attaching two infinite leads L_1^{∞} and L_2^{∞}. Using microwave coaxial cables we constructed the two microwave isoscattering networks shown in Fig. 10.1c, d. In order to preserve the same approximate size of the graphs in Fig. 10.1a, b and the networks in Fig. 10.1c, d, respectively, the lengths of the graphs were rescalled down to the physical lengths of the networks, which differ

from the optical ones by the factor $\sqrt{\varepsilon}$, where $\varepsilon \simeq 2.08$ is the dielectric constant of a homogeneous material used in the coaxial cables.

The graph in Fig. 10.1a consists of $n = 4$ vertices connected by $B = 4$ bonds. The valency of the vertices 1 and 2 including leads is $v_{1,2} = 4$ while for the other ones $v_i = 1$. The vertices with the numbers $1, 2$ and 3 satisfy the Neumann vertex conditions while for the vertex 4, the Dirichlet condition is imposed. The second graph (see Fig. 10.1b) consists of $n = 6$ vertices connected by $B = 5$ bonds. The vertices with numbers $1, 2, 3$ and 5, satisfy the Neumann vertex conditions, while for the vertices 4 and 6 we have the Dirichlet ones.

Each system is described in terms of 2×2 scattering matrix $S(\nu)$

$$S(\nu) = \begin{pmatrix} S_{1,1}(\nu) & S_{1,2}(\nu) \\ S_{2,1}(\nu) & S_{2,2}(\nu) \end{pmatrix}. \tag{10.11}$$

The scattering matrix $S(\nu)$ relates the amplitudes of the incoming and outgoing waves of frequency ν in both leads.

It was shown in [12] that the graphs presented in Fig. 10.1a, b are isoscattering. As a consequence of this property the phases of the determinants of the scattering matrices of the graphs should be equal for all values of ν

$$\mathrm{Im}\Big[\log\Big(\det\big(S^{(I)}(\nu)\big)\Big)\Big] = \mathrm{Im}\Big[\log\Big(\det\big(S^{(II)}(\nu)\big)\Big)\Big]. \tag{10.12}$$

In order to measure the two-port scattering matrix $S(\nu)$ we connected the vector network analyzer (VNA) Agilent E8364B to the vertices 1 and 2 of the microwave networks shown in Fig. 10.1c, d and performed measurements in the frequency range ν = 0.01–1.5 GHz. he connection of the VNA to a microwave network is equivalent to attaching of two infinite leads to quantum graphs. Therefore, Fig. 10.1a, b apply to our experiment as well.

The optical lengths of the bonds of the microwave networks had the following values:

$$\begin{aligned} a &= 0.0985 \pm 0.0005\,\mathrm{m}, & 2a &= 0.1970 \pm 0.0005\,\mathrm{m} \\ b &= 0.1847 \pm 0.0005\,\mathrm{m}, & 2b &= 0.3694 \pm 0.0005\,\mathrm{m} \\ c &= 0.2420 \pm 0.0005\,\mathrm{m}, & 2c &= 0.4840 \pm 0.0005\,\mathrm{m} \end{aligned}$$

The uncertainties in the bonds' lengths of the networks are due to the preparation of Neumann $v_{1,2} = 4$ and Dirichlet vertices. In the case of the first ones the internal leads of the cables were soldered together while the Dirichlet vertices were prepared by closing the cables with brass caps to which the internal and external conductors of the coaxial cables were soldered.

In the case of the microwave networks, where one deals with losses in the microwave cables [17], not only the phase of the determinant $\phi = \mathrm{Im}\Big[\log\Big(\det\big(S(\nu)\big)\Big)\Big]$ but the amplitude $|\det\big(S(\nu)\big)|$ as well gives the insight into the resonant structure of the system. The amplitudes and the phases of the determinants of the scattering

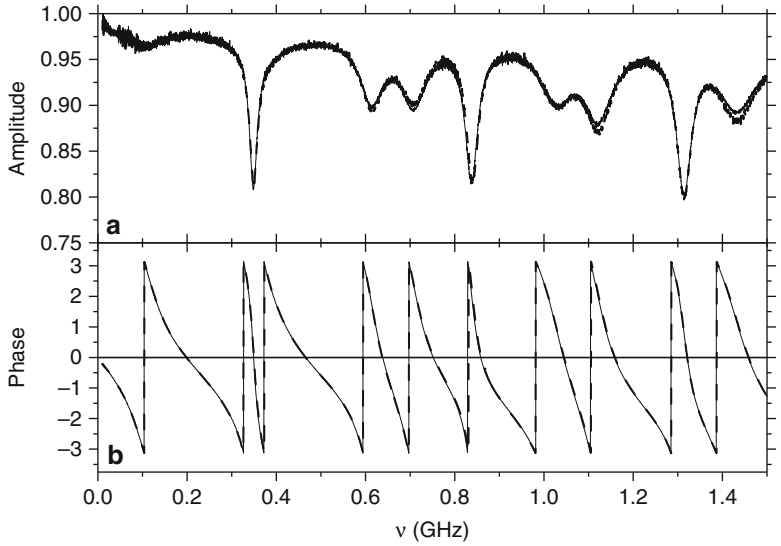

Fig. 10.2 (**a**) The amplitude of the determinant of the scattering matrix obtained for the microwave networks with $n = 4$ (*dashed line*) and $n = 6$ (*solid line*) vertices. (**b**) The phase of the determinant of the scattering matrix obtained for the microwave networks with $n = 4$ (*dashed line*) and $n = 6$ (*solid line*) vertices. The results are presented in the frequency range 0.01–1.5 GHz

matrices of the experimentally studied networks are shown in Fig. 10.2. Figure 10.2 shows that especially for lower frequencies 0.01–1.0 GHz there is an excellent agreement between the results obtained for the both networks. The amplitudes of the determinants are so close to each other that the differences between them are hardly resolved in Fig. 10.2a. The phases of the determinants are in very good agreement in the full range of the investigated frequency ν = 0.01–1.5 GHz. Therefore, our experimental results strongly suggest that it is not possible to listen to the shape of a network.

Some small differences between the amplitudes appearing for $\nu > 1$ GHz are due to different lengths of the networks. As it was discussed earlier the bonds' lengths are known only with a certain accuracy. In order to check the influence of different bonds' lengths on obtained results we performed numerical calculations which took into account also the internal absorption of microwave cables [17]. We found that at certain realizations of the networks lengths the results, not shown here, mimic the same behavior visible in Fig. 10.2a.

The networkss considered in this paper have an additional important property, namely the scattering matrices of the networks are conjugated to each other by the following transplantation relation

$$S^{(II)}(\nu) = T^{-1} S^{(I)}(\nu) T, \tag{10.13}$$

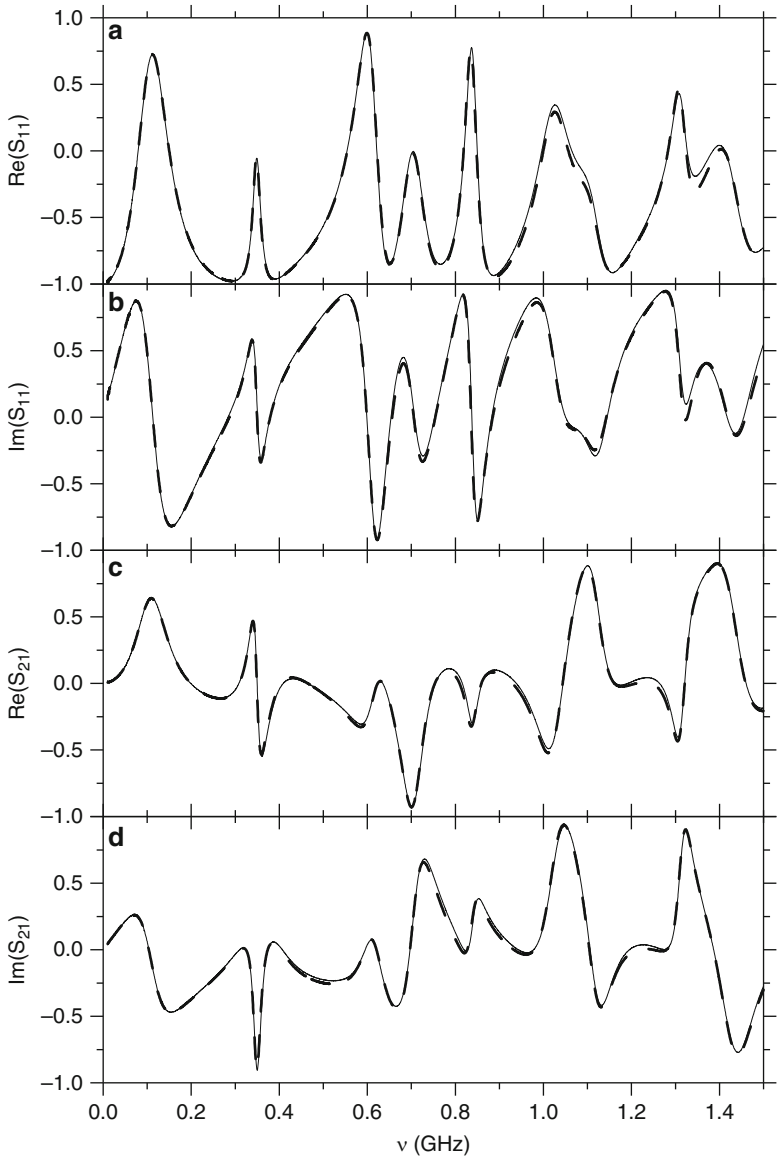

Fig. 10.3 (**a**) The real and (**b**) imaginary parts of the matrix element $\tilde{S}^{(I)}_{1,1}(\nu)$ of the transformed scattering matrix (*dashed line*) for the system with $n = 4$ vertices. The obtained results are compared to the scattering matrix elements $S^{(II)}_{1,1}(\nu)$ of the graph with $n = 6$ vertices (*solid line*). (**c**) The real and (**d**) imaginary parts of the matrix element $\tilde{S}^{(I)}_{2,1}(\nu)$ of the transformed scattering matrix (*dashed line*) for the system with $n = 4$ vertices. The results are compared to the scattering matrix element $S^{(II)}_{21}(\nu)$ of the graph with $n = 6$ vertices (*solid line*). The results are presented in the frequency range 0.01–1.5 GHz

where $T = \begin{pmatrix} 1 & -1 \\ 1 & 1 \end{pmatrix}$. It is worth noting that the matrix T does not depend on the frequency and the Eq. (10.13) is valid for all values of ν.

To check the transplantation relation expressed by Eq. (10.13) we transformed experimentally measured scattering matrix of the first network $\tilde{S}^{(I)}(\nu) = T^{-1}S^{(I)}(\nu)T$ and compared it to the scattering matrix of the second network $S^{(II)}(\nu)$. In Fig. 10.3 we present the results for the real and imaginary parts of $S_{1,1}$ and $S_{2,1}$ elements, respectively.

Figure 10.3 clearly shows that the transplantation relation for the real and imaginary parts of $S_{1,1}(\nu)$ and $S_{2,1}(\nu)$ elements works very well. Some small differences seen for $\nu > 1$ GHz are caused, as previously, by small differences in the cables' lengths.

Summarizing, we investigated experimentally scattering properties of two microwave networks and demonstrated that they are isoscattering, i.e., the phases and amplitudes of the determinant of the two-port scattering matrices are the same, within the experimental errors, for all the frequencies considered. We also investigated the validity of the transplantation relation between the two-port scattering matrices of the two isoscattering microwave networks. It was shown that using this relation it is possible to reconstruct the scattering matrix of each investigated network using the scattering matrix of the other one. Results presented in this paper clearly demonstrate that our experimental setup can be successfully used to investigate properties of any quantum graph, also with highly complicated topology, see, e.g., [17, 23, 26, 52] showing a great research potential of quantum simulations based on microwave networks.

This work was partially supported by the Ministry of Science and Higher Education grant No. N N202 130239.

References

1. Hul O, Ławniczak M, Bauch S, Sawicki A, Kuś M, Sirko L (2012) Are scattering properties of graphs uniquely connected to their shapes? Phys Rev Lett 109:040402
2. Kac M (1966) Can one hear the shape of the drum? Am Math Mon 73:1
3. Gordon C, Webb D, Wolpert S (1992) Isospectral plane domains and surfaces via Riemannian orbifolds. Invent Math 110:1
4. Gordon C, Webb D, Wolpert S (1992) One cannot hear the shape of a drum. Bull Am Math Soc 27:134
5. Sunada T (1985) Riemannian coverings and isospectral manifolds. Ann Math 121:169
6. Sridhar S, Kudrolli A (1994) Experiments on not hearing the shape of drums. Phys Rev Lett 72:2175
7. Dhar A, Rao DM, Shankar U, Sridhar S (2003) Isospectrality in chaotic billiards. Phys Rev E 68:026208
8. Okada Y, Shudo A, Tasaki S, Harayama T (2005) Can one hear the shape of a drum?: revisited. J Phys A 38:L163
9. Gutkin B, Smilansky U (2001) Can one hear the shape of a graph? J Phys A 34:6061
10. Band R, Parzanchevski O, Ben-Shach G (2009) The isospectral fruits of representation theory: quantum graphs and drums. J Phys A 42:175202

11. Parzanchevski O, Band R (2010) Linear representations and isospectrality with boundary conditions. J Geom Anal 20:439
12. Band R, Sawicki A, Smilansky U (2010) Scattering from isospectral quantum graphs. J Phys A 43:415201
13. Band R, Sawicki A, Smilansky U (2011) Note on the role of symmetry in scattering from isospectral graphs and drums. Acta Phys Pol. A 120:A149
14. Gnutzmann S, Smilansky U (2006) Quantum graphs: applications to quantum chaos and universal spectral statistics. Adv Phys 55:527
15. Dick KA, Deppert K, Larsson MW, Märtensson T, Seifert W, Wallenberg LR, Samuelson L (2004) Synthesis of branched 'nanotrees' by controlled seeding of multiple branching events. Nat Mater 3:380
16. Heo K et al (2008) Large-Scale assembly of silicon nanowire network-based devices using conventional microfabrication facilities. Nano Lett 8:4523
17. Hul O, Bauch S, Pakonski P, Savytskyy N, Życzkowski K, Sirko L (2004) Experimental simulation of quantum graphs by microwave networks. Phys Rev E 69:056205
18. Jones DS (1964) Theory of electromagnetism. Pergamon Press, Oxford
19. Landau LD, Lifshitz EM (1960) Electrodynamics of continuous media. Pergamon Press, Oxford
20. Goubau G (1961) Electromagnetic waveguides and cavities. Pergamon Press, Oxford
21. Kottos T, Smilansky U (1999) Periodic orbit theory and spectral statistics for quantum graphs. Ann Phy 274:76
22. Hul O, Tymoshchuk O, Bauch S, Koch PM, Sirko L (2005) Experimental investigation of Wigner's reaction matrix for irregular graphs with absorption. J Phys A 38:10489
23. Ławniczak M, Hul O, Bauch S, Šeba P, Sirko L (2008) Experimental and numerical investigation of the reflection coefficient and the distributions of Wigner's reaction matrix for irregular graphs with absorption. Phys Rev E 77:056210
24. Ławniczak M, Bauch S, Hul O, Sirko L (2009) Experimental investigation of properties of hexagon networks with and without time reversal symmetry. Phys Scr T135:014050
25. Ławniczak M, Hul O, Bauch S, Sirko L (2009) Experimental and numerical studies of one-dimensional and three-dimensional chaotic open systems. Acta Phys Pol A 116:749
26. Ławniczak M, Bauch S, Hul O, Sirko L (2010) Experimental investigation of the enhancement factor for microwave irregular networks with preserved and broken time reversal symmetry in the presence of absorption. Phys Rev E 81:046204
27. Blümel R, Buchleitner A, Graham R, Sirko L, Smilansky U, Walther H (1991) Dynamic localization in the microwave interaction of rydberg atoms and the influence of noise. Phys Rev A 44:4521
28. Bellermannn M, Bergemann T, Haffmanns A, Koch PM, Sirko L (1992) Electric-field dependence of E1 transitions between highly excited hydrogen Stark sublevels. Phys Rev A 46:5836
29. Sirko L, Yoakum S, Haffmans A, Koch PM (1993) Microwave-driven He Rydberg atoms: Floquet-state degeneracy lifted by a second frequency, Stueckelberg oscillations, and their destruction by added noise. Phys Rev A 47:R782
30. Sirko L, Koch PM (1995) The pendulum approximation for the main quantal resonance in periodically driven Hydrogen atoms. Appl Phys B 60:S195
31. Sirko L, Haffmans A, Bellermann MRW, Koch PM (1996) Microwave "ionization" of excited hydrogen atoms: frequency dependence in a resonance zone. Europhys Lett 33:181
32. Sirko L, Zelazny SA, Koch PM (2001) Use of the relative phase in a bichromatic field pulse to control a quasienergy gap. Phys Rev Lett 87:043002
33. Sirko L, Koch PM (2002) Control of common resonances in bichromatically driven hydrogen atoms. Phys Rev Lett 89:274101
34. Stöckmann HJ, Stein J (1990) "Quantum" chaos in billiards studied by microwave absorption. Phys Rev Lett 64:2215
35. Sridhar S (1991) Experimental observation of scarred eigenfunctions of chaotic microwave cavities. Phys Rev Lett 67:785

36. Alt H, Gräf H-D, Harner HL, Hofferbert R, Lengeler H, Richter A, Schardt P, Weidenmüller A (1995) Gaussian orthogonal ensemble statistics in a microwave stadium billiard with chaotic dynamics: Porter-Thomas distribution and algebraic decay of time correlations. Phys Rev Lett 74:62
37. So P, Anlage SM, Ott E, Oerter RN (1995) Wave chaos experiments with and without time reversal symmetry: GUE and GOE statistics. Phys Rev Lett 74:2662
38. Stoffregen U, Stein J, Stöckmann H-J, Kuś M, Haake F (1995) Microwave billiards with broken time reversal symmetry. Phys Rev Lett 74:2666
39. Haake F, Kuś M, Šeba P, Stöckmann H-J, Stoffregen U (1996) Microwave billiards with broken time reversal invariance. J Phys A 29:5745
40. Sirko L, Koch PM, Blümel R (1997) Experimental identification of non-Newtownian orbits produced by ray splitting in a dielectric-loaded microwave cavity. Phys Rev Lett 78:2940
41. Bauch S, Błędowski A, Sirko L, Koch PM, Blümel R (1998) Signature of non-Newtownian orbits in ray splitting cavities. Phys Rev E 57:304
42. Sirko L, Bauch S, Hlushchuk Y, Koch PM, Blümel R, Barth M, Kuhl U, Stöckmann H-J (2000) Observation of dynamical localization in a rough microwave cavity. Phys Lett A 266:331–335
43. Blümel R, Koch PM, Sirko L (2001) Ray-splitting billiards. Found Phys 31:269
44. Hlushchuk Y, Sirko L, Kuhl U, Barth M, Stöckmann H-J (2001) Experimental investigation of a regime of Wigner ergodicity in microwave rough billiards. Phys Rev E 63:046208
45. Savytskyy N, Bauch S, Błędowski A, Hul O, Sirko L (2002) Properties of eigenfunctions in the quantum cantori regime. Acta Phys Pol B 33:2123
46. Savytskyy N, Hul O, Sirko L (2004) Experimental investigation of nodal domains in the chaotic microwave rough billiard. Phys Rev E 70:056209
47. Hul O, Savytskyy N, Tymoshchuk O, Bauch S, Sirko L (2005) Investigation of nodal domains in the chaotic microwave ray-splitting rough billiard. Phys Rev E 72:066212
48. Deus S, Koch PM, Sirko L (1995) Statistical properties of eigenfrequency distribution of three-dimensional microwave cavities. Phys Rev E 52:1146
49. Dörr U, Stöckmann H-J, Barth M, Kuhl U (1998) Scarred and chaotic field distributions in a three-dmensional Sinai-microwave resonator. Phys Rev Lett 80:1030
50. Dembowski C, Dietz B, Gräf H-D, Heine A, Papenbrock T, Richter A, Richter C (2002) Experimental test of a trace formula for a chaotic three-dimensional microwave cavity. Phys Rev Lett 89:064101-1
51. Tymoshchuk O, Savytskyy N, Hul O, Bauch S, Sirko L (2007) Experimental investigation of electric field distributions in a chaotic three-dimensional microwave rough billiard. Phys Rev E 75:037202
52. Hul O, Sirko L (2011) Parameter-dependent spectral statistics of chaotic quantum graphs: Neumann versus circular orthogonal ensemble boundary conditions. Phys Rev E 83:066204

Chapter 11
Particle Dynamics in Kicked Quantum Networks

Valijon Eshniyozov, Jambul Yusupov, Davron Matrasulov, and Inomjon Ibragimov

Abstract Particle dynamics in a periodically driven quantum network is studied by considering delta-kicked quantum star graph is studied. Quantum dynamics is treated by solving Schrodinger equation with time-dependent boundary conditions given on graphs. Time-dependence of the average kinetic energy is analyzed. Space-time evolution of the Gaussian wave packet is treated.

11.1 Introduction

Particle dynamics confined to networks and discrete structures is of importance in many topics of nanoscale physics. Such systems can be effectively described by one dimensional Schrodinger equation with the boundary conditions given on graphs [1–3], i.e. quantum graphs.

Graphs are the systems consisting of bonds which are connected at the vertices. The bonds are connected according to a rule which is called topology of a graph. Topology of a graph is given in terms of adjacency matrix [1, 2]:

$$C_{ij} = C_{ji} = \begin{cases} 1 & \text{if } i \text{ and } j \text{ are connected} \\ 0 & \text{otherwise} \end{cases} \qquad i, j = 1, 2, \ldots, V.$$

V. Eshniyozov (✉)
Department of Physics, National University of Uzbekistan, Tashkent 100174, Uzbekistan
e-mail: valijonbek@mail.ru

J. Yusupov • I. Ibragimov
Department of Energy, Turin Polytechnic University in Tashkent, Tashkent, Uzbekistan
e-mail: j.yusupov@polito.uz

D. Matrasulov
Department of Energy, Laboratory for Advanced Studies, Turin Polytechnic University in Tashkent, Tashkent, Uzbekistan

R. Egger et al. (eds.), *Low-Dimensional Functional Materials*, NATO Science for Peace and Security Series B: Physics and Biophysics, DOI 10.1007/978-94-007-6618-1_11,

Earlier, quantum graphs were extensively studied in the context of quantum chaos theory [1–3]. Strict mathematical formulation of the boundary conditions was given by Kostrykin and Schrader [4]. Inverse problems on quantum graphs have been studied in Refs. [5–7]. An experimental realization of quantum graphs on (optical) microwave waveguide networks is discussed in the Ref. [8].

Despite that fact that different issues of quantum graphs and their applications have been discussed in the literature, the problem of driven graphs has not yet been treated. In this paper we study particle dynamics in periodically driven graphs by considering, as a perturbation, delta-kicking potential. Quantum dynamics of delta-kicked systems was extensive topic in the context of quantum chaos and related issues [9–13]. Remarkable feature of kicked quantum system is so-called quantum localization which implies suppression of diffusive growth of the average kinetic energy as a function of time [10]. For classical kicked systems energy grows linearly as a function of time [9, 10]. Such phenomenon can be considered as an analog of Anderson localization [10]. We consider delta-kicked particle dynamics in most simplest graph topology, so-called star graph. In particular, we study wave-packet evolution in such system and time-dependence of the average kinetic energy.

11.2 Schrodinger Equation on Graphs

Quantum particle dynamics on a graph is described by one-dimensional multi-component equation Schrödinger equation [1, 2] (in the units $\hbar = 2m = 1$):

$$-i\frac{d^2\Psi_b(x)}{dx^2} = k^2\Psi_b(x), \quad b = (i, j), \tag{11.1}$$

where b denotes a bond connecting ith and jth vertices, and for each bond b, the component Ψ_b of the total wave function Ψ_b is a solution of Eq. (11.1). In Eq. (11.1) components are related through the boundary conditions, providing continuity and current conservation [1]:

$$\begin{cases} \bullet \text{ Continuity,} \\ \Psi_{i,j}|_{x=0} = \varphi_i, \;\; \Psi_{i,j}|_{x=L_{i,j}} = \varphi_j \;\text{ for all }\; i < j \;\text{ and }\; C_{i,j} \neq 0 \\ \bullet \text{ Current conservation,} \\ \sum_{j<i} C_{i,j}\left(iA_{j,i} - \frac{d}{dx}\right)\Psi_{j,i}(x)\Big|_{x=L_{i,j}} \\ + \sum_{j>i} C_{i,j}\left(iA_{i,j} - \frac{d}{dx}\right)\Psi_{i,j}(x)\Big|_{x=0} = \lambda_i\varphi_i. \end{cases} \tag{11.2}$$

Here the parameters λ_i are free parameters which determine the type of boundary conditions. In particular, the special case of zero λ_i corresponds to Neumann boundary conditions. Dirichlet boundary conditions correspond to the case when all the $\lambda_i = \infty$. Solution of Eq. (11.1) obeying the above boundary conditions can be written as

$$\Psi_{i,j} = \frac{C_{i,j}}{\sin kL_{i,j}}(\varphi_i \sin k(L_{i,j} - x) + \varphi_j \sin kx),$$

where the quantities φ_i are the solutions of the following algebraic system following from continuity conditions:

$$\sum_{j \neq i} \frac{kC_{i,j}}{\sin kL_{i,j}}(-\varphi_i \cos kL_{i,j} + \varphi_j) = \lambda_i \varphi_i.$$

The eigenvalues of Eq. (11.1) can be found from the spectral equation

$$\det(h_{i,j}(k)) = 0$$

where

$$h_{i,j}(k) = \begin{cases} -\sum\limits_{m \neq i} C_{i,m} \cot kL_{i,m} - \frac{\lambda_i}{k}, & i = j \\ C_{i,j} \sin^{-1} kL_{i,j}, & i \neq j \end{cases}$$

In special case of star graph the boundary conditions can be written as [14]

$$\begin{cases} \phi_1|_{y=0} = \phi_2|_{y=0} = \ldots = \phi_N|_{y=0}, \\ \phi_1|_{y=l_1} = \phi_2|_{y=l_2} = \ldots = \phi_N|_{y=l_N} = 0, \\ \sum\limits_{j=1}^{N} \frac{\partial}{\partial y}\phi_j|_{y=0} = 0. \end{cases} \tag{11.3}$$

The eigenvalues of star graph can be found from the following spectral equation [14]

$$\sum_{j=1}^{N} \tan^{-1}(k_n l_j) = 0.$$

Corresponding eigenfunctions are given as [14]

$$\phi_j^{(n)} = \frac{B_n}{sin(k_n l_j)} sin(k_n(l_j - y))$$

where

$$B_n = \sqrt{\frac{2}{\sum_j \frac{l_j + sin(2k_n l_j)}{sin^2(k_n l_j)}}}.$$

11.3 Kicked Star Graph

Consider quantum particle on primary star graph in the presence of an external time-periodic potential. Such system is described by the following time-dependent Schrodinger equation:

$$i\frac{\partial\Psi(x,t)}{\partial t} = [-\frac{d^2}{dx^2} - \varepsilon\cos x\delta_T(t)]\Psi(x,t),\ b = 1,\ldots,N. \tag{11.4}$$

where

$$\delta_T(t) = \sum_{l=-\infty}^{\infty}\delta(t-lT)$$

with T being the kicking period.

Equation (11.4) can be analytically integrated over a single kicking period. To do this we note that the solution of Eq. (11.4) can be expanded in terms of complete set of solutions of Eq. (11.1) as

$$\Psi(x,t) = \sum_{j,n} A_n(t)\phi_{j,n}(x) \tag{11.5}$$

Integrating Eq. (11.4) over the single period, T using the same prescription as in the case of kicked rotor [9, 10] for time evolution of $A_n(t)$ during one kicking period we have

$$B_m(t+T) = \sum_m A_m(t)V_{mn}e^{-iE_mT}, \tag{11.6}$$

where E_n is the eigenvalues of unperturbed star graph.

$$V_{mn} = \sum_j^N \int_0^{l_j} \phi^*_{j,m}(x)e^{i\varepsilon\cos x}\phi_{j,n}(x)dx,$$

Using Eq. (11.6) we can compute wave function for arbitrary number of kicks and average kinetic energy as

$$< E(t) >= -\frac{1}{2}\sum_j^N \int \Psi^*_j(x,t)\frac{d^2\Psi_j(x,t)}{dx^2}dx = -\frac{1}{2}\sum_j^N |A_n(t)|^2E_n. \tag{11.7}$$

In Fig. 11.1 $< E(t) >$ is plotted as a function of time for the values of the kicking strength.

As is seen from these plots, the average energy is a periodic function of time with the period much longer than that of kicking period. This behavior is completely different than that in the case of kicked rotor [10] and kicked one dimensional box [12]. Such a periodicity may be caused by more complicated structure of the graph which implies different (than those for kicked rotor or box) boundary conditions in the Schrodinger equation.

Furthermore, we consider wave packet evolution in kicked star graph by taking the wave function at $t = 0$ (for the first bond) as the following Gaussian wave packet:

$$\Psi_1(x,0) = \Phi(x) = \frac{1}{\sqrt{2\pi\sigma}}e^{-\frac{(x-\mu)^2}{2\sigma}}, \tag{11.8}$$

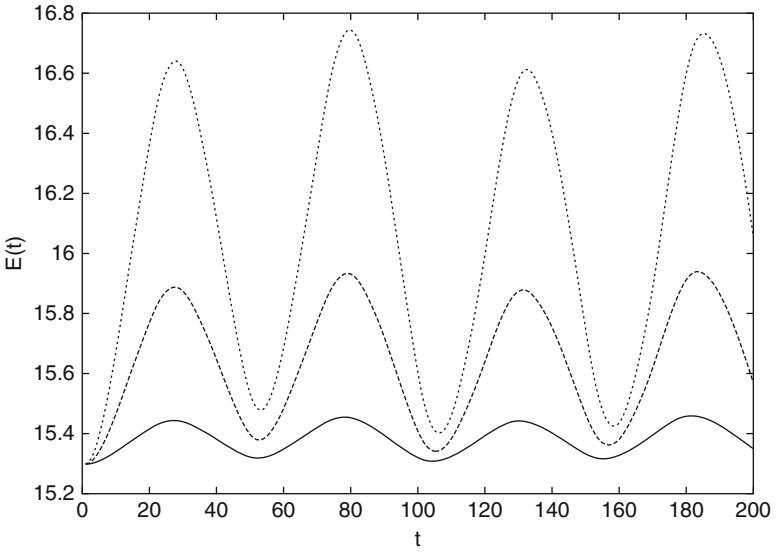

Fig. 11.1 Average kinetic energy as a function of time for the values of the kicking strength: $\varepsilon = 0.3$ (*dotted*), $\varepsilon = 0.2$ (*dashed*) and $\varepsilon = 0.1$ (*solid*) at the kicking period, $T = 0.001$

with σ being the width of the packet. For other bonds initial wave function is assumed to be zero, i.e. $\Psi_2(x,0) = \Psi_3(x,0) = 0$. Then for the initial values of the functions $\varphi^{(j)}(y,t)$ in Eq. (11.5) we have

$$\varphi_j(y,0) = L(0)e^{-i\frac{L(0)\dot{L}(0)}{4}y^2}\Phi(y).$$

Correspondingly, the expansion coefficients at $t = 0$ can be written as

$$C_n(0) = \sum_j \int_0^{l_j} \varphi_j(y,0)\phi_j^{(n)*}(y).$$

Figure 11.2 presents the time evolution of the Gaussian wave packet on kicked star graph for kicking parameters $\varepsilon = 0.1$ and $T = 0.01$ at time moments $t = 100T$, $300T$ and $500T$. As shows these plots, complete dispersion of the wave packet is not possible even for high number of kicks due to the confined nature of the system. Also, wave packet revival can be observed in such system.

In this work we have studied quantum dynamics of a delta kicked particle in a star graph by considering time-dependence of the average kinetic energy and wave packet evolution. Obtained preliminary results show that unlike the case of delta-kicked rotor, average kinetic energy of a kicked particle in star graph is a periodic function of time. Absence of complete dispersion of the wave packet in such system is also shown. Forthcoming studies should be focused on the existence of resonances and wave packet revivals in the above system.

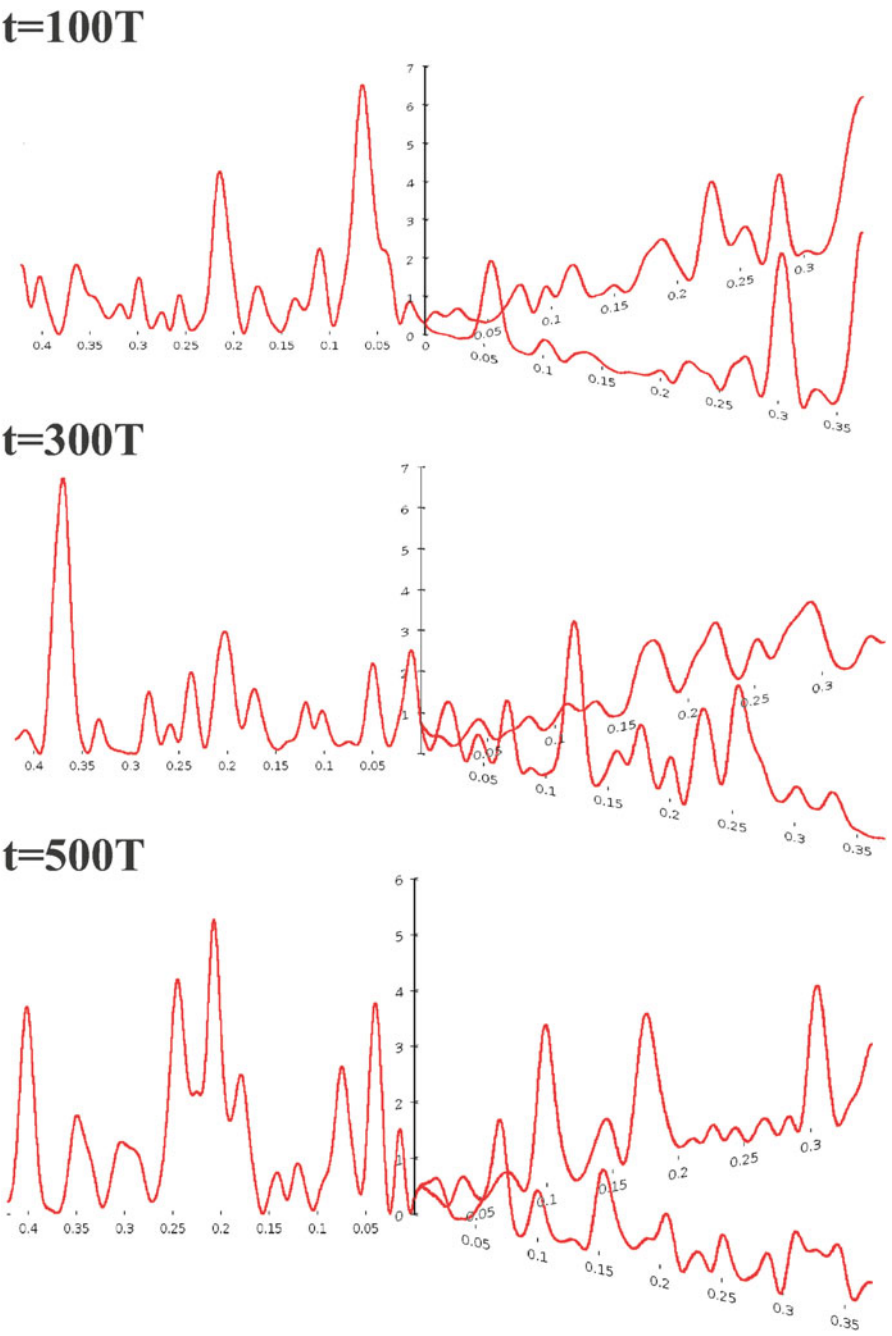

Fig. 11.2 Time evolution of the Gaussian wave packet in kicked quantum star graph for kicking parameters $\varepsilon = 0.1$, $T = 0.001$

References

1. Kottos T, Smilansky U (1999) Ann Phys 76:274
2. Gnutzmann S, Smilansky U (2006) Adv Phys 55:527
3. Gnutzmann S, Keating JP, Piotet F (2010) Ann Phys 325:2595
4. Kostrykin R, Schrader R (1999) J Phys A 32:595
5. Gutkin B, Smilansky U (2001) J Phys A 31:6061
6. Boman J, Kurasov P (2005) Adv Appl Math 35:58
7. Cheon T, Exner P, Turek O (2010) Ann Phys 325:548
8. Hul O et al (2004) Phys Rev E 69:056205
9. Casati et al (1979) Lecture notes in physics, vol 93. Springer, Berlin, p 334
10. Izrailev GM (1990) Phys Rep 196:299
11. Buchleitner A, Delande D, Zakrzewski J (2002) Phys Rep 368:409
12. Sankaranarayanan R, Sheorey VB (2005) Phys Lett A 338:288
13. Haug F et al (2005) Phys Rev 71:043803
14. Keating JP (2006) Contemp Math 415:191

Chapter 12
Breathing Star Graph

Davron Matrasulov, Jambul Yusupov, Karimjon Sabirov, and Zarif Sabirov

Abstract In this paper we study quantum star graphs with time-dependent bond lengths. Quantum dynamics is treated by solving Schrodinger equation with time-dependent boundary conditions given on graphs. Time-dependence of the average kinetic energy is analyzed. Space-time evolution of the Gaussian wave packet is treated for harmonically breathing star graph.

Quantum graphs are convenient models for describing particle dynamics a graph driven by time-dependent forces.

As the physical systems quantum graphs were considered by Kottos and Smilansky as a toy model for quantum chaos [1].

Initially, the idea for studying of a system confined to a graph dates back to the Ref. [2] where using the graphs for modeling free electron motion in organic molecules was suggested. By now quantum graphs found numerous applications in modeling different discrete structures and networks in nanoscale physics (e.g., see reviews [1, 3, 4] and references therein). Strict formulation of the boundary conditions for the Schrodinger equation on graphs can be found in the Ref. [5].

An important problem which is still is remaining as less-studied is the particle dynamics driven graphs. A kind of such system is the case when driven force is caused by time-dependent boundary conditions, i.e. time-dependent bond length. In this work we treat the problem of particle dynamics in a star graph with

D. Matrasulov
Department of Energy, Laboratory for Advanced Studies, Turin Polytechnic University in Tashkent, Tashkent, Uzbekistan

J. Yusupov (✉) • Z. Sabirov
Department of Energy, Turin Polytechnic University in Tashkent, Tashkent, Uzbekistan
e-mail: j.yusupov@polito.uz

K. Sabirov
Department of Physics, National University of Uzbekistan, Tashkent, Uzbekistan
e-mail: karimjon_80@mail.ru

R. Egger et al. (eds.), *Low-Dimensional Functional Materials*, NATO Science for Peace and Security Series B: Physics and Biophysics, DOI 10.1007/978-94-007-6618-1_12,

time-dependent length of the bonds assuming that only one edge of the each bond of moving. Such system may arise in different nanoscale and discrete structures, where the boundaries of confinement are not static. Also, particle dynamics in time-dependent graphs is of importance from the viewpoint of quantum Fermi acceleration in networks and discrete quantum systems.

Treatment of such system requires solving the Schrödinger equation with time-dependent boundary conditions. Detailed study of such problem for time-dependent box can be found in series of papers by Makowski and co-authors [6–8] and in more recent paper by Glasser et al. [9].

Graphs are the systems consisting of bonds which are connected at the vertices. The bonds are connected according to a rule which is called topology of a graph. Topology of a graph is given in terms of adjacency matrix [1, 3]:

$$C_{ij} = C_{ji} = \begin{cases} 1 & \text{if } i \text{ and } j \text{ are connected} \\ 0 & \text{otherwise} \end{cases} \qquad i, j = 1, 2, \ldots, V.$$

Quantum dynamics of a particle on a graph is described by one-dimensional Schrödinger equation [1, 3] (in the units $\hbar = 2m = 1$):

$$-i\frac{d^2\Psi_b(x)}{dx^2} = k^2\Psi_b(x), \quad b = (i, j), \tag{12.1}$$

where b denotes a bond connecting ith and jth vertices, and for each bond b, the component Ψ_b of the total wavefunction Ψ_b is a solution of the Eq. (12.1).

In particular, for quantum start graph the boundary conditions can be written as [10]:

$$\begin{cases} \phi_1|_{y=0} = \phi_2|_{y=0} = \ldots = \phi_N|_{y=0}, \\ \phi_1|_{y=l_1} = \phi_2|_{y=l_2} = \ldots = \phi_N|_{y=l_N} = 0, \\ \sum\limits_{j=1}^{N} \frac{\partial}{\partial y}\phi_j|_{y=0} = 0. \end{cases} \tag{12.2}$$

The eigenvalues can be found by solving the following equation [10]

$$\sum_{j=1}^{N} \tan^{-1}(k_n l_j) = 0$$

where corresponding eigenfunctions are given as [10]

$$\phi_j^{(n)} = \frac{B_n}{sin(k_n l_j)} sin(k_n(l_j - y))$$

$$B_n = \sqrt{\frac{2}{\sum_j \frac{l_j + sin(2k_n l_j)}{sin^2(k_n l_j)}}}.$$

For time-dependent graph the bonds are time-varying, i.e., L_j is a function of time. In this case particle dynamics in graph is described by the following time-dependent Schrödinger equation:

$$i\frac{\partial}{\partial t}\Psi_j(x,t) = -\frac{\partial^2}{\partial x^2}\Psi_j(x,t),\ \ 0 < x < L_j(t),\ j = 1,\ldots,N, \tag{12.3}$$

with N being the number of bonds.

Furthermore, we will consider the boundary conditions given by

$$\begin{cases} \Psi_1|_{x=0} = \Psi_2|_{x=0} = \ldots = \Psi_N|_{x=0}, \\ \Psi_1|_{x=L_1(t)} = \Psi_2|_{x=L_2(t)} = \ldots = \Psi_N|_{x=L_N(t)} = 0, \\ \sum\limits_{j=1}^{N} \frac{\partial}{\partial x}\Psi_j|_{x=+0} = 0. \end{cases}$$

These boundary conditions imply that only those edges which are not connected are moving while center (branching point) is fixed. We assume that $L_j(t)$ is given as $L_j(t) = l_j L(t)$, where $L(t)$ is a continuous function and l_j are the positive constants. Then using the coordinate transformation

$$y = \frac{x}{L(t)},$$

Eq. (12.3) can be rewritten as

$$i\frac{\partial}{\partial t}\Psi_j(y,t) = -\frac{1}{L^2}\frac{\partial^2}{\partial y^2}\Psi_j(y,t) + i\frac{\dot{L}}{L}y\frac{\partial}{\partial y}\Psi_j(y,t),\ \ 0 < y < l_j,\ j = 1,\ldots,N. \tag{12.4}$$

It is clear that the Schrödinger operator in the right hand side of Eq. (12.4) is not Hermitian due to the presence of second term. Therefore using the transformation

$$\Psi_j(y,t) = \frac{1}{\sqrt{L}}e^{i\frac{L\dot{L}}{4}y^2}\varphi_j(y,t),$$

we can make it Hermitian as

$$i\frac{\partial}{\partial t}\varphi_j(y,t) = -\frac{1}{L^2}\frac{\partial^2}{\partial y^2}\varphi_j(y,t) + \frac{L\ddot{L}}{4}y^2\varphi_j(y,t),\ \ 0 < y < l_j,\ j = 1,\ldots,N. \tag{12.5}$$

We note that the above transformations of the wave function remain the boundary conditions unchanged.

In this paper we consider harmonically breathing graph, i.e. the case when time-dependence of $L(t)$ is given as

$$L(t) = b + a\cos\omega t$$

with $\omega = \frac{2\pi}{T}$ being oscillation frequency and T is the oscillation period. It is clear that in this case time and coordinate variables in Eq. (12.5) cannot be separated. Expanding $\varphi(y,t)$ in Eq. (12.5) in terms of the complete set of static graphs wave functions as

$$\varphi_j(y,t) = \sum_n C_n(t)\phi_j^{(n)}(y), \tag{12.6}$$

and inserting this expansion into Eq. (12.5) we have

$$\dot{C}_m(t) = \sum_n M_{mn}C_n(t)$$

where

$$M_{mn} = -i\frac{k_m^2}{L^2(t)} - i\frac{L\ddot{L}}{4}\sum_j \int_0^{l_j} y^2 \phi_j^{(n)}\phi_j^{(m)} dy$$

The quantity we are interested to compute is the average kinetic energy which is defined as

$$E(t) = \langle\psi|H|\psi\rangle = \sum_{j=1}^{N} \int_0^{L_j(t)} \left|\frac{\partial\psi_j(x,t)}{\partial x}\right|^2 dx. \tag{12.7}$$

In Fig. 12.1 the time dependence of the average kinetic energy of the harmonically breathing star graph is presented for different values of the breathing frequency and amplitude. As it can be seen from these plots, $< E(t) >$ is almost periodic for $\omega = 0.5$ and $a = 1$, while for $\omega = 10$ and $a = 1$ such a periodicity is completely broken and energy grows in time. For $\omega = 10$ and $a = 20$ the behavior of $< E(t) >$ demonstrates "quasiperiodic behavior". Appearing of periodic behavior in $< E(t) >$ can be explained by synchronization of the motion of particle with the frequency. The lack of such synchronization causes breaking of the periodicity of the average energy in time.

Furthermore, we consider wave packet evolution in harmonically breathing star graph by taking the wave function at $t = 0$ (for the first bond) as the following Gaussian wave packet:

$$\Psi_1(x,0) = \Phi(x) = \frac{1}{\sqrt{2\pi\sigma}} e^{-\frac{(x-\mu)^2}{2\sigma}}, \tag{12.8}$$

with σ being the width of the packet. For other bonds initial wave function is assumed to be zero, i.e. $\Psi_2(x,0) = \Psi_3(x,0) = 0$. Then for the initial values of the functions $\varphi^{(j)}(y,t)$ in Eq. (12.6) we have

$$\varphi_j(y,0) = L(0)e^{-i\frac{L(0)\dot{L}(0)}{4}y^2}\Phi(y).$$

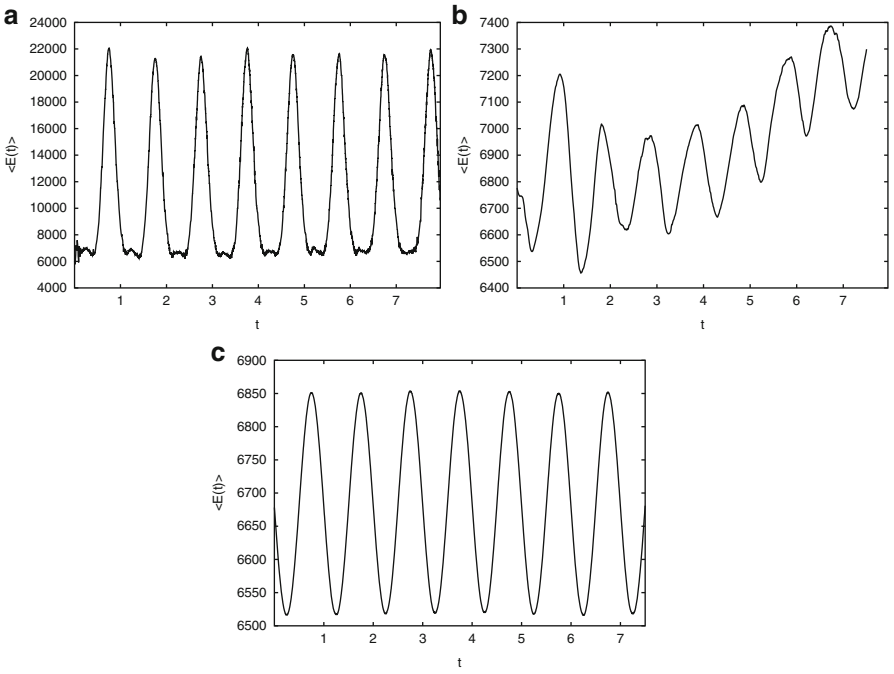

Fig. 12.1 Time-dependence of the average kinetic energy for harmonically oscillating primary star graph. Time is presented in the units of oscillation period $T = \frac{2\pi}{\omega}$. (**a**) $\omega = 10$ and $a = 20$; (**b**) $\omega = 10$ and $a = 1$; (**c**) $\omega = 0.5$ and $a = 1$

Correspondingly, the expansion coefficients at $t = 0$ can be written as

$$C_n(0) = \sum_j \int_0^{l_j} \varphi_j(y,0)\phi_j^{(n)*}(y).$$

In calculation of the wave packet evolution we choose the initial condition as the Gaussian wave packet being on the first bond only, while for other two bonds the wave functions at $t = 0$ are taken as zero. In Fig. 12.2 the time evolution of the wave packet is plotted for harmonically breathing primary star graph whose bonds oscillate according to the law $L(t) = 40 + a\cos\omega t$. The oscillation parameters (frequency and amplitude) are chosen as follows: (a) $\omega = 10,\ a = 20$; (b) $\omega = 10,\ a = 1$; (c) $\omega = 0.5,\ a = 1$. Figure 12.2a presents wave packet evolution in static(time-independent) star graph. At $t = 0$ a Gaussian packet of the width σ and velocity v_0 is assumed being in the first bond. As it can be seen from these plots, for higher frequencies dispersion of the packet and its transition to other bonds occur more faster compared to that for smaller frequencies. Again, an important role plays here possible synchronization between the bond edge and wave packets motions. Existence or absence of such synchronization defines how the collision of the packet

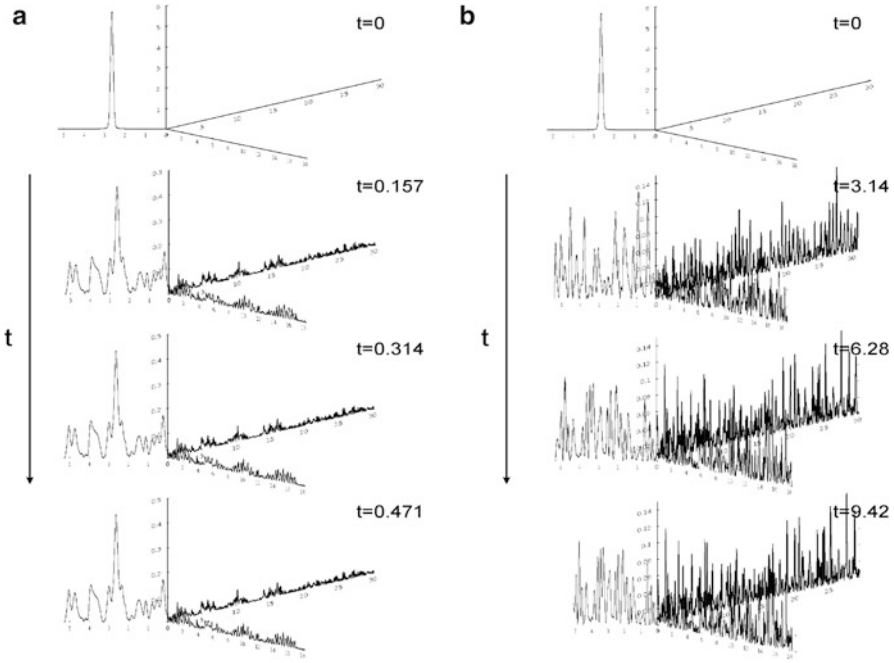

Fig. 12.2 Time evolution of the Gaussian wave packet given by Eq. (12.8) for the parameters: (**a**) Wave packet evolution in static star graph; (**b**) $\omega = 0.5,\ a = 1$

with the bond edges will occur and how extensively it gains or loses its energy. Therefore more detailed treatment of the wave packet dynamics in harmonically breathing graphs should be based on the analysis of the role of synchronization and its criterions.

Thus we have treated time-dependent quantum star graph by considering harmonically breathing bonds. Time-dependence of the average kinetic energy and space-time evolution of the Gaussian wave packet are studied by solving the Schrodinger equation with time-dependent boundary conditions. It is found that for certain frequencies energy is a periodic function of time, while for others it can be non-monotonically growing function of time. Such a feature can be caused by possible synchronization of of the particles motion and the motions of the moving edges of graph bonds. Similar feature can be seen also from the analysis of the wave packet evolution. The above study can be useful for the treatment of particle transport in different discrete structures, such as molecular and quantum wire networks, networks of carbon nanotubes, crystal lattices, and others nanoscale systems that can be modeled by quantum graphs.

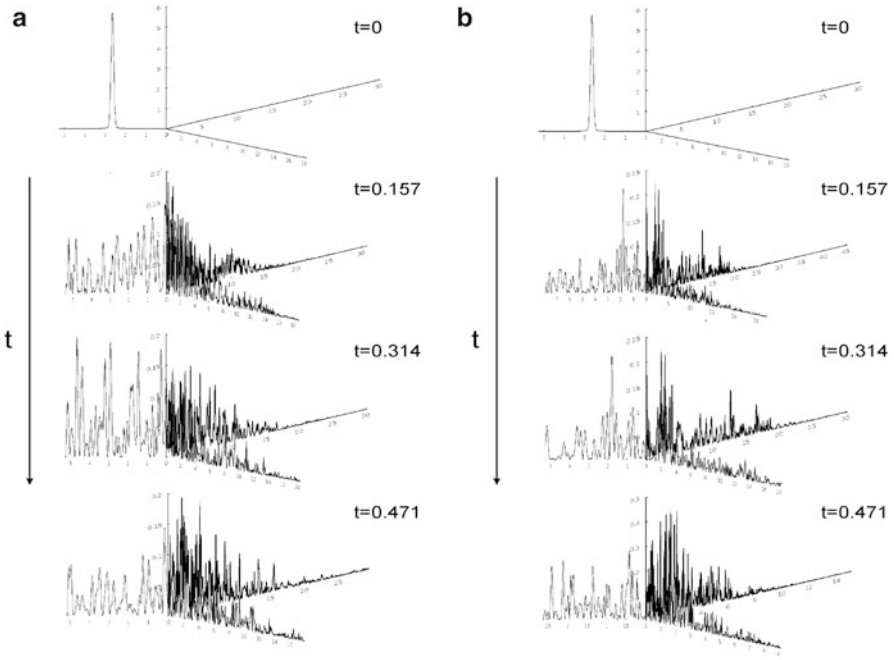

Fig. 12.3 Time evolution of the Gaussian wave packet given by Eq. (12.8) for the parameters: (**a**) $\omega = 10,\ a = 20$; (**b**) $\omega = 10,\ a = 1$

References

1. Kottos T, Smilansky U (1999) Ann Phys 76:274
2. Pauling L (1936) J Chem Phys 4:673
3. Gnutzmann S, Smilansky U (2006) Adv Phys 55:527
4. Gnutzmann S, Keating JP, Piotet F (2010) Ann Phys 325:2595
5. Kostrykin R, Schrader R (1999) J Phys A 32:595
6. Makowski AJ, Dembinski ST (1991) Phys Lett A 154:217
7. Makowski AJ, Peplowski P (1992) Phys Lett A 163:142
8. Makowski AJ (1992) J Phys A 25:3419
9. Glasser ML, Mateo J, Negro J, Nieto LM (2009) Chaos Solitons Fractals 41:2067
10. Keating JP (2006) Contemp Math 415:191

Chapter 13
Time-Independent Nonlinear Schrödinger Equation on Simplest Networks

Karimjon Sabirov, Zarif Sabirov, Donyor Babajanov, and Davron Matrasulov

Abstract We treat the time-independent (cubic) nonlinear Schrödinger equation (NLSE) on simplest networks. In particular, the solutions are obtained for star and tree graphs with the boundary conditions providing vertex matching and flux conservation. It is shown that the method can be extended to the case of arbitrary number of bonds in star graphs and for other simplest topologies.

13.1 Introduction

The nonlinear evolution equations were the topic of extensive research during the last half century. Special attention among others has attracted nonlinear Schrodinger equation whose detailed treatment started in the pioneering studies by Zakharov and Shabat in early seventies of the last century [1–3]. Such an interest is mainly caused by the possibility for obtaining soliton solution of NLSE and its various practical applications in different branches of physics. Initially, the applications of NLSE and other nonlinear evolution equations having soliton solutions were mainly focussed in optics, acoustics, particle physics, hydrodynamics and biophysics. However, special attention NLSE and its soliton solutions have attracted because of the recent

K. Sabirov (✉)
Department of Physics, National University of Uzbekistan, Tashkent, Uzbekistan
e-mail: karimjon_80@mail.ru

Z. Sabirov • D. Babajanov
Department of Energy, Turin Polytechnic University in Tashkent, Tashkent, Uzbekistan

D. Matrasulov
Department of Energy, Laboratory for Advanced Studies, Turin Polytechnic University in Tashkent, Tashkent, Uzbekistan

R. Egger et al. (eds.), *Low-Dimensional Functional Materials*, NATO Science for Peace and Security Series B: Physics and Biophysics, DOI 10.1007/978-94-007-6618-1_13,

progress made in the physics and Bose-Einstein condensates (BEC). Namely, due to the fact that the dynamics of BEC is governed by Gross-Pitaevski equation which is NLSE with cubic nonlinearity, finding the soliton solution of NLSE with different confining potentials and boundary conditions is of importance for this area of physics.

During the last few decades NLSE and its soliton solutions have been treated in the context of fiber optics, photonic crystals, acoustics BEC and other topics (see books [4–8] and references therein). Both, stationary and time-dependent NLSE were extensively studied for different trapping potentials in the context of BEC. In particular, the stationary NLSE was studied for box boundary conditions [9, 10] and the square well potential [11–14].

In this work we explore the time-independent NLSE on networks by modeling the latter by graphs. Graphs are the systems consisting of bonds which are connected at the vertices [15]. The bonds are connected according to a rule that is called topology of a graph. Topology of a graph is given in terms of so-called adjacency matrix which can be written as [16, 17]:

$$C_{ij} = C_{ji} = \begin{cases} 1 & \text{if } i \text{ and } j \text{ are connected,} \\ 0 & \text{otherwise,} \end{cases} \qquad i, j = 1, 2, \ldots, V.$$

Earlier, the linear Schrödinger equation on graphs was treated in different contexts (e.g., see reviews [16–18] and references therein). In this case the eigenvalue problem is given in terms of the boundary conditions providing continuity and current conservation [16–22].

Despite the progress made in the study of the linear Schrödinger equation on graphs, corresponding nonlinear problem, i.e., NLSE on graphs is still remaining as less-studied topic. This is mainly caused by difficulties that appear in the case of NLSE on graphs, especially, for the time-dependent problem. In particular, the problem becomes rather nontrivial and it is not so easy to derive conservation laws [28]. However, during the last couple of years there were some attempts to treat time-dependent [28, 29] and the stationary [30, 32] NLSE on graphs. Soliton solutions and connection formulae are derived for simple graphs in the Ref. [28]. The problem of fast solitons on star graphs is treated in the Ref. [29]. In particular, the estimates for the transmission and reflection coefficients are obtained in the limit of very high velocities. The problem of soliton transmission and reflection is studied in [30] by solving numerically the stationary NLSE on graphs.

In [31] dispersion relations for linear and nonlinear Schrödinger equations on networks are discussed. More recent treatment of the stationary NLSE in the context of scattering from nonlinear networks can be found in the Ref. [32]. In particular, the authors discuss transmission through a complex network of nonlinear one-dimensional leads and found the existence of the high number of sharp resonances dominating in the scattering process. The stationary NLSE with power focusing nonlinearity on star graphs was studied in very recent paper [33], where existence of the nonlinear stationary states are shown for $\delta-$type boundary conditions. In particular, the authors of [33] considered a star graph with N semi-infinite bonds,

for which they obtain the exact solutions for the boundary conditions with $\alpha \neq 0$. The properties of the ground state wave function are also studied by considering separately the cases of odd and even N. In this work we treat NLSE on simplest graphs with finite-length bonds, aiming at obtaining its exact solutions for some types of the boundary conditions.

An important applications of NLSE on networks is Bose-Einstein condensation (BEC) and transport of BEC in networks. This issue has been extensively discussed recently in the literature [24–27]. We note that networks can be used as the traps for BEC experiments.

It is important to notice that earlier the problem of soliton transport in discrete structures and networks was mainly studied within the discrete NLSE [23]. However, such an approach doesn't provide comprehensive treatment of the problem and one needs to use continuous NLSE on graphs. The aim of this work is the formulation and solution of stationary NLSE on simplest graphs such as star, tree and loop which can be considered as exactly solvable topologies.

13.2 Time-Independent NLSE on Primary Star Graph

The problem we want to treat is the stationary (time-independent) NLSE with cubic nonlinearity on the primary star graph. The star graph is a three or more bonds connected to one vertex (branching point). The primary star graph consisting of three bonds, b_1, b_2, b_3, is plotted in Fig. 13.1. The coordinate, x_1 on the bond b_1 varies from 0 to L_1, while for the bonds $b_k, k = 2,3$ the coordinates, x_k, vary from L_1 to L_k. At the branching point we have $x_k = L_1$. In the following we will use the notation x instead of x_k, $(k = 1,2,3)$. Then the time-independent NLSE can be written for each bond as

$$-\psi_j'' \pm \beta_j |\psi_j|^2 \psi_j = \lambda^2 \psi_j,\ \beta_j > 0,\ j = 1,2,3. \tag{13.1}$$

Eq. (13.1) is a multi-component equation in which components are mixed through the boundary conditions and conservation laws. More detail analysis of the boundary conditions on graphs can be found in the Refs. [19, 22].

In this paper we will consider the following boundary conditions:

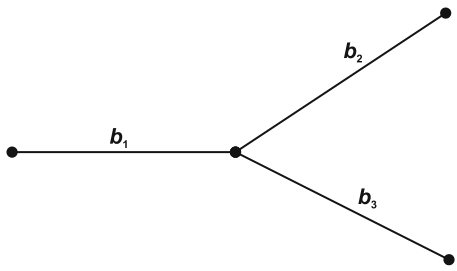

Fig. 13.1 Primary star graph consisting of three bonds

$$\psi_1(L_1) = A_2\psi_2(L_1) = A_3\psi_3(L_1),$$
$$\left[\frac{\partial}{\partial x}\psi_1(x) - \frac{1}{A_2^*}\frac{\partial}{\partial x}\psi_2(x) - \frac{1}{A_3^*}\frac{\partial}{\partial x}\psi_3(x)\right]|_{x=L_1} = \alpha\psi_1(L_1),\ \ A_2A_3 \neq 0.$$

The first boundary condition is matching condition and becomes continuity in special case $A_2 = A_3 = 1$, while second condition in this special case coincides with current conservation (α is assumed to be real) considered, for example, in the Refs. [16, 17]. We note that the eigenvalues of the linear Schrodinger equation on graphs can be found by solving a linear algebraic system following from the boundary conditions [16]. However, as we will see in the next section, for the stationary NLSE on graphs the boundary conditions lead to a system of transcendental equations and one should show the existence of its roots.

Consider the following time-independent NLSE with repulsive nonlinearity

$$-\psi_j'' + \beta_j|\psi_j|^2\psi_j = \lambda^2\psi_j,\ \beta_j > 0,\ j = 1,2,3. \tag{13.2}$$

given on the primary star graph presented in Fig. 13.1. The boundary conditions are given as (λ is real; $A_2 = \sqrt{\beta_2/\beta_1}$, $A_3 = \sqrt{\beta_3/\beta_1}$, $\alpha = 0$):

$$\psi_1(x)|_{x=0} = 0,\ \psi_2(x)|_{x=L_2} = \psi_3(x)|_{x=L_3} = 0, \tag{13.3}$$

$$\sqrt{\beta_1}\psi_1(L_1) = \sqrt{\beta_2}\psi_2(L_1) = \sqrt{\beta_3}\psi_3(L_1), \tag{13.4}$$

$$\left[\frac{1}{\sqrt{\beta_1}}\frac{\partial}{\partial x}\psi_1(x) - \frac{1}{\sqrt{\beta_2}}\frac{\partial}{\partial x}\psi_2(x) - \frac{1}{\sqrt{\beta_3}}\frac{\partial}{\partial x}\psi_3(x)\right]|_{x=L_1} = 0, \tag{13.5}$$

and the wave function is normalized as follows:

$$\sum_{j=1}^{3}\int_{b_j}|\psi_j(x)|^2dx = 1. \tag{13.6}$$

Dirichlet type boundary conditions are chosen in Eq. (13.3) due to their simplicity and their direct relevance to physical systems. It is easy to realize such conditions in physical systems than other ones.

The solution of Eq. (13.2) can be written as

$$\psi_j(x) = f_j(x)e^{i\gamma_j},\ j = 1,2,3, \tag{13.7}$$

where $\gamma_j = const$, $f_j(x)$ is a real function obeying the equation

$$-f_j'' + \beta_j f_j^3 = \lambda^2 f_j. \tag{13.8}$$

The following relations can be obtained from the boundary conditions given by Eq. (13.4)

$$e^{i\gamma_1}\sqrt{\beta_1}f_1(L_1) = e^{i\gamma_2}\sqrt{\beta_2}f_2(L_1) = e^{i\gamma_3}\sqrt{\beta_3}f_3(L_1),$$

which lead to

$$\gamma_1 = \gamma_2 = \gamma_3 = \gamma,$$
$$\sqrt{\beta_1} f_1(L_1) = \sqrt{\beta_2} f_2(L_1) = \sqrt{\beta_3} f_3(L_1).$$

It is clear that the functions f_1, f_2, f_3 should obey Eqs. (13.3), (13.4), (13.5), and (13.6).

Exact solutions of Eq. (13.8) for finite interval and periodic boundary conditions can be found in the Refs. [9, 10]. Here we consider this problem for the graph boundary conditions given by Eq. (13.3). Solution of Eq. (13.8) satisfying these boundary conditions can be written as

$$\begin{aligned} f_1(x) &= B_1 sn(\alpha_1 x|k_1), \\ f_2(x) &= B_2 sn(\alpha_2 (x - L_2)|k_2), \\ f_3(x) &= B_3 sn(\alpha_3 (x - L_3)|k_3), \end{aligned}$$

where $sn(ax|k)$ are the Jacobian elliptic functions [34].

Inserting the last equation into Eq. (13.8) and comparing the coefficients of similar terms we have

$$B_j = \sigma_j \sqrt{\frac{2}{\beta_j}} \alpha_j k_j, \quad \lambda^2 = \alpha_j^2 \left(1 + k_j^2\right), \; j = 1, 2, 3, \tag{13.9}$$

where $\sigma_j = \pm 1 \; j = 1, 2, 3$.

Using Eqs. (13.4), (13.5), and (13.6) and the relations [34]

$$\int_a^b sn^2(\alpha(x-c)|k)\, dx = \frac{1}{k^2} \int_a^b \left[1 - dn^2(\alpha(x-c)|k)\right] dx$$

$$= \frac{1}{k^2}(b-a) - \frac{1}{\alpha k^2} E\left[am(\alpha(b-c))|k\right] + \frac{1}{\alpha k^2} E\left[am(\alpha(a-c))|k\right],$$

we obtain the system of transcendental equations with respect to α_j and k_j $(j = 1, 2, 3)$, which gives us the spectrum of the eigenvalues stationary NLSE on primary star graph:

$$\begin{aligned} \sqrt{\beta_1} B_1 sn(\alpha_1 L_1|k_1) = \\ = \sqrt{\beta_2} B_2 sn(\alpha_2 (L_1 - L_2)|k_2) \\ = \sqrt{\beta_3} B_3 sn(\alpha_3 (L_1 - L_3)|k_3), \end{aligned} \tag{13.10}$$

$$\begin{aligned} &\frac{B_1 \alpha_1}{\sqrt{\beta_1}} cn(\alpha_1 L_1|k_1)\, dn(\alpha_1 L_1|k_1) - \frac{B_2 \alpha_2}{\sqrt{\beta_2}} cn(\alpha_2 (L_1 - L_2)|k_2)\, dn(\alpha_2 (L_1 - L_2)|k_2) \\ &- \frac{B_3 \alpha_3}{\sqrt{\beta_3}} cn(\alpha_3 (L_1 - L_3)|k_3)\, dn(\alpha_3 (L_1 - L_3)|k_3) = 0, \end{aligned} \tag{13.11}$$

$$\frac{B_1^2}{k_1^2}L_1 + \frac{B_2^2}{k_2^2}(L_2 - L_1) + \frac{B_3^2}{k_3^2}(L_3 - L_1) =$$

$$= 1 + \frac{B_1^2}{k_1^2\alpha_1}E\left[am(\alpha_1 L_1|k_1)|k_1\right] + \frac{B_2^2}{k_2^2\alpha_2}E\left[am(\alpha_2(L_2 - L_1)|k_2)|k_2\right] +$$

$$+ \frac{B_3^2}{k_3^2\alpha_3}E\left[am(\alpha_3(L_3 - L_1)|k_3)|k_3\right]. \tag{13.12}$$

Here $E(\varphi|k)$ and $am(u|k)$ are the incomplete elliptic integral of the second kind and the Jacobi amplitude, respectively.

In general case this system can be solved using the different (e.g., Newton's or Krylov's method) iteration schemes. However, below we will show solvability of this system for two special cases.

Let

$$\frac{4n_1 + 1}{L_1} = \frac{4n_2 + 1}{L_2 - L_1} = \frac{4n_3 + 1}{L_3 - L_1},$$

where $n_1, n_2, n_3 \in \mathbf{N} \cup \{0\}$.

Choosing

$$\alpha_1 = \frac{4n_1 + 1}{L_1}K(k_1),\ \alpha_2 = \frac{4n_2 + 1}{L_2 - L_1}K(k_2),\ \alpha_3 = \frac{4n_3 + 1}{L_3 - L_1}K(k_3),$$

we have

$$\alpha_1 = \alpha_2 = \alpha_3 = \alpha,\ k_1 = k_2 = k_3 = k,\ \sigma_1 = 1,\ \sigma_2 = \sigma_3 = -1.$$

Here $K(k)$ is the complete elliptic integral of the first kind.

It is clear that Eqs. (13.10) and (13.11) are valid under these conditions. Using Eq. (13.12) and the relations

$$am(u + 2K(k)|k) = \pi + am(u|k),$$

$$E(n\pi \pm \varphi|k) = 2nE(k) \pm E(\varphi|k),$$

we have

$$g(k) \equiv 2\frac{(4n_1 + 1)^2}{L_1^2}\left(\frac{L_1}{\beta_1} + \frac{L_2 - L_1}{\beta_2} + \frac{L_3 - L_1}{\beta_3}\right)K(k)\left(K(k) - E(k)\right) - 1 = 0. \tag{13.13}$$

Solvability of Eq. (13.13) is equivalent to that of NLSE on primary star graph. Therefore we will prove solvability of this equation. Indeed, it follows from the relations

$$\lim_{k\to 0} g(k) = -1,\ \lim_{k\to 1} g(k) = +\infty,$$

and from the fact that $g(k)$ is a continuous function of k on the interval $(0;1)$, that Eq. (13.13) has a root.

Now we consider another special case given by the relations

$$\alpha_1 = \frac{(-1)^{n_1} p + 2n_1 K(k_1)}{L_1},\ \alpha_2 = \frac{(-1)^{n_2} p + 2n_2 K(k_2)}{L_2 - L_1},\ \alpha_3 = \frac{(-1)^{n_3} p + 2n_3 K(k_3)}{L_3 - L_1},$$

where $-K(k_j) \le p \le K(k_j)$, $n_j \in \mathbf{N}$, $j = 1,2,3$ and n_1, n_2, n_3 cannot be odd or even at the same time and show existence of the solution of the system given by Eqs. (13.10), (13.11), and (13.12). From Eqs. (13.9) and (13.10) we obtain

$$\alpha_1 = \alpha_2 = \alpha_3 = \alpha,\ k_1 = k_2 = k_3 = k,\ \sigma_1 = 1,\ \sigma_2 = \sigma_3 = -1.$$

From Eq. (13.11) we have

$$\frac{(-1)^{n_1}}{\beta_1} + \frac{(-1)^{n_2}}{\beta_2} + \frac{(-1)^{n_3}}{\beta_3} = 0.$$

Furthermore, it follows from the last equation and Eq. (13.12) that

$$g(k) \equiv 4\left(\frac{(-1)^{n_1} p + 2n_1 K(k_1)}{L_1}\right)\left(\frac{n_1}{\beta_1} + \frac{n_2}{\beta_2} + \frac{n_3}{\beta_3}\right)(K(k) - E(k)) - 1 = 0. \tag{13.14}$$

Therefore we have

$$\lim_{k\to 0} g(k) = -1,\ \lim_{k\to 1} g(k) = +\infty.$$

Since $g(k)$ is a continuous function of k on the interval $(0;1)$, it follows from the last relations that Eq. (13.14) has a root. Unlike the first special case, the second case describes primary star graph, with connected bonds.

13.3 Other Simplest Graphs

To extend the above approach to the case of other topologies, we consider a simplest topology, tree graph plotted in Fig. 13.2. Such an extension can be done using the same approach as that in the Ref. [28].

We seek the solution of Eq. (13.8) on the each bonds in the form

$$f_b = B_b sn\left(\alpha_b x + \delta_b \,|k_b\right),$$

where δ_b are parameters that can be determined by the given boundary conditions: $\delta_1 = 0,\ \delta_{1ij} = -\alpha_{1ij} L_{1ij}$.

Let us assume that the following relations are valid:

$$\frac{4n_1 + 1}{L_1} = \frac{4(n_{1i}^{(2)} - n_{1i}^{(1)})}{L_{1i} - L_1} = \frac{4n_{1ij} + 1}{L_{1ij} - L_{1i}},\ i = 1,2,\ j = 1,2,3$$

Fig. 13.2 Tree graph

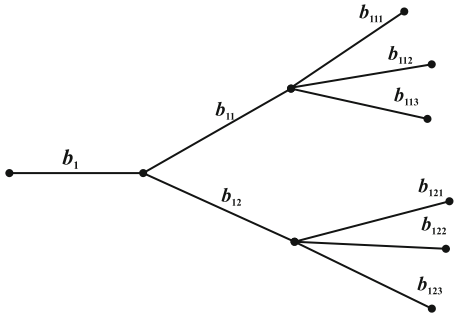

where $n_1, n_{1i}, n_{1ij} \in \mathbf{N} \cup \{0\}, n_{1i}^{(2)} > n_{1i}^{(1)}$ and

$$\alpha_1 = \frac{4n_1+1}{L_1}K(k_1), \quad \alpha_{1i} = \frac{4(n_{1i}^{(2)} - n_{1i}^{(1)})}{L_{1i} - L_1}K(k_{1i}),$$

$$\alpha_{1ij} = \frac{4n_{1ij}+1}{L_{1ij} - L_{1i}}K(k_{1ij}), \quad \delta_{1i} = \left(\frac{4(n_{1i}^{(1)}L_{1i} - n_{1i}^{(2)}L_1)}{L_{1i} - L_1} + 1\right)K(k_{1i}).$$

Then it is easy to show that these relations lead to equations

$$\alpha_1 = \alpha_{1i} = \alpha_{1ij} = \alpha,\ k_1 = k_{1i} = k_{1ij} = k,\ \sigma_1 = \sigma_{1i} = 1,\ \sigma_{1ij} = -1.$$

Therefore we have

$$g(k) \equiv 2\frac{(4n_1+1)^2}{L_1^2}\left\{\frac{L_1}{\beta_1} + \sum_{i=1}^{2}\left[\frac{L_{1i} - L_1}{\beta_{1i}} + \sum_{j=1}^{3}\frac{L_{1ij} - L_{1i}}{\beta_{1ij}}\right]\right\}K(k) \times (K(k) - E(k)) - 1 = 0. \tag{13.15}$$

Solvability of the last equation is obvious.

Consider also the case given by the relations

$$\alpha_1 = \frac{-(-1)^{n_1}p_1 + 2n_1K(k_1)}{L_1},$$

$$\alpha_{1i} = \frac{(-1)^{n_{1i}^{(2)}}p_{1i} - (-1)^{n_{1i}^{(1)}}p_1 + 2(n_{1i}^{(2)} - n_{1i}^{(1)})K(k_{1i})}{L_{1i} - L_1},$$

$$\alpha_{1ij} = \frac{-(-1)^{n_{1ij}}p_{1i} + 2n_{1ij}K(k_{1ij})}{L_{1ij} - L_{1i}},$$

$$\delta_{1i} = \frac{(-1)^{n_{1i}^{(1)}}p_1L_{1i} - (-1)^{n_{1i}^{(2)}}p_{1i}L_1 + 2(n_{1i}^{(1)}L_{1i} - n_{1i}^{(2)}L_1)K(k_{1i})}{L_{1i} - L_1}.$$

where $-K(k_{1,1i}) < p_1 < K(k_{1,1i}),\ -K(k_{1i,1ij}) < p_{1i} < K(k_{1i,1ij})$.

One can obtain from the vertex conditions

$$\alpha_1 = \alpha_{1i} = \alpha_{1ij} = \alpha,\ k_1 = k_{1i} = k_{1ij} = k$$

and

$$\frac{(-1)^{n_1}}{\beta_1} - \sum_{i=1}^{2} \frac{(-1)^{n_{1i}^{(1)}}}{\beta_{1i}} = 0,\ \frac{(-1)^{n_{1i}^{(2)}}}{\beta_1} + \sum_{j=1}^{3} \frac{(-1)^{n_{1ij}}}{\beta_{1ij}} = 0.$$

It follows from the normalization condition that

$$g(k) \equiv\ 4\left(\frac{(-1)^{n_1} p + 2n_1 K(k)}{L_1}\right) \cdot \cdot \left(\frac{n_1}{\beta_1} + \sum_{i=1}^{2}\left[\frac{n_{1i}^{(2)} - n_{1i}^{(1)}}{\beta_{1i}} + \sum_{j=1}^{3} \frac{n_{1ij}}{\beta_{1ij}}\right]\right)(K(k) - E(k)) - 1 = 0.$$

Solvability of the last equation follows from the properties of the function $g(k)$. The same prescription can be repeated for loop graphs and combinations of loop and star graphs that give us similar treatment for these topologies.

13.4 Conclusions

We have studied time-independent NLSE with cubic nonlinearity for simplest networks and obtained explicit solutions for primary star and tree graphs are obtained by considering matching and flux conservation boundary conditions. Unlike the previous studies [28, 29, 32], the lengths of the bonds are considered as finite. Therefore our work can be considered as an extension of the earlier results by L.D. Carr et al. [9, 10, 12] to the case of networks. The method can be extended to other simplest graph topologies and their combinations.

References

1. Zakharov VE, Shabat AB (1972) Sov Phys JETP 34:62
2. Zakharov VE, Shabat AB (1974) Funct Anal Appl 8:226
3. Zakharov VE, Shabat AB (1979) Funct Anal Appl 13:166
4. Kivshar YS, Agarwal GP (2003) Optical solitons: from fibers to photonic crystals. Academic, San Diego
5. Ablowitz MJ, Clarkson PA (1999) Solitons, nonlinear evolution equations and inverse scattering. Cambridge University Press, Cambridge
6. Pethick CJ, Smith H (2002) Bose-Einstein condensation in dilute gases. Cambridge University Press, Cambridge
7. Pitaesvki L, Stringari S (2003) Bose-Einstein condensation. Oxford University Press, Oxford
8. Dauxois T, Peyrard M (2006) Physics of solitons. Cambridge University Press, Cambridge

9. Carr LD, Clark CW, Reinhardt WP (2000) Phys Rev A 62:063610
10. Carr LD, Clark CW, Reinhardt WP (2000) Phys Rev A 62:063611
11. DAgosta R, Malomed BA, Presilla C (2000) Phys Lett A 275:424
12. Carr LD, Mahmud KW, Reinhardt WP (2001) Phys Rev A 64:033603
13. Rapedius K, Witthaut D, Korsch HJ (2006) Phys Rev A 73:033608
14. Infeld E, Zin P, Gocalek J, Trippenbach M (2006) Phys Rev E 74:026610
15. Harary F (1969) Graph theory. Addison-Wesley, Reading
16. Kottos T, Smilansky U (1999) Ann Phys 76:274
17. Gnutzmann S, Smilansky U (2006) Adv Phys 55:527
18. Gnutzmann S, Keating JP, Piotet F (2010) Ann Phys 325:2595
19. Exner P, Seba P, Stovicek P (1988) J Phys A 21:4009–4019
20. Exner P, Seba P (1989) Rep Math Phys 28:7
21. Kostrykin V, Schrader R (1999) J Phys A 32:595
22. Kuchment P (2004) Wave Random Media 14:S107
23. Burioni R, Cassi D, Sodano P, Trombettoni A, Vezzani A (2006) Chaos 15:043501; Physica D 216:71
24. Leboeuf P, Pavloff N (2001) Phys Rev A 64:033602
25. Bongs K et al (2001) Phys Rev A 63:031602 (R)
26. Paul T, Hartung M, Richter K, Schlagheck P (2007) Phys Rev A 76:063605
27. de Oliveira IN (2010) Phys Rev E 81:030104(R)
28. Sobirov Z, Matrasulov D, Sabirov K, Sawada S, Nakamura K (2010) Phys Rev E 81:066602
29. Adami R, Cacciapuoti C, Finco D, Noja D (2011) Rev Math Phys 23:4
30. Cascaval RC, Hunter CT (2010) Libertas Math 30:85
31. Banica V, Ignat L (2011) J Phys A 52:083703
32. Gnutzmann S, Smilansky U, Derevyanko S (2011) Phys Rev A 83:033831
33. Adami R, Cacciapuoti C, Finco D, Noja D (2012) J Phys A 45:192001
34. Bowman F (1961) Introduction to elliptic functions, with applications. Dover, New York

Chapter 14
$1/(N-1)$ Expansion for an SU(N) Impurity Anderson Model: A New Large-N Scheme Based on a Perturbation Theory in U

Akira Oguri, Rui Sakano, and Tatsuya Fujii

Abstract Low-energy properties of an SU(N) Anderson model are studied, using the $1/(N-1)$ expansion based on a perturbation theory in the Coulomb interaction U. This approach is different from conventional large N theories, such as from the usual $1/N$ expansion and the non-crossing approximation based on the expansion in the hybridization matrix element between the impurity orbital and conduction band. In our approach the scaling factor $N-1$ appears as the total number of interacting orbitals excluding the one prohibited by the Pauli principle, and it captures the low-energy local Fermi-liquid behavior correctly. We find that the next-leading-order results of the renormalized parameters agree closely with the numerical renormalization group results in a wide range of electron fillings at $N=4$, where the degeneracy is still not so large. This ensures the reliability of the next-leading order results for $N>4$. Furthermore, we apply this approach to nonequilibrium current through a quantum dot in the Kondo regime.

14.1 Introduction

The Anderson impurity has been studied extensively as one of the most important model for strongly correlated electrons systems [1]. For instance, in quantum dots the universal Kondo behavior of the steady current [2–7] and shot noise [8–14] at small bias voltages can be described in terms of the quasi-particles of a local Fermi liquid.

A. Oguri (✉)
Department of Physics, Osaka City University, Sumiyoshi-ku, Osaka, Japan
e-mail: oguri@sci.osaka-cu.ac.jp

R. Sakano • T. Fujii
Institute for Solid State Physics, University of Tokyo, Kashiwa, Chiba, Japan

R. Egger et al. (eds.), *Low-Dimensional Functional Materials*, NATO Science for Peace and Security Series B: Physics and Biophysics, DOI 10.1007/978-94-007-6618-1_14,

The Kondo behavior has also been studied for the quantum dots with the orbital degeneracy [15–19], where the essential feature of the universality may be deduced from the low-energy properties of an SU(N) Anderson model. The exact numerical renormalization group (NRG) approach [20] is applicable to this model for small degeneracies $N \leq 4$ [17,21–24], which for $N = 2$ corresponds to the spin degeneracy. Conventional large N theories, such as the $1/N$ expansion and the non-crossing approximation (NCA), were also successfully applied to various situations [25–28]. These approaches are based on the expansion in the hybridization matrix element between the impurity and conduction band, and are applicable mainly to the cases for small electron (or hole) fillings. It is still necessary to develop alternative approaches in order to explore a wide parameter space of the Anderson impurity.

Recently, we proposed a completely different approach, using a scaling that takes $u = (N-1)U$ as an independent variable [29,30]. The factor $N-1$ appears naturally as it represents the number of interacting orbitals, excluding the one prohibited by the Pauli principle. With this scaling the perturbation series in U can be reorganized as an expansion in powers of $1/(N-1)$, using a standard Feynman diagrammatic technique. To leading order in $1/(N-1)$ it describes the Hartree-Fock random phase approximation (HF-RPA), and the higher-order corrections systematically generate the fluctuations beyond the HF-RPA. As the unperturbed Hamiltonian includes the hybridization between the impurity and conduction bands, this approach naturally describes the Fermi-liquid state.

In this report, we discuss the low-energy properties equilibrium, carrying out the calculations to the next-leading order. We also apply the $1/(N-1)$ expansion to nonequilibrium current through a quantum dot in the Kondo regime.

14.2 Model and Formulation

We consider an SU(N) impurity Anderson model with finite interaction U, given by $H = H_d + H_U + H_T + H_c$,

$$H_d = \sum_{m=1}^{N} E_d\, n_{dm}, \qquad E_d = \varepsilon_d + \langle n_{dm}\rangle (N-1)U, \tag{14.1}$$

$$H_U = \sum_{m\neq m'} \frac{U}{2}\left[n_{dm} - \langle n_{dm}\rangle\right]\left[n_{dm'} - \langle n_{dm'}\rangle\right], \tag{14.2}$$

$$H_T = \sum_{\nu=L,R}\sum_{m=1}^{N} v_\nu \left(d_m^\dagger \psi_{\nu m} + \psi_{\nu m}^\dagger d_m\right), \qquad \psi_{\nu m} = \int_{-D}^{D} d\varepsilon \sqrt{\rho}\, c_{\varepsilon\nu m}, \tag{14.3}$$

$$H_c = \sum_{\nu=L,R}\sum_{m=1}^{N} \int_{-D}^{D} d\varepsilon\, \varepsilon\, c_{\varepsilon\nu m}^\dagger c_{\varepsilon\nu m}, \tag{14.4}$$

Here, $d_m^\dagger$ is the creation operator for an electron with energy ε_d and orbital m $(=1,2,\cdots,N)$ in the impurity site, and $n_{dm} = d_m^\dagger d_m$. The operator $c_{\varepsilon\nu m}^\dagger$ creates a conduction electron in lead ν with the normalization $\{c_{\varepsilon\nu m}, c_{\varepsilon'\nu'm'}^\dagger\} = \delta_{\nu\nu'}\delta_{mm'}\delta(\varepsilon-\varepsilon')$. The hybridization energy scale is given by $\Delta \equiv \Gamma_L + \Gamma_R$, with $\Gamma_\nu = \pi\rho\, v_\nu^2$ and $\rho = 1/(2D)$. We consider the parameter region where D is much larger than the other energy scales; $\max(\Delta, |\varepsilon_d|, U) \ll D$.

The imaginary-frequency Green's function for the impurity level is given, for $|\omega| \ll D$, by

$$G(i\omega) = \frac{1}{i\omega - E_d + i\Delta\,\mathrm{sgn}\omega - \Sigma(i\omega)}, \tag{14.5}$$

where $\Sigma(i\omega)$ is the self-energy due to H_U. The ground-state average of the local charge, $\langle n_{dm}\rangle$, can be deduced from the phase shift,

$$\langle n_{dm}\rangle = \frac{\delta}{\pi}, \qquad \delta \equiv \cot^{-1}\left(\frac{E_d^*}{\Delta}\right), \qquad E_d^* \equiv E_d + \Sigma(0)\,. \tag{14.6}$$

The renormalized parameters are defined by

$$\frac{1}{z} \equiv 1 - \left.\frac{\partial\Sigma(i\omega)}{\partial i\omega}\right|_{\omega=0}, \qquad \tilde{\varepsilon}_d \equiv z E_d^*, \qquad \tilde{\Delta} \equiv z\Delta. \tag{14.7}$$

Furthermore, the enhancement factor for spin and charge susceptibilities, $\tilde{\chi}_s \equiv \tilde{\chi}_{mm} - \tilde{\chi}_{mm'}$ and $\tilde{\chi}_c \equiv \tilde{\chi}_{mm} + (N-1)\,\tilde{\chi}_{mm'}$, can be expressed in terms of z and the vertex function $\Gamma_{mm';m'm}(i\omega_1, i\omega_2; i\omega_3, i\omega_4)$ for $m \neq m'$ [31],

$$\tilde{\chi}_{mm} = \frac{1}{z}, \qquad \tilde{\chi}_{mm'} = -\frac{\sin^2\delta}{\pi\Delta}\,\Gamma_{mm';m'm}(0,0;0,0), \tag{14.8}$$

and $\tilde{U} \equiv z^2\Gamma_{mm';m'm}(0,0;0,0)$ for $m \neq m'$ represents the residual interaction between the quasi-particles.

It is essential for $N > 2$ to scale the bare and renormalized interactions by multiplying a factor $N-1$ as [29],

$$g \equiv \frac{(N-1)\,U}{\pi\Delta}\,, \qquad \tilde{g} \equiv \frac{(N-1)\,\tilde{U}}{\pi\tilde{\Delta}}\,. \tag{14.9}$$

For general electron fillings, the change in the local density of states $-\frac{1}{\pi}\,\mathrm{Im}\,G(i0^+) = \sin^2\delta/(\pi\Delta)$ should also be included in the scaling parameters, such that [30]

$$K^* \equiv g\sin^2\delta, \qquad \tilde{K} \equiv \tilde{g}\sin^2\delta. \tag{14.10}$$

With these parameters, the Wilson ratio $R \equiv z\tilde{\chi}_s$ and that for the charge sector can be expressed in the form,

$$R = 1 + \frac{\tilde{K}}{N-1}, \qquad z\tilde{\chi}_c = 1 - \tilde{K}. \tag{14.11}$$

The rescaled coupling $\tilde{K}$ varies in the range $0 \le \tilde{K} \le 1$, and approaches the upper bound $\tilde{K} \to 1$ in the case of $\tilde{\chi}_c \to 0$ where the charge fluctuation is suppressed.

The renormalized impurity level E_d^* determines the charge distribution near the impurity, and should be treated carefully. We reorganize the perturbation expansion such that E_d^* enters the unperturbed Green's function $G_0(i\omega)$,

$$G_0(i\omega) = \frac{1}{i\omega - E_d^* + i\Delta\,\mathrm{sgn}\,\omega}, \qquad \{G(i\omega)\}^{-1} = \{G_0(i\omega)\}^{-1} - \overline{\Sigma}(i\omega). \tag{14.12}$$

Correspondingly, the unperturbed part of Hamiltonian H_0 and the perturbation part $\overline{H}_U$ are chosen to be

$$H_0 = H_d + H_c + H_T + \sum_{m=1}^{N} \Sigma(0)\, n_{dm}, \qquad \overline{H}_U = H_U - \sum_{m=1}^{N} \lambda\, n_{dm}, \tag{14.13}$$

where $\lambda = \Sigma(0)$ is the counter term. The redefined self-energy $\overline{\Sigma}(i\omega)$ represents the corrections due to $\overline{H}_U$, and is generally a function of E_d^* and λ. These two parameters are determined by the renormalization condition

$$\overline{\Sigma}(0) = 0, \tag{14.14}$$

and Eq. (14.1) which can be expressed in the following form, using the Friedel sum rule

$$\frac{\xi_d}{\Delta} = \frac{E_d^* - \lambda}{\Delta} + g\tan^{-1}\left(\frac{E_d^*}{\Delta}\right), \qquad \text{where} \quad \xi_d \equiv \varepsilon_d + \frac{(N-1)U}{2}. \tag{14.15}$$

Specifically, at half-filling $\xi_d = 0$, the two parameters vanish $E_d^* = 0$ and $\lambda = 0$.

14.3 $1/(N-1)$ Expansion

The perturbation expansion with respect to $\overline{H}_U$ can be classified according to the power of $1/(N-1)$, by choosing the scaled interaction g as an independent variable instead of bare U. The counter term can also be expanded such that

$$\lambda = \sum_{k=0}^{\infty} \frac{\lambda_k}{(N-1)^k} , \tag{14.16}$$

and the coefficient λ_k is determined by the requirement of the renormalization condition Eq. (14.14) is satisfied to each order in the $1/(N-1)$ expansion.

14.3.1 Zeroth Order

At zero order with respect to $1/(N-1)$, the limit of $N \to \infty$ is taken at fixed g. Then, the counter term is zero $\lambda = 0$, and thus E_d^* which is determined by Eq. (14.15) takes the HF value,

$$\frac{\xi_d}{\Delta} = \frac{E_{d:\mathrm{HF}}^*}{\Delta} + g \tan^{-1}\left(\frac{E_{d:\mathrm{HF}}^*}{\Delta}\right) . \tag{14.17}$$

Note that the contribution of the tadpole diagrams and that of $-U\sum_{m\neq m'}\langle n_{dm'}\rangle n_{dm}$, which is the bilinear part of H_U defined in Eq. (14.2), cancel each other.

14.3.2 Leading Order

The leading order corrections in the $1/(N-1)$ expansion arise form a series of the bubble diagrams of the RPA type indicated in Fig. 14.1 because each fermion loop gives a factor of order $(N-1)$ through a sum over the orbital index m. The contribution of the double wavy line is given by

$$\mathscr{U}_{\mathrm{bub}}(i\omega) = U + U\sum_{k=1}^{\infty} A_k \left[-U\,\chi_0(i\omega)\right]^k , \tag{14.18}$$

Here, the coefficient arises from the summations over the orbital indices for a series of k fermion loops,

$$A_k = \frac{(N-1)^{k+1} - (-1)^{k+1}}{N} = (N-1)^k \sum_{p=0}^{k} \left(\frac{-1}{N-1}\right)^p . \tag{14.19}$$

Fig. 14.1 The leading order diagrams in the $1/(N-1)$ expansion. The *wavy* and *solid lines* indicate U and G_0, respectively. Each fermion loop gives a factor of order $(N-1)$ through a sum over the different orbitals

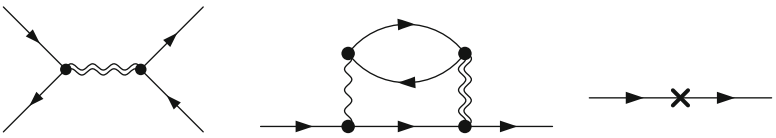

Fig. 14.2 The diagrams which provide the order $1/(N-1)$ contributions. The cross (×) denotes $-\lambda$ of the counter term

The contribution of a single particle-hole bubble is given by

$$\chi_0(i\omega) = -\int_{-\infty}^{\infty} \frac{d\omega'}{2\pi} G_0(i\omega + i\omega') G_0(i\omega') = \frac{1}{\pi} \frac{\Delta}{|\omega|(|\omega|+2\Delta)} \log\left[\frac{(|\omega|+\Delta)^2 + E_d^{*2}}{\Delta^2 + E_d^{*2}}\right]. \tag{14.20}$$

Note that $\pi\Delta\chi_0(0) = 1/[1+(E_d^*/\Delta)^2] = \sin^2\delta$.

The order $1/(N-1)$ term of $\Gamma_{mm';m'm}(0,0;0,0)$ arises from the first diagram in Fig. 14.2, which gives the leading order corrections to $\tilde{K}$,

$$\tilde{K} = \frac{K^*}{1+K^*} + O\left(\frac{1}{N-1}\right). \tag{14.21}$$

From Eqs. (14.11) and (14.21), the Wilson ratio R is determined to order $1/(N-1)$. The order $1/(N-1)$ corrections to the self-energy, $\overline{\Sigma}_1(i\omega)$, arise from the other diagrams in Fig. 14.2, as

$$\overline{\Sigma}_1(i\omega), = \Sigma_1(i\omega) - \lambda \ + O\left(\frac{1}{(N-1)^2}\right), \tag{14.22}$$

$$\Sigma_1(i\omega) = \frac{(g\pi\Delta)^2}{N-1} \int \frac{d\omega'}{2\pi} \frac{\chi_0(i\omega') G_0(i\omega - i\omega')}{1+g\pi\Delta\chi_0(i\omega')}. \tag{14.23}$$

From this self-energy correction, the renormalization factor z can be calculated to order $1/(N-1)$.

14.3.3 Next Leading Order

Fluctuations and correlation effects beyond the RPA appear first through the next-leading-order terms in the $1/(N-1)$ expansion. In this section we discuss the calculations of z, R, and other renormalized parameters to order $1/(N-1)^2$.

Figure 14.3 shows the vertex diagrams which give order $1/(N-1)^2$ corrections to the Wilson ratio R, defined in Eq. (14.11). Note that the contributions of the

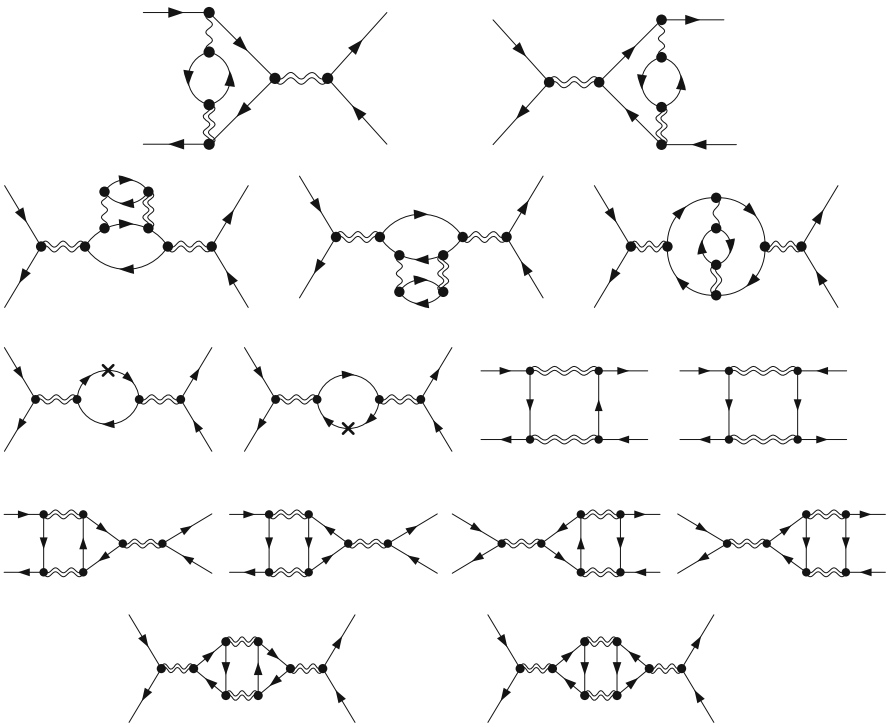

Fig. 14.3 The order $1/(N-1)^2$ diagrams for the vertex correction $\Gamma_{mm';m'm}(0,0;0,0)$ for $m \neq m'$. Specifically, in the particle-hole symmetric case where $\xi_d = 0$, only contributions of the first 5 diagrams remain finite

same order also arise from the first diagram of Fig. 14.2 through the higher-order component of $\mathscr{U}_{\rm bub}(i\omega)$, which can be extracted using Eq. (14.19). These corrections determines $\tilde{K}$ to order $1/(N-1)$. Summing up all the same order contributions, we obtain

$$\tilde{K} = \frac{K^*}{1+K^*} \frac{1+\frac{K^*}{N-1}\left[1+\left(2-\frac{K^*}{1+K^*}\right)\mathscr{I}_S - \frac{1}{1+K^*}\mathscr{I}_A\right]}{1+\frac{K^*}{N-1}\left[\frac{K^*}{1+K^*}+\mathscr{I}_S\right]} + O\left(\frac{1}{(N-1)^2}\right), \tag{14.24}$$

where

$$\mathscr{I}_S = \frac{1}{\chi_0(0)}\int\frac{d\omega}{2\pi}\{G_0(i\omega)\}^2\frac{g\pi\Delta\chi_0(i\omega)}{1+g\pi\Delta\chi_0(i\omega)}, \tag{14.25}$$

$$\mathscr{I}_A = \frac{1}{\chi_0(0)}\int\frac{d\omega}{2\pi}\frac{1}{2}\left[\frac{G_0(i\omega)+G_0(-i\omega)}{1+g\pi\Delta\chi_0(i\omega)}\right]^2. \tag{14.26}$$

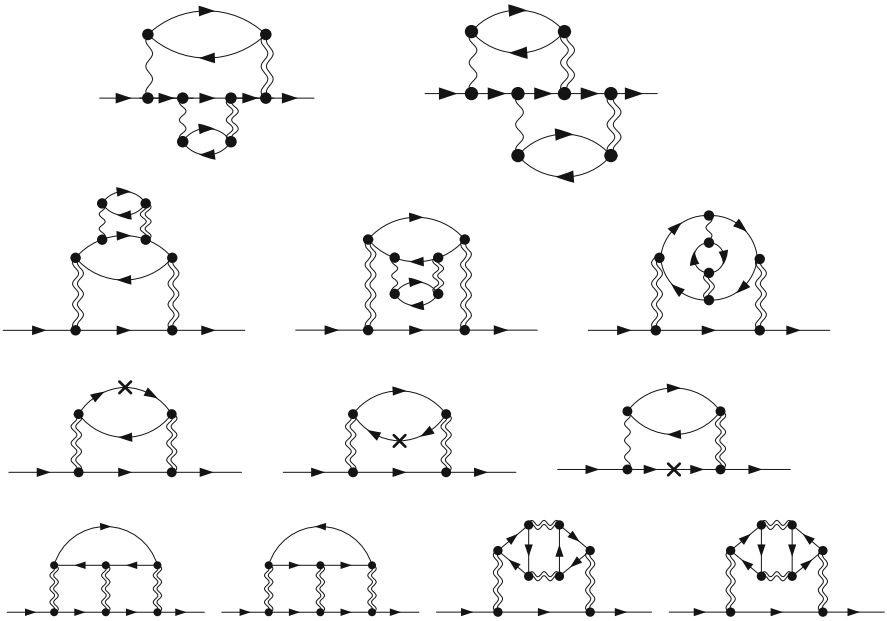

Fig. 14.4 The order $1/(N-1)^2$ diagrams for the self-energy $\overline{\Sigma}(i\omega)$. Specifically, in the particle-hole symmetric case where $\xi_d = 0$, only contributions of the first 5 diagrams remain finite

Note that the prefactor $K^*/(1+K^*)$ in the right-hand side of Eq. (14.24) is required to be calculated to order $1/(N-1)$, by including the energy shift due to Eq. (14.23).

Similarly, the order $1/(N-1)^2$ self-energy corrections to the self-energy $\overline{\Sigma}_2(i\omega)$ arise from the diagrams shown in Fig. 14.4, and also from the second and third diagrams in Fig. 14.2 through the higher-order component of $\mathscr{U}_{\rm bub}(i\omega)$. We have also calculated the order $1/(N-1)^2$ self-energy, and have obtained the renormalization factor z, E_d^*, λ, and the phase shift δ to the next leading order [29, 30].

We have also carried out NRG calculations for $N = 4$, and have compared with the $1/(N-1)$ expansion results which are obtained up to order $1/(N-1)^2$ for both the particle-hole symmetric case of $\xi_d = 0$ and the asymmetric case of $\xi_d \neq 0$.

14.4 Results at Half-Filling

We discuss the results obtained in the particle-hole symmetric case $\xi_d = 0$ in this section. In this case the phase shift is locked at the value of $\delta = \pi/2$, and thus the renormalized couplings $\tilde{K}$ and $\tilde{g}$ become the same.

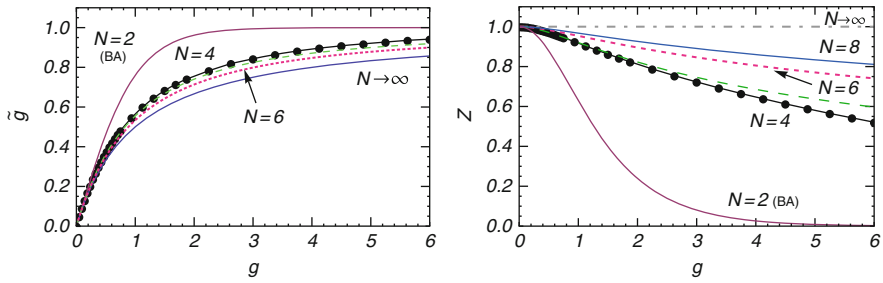

Fig. 14.5 Renormalized parameters $\tilde{g}$ and z in the particle-hole symmetric case $\varepsilon_d = -(N-1)U/2$ as functions of the scaled Coulomb interaction g for $N = 2$ (Bethe ansatz [32]), and for $N = 4, 6, 8$ (next-leading order in the $1/(N-1)$ expansion). For $N = 4$, the NRG results are also shown with the solid circle (•). In the $N \to \infty$ limit, $\tilde{g}$ and z approach $\tilde{g} \to g/(1+g)$ and $z \to 1.0$, respectively (color figure online)

14.4.1 Renormalized Parameters

Figure 14.5 shows the results of the renormalized parameters, $\tilde{g}$ and z, as a function of g. We see the very close agreement between the NRG and the next-leading-order results in the $1/(N-1)$ expansion for $N = 4$, especially for the renormalized coupling $\tilde{g}$. The two curves of $\tilde{g}$ for $N = 4$, almost overlap each other over the whole range of g although the next-leading-order results (green dashed line) are slightly smaller than those of the NRG (solid circles). As N increases, $\tilde{g}$ varies rapidly towards the RPA value $\tilde{g} \to g/(1+g)$ that is asymptotically exact in the limit of $N \to \infty$. We also see that the value that $\tilde{g}$ can take is bounded in a very narrow region between the curve for $N = 4$ and that for the $N \to \infty$ limit.

The order $1/(N-1)^2$ results for the renormalization factor z, shown in Fig. 14.5, also agree well with the NRG results for $N = 4$ at $g \lesssim 3.0$, or equivalently in the region where $\tilde{g} \lesssim 0.8$. This indicates that the next-leading-order results also reproduce the Kondo energy scale, $\tilde{\Delta} = z\Delta$, properly from the weak-coupling to intermediate-coupling regions, where $\tilde{g}$ is still not closed to the value 1.0 of the strong coupling limit.

14.4.2 Nonequilibrium Properties

The $1/(N-1)$ expansion can be applied to nonequilibrium transport at finite bias voltage V. To be specific, we consider a steady state, choosing the lead-dot couplings and chemical potentials in the leads to be symmetric: $\Gamma_L = \Gamma_R$ and $\mu_L = -\mu_R$ $(= eV/2)$. In this case, an exact expression can be derived for the retarded Green's function at low energies up to order ω^2, T^2, and $(eV)^2$ in the particle-hole symmetric case [5, 17],

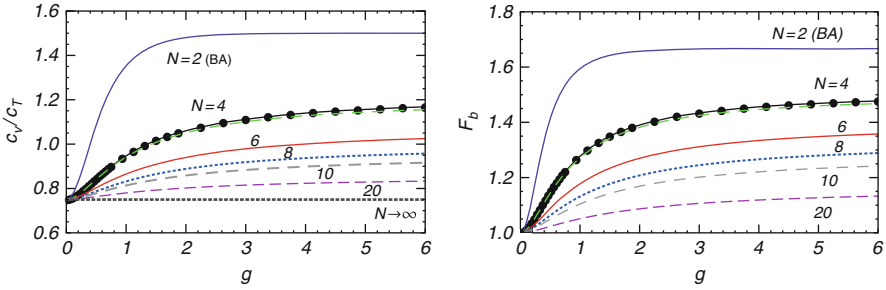

Fig. 14.6 The ratio c_V/c_T and the Fano factor for the current noise F_b in the particle-hole symmetric case $\varepsilon_d = -(N-1)U/2$ as functions of the scaled Coulomb interaction g for $N = 2$ (Bethe ansatz [32]), and for $N = 4, 6, 8, 10, 20, \infty$ (next-leading order in the $1/(N-1)$ expansion). For $N = 4$, the NRG results are also shown with the solid circle (•). In the $N \to \infty$ limit, c_V/c_T and F_b approach $c_V/c_T \to 3/4$ and $F_b \to 1$, respectively (color figure online)

$$G^r(\omega) \simeq \frac{z}{\omega + i\tilde{\Delta} + i\dfrac{\tilde{g}^2}{2(N-1)\tilde{\Delta}}\left[\omega^2 + \dfrac{3}{4}(eV)^2 + (\pi T)^2\right]}. \tag{14.27}$$

The differential conductance for the current through the impurity can be deduced from $G^r(\omega)$, using the formula by Meir-Wingreen [33] and Hershfield [34],

$$\frac{dJ}{dV} = \frac{Ne^2}{h}\left[1 - c_T\left(\frac{\pi T}{\tilde{\Delta}}\right)^2 - c_V\left(\frac{eV}{\tilde{\Delta}}\right)^2 + \cdots\right], \tag{14.28}$$

$$c_T = \frac{1}{3}\left(1 + \frac{2\tilde{g}^2}{N-1}\right), \qquad c_V = \frac{1}{4}\left(1 + \frac{5\tilde{g}^2}{N-1}\right). \tag{14.29}$$

The low-energy behavior is characterized by the two parameters, $\tilde{g}$ in the coefficients and $\tilde{\Delta}$ the energy scale, which depend on N. The left panel of Fig. 14.6 shows the ratio of c_V to c_T as a function of g for several N, using Eq. (14.24) for $N \geq 6$. The ratio takes a value in the range $3/4 \leq c_V/c_T \leq (3/4)(N+4)/(N+1)$. The order $1/(N-1)$ results for $\tilde{g}$ are numerically almost exact for $N > 4$ as mentioned, and thus the results shown in Fig. 14.6 capture orbital effects correctly. Note that in our definition, the experimental value by Grobis et al. [2] should be rescaled by a factor π^2 as $c_V/c_T = 0.99 \pm 0.15$, and that of Scott et al. [3] as $c_V/c_T = 0.50 \pm 0.1$.

As another application of Eq. (14.24), we also consider the shot noise

$$S = \int_{-\infty}^{\infty} dt\, \langle \delta\hat{J}(t)\delta\hat{J}(0) + \delta\hat{J}(0)\delta\hat{J}(t)\rangle, \qquad \delta\hat{J}(t) \equiv \hat{J}(t) - \langle J\rangle, \tag{14.30}$$

where $\delta\hat{J}(t)$ is the current operator. At $T = 0$, S has been calculated to order $(eV)^3$ for the symmetric Anderson model for $N = 2$ [13, 14], and for general N [17],

$$S = \frac{Ne^2}{h}\frac{1}{6}\left(1 + \frac{9\tilde{g}^2}{N-1}\right)\left(\frac{eV}{\tilde{\Delta}}\right)^2 e|V|\,. \tag{14.31}$$

The Fano factor F_b is defined as the ratio of S to the backscattering current $J_b = NeV/h - J$, and has been obtained in the form [17],

$$F_b \equiv \frac{S}{2eJ_b} = \frac{1+\frac{9\tilde{g}^2}{N-1}}{1+\frac{5\tilde{g}^2}{N-1}} . \tag{14.32}$$

The Fano factor takes the value of $F_b = 1$ in the noninteracting case and takes the maximum value $F_b \to (N+8)/(N+4)$ in strong coupling limit $g \to \infty$ where the renormalized coupling converges to $\tilde{g} \to 1$. The right panel of Fig. 14.6 shows the order $1/(N-1)$ results for F_b as functions of the scaled Coulomb interaction for several values of N. We see the close agreement between the NRG and the next-leading-order results for $N = 4$ again. As N increases, $\tilde{g}$ converges rapidly to the value, $\tilde{g} \simeq g/(1+g)$, for the large N limit, as mentioned in the above. Thus, for $N \gtrsim 8$, the N dependence is determined essentially by the factor $1/(N-1)$, seen explicitly in Eq. (14.32). In the limit of $N \to \infty$, the Fano factor approaches the Poisson value $F_b = 1$ as fluctuations due to electron correlations are suppressed and the mean-field theory becomes asymptotically exact.

14.5 Results in the Particle-Hole Asymmetric Case

We have also carried out the NRG calculations for $N = 4$, and have compared with the results of the $1/(N-1)$ expansion. We find generally that the next-leading-order results agree well with the NRG results, especially for small interactions $g \lesssim 3.0$.

In Fig. 14.7, comparisons are made for $\langle n_{dm} \rangle$, $\sin^2\delta$ and $\tilde{\varepsilon}_d$, choosing a rather large value $g = 6.0$ for the interaction. We see the very close agreement between the order $1/(N-1)^2$ results (red sold line) and the NRG results (solid circles) over the whole region of ξ_d. The order $1/(N-1)$ results, corresponding to the HF-RPA, are also plotted in Fig. 14.7 with the green dash-dot line although they are almost concealed under the red solid line. Nevertheless, a small deviation is visible near $\xi_d/(\pi\Delta g) \simeq \pm 0.4$, showing that the order $1/(N-1)^2$ corrections improve the results closer to the exact NRG results. We also see in the figure that the renormalized impurity level $\tilde{\varepsilon}_d$ stays close to the Fermi level near half-filling, where $\xi_d \simeq 0.0$. Note that the zeroth-order results for $\langle n_{dm} \rangle$, $\sin^2\delta$ and $\tilde{\varepsilon}_d$ can also be regarded as exact results in the large N limit. Therefore, as N increases from $N = 4$ to ∞, these quantities vary in a narrow region between the red-solid and blue dashed lines.

The renormalized parameters $\tilde{K}$ and z are plotted for $N = 4$ in the lower two panels of Fig. 14.7. We see that the next-leading-order results (red solid line) significantly improve the leading-order ones (green dash-dot line), and become close to the exact NRG values (solid circles). However, as the chosen value of the interaction $g = 6.0$ is relatively large, the NRG results show an oscillatory behavior. This corresponds to the Coulomb oscillation, which in the atomic limit of $\Delta = 0$ occurs discontinuously at $-\varepsilon_d/U = 0, 1, 2, \ldots, N-1$. Truncation of the

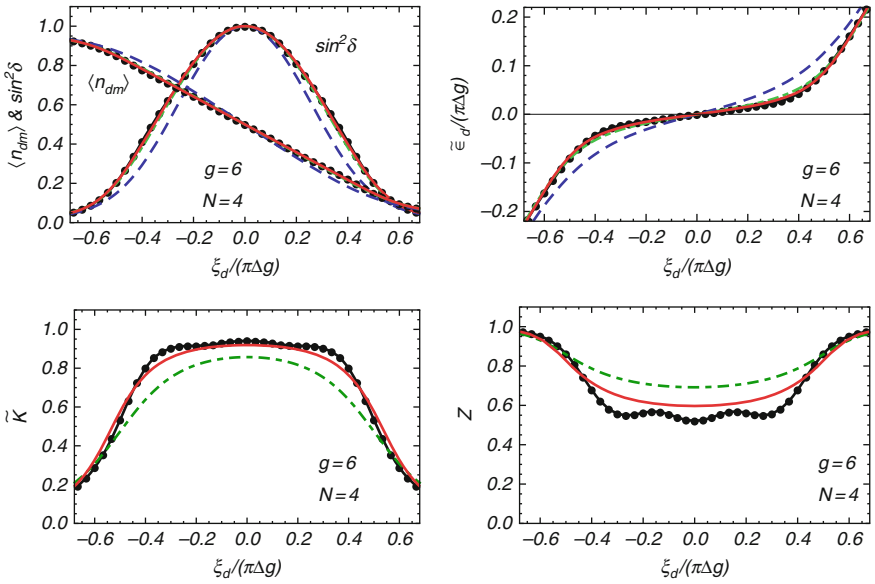

Fig. 14.7 $1/(N-1)$ expansion results of $\langle n_{dm}\rangle = \delta/\pi$, $\sin^2\delta$ and $\tilde{\varepsilon}_d$ (*upper panels*), and $\tilde{K}$ and z (*lower panels*) are plotted vs ξ_d for $N = 4$ choosing $g = 6.0$. The circles (•) represent the NRG results. The *red solid line* represent the next-leading-order results. The leading-order HF-RPA results are plotted with the *green dash-dot line*, which in the upper two panels is almost concealed under the *red solid line*. The *blue dashed line denotes* the zeroth-order HF results (color figure online)

$1/(N-1)$ expansion does not reproduce the oscillatory behavior. Nevertheless, we see in Fig. 14.7 that the next-leading-order results of $\tilde{K}$ approach closely to the exact NRG results. Furthermore, the order $1/(N-1)^2$ results of the renormalization factor z approach closely the maxima, emerging at $\xi_d/(\pi\Delta g) \simeq \pm 0.15$ in a mixed-valence region in between two adjacent integer charge states. Therefore, we expect that the fluctuations beyond the RPA, taken into account to order $1/(N-1)^2$, can describe reasonably an upper envelop of the waving curve for $N \geq 4$.

In Fig. 14.8 the next-leading-order results of $\tilde{K}$ and z for $g = 6.0$ are plotted vs ξ_d for several values of N ($= 4, 6, \ldots, \infty$), together with the NRG results for $N = 2$ (orange dash-dot line) and the exact values in the $N \to \infty$ limit (gray dashed line). As N increases, $\tilde{K}$ converges rapidly to the asymptotic value for the large N limit. We also see that the value that $\tilde{K}$ can take at $N \geq 4$ is bounded in a very narrow region between the curve for $N = 4$ and the one for the $N \to \infty$ limit given by $\tilde{K} \to K^*/(1+K^*)$. The renormalization factor z varies in a wider range $0.6 \lesssim z \leq 1.0$ at $|\xi_d|/(\pi\Delta g) \lesssim 0.3$ as the degeneracy increases from $N = 4$. As N increases, the order $1/(N-1)^2$ corrections dominate the fluctuations beyond the RPA, and capture correctly the correlation effects, especially in the mixed-valence regime.

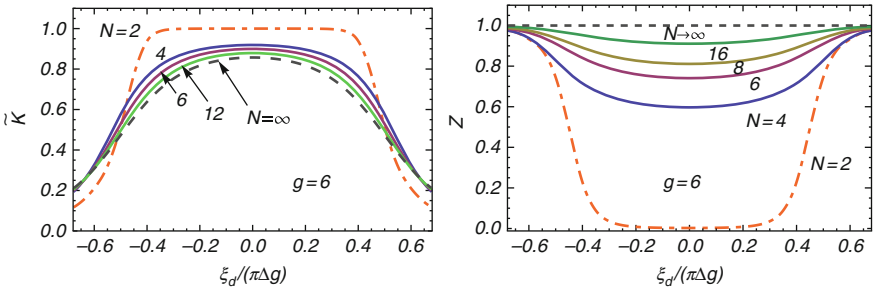

Fig. 14.8 Next leading-order results for $\tilde{K}$ and z plotted vs ξ_d for $g = 6.0$, for several N ($= 4, 6, \ldots, \infty$). The *orange dash-dot line* represents the NRG results for $N = 2$ (color figure online)

14.6 Summary

In summary, we have applied the $1/(N-1)$ expansion to the SU(N) Anderson model both in a wide range of electron fillings, and have described the next-leading-order results in a wide parameter region. We have also discussed the nonequilibrium current and current noise for $N > 4$ at low energies in the particle-hole symmetric case.

Acknowledgements The authors thank T. Kato and A.C. Hewson for discussions. This work is supported by the JSPS Grant-in-Aid for Scientific Research C (No. 23540375, and No. 24540316). Numerical computation was partly carried out at the Yukawa Institute Computer Facility.

References

1. Hewson AC (1993) The Kondo problem to heavy fermions. Cambridge University Press, Cambridge
2. Grobis M, Rau IG, Potok RM, Shtrikman H, Goldhaber-Gordon D (2008) Phys Rev Lett 100:246601
3. Scott GD, Keane ZK, Ciszek JW, Tour JM, Natelson D (2009) Phys Rev B 79:165413
4. Kaminski A, Yu Nazarov V, Glazman LI (2000) Phys Rev B 62:8154
5. Oguri A (2001) Phys Rev B 64:153305
6. Fujii T, Ueda K (2003) Phys Rev B 68:155310
7. Hewson AC, Bauer J, Oguri A (2005) J Phys Condes Matter 17:5413
8. Zarchin O, Zaffalon M, Heiblum M, Mahalu D, Umansky V (2008) Phys Rev B 77:241303
9. Yamauchi Y, Sekiguchi K, Chida K, Arakawa T, Nakamura S, Kobayashi K, Ono T, Teruo, Fujii T, Sakano R (2011) Phys Rev Lett 106:17660
10. Gogolin AO, Komnik A (2006) Phys Rev B 73:195301
11. Gogolin AO, Komnik A (2006) Phys Rev Lett 97:016602
12. Golub A (2006) Phys Rev B 73:233310
13. Sela E, Malecki J (2009) Phys Rev B 80:233103
14. Fujii T (2010) J Phys Soc Jpn 79:044714
15. Delattre T, Feuillet-Palma C, Herrmann LG, Morfin P, Berroir J-M, Fève G, Plaçais B, Glattli DC, Choi M-S, Mora C, Kontos T (2009) Nat Phys 5:208

16. Mora C, Vitushinsky P, Leyronas X, Clerk AA, Le Hur K (2009) Phys Rev B 80:155322
17. Sakano R, Fujii T, Oguri A (2011) Phys Rev B 83:075440
18. Sakano R, Oguri A, Kato T, Tarucha S (2011) Phys Rev B 83:241301
19. Sakano R, Nishikawa Y, Oguri A, Hewson AC, Tarucha S (2012) Phys Rev Lett 108:056402
20. Krishna-murthy HR, Wilkins JW, Wilson KG (1980) Phys Rev B 21:1003
21. Izumida W, Sakai O, Shimizu Y (1998) J Phys Soc Jpn 67:2444
22. Choi M-S, López R, Aguado R (2005) Phys Rev Lett 95:067204
23. Anders FB, Logan DE, Galpin MR, Finkelstein G (2008) Phys Rev Lett 100:086809
24. Nishikawa Y, Crow DJG, Hewson AC (2010) Phys Rev B 82:245109
25. Coleman P (1983) Phys Rev B 28:5255
26. Bickers N (1987) Rev Mod Phys 59:845
27. Haule K, Kirchner S, Kroha J, Wölfle P (2001) Phys Rev B 64:155111
28. Otsuki J, Kuramoto Y (2006) J Phys Soc Jpn 75:064707
29. Oguri A, Sakano R, Fujii T (2011) Phys Rev B 84:113301
30. Oguri A (2012) Phys Rev B 85:155404
31. Yoshimori A (1976) Prog Theor Phys 55:67
32. Zlatić V, Horvatić B (1983) Phys Rev B 28:6904
33. Meir Y, Wingreen NS (1992) Phys Rev Lett 68:2512
34. Hershfield S, Davies JH, Wilkins JW (1992) Phys Rev B 46:7046

Chapter 15
OPV Tandems with CNTS: Why Are Parallel Connections Better Than Series Connections

Kamil Mielczarek, Alexander Cook, Alexander Kuznetsov, and Anvar Zakhidov

Abstract The efficiency of organic photovoltaic cells can be increased in tandem OPV structures with complementary light absorption in top and bottom sub-cells. We demonstrate that strong transparent CNT sheets can be used as an effective charge collector interlayer in OPV and hybrid tandem solar cells. Most importantly we show that CNT sheets can be used in monolithic parallel tandems (P-T) as common a electrode interconnect between top and bottom sub-cells. For achieving good performance one of these subcells in P-T should be of inverted type. We achieved good inversion in OPV, using ZnO nanoparticles, which act as hole barrier layers and invert a typical anode ITO into a cathode. With this inverted bottom cell the efficiency of P-T is significantly improved, as compared to our earlier results. We briefly discuss the modeling analysis of OPV tandems and derive an optimal set of parameters, for highest efficiency P-T. Our simple model shows that for tandems with unbalanced photocurrents but similar open circuit voltages the optimized P-T architecture is always better than conventional series tandem (S-T) geometry. Indeed the experimental comparison of P-T with S-T for hybrids of OPV and dye sensitized solar cells demonstrate the imporved efficiency of the former.

15.1 Introduction

Tandems of nanostructured solar cells can provide additional boost to the solar cells efficiency by absorbing larger portions of the solar spectrum [1, 2]. Particularly promising are tandems of organic PV cells: the highest achieved 8.9 % power

K. Mielczarek • A. Cook • A. Kuznetsov • A. Zakhidov (✉)
Department of Physics and Alan G. MacDiarmid Nanotech Institute,
University of Texas at Dallas 800 West Campbell Road Richardson, Texas 75080
e-mail: Kamil.m@utdallas.edu; abc072000@utdallas.edu; Avgust.kuznetsov@gmail.com; zakhidov@utdallas.edu

R. Egger et al. (eds.), *Low-Dimensional Functional Materials*, NATO Science for Peace and Security Series B: Physics and Biophysics, DOI 10.1007/978-94-007-6618-1_15,

conversion efficiency has been obtained in small molecule OPV with p-i-n structure of each subcell [3]. Monolithic tandems need electrically conductive interconnects, which is not easy to create through usual metals. In this case the conventional series tandem with increased photovoltage V_{OC} has tunneling type interconnecting layer, which is possible in p- and n-doped structures. Since usual OPVs with a bulk heterojunction (BHJ) do not have doped transport layers, the problem of having a transparent interlayer in such BHJ devices is of special importance. We show in this paper, that transparent CNT sheets can serve as very good interlayers. Moreover CNT charge collectors allow to enable a new type of monolithic parallel structure, which is more efficient for OPVs with undoped organic layers. We will discuss below the conditions when parallel tandems are better than series tandems. Moreover hybrid tandems made with sub-cells of different nature: small molecule and polymeric, or inorganic and organic or even dye sensitized photovoltaic cells and OPVs, may have quite different parameters: largely non-balanced photocurrents, distinct voltages and filling factors. Therefore, to maximize a tandems efficiency certain new design requirements become important arising from the electric circuit analysis of each sub-cell should be fulfilled [2, 4, 5]. Using the single-diode model, it has been shown in our first paper of this series, that parallel connections of dis-similar solar cells are more beneficial in hybrid tandems, as compared to conventional series connections, mentioned above. We demonstrate in the present paper several experimental examples of tandems of two polymeric OPVs [1], tandems of small molecule organic and polymeric OPV/PPV [2, 5], and tandems of OPV and DSSC with largely differing parameters and compare with predictions of our model analysis. We prove that indeed the equilibration of the open circuit voltages of the individual cells is important in parallel hybrid tandems, while both short circuit current and fill factor should be matched for in-series tandems. We also prove that parallel connection is preferable when a tandem consists of two solar cells with unbalanced photocurrents [1, 2, 5]. We demonstrate an organic photovoltaic (OPV) cell connected in a parallel electrical tandem configuration utilizing organic materials with complementary absorption spectra and free-standing transparent single wall (SWNT) and multiwall carbon nanotubes (MWNT) as an interlayer common electrode. In first part of the paper we demonstrate an improvement of the previous work [1] by utilizing proper inversion layers, which allow to adjust energy levels and obtain an improved efficiency. The inversion is preformed using both charge selective metal oxide layers (ZnO and MoO_3) and n-type doped organic materials [6, 7]. Each cell was characterized independently and the short circuit current of the tandem device is shown to be larger than that of each sub cell. An overall increase in efficiency is observed and attributed to enhanced spectral coverage due to active layers with complementary absorption spectra and the effective use of transparent SWNTs and MWNTs, prepared by invented in UTD proprietary process of dry self-assembly.

15.2 Organic Photovoltaics: Device Operation and Characterization

In order to understand the device operations of inverted and multijunction OPVs a basic understanding of OPVs is required. The first OPV with any significant power conversion efficiency was the organic equivalent to the successful p-n junction structure of inorganic photovoltaics and was developed by Tang in 1985 [8]. The similarities between Tang's OPV and traditional p-n junction photovoltaics as well as the evolution and improvements of Tang's structure will be briefly described as a segway into the operation and necessity for the inverted OPV structure.

15.2.1 Organic Photovoltaics

Organic photovoltaics are based on organic molecular and polymeric semi-conducting materials which are formed when the molecular structure presents a backbone in which the carbon, nitrogen, oxygen and sulfur atoms are sp^2 hybridized and posses π-atomic orbitals. These orbitals overlap, or are conjugated, along the backbone of the material and result in the formation of delocalized π molecular orbitals. The electronic levels of organic semi-conductors are identified as the highest occupied molecular orbital (HOMO) and lowest unoccupied molecular orbital (LUMO) which are analogous to the valence and conduction bands within inorganic semi-conductors respectively [9]. Unlike inorganic semi-conductors, which have well defined 3-D crystal lattice structures that result in high carrier mobilities (on the order of 10^2–10^3 $cm^2/V{\cdot}s$), organic semi-conductors only have ordering along the molecular backbone through overlapping π orbitals and as a result require a 'hopping' type mechanism to facilitate charge propagation from one molecular unit or polymer chain to another. This hopping mechanism results in charge carrier mobilities which are strongly dependent on the layer morphology; largely amorphous films have mobilities from 10^{-6} to 10^{-3} $cm^2/V{\cdot}s$ while highly ordered films can have mobilities ≥ 1 $cm^2/V{\cdot}s$ [10].

15.2.1.1 Structure and Operation

Organic materials do not have well ordered lattice structures so substitutional doping, as is the case for inorganic p- and n-type materials, is not possible. Rather, materials are selected as electron-donating and electron-accepting based on their HOMO and LUMO levels with respect to one another. An electron-donating material, or Donor, has a high HOMO level, or low ionization potential. While

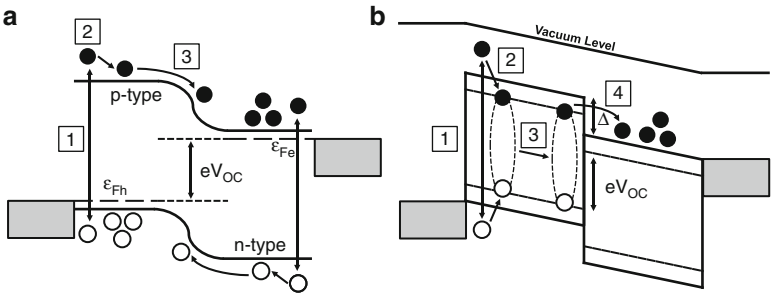

Fig. 15.1 (**a**) Is an energy diagram depicting a p-n junction where a photon with energy larger than the band-gap of the p-type material is absorbed (step A-1) followed by thermalization to the conduction band in step A-2. In step A-3 the electron in the conduction band of the p-type material moves towards the p-n junction through diffusion and is swept to the n-type material under the influence of the internal electric field and collected. (**b**) Shows the organic equivalent of the p-n junction operating at a voltage near the maximum power point, where a photon is absorbed in the donor material (step B-1) and the electron-hole pair quickly relaxes to the excitonic levels (step B-2). In step B-3 the exciton diffuses to the donor-acceptor junction, where if appropriate energy conditions are satisfied the exciton dissociates (step B-4) into free charge carriers

electron-accepting materials, or acceptors, have a low lying LUMO level, or high electron affinity. Donor and Acceptor materials are analogous to p-type and n-type materials respectively for inorganic semi-conductors. In 1985, Tang developed an organic photovoltaic (OPV) device with a power conversion efficiency of 1 % by using a two layer system of copper phthalocyanine (CuPc) donor material and a perylene tetracarboxylic (PTC) derivative as an acceptor which was similar to a p-n junction sandwiched between a transparent electrode of Indium-Tin-Oxide and Silver [8].

The structure shown in Fig. 15.2b corresponds to the structure developed by Tang and draws parallels between p- and n-type materials used within inorganic photovoltaics. Unlike inorganic semi-conductors, which are doped, organic materials are intrinsic semi-conductors. The bilayer device developed by Tang is represented in an energy level diagram (Fig. 15.1a) much the same way a p-n junction can be. In step 1 of Fig. 15.1b a photon with an average energy greater than the optical band gap of either organic layer is absorbed, in this case absorption occurs within the donor material. After absorption, thermalization occurs and the excited electron relaxes to the excitonic level (step 2). The exciton consists of an excited electron bound through Coulomb attraction to the remaining hole within the same organic molecule. The exciton diffuses to the heterojunction between the donor and acceptor materials in step 3. Exciton dissociation into free charge carriers, an electron on the acceptor material and hole on donor material occurs, at step 4. However, the requirements for step 4 to occur are:

- The exciton formed on the donor material must be generated within a certain distance from the donor/acceptor heterojunction. This distance is the exciton

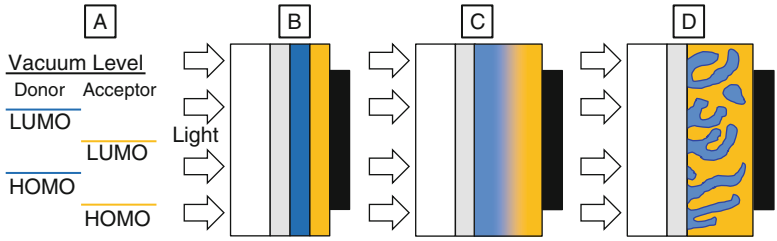

Fig. 15.2 (**a**) Shows the energetic relation of the donor's HOMO-LUMO levels with respect to the Acceptor in order for efficient charge separation. Unlike inorganic semiconductors, p-type and n-type materials are determined with respect to each other not on dopants. (**b**–**d**) Show the cross sectional evolution of organic photovoltaic devices. (**b**) Is representative of Tang's bilayer structure, where light passes through the transparent anode and is incident upon the donor material where exciton formation occurs. Excitons are dissociated at the interface between donor (*blue*) and acceptor (*yellow*) and electrons are collected at the cathode (*black*). (**c**) Is representative of the mixed interlayer structure, where the donor and acceptor are mixed through codeposition at the interface, this creates more interfacial area for exciton dissociation. (**d**) Represents the most common device cross section for polymer based devices, the bulk heterojunction (BHJ) where polymer and fullerene are mixed together in a common solvent and form a blended layer with an extremely large interfacial area (color figure online)

diffusion length (L_D), and is $L_D = \sqrt{D\tau}$ where D is the diffusion coefficient of the material and τ is the excitons lifetime. For most organic materials L_D is typically 10–20 nm [11, 12].

- In order for efficient exciton dissociation the difference between LUMO levels of donor and acceptor materials at the heterojunction, denoted as Δ in Fig. 15.1b must be larger than the excitons binding energy. The excitonic binding energy in organics is large, typically 400 meV or larger. For inorganic semi-conductors the binding energy is only a few meV (this is on the order of thermal energy, $k_BT(300\ K) = 26$ meV), which is why excited charge carriers are considered essentially free [13, 14].

After exciton dissociation occurs (step 4) the free charge carriers are swept to the collecting electrodes under the influence of an internal electric field which is due to a built-in potential from the difference in work functions, Φ, of the two electrodes [15].

Tang's seminal device addressed the problem with exciton dissociation through the inclusion of a donor organic semi-conductor (CuPc) and an acceptor material (PTC) which provided a interface where the energy difference between the materials LUMO levels was sufficient to allow for dissociation and the creation of free charge carriers. The absorbing layer, the layer in which the exciton is originally formed, must be limited to a thickness of approximately the exciton diffusion length ($d \sim L_D \sim$ 10–20 nm), otherwise the photo-generated exciton will not be able to diffuse to the Donor-Acceptor interface and will recombine. The limited L_D results in a careful balance between light absorption and exciton dissociation, this is known

as the exciton bottleneck [16–18]. The exciton bottleneck problem is addressed through the use of bulk heterojunction (BHJ) active layers, where the donor and acceptor materials are co-deposited for molecular organic semi-conductors [19] or where two materials are mixed together in solution as was originally described by the Heeger [20] and Friend [21] groups, the structures are shown as cross-section representations in Fig. 15.2c, d for molecular and polymeric BHJs respectively. Devices employing the BHJ active layer have a donor-acceptor interface distributed throughout the photo-active layer and require phase separation between the donor and acceptor materials which is achieved through precise control of the nanoscale morphology. Many methods have been used to control the nanoscale morphology including thermal annealing [22], solvent annealing or slow drying [23], careful solvent selection [24, 25] and processing additives [26]. More recently the exciton bottleneck and morphology problems are being simultaneously addressed through careful nanoscale pattering of the donor-acceptor interface using nano-imprint lithography [4, 27, 28].

15.2.1.2 Operation and Role of Charge Collectors

The requirements on charge collectors for organic photovoltaics are more demanding than for inorganic devices, in the basic structure shown in Fig. 15.1b the work function of each charge collector is important and responsible for the internal electric field. The electric field is given by the difference in the two work functions and the separation distance between them:

$$V = \frac{\Phi_{Anode} - \Phi_{Cathode}}{e} \tag{15.1}$$

$$\mathbf{E} = V/d \tag{15.2}$$

The work function, transparency, and low sheet resistance requirements have been the main requirements for passive/planar electrodes. However, in order to increase the exciton dissociation efficiency and the power conversion efficiency an active charge collector can be designed. The ideal charge collector for all structures, conventional, inverted, series and parallel, will satisfy the following basic criteria for undoped organic photovoltaics:

- **Optically Transparent**. This is required by at least one of the electrodes used in order to allow photo-excitation of the active layer.
- **High (Low) Work Function**. This will provide the internal electric field as described by Eq. (15.2).
- **3-D Geometry and Topology**. Having electrodes which are embedded into the active layer will allow for more charges to be collected by reducing the distance a charge must travel. Furthermore, the electric field can be enhanced at the tips of the charge collectors.

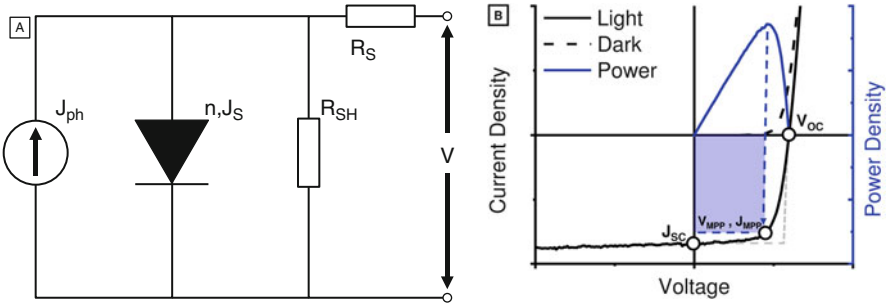

Fig. 15.3 (**a**) Is the equivalent circuit model of a p-n junction type solar cell which includes both shunt (R_{SH}) and series (R_S) parasitic resistances. (**b**) Is a typical current-voltage curve of a photovoltaic device operating under illumination (*solid black curve*) and in dark conditions (*dashed black curve*). Also included are the open-circuit voltage (V_{OC}), short-circuit current (J_{SC}) as well as the power output curve for the illuminated device with the maximum power point (*MPP*) marked on both the power curve and the corresponding location on the current-voltage curve

- **Selectivity of Charge Carriers**. The charge collectors should be selective to either electrons or holes, this will prevent them from functioning as recombinations sites which is important in the case of devices utilizing the bulk heterojunction active layer.
- **Low Sheet Resistance**. High conductivity will lead to a lower series resistance and ensure high fill factors.
- **Low Charge Transfer Resistance (R_{CT})**. Electrodes which have no trap states and form intimate contact with active layer material are critical in allowing all charges to be transfered to the charge collectors.
- **Tunable Geometry**. The ideal charge collector should have a tunable geometry so that it can best match the specific properties of the active layer materials.

15.2.1.3 Electrical Characteristics and Modeling

Organic photovoltaics based on the inorganic p-n junction structure (i.e. most donor-acceptor systems excluding dye-sensitized solar cells which are based on a different model [29]) can be modeled using the Shockley diode equation and an equivalent circuit shown in Fig. 15.3a. The equivalent circuit for an organic photovoltaic device under illumination (Fig. 15.3a) consists of a diode with a reverse saturation current, J_S and an ideality factor, n, as well as a current source J_{PH} corresponding to the photo-generated current. Parasitic resistances are included in the form of : (a) shunt resistance, R_{SH}, which needs to be maximized and represents loss of charge carriers through leakage paths, traps, and other structural defects and; (b) a series resistance, R_S, which needs to be minimized and represents the limited conductivity of the material, contact resistance between the material and electrodes as well as the

resistance between interconnects within the photo-active material. The equivalent circuit can expressed as a modified Shockley equation :

$$J = J_S \left\{ \exp\left(\frac{V - JR_S}{nV_T} \right) - 1 \right\} + \frac{V - JR_S}{R_{SH}} - J_{PH} \tag{15.3}$$

where $V_T = e/k_B T$ is the thermal voltage, currents (J_S and J_{PH}) are in units of A/cm^2, R_S and R_{SH} are given in units Ω-cm^2. Careful analysis and manipulation of Eq. (15.3) can lead to a functional form for current density (Eq. 15.4),

$$J(V) = \frac{nV_T}{R_S} W_{k=0} \left\{ \frac{J_S R_S R_{SH}}{nV_T(R_S + R_{SH})} \exp\left(\frac{R_{SH}}{nV_T} \frac{V + (J_{PH} + J_S)R_S}{R_S + R_{SH}} \right) \right\} - \frac{(J_{PH} + J_S)R_{SH} - V}{R_S + R_{SH}} \tag{15.4}$$

where $W_{k=0}$ is the k=0 branch of the Lambert-W function. This functional form can allow for all circuit parameters to be extracted and used for cell simulation in circuit simulators such as SPICE.

Under illumination the power density generated by a photovoltaic cell can be calculated by multiplying each current-voltage pair in the fourth quadrant, the maximum power density will correspond to the maximum power point (MPP) with a current-voltage pair (V_{MPP},J_{MPP}). The total power conversion efficiency (PCE), η, will be given by:

$$\eta = \frac{V_{OC} J_{SC} FF}{P_{IN}} \tag{15.5}$$

$$FF = \frac{V_{MPP} J_{MPP}}{V_{OC} J_{SC}} \tag{15.6}$$

where P_{IN} is the incident power and FF is given by Eq. (15.6) and corresponds to the ratio between the maximum area in the forth quadrant and the maximum area within the current-voltage curve of the device. Figure 15.3b graphically illustrates all parameters used in the calculation of the power conversion efficiency.

15.3 Tandem Organic Photovoltaics and the Role of the Inverted Geometry

A general advantage of the tandem of multi-junction OPV structure is its multi-absorption ranges. The wavelength distribution of the solar spectrum has a wide range, covering the UV to IR. Although there are many kinds of organic materials (small molecule or polymeric) that are used as photoactive layers for OPV cells, the individual materials have specific and narrow absorption ranges. Hence, only a

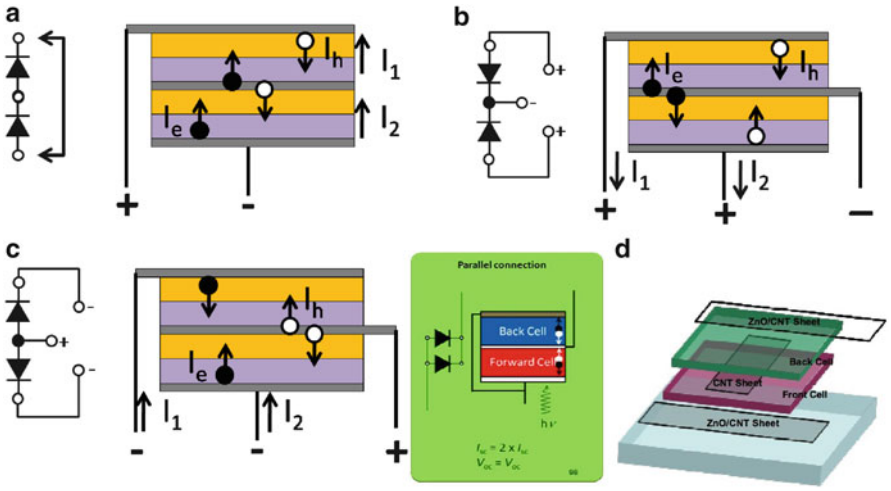

Fig. 15.4 (**a**) Conventional series OPV tandem connection, (**b**) the concept of a parallel tandem with CNT active interlayer as anode. (**d**) New concept of inverted parallel tandem with CNT cathode interlayer. Transparent ITO of a bottom cell on (**c**) can be 'inverted' into a cathode by electron selective ZnO layer, also known as hole barrier layer. This concept of a parallel tandem with CNT active interlayer collecting charges of same sign (shown by *filled* and *empty circles* with *arrows*) from each of sub-cells, allows to increase the total current. (**d**) Shows schematics of electrical connections of top and bottom cells and the conceptual design of layers in P-T with CNT

part of the solar spectrum is effective in generating the photo carriers in a single junction PV cell. By using materials with a different absorption range for each OPV cell of the tandem structure, the total absorption range of the tandem OPV cell can be the superposition of the each material. This has been demonstrated for different OPVs, but all previous tandems were series tandems (S-Ts) [30, 31], in which the interconnect is a recombination layer, and plays the role of a floating electrode. We suggested different monolithic geometry: a parallel tandem (P-T), which is enabled with CNT transparent charge collector. We discuss the advantages of P-T and why their is a need for an inverted OPVs as one of the sub-cells.

15.3.1 General Concept of Parallel-Tandem Versus Series-Tandem

In series connected tandem cells, the holes are coming from the bottom cell, while electrons are arriving from the top cell (Fig. 15.4a) so the transfer of the charge at the interface in a monolithic tandem requires that the holes recombine with the electrons. The voltages of top and bottom cells add, while the lowest current can pass through the series tandem, and current balancing is required. In contrast, for

a parallel tandem the photocurrents add $I = I_{BOT} + I_{TOP}$ in a charge collecting interlayer, while the average voltage is generated (Fig. 15.4b, c).

Advantages of Parallel Tandem Compared to Series Tandem Configuration

1. Does not need the photocurrent balancing: top and bottom OPV cells may have largely different I_{SC}
2. Can connect PVs with very different photocurrents I_{SC}, but similar or close enough V_{OC}.
3. The transparent interlayer plays a role of a common electrode, that is a charge collector and is an active electrode, i.e. should have low serial resistance and leads attached to it.
4. No other electrodes, but only continuous strong t-CNT can be used as an active interlayer since it needs to be continuous (contrary to flakes of charge recombination interlayer in in-series connection)

In P-T type of connection of OPVs, one of sub-cells should be inverted, as compared to S-T, since in P-T the top and bottom electrodes are either both anodes (large work function, such as ITO) or both cathodes (low work function, such as Al). However, one of outer electrodes also needs to be transparent, which means that a transparent anode, such as ITO should be inverted into a cathode by coating it with a selective layer.

15.3.2 Interconnection Layers in Parallel and Series Tandems

Moreover the P-T needs a central common electrode to be an active charge collector, with a low serial resistance as well as high optical transparency, which is not easy with conventional metallic materials. Only strong transparent sheets of carbon nanotubes (coated if needed with inversion layers, as described below) allow the new type of inverted parallel connection, since it permits the attachment of the outer lead to the interconnect, (while in previous series connections the leads were not required). The growth of these carbon nanotubes is sufficiently understood and large scale forests can be grown in CVD reactors as seen in Fig. 15.5. Under proper growth conditions forests can have dense enough CNT growth that all individual CNTs are connected. With this interconnection between individual CNTs, when a segment of forest is pulled from substrate it begins to pull it's adjacent neighbors, when this happens the forest is said to be *spinable*. Spinable forests are desireable for many applications, of particular interest is the interlayer common electrode for tandem cells because of their processability, high conductivity, low sheet resistance and high optical transparency. The spinable forests can be collected into free standing sheets which are laminated onto any surface, including OPVs, this is shown in the last segment of Fig. 15.5.

A tandem OPV cell with a transparent titanium oxide layer has been reported and it was fabricated by all-solution processing. All of the previous reports were focused

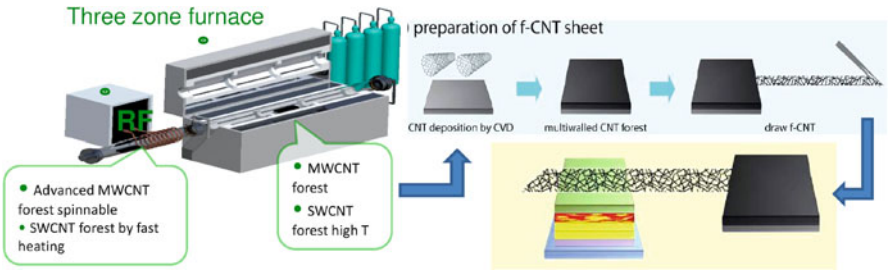

Fig. 15.5 Flow chart demonstrating the growth and application process of CNTs. At first, a CVD chamber is heated using RF heating, depending on the temperature and duration of the heating the type and length of CNTs can be controlled. Once a forest is grown, the CNTs can be pulled into a sheet (*top right* of figure) for collection or application. The final step shows the pulled CNT sheet being laminated on a device to be used as an electrode or interlayer electrode

on the tandem OPV cells with series connections (except recently by Guo et. al. [32], which follows our original work [1]). A property of the S-T series connection is an increased V_{OC}: the V_{OC} of tandem cell in the series connection is expected to be the sum of the V_{OC} of each individual cell. In contrast, as we have demonstrated a tandem PV cell [1] with parallel connection has an increased short circuit current density (J_{SC}). The total J_{SC} in the parallel configuration (in ideal case of equal V_{OC} of sub-cells) is the sum of J_{SC} contributed by each individual cell. We show below by modeling how this can be optimized for case of different V_{OC} of sub-cells. As an intermediate layer for the thin film tandem OPV, it needs to be thin and smooth enough to prevent shorting. Thus, typical intermediate layers for the S-T tandem OPV are limited to ultra thin layers of metals or oxides. These intermediate layers are a kind of 'floating' layer in the OPV structure. These layers usually are in form of flakes and cannot be connected with an external circuit directly. For P-T OPVs, an intermediate layer is needed, which can be connected directly from the external circuit. This is a challenge and to the best of our knowledge, there are no report about the tandem OPV cell with parallel connection with strong mechanical continuous layers with good transparency.

15.3.3 Parallel Tandem OPV with Inverted Bottom Layer

Originally reported P-T [1] demonstrated increased J_{SC}, but the efficiency was very low. The reason for this was clear: although the central CNT interlayer was a common anode, the bottom cell had ITO as electrode, which was also an anode, and thus generated a very low V_{OC} between two anode type electrodes, both with high work functions. In order to increase the V_{OC} of bottom cell, the cell needs to be inverted with a transparent cathode, i.e. ITO inverted into a cathode, as is described below.

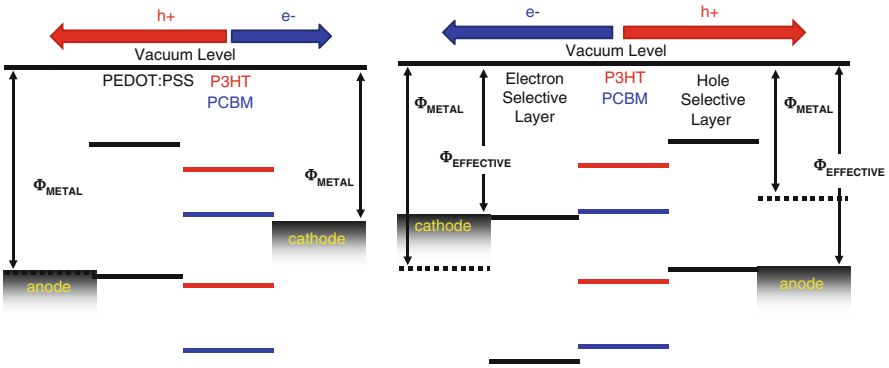

Fig. 15.6 Energy band diagrams for the conventional OPV (*left*) and the inverted OPV (*right*) geometries. The inverted geometry uses electron and hole selective layers to modify the work functions to the effective values

The work presented demonstrate the functionality of various inorganic oxides as charge selective layers for use within the OPV stack. The incorporation of these charge selective layers will be extended into semi-transparent devices employing either MWNTs or SWNTs as electrodes. This is essential in creating either a front or back sub-cell for use in parallel tandem structures, where one of the electrodes is common to both sub-cells and is required to be transparent. The charge selective inorganic oxides can be used as either an electron transport layer, also referred to as a hole blocking layer (HBL), or as a hole transport layer (HTL) which can be referred to as an electron blocking layer (EBL) depending on the electronic levels in relation to polymeric levels. These charge selective layers allow for the polarity of the devices, which is normally determined by the work function of the electrodes in relation to the HOMO and LUMO levels of the acceptor and donor materials, to be inverted.

A general energy band diagram for both conventionally structured OPVs (c-OPVs) and inverted OPVs (i-OPVs) is shown in Fig. 15.6. The electrodes are labeled and arrows depict the direction in which holes and electrons flow. In the c-OPV, left side of Fig. 15.6, structure the direction of charge flow is determined by the internal electric field generated by the difference in work functions of the two electrodes, electrons (holes) move under influence of the electric field towards the low (high) work function cathode (anode). For i-OPVs the internal electric field is still created by the work functions of the electrodes, however the values of the electrodes work functions are modified to new "effective" values.

15.3.3.1 ZnO Nanoparticles as an Electron Transport Layer

Inverting the ITO anode into a cathode is best accomplished by metal oxides such as titanium dioxide or zinc oxide. Titanium dioxide has been demonstrated in dye

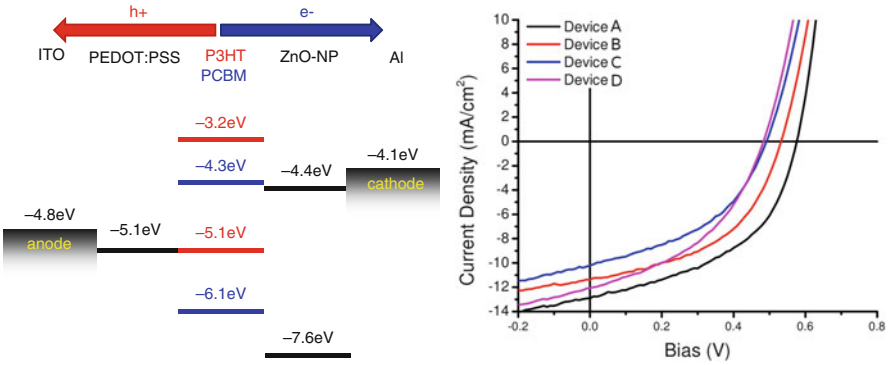

Fig. 15.7 c-OPV devices were fabricated but included a ZnO-NP electron transport layer between the active layer and the aluminum cathode. The energy band diagram is shown on the *left* and the current-voltage characteristics are shown on the *right*. The performance of the device decreases with decreasing thickness of the ETL

sensitized solar cells with great success when in the anatase crystalline phase due to its high photoconductivity and electron mobility [33]. However, these characteristics require sintering at temperatures in excess of 350 °C [34], which is too high for organic materials. Zinc Oxide nanoparticles (ZnO-NP) have been demonstrated as an alternative to fullerenes as an acceptor [35] in bulk heterojunction devices and are a strong candidate as an n-type charge selective layer for use in inverted solar cells. ZnO-NPs are simple to synthesize, can be dispersed in alcohols, and do not require any further treatment such as annealing, sintering, or hydrolysis after deposition [36]. The ZnO-NPs are a wide band gap inorganic semiconductor, thus can provide a large optical window for incoming photons to be absorbed within the photo-active polymeric layers. Additionally, a deep HOMO level prevents holes from reaching the cathode.

To evaluate the effectiveness of the zinc oxide nanoparticles, conventional device structures were fabricated in which a layer of ZnO-NP were spin coated on top of the polymer to form a hole blocking layer. The device schematic and resulting JV curves are shown in Fig. 15.7 while device characteristics are tabulated in Table 15.1 as devices A-D. The JV curves show a high J_{SC} this is only possible if the ZnO-NPs have electron mobilities comparable or larger than the fullerene network within the bulk heterojunction, otherwise there would be charge build up and the JV curves would show an S-shape [37].

Table 15.1 A summary of device performance based on the inclusion of either hole or electron transport layers, and the effect of transport layer thickness

Device	HTL	Anode	ETL	Cathode	V_{OC} V	J_{SC} mA/cm^2	FF	PCE %
ZnO-NP ETL								
A	PEDOT:PSS	ITO	1500 RPM	Al	0.58	12.9	0.47	3.53
B			2000 RPM		0.54	11.4	0.47	2.91
C			2500 RPM		0.50	10.2	0.43	2.11
D			3000 RPM		0.49	12.0	0.42	2.50

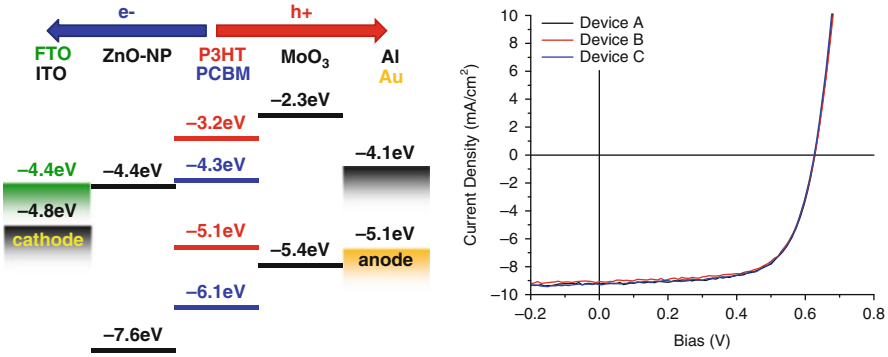

Fig. 15.8 Energy band diagram (*left*) and current-voltage (*right*) figures for devices with various electrode pairings (Device A: ITO/Al, Device B: ITO/Au, and Device C: FTO/Al) all showing comparable performance

15.3.4 Inverted Devices with Transparent Carbon Nanotubes

To demonstrate the effectiveness of ZnO-NPs and MoO_3 as inversion layers for i-OPVs, several inverted devices were created employing electrodes with different work functions. The robustness of this configuration was demonstrated by using two different transparent conducting oxides, FTO and ITO, with work functions ~ -4.4 and $\sim -$s4.8 eV respectively, were used as cathodes. Similarly, the anodes were varied using gold and aluminum with work functions of -5.1 and -4.1 eV respectively. The device schematics and JV characteristics are shown in Fig. 15.8 with performance characteristics shown in Table 15.2 as devices A-C. Remarkably, all configurations show nearly identical JV characteristics despite having different anode and cathode materials. The different electrode materials would normally change the internal electric field and could, in the case of ITO/Al, have an electric field that is opposite to the preferred direction for charges to travel. The use of charge selective barrier layers causes the build up of blocked charges at the interfaces and a change to the work function of the electrode behind the barrier to a new work function. This change to the work function as well as build of charges generates a new internal electric field that is oriented in the correct direction.

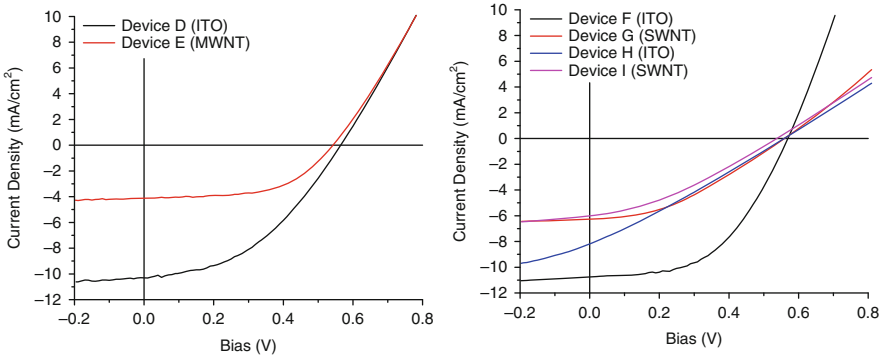

Fig. 15.9 Current-Voltage curves for i-OPV devices which are semi-transparent and use either MWNTs (*left*) or SWNTs (*right*) as anodes. The side being illuminated is denoted in parentheses

15.3.4.1 Inverted Devices with a MWNT Anode

The i-OPV structure, with solution processed ZnO-NPs as an effective ETL and thermally evaporated MoO_3 as a HTL, was extended to incorporate MWNTs as an anode. The MWNTs would be used as a standalone anode while ITO would be converted to a cathode. The MWNTs used were densified using Hydrofluoroether (HFE) because of its 'orthogonal' nature; it is inert as a solvent for the materials used within this i-OPV.

For the devices with ITO/MWNT cathode/anode configuration illumination from either side of the device was preformed because both electrodes are optically transparent. Device performance was dependent on which side was illuminated. JV curves are shown in Fig. 15.9 with the side being illuminated being labeled in parenthesis and device performance is described in Table 15.2 as devices D and E. When illuminated through ITO higher performance was observed due to a $\sim 2\times$ improvement in J_{SC} when compared with the performance of the device illuminated through the MWNT electrode. This significant change in J_{SC} can be explained by the optical transmission of the MWNTs, which is ~ 48 % transmission when averaged over perpendicular and parallel (with regards to the orientation of MWNT strands) orientations.

15.3.4.2 Inverted Devices with a SWNT Anode

In order to improve on the performance of the semi-transparent i-OPV with a MWNT top anode, SWNTs can be used. Much progress has been made in the field of SWNT growth, and it is possible to produce films with low defects, high transparency, and high electrical conductivity [38–40]. SWNTs which were synthesized in a floating catalyst reactor [41] and deposited onto millipore filters for use as transferable electrodes were used. The SWNT films are named after the number of minutes that nanotubes were collected within the reactor; the longer the

Table 15.2 A summary of inverted devices

Device	HTL	Anode	ETL	Cathode	V_{OC} V	J_{SC} mA/cm^2	FF	PCE %
Various electrodes								
A	MoO_3	ITO	ZnO-NP	Al	0.63	9.2	0.67	3.91
B				Au	0.63	9.1	0.66	3.82
C		FTO		Al	0.63	9.3	0.66	3.88
MWNT cathode								
D	MoO_3	ITO*	ZnO-NP	MWNT	0.57	10.3	0.42	2.48
E				*	0.55	4.1	0.55	1.25
SWNT cathode								
F	MoO_3	ITO*	ZnO-NP	16 min	0.56	10.7	0.51	3.12
G				*	0.56	6.2	0.37	1.31
H		*		8 min	0.56	8.2	0.27	1.25
I				*	0.54	6.0	0.33	1.09

The asterisk (*) denotes which side was illuminated for the semi-transparent device

duration the more opaque and conductive the nanotube films. SWNTs exhibit lower sheet resistances and higher optical transparency than the MWNTs used for the previous devices which make them a candidate for a transparent electrode to be used within our i-OPVs as well as parallel tandem devices.

To form a transparent anode, SWNT sheets were laminated on top of a MoO_3 film on an inverted device similar in structure to those described previously. The devices were measured with the side being illuminated being noted within the parenthesis of Fig. 15.9 and device performance characteristics are noted in Table 15.2 as devices F-I. The "16 min" (devices F and G) sample having a sheet resistance of 200 $\Omega/\square$ and transmittance of 60 % show the highest performance when illuminated through the highly transparent ITO layer due to the SWNTs low sheet resistance. However, when illuminated through the SWNT side, a 40 % reduction in the current is seen and the fill factor is reduced. This is not the case for the more transparent sample, "8 min" (devices H and I), which has a sheet resistance of 500 $\Omega/\square$ and transmittance of 90 %; the device shows nearly the same performance when illuminated through either the ITO or SWNT as the electrodes are almost equally transparent.

This work demonstrates how using wide band-gap inorganic metal oxides, ZnO-NPs and MoO_3, as electron and hole transport layer respectively can efficiently invert the polarity of organic photovoltaic devices. Inverted OPVs with various electrode configurations were demonstrated, including the configuration where the internal electric field due to the difference in electrode work functions would be opposite to the direction of current through the device. The work was also extended to the case where MWNTs were used to create semi-transparent devices and improved upon through the use of high quality SWNT films. Such semi-transparent i-OPVs are critical in creating efficient front cells for use in parallel tandems, where the interlayer electrode must be transparent, conductive, and function as a common anode or cathode.

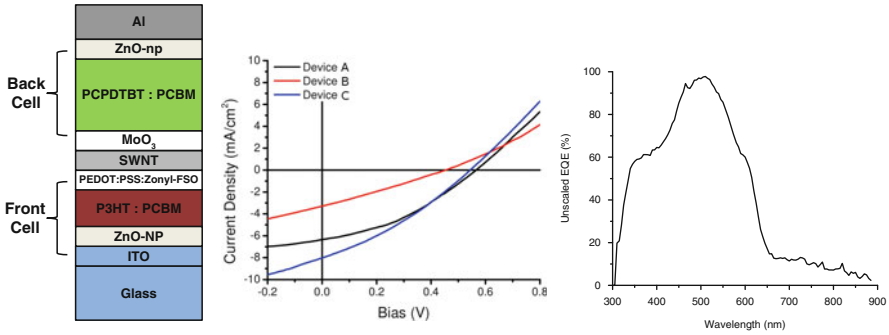

Fig. 15.10 Structure (*left*), current-voltage characteristics (*center*) and EQE (*right*) for a parallel tandem cell with two polymeric absorbers

15.3.4.3 Polymeric Parallel Tandem OPV with Inverted Sub-Cell

The parallel tandem architecture using two polymer based sub-cells rather than a polymeric front sub-cell and vacuum processed small molecule sub-cell as was previously done is demonstrated in this section [1]. For this work, the front sub-cell was an inverted P3HT:PCBM bulk heterojunction using ZnO nanoparticles as an electron transport layer and is combined with PEDOT:PSS which is mixed with a surfactant developed by DuPont, Zonyl-FSO. Zonyl-FSO has the property of reducing the surface tension of aqueous solutions at low concentrations. This is critical because PEDOT:PSS is an aqueous dispersion while the polymer film is hydrophobic. Therefore PEDOT:PSS does not adhere to the surface. With the Zonyl-FSO additive, the surface tension of PEDOT:PSS is reduced to where films of PEDOT:PSS are possible on top of P3HT:PCBM. Furthermore, the PEDOT:PSS film is not soluble in the organic solvent used for the back-cell therefore it provides a protective barrier for the P3HT:PCBM based front-cell. The interlayer electrode is SWNTs which have been laminated between the PEDOT:PSS and MoO_3 hole transport layers. The back-cell is based on PCPDTBT, a small band-gap donor material and PCBM acceptor material. The back-cell employs a ZnO-NP electron transport layer to provide an additional spatial buffer between the SWNT interlayer electrode and the top aluminum cathode. The layer structure is shown on the left of Fig. 15.10, the corresponding J-V curve for the parallel tandem cell is shown in the center Fig. 15.10 and device performance is in Table 15.3. From the external quantum efficiency, it is clear that the tandem cell has spectral contributions from both the P3HT:PCBM front cell, in the range of 400–650 nm, and from the PCPDTBT:PCBM back cell, in the range of 650–900 nm (right of Fig. 15.10).

This work combines structures and materials from previous sections to build monolithic tandem devices which have enhanced spectral sensitivity, properly inverted sub-cell architectures, and utilize SWNTs as transparent interlayer anodes. Furthermore, this work utilizes fitting and circuit modeling to analyze each sub-cells performance and describe some of the processes which can hinder performance

Table 15.3 Table summarizing the performance of various parallel tandem cells

Device	HTL	ETL	Anode	Cathode	V_{OC} V	J_{SC} mA/cm^2	FF	PCE %
Tandem from Ref. [1]								
(Front)	PEDOT:PSS	None	MWNT	ITO	0.51	2.3	0.26	0.30
(Back)		BCP		Al	0.42	1.8	0.28	0.21
(Tandem)				ITO/Al	0.46	2.6	0.26	0.31
P3HT:PCBM/PCPDTBT:PCBM polymeric tandem								
A (Front)	PEDOT:PSS:Zonyl-FSO	ZnO-NP	SWNT, 8 min	ITO	0.56	6.3	0.36	1.30
B (Back)	MoO_3			Al	0.46	3.3	0.26	0.41
C (Tandem)	PEDOT:PSS/MoO_3			ITO/Al	0.54	8.1	0.31	1.38

within parallel tandem devices. In this work, past work on parallel tandems has been improved and extended from polymeric/small molecule tandems to polymeric/polymeric tandems.

15.4 Tandem Organic Photovoltaics

15.4.1 Modeling and Comparison of Parallel and Series Tandems

Below is the short summary, which allows to compare the series (S-T) and parallel tandems (P-T) for connections of three types of different model OPV cells, which have different parameters, particularly have different FF, and different V_{OC}. The question we address is following: if cells have largely different FF and largely different V_{OC} and I_{SC}, which connection is better: usual S-T, or our monolithic P-T with a common central electrode.

Parallel and series connections of three different solar cells with the following parameters were investigated. Cell 1 had I_{Ph} = 7 mA; $I_O = 1\times10^{-11}$ mA; Rs = 10 Ω; Rsh = 1,000 Ω; n = 1. Cell 2 had reverse saturation current $I_O = 1\times10^{-5}$ mA, which decreased the open circuit voltage twice as compared to cell 1. Cell 3 had higher series resistance Rs = 200 Ω which decreased the short circuit current twice as compared to cell 1 (Table 15.4). The I-V curves of solar cells 1, 2, and 3 are shown in Fig. 15.11a. Figure 15.11c, d show the IV curves of the individual cells (black lines) as well as the series (green) and parallel (red) connections of the corresponding cells.

If two identical cells are connected in series, the V_{OC} is doubled, while I_{SC} remains the same as for one cell. When individual solar cells are different, V_{OC} of a tandem equals to the sum of open circuit voltages for each cell (see Table 15.4). The losses in efficiency of a series tandem arise from the reduction of the short circuit current. When the tandem is shorted, the cell with the lower I_{SC} partially consumes the current from the cell with the higher I_{SC} in order to equilibrate the

Table 15.4 Open circuit voltage (V_{OC}), short circuit current (I_{SC}), fill factor (FF), and efficiency (η) of the individual solar cells and the series and parallel tandems

Cell type	V_{OC} V	I_{SC} mA	FF	η %
Cell 1	0.703	6.93	0.70	3.42
Cell 2	0.347	6.93	0.57	1.38
Cell 3	0.703	3.41	0.25	0.60
Series 1-2	1.049	6.93	0.66	4.79
Series 1-3	1.405	6.00	0.26	2.23
Series 2-3	1.049	4.68	0.25	1.25
Parallel 1-2	0.429	13.86	0.51	3.05
Parallel 1-3	0.703	10.34	0.53	3.82
Parallel 2-3	0.369	10.34	0.50	1.92

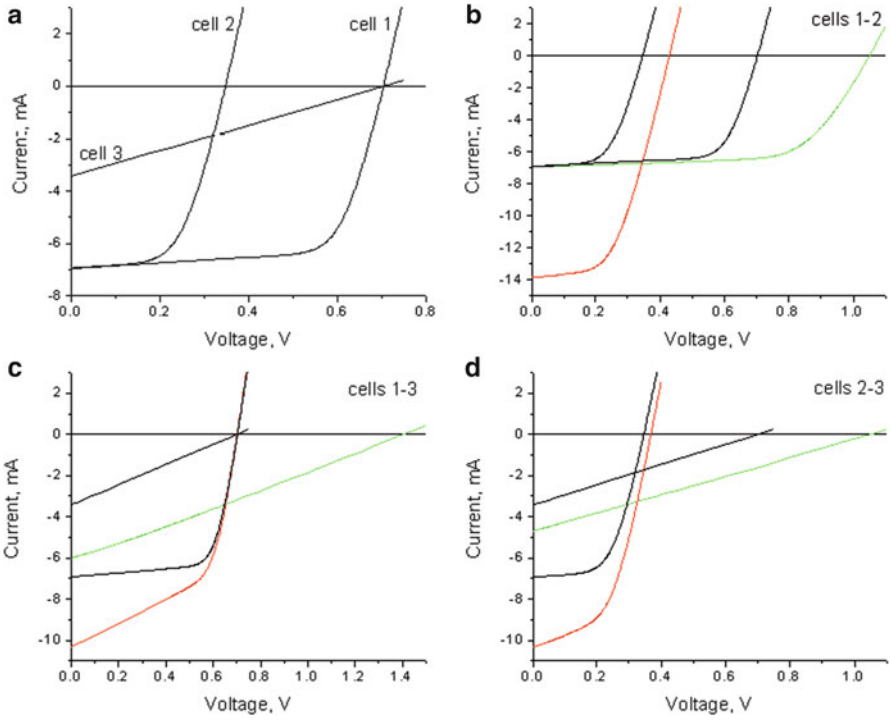

Fig. 15.11 (**a**) Shows the individual cells current-voltage curves which will be used for modeling. (**b–d**) Combination of various cells in either series (*green*) or parallel (*red*) configurations

system. Also, if the short circuit currents of the individual cells are not equilibrated, the tandems fill factor is reduced to almost that of the low-performing cell. Thus, in order to maximize the efficiency of a series tandem it is important to have similar short circuit currents and fill factors of individual cells.

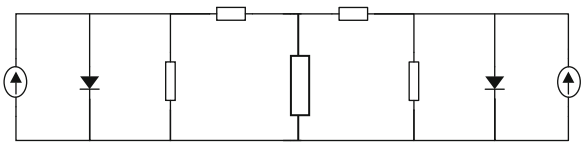

Fig. 15.12 The figure shows an equivalent circuit for P-T connections

In the case of a parallel connection of two solar cells, the tandems I_{SC} equals to the sum of the short circuit currents in each cell (see Table 15.4). The open circuit voltage of a parallel tandem is greatly reduced if it is not balanced in the individual cells. This happens because the voltage from the cell with higher V_{OC} partially drops on the other cell. Thus, in order to maximize the parallel tandems efficiency it is important to equilibrate open circuit voltages of individual cells.

In addition, rigorous analysis of the parallel tandems characteristic equation shows that for $R_S < R_{SH}$, the reduction in the parallel tandems fill factor is much smaller than that in a series tandem. That is why the parallel tandem performs better than the series one, when both the I_{SC} and V_{OC} of the individual cells are substantially different (Fig. 15.11d).

15.4.2 Open Circuit Voltage Optimization for Parallel Tandems: Summary of Model Analysis

We have considered the parallel connection P-T of two solar cells with different open-circuit voltages (V_{OC}) and also different FF of sub-cells. We have derived analytical expressions for V_{OC} of the parallel tandem in four different simplified cases, refering to *"good"* or *"bad"* filling factor of sub-cells. Obviously the best situation is *"good-good"*, and the worst is *"bad-bad"*, with intermediated cases in between, also shown in Fig. 15.12. Examined cases represent the vast majority of real-life solar cells. The obtained results were verified by comparison with experimental data. We have also shown how it is possible to minimize the V_{OC} losses in parallel tandems by adjusting parameters, particularly the FF of individual sub-cells. The summary of results are shown below in diagram form for simplicity, while the full analysis can be found in the original paper [42].

The total photocurrent in P-T can be described as a sum of two currents in each sub-cell:

$$I_{Ph,1} + I_{Ph,2} = I_{O,1}\left\{\exp\left(\frac{V_{OC}^T + IR_{S,1}}{n_1\alpha}\right) - 1\right\} + \frac{V_{OC}^T - IR_{S,1}}{R_{SH,1}} + I_{O,2}\left\{\exp\left(\frac{V_{OC}^T + IR_{S,2}}{n_2\alpha}\right) - 1\right\} + \frac{V_{OC}^T - IR_{S,2}}{R_{SH,2}} \tag{15.7}$$

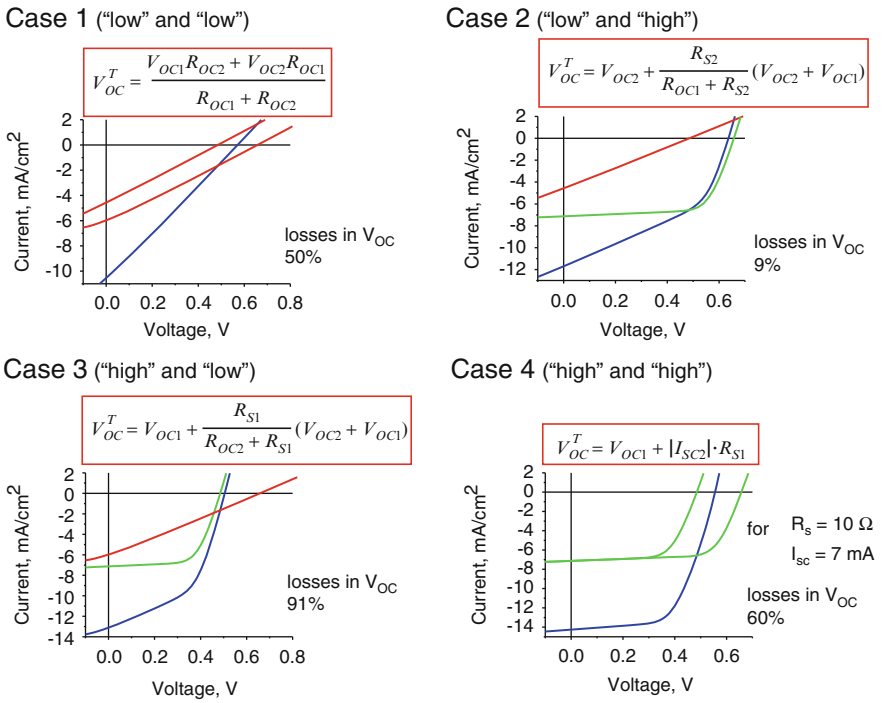

Fig. 15.13 The figure I-V curves for the cases of devices with *"good"* and *"bad"* FF and V_{OC} as well as the resulting parallel tandem cell

It is convenient to calculate a differential resistance R_{OC} at $V=V_{OC}$,

$$R_{OC} = \left.\frac{dV}{dI}\right|_{V=V_{OC}} = R_S + \frac{R_{SH}}{1 + \frac{R_{SH}(I_{Ph}+I_O)-V_{OC}}{n\alpha}},\ \alpha = \frac{V_{OC,2} - V_{OV}^{T}}{V_{OC,2} - V_{OC,1}} \tag{15.8}$$

Also we introduce the losses of V_{OC} defined as α, expression for which is shown above.

We consider now each case of connecting low FF sub-cell (*"bad"* sub-cell) with high FF (*"good"* cell) separately below

The four cases show on the diagram above represent the different scale of losses in total photovoltage V_{OC}^{T} generated by P-T, depending on the difference of $V_{OC,1}$ and $V_{OC,2}$ and their relative position and FF for each of sub-cells. As one scan se the minimal losses in V_{OC} correspond to case 2, when cell with lower $V_{OC,1}$ has low FF (i.e. is a *"bad"* one), while cell with higher $V_{OC,2}$, has high FF (i.e. is a *"good"* one). So when making a P-T one should design it in such a way, that the cell with higher V_{OC} should have best FF. the losses in this case are about 9 % or even less. On the other hand the highest losses of 91 % are for opposite Case 3 when lower $V_{OC,1}$ cell has high FF, while higher $V_{OC,2}$ cell has low FF. In Cases 1 and 4 the losses of Voc are nearly equal 50–60 %.

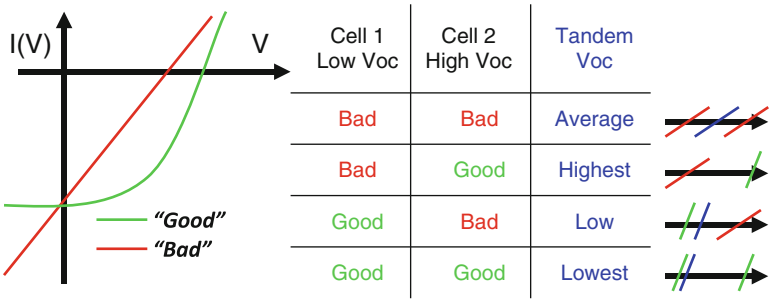

Fig. 15.14 Optimization of total photovoltage V_{OC}^{T} of parallel-tandem OPV, depending of FF of sub-cells

This results are summarized below in Fig. 15.14. For V_{OC}^{T} optimization by losses:

15.4.3 Experimental Comparison of Non-monolithic Series and Parallel Tandems

Two semitransparent OPV have been created with polymers of different band gaps P3HT and PCPDBT. The P3HT cell has been inverted using ZnO and MoO_3 as hole and electron blocking layers respectively and SWNT act as a transparent anode. While the PCPDTBT cell is conventionally structured and has layer of ZnO as a hole blocking layer between the polymer and SWNT cathode. The device performance is summarized in Table 15.5 and the JV curves for the cells are shown in Fig. 15.15.

In order to check which connection is beneficial, the two types of non-monolithic tandems have been created by attaching one cell on the top of the other (as shown on Fig. 15.15 inset) and electrical connections have been made from outside, corresponding to S-T and P-T structure. The J-V curves have been measured in exactly the same conditions, and the FF and PCE have been extracted and compared, as presented at Table 15.5. Surprisingly the S-T connection has developed unexpectedly low FF $\sim$ 0.39, after connection (as seen on the purple J-V curve). On the other hand the P-T shows much better performance with FF $\sim$ 0.49, slightly decreased as compared to best sub-cell (FF of 0.61) as seen on green color J-V curve on Fig. 15.15.

In quite good agreement with the results of our simple model, as described in previous section, the P-T has shown increased total photocurrent, I_{SC}^{T} = 11.44 $\sim$ 5. 9 + 8 4 = 14.3 (with reasonable losses of $\sim$ 3.1 mA/cm^2 due to shading effects). The total V_{OC}^{T} is indeed between V^1=0.57 V and V^2=0.69 V and equal to 0.60, nearly in the middle, since both FF are high. The model predicts, that total V_{OC}^{T} should be closer to that one, which has higher FF. Indeed the exact expression for V_{OC}^{T} in case of two sub-cells with good FF is :

$$V_{OC}^{T} = V_{OC,1} + |I_{SC,2}| \cdot R_{S,1} \tag{15.9}$$

Table 15.5 Tabulated values of single P3HT and PCPDTBT cells as well as the non-monolithic parallel and series tandems

Cell Type	V_{OC} V	J_{SC} mA/cm^2	FF	η %
P3HT top	0.57	5.93	0.61	2.06
PCPDTBT bottom	0.69	8.47	0.39	2.29
Parallel	0.60	11.44	0.49	3.35
Series	1.22	5.27	0.39	2.53

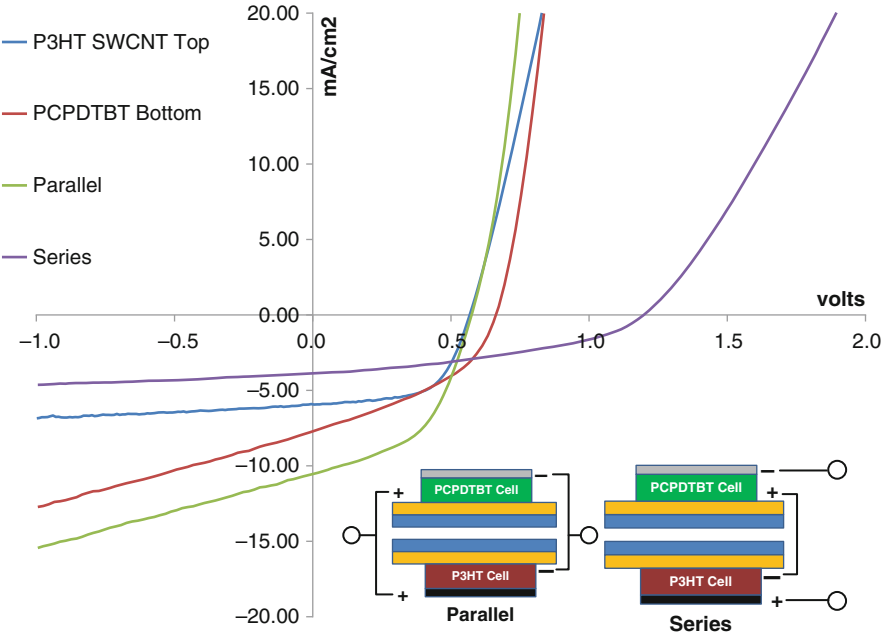

Fig. 15.15 Current-Voltage curves of single cells tested, semi-transparent P3HT top cell and opaque PCPDTBT bottom cell, as well as the non-monolithic tandem cells. The inset of the plot shows a graphical representation of the cells physical configuration as well as electrical connections for both parallel and series connections

which gives losses of 50 % . V_{OC} is right in the middle of both V_{OC}. For S-T the total V_{OC} = 1.22 V, which is close to 0.57 + 0.69 = 1.26 V, with negligible losses due to shading effect. The losses of J_{SC} are unfortunately large: J^{T}_{SC} = 5.27 mA/cm^2, which is even smaller than the J_{SC} of weakest sub cell $J_{SC,1}$ = 5.9 mA/cm^2. This is due to shading effect and probably reflects the loss of FF.

15.5 Conclusions

Series and parallel connections of solar cells were analyzed using the results of a simple single-diode model. We demonstrated that to maximize the efficiency of series tandems it is important not only to match the short circuit currents but also the

FF: fill factors of the individual cells. In parallel tandems, the open circuit voltages should be equilibrated, i.e. chosen close to each other. In general, if two solar cells are not balanced, then the parallel connection is preferable due to smaller losses in the fill factor. We also showed that the direct connection of two unbalanced solar cells can result in overall lower efficiency when one of the cells is much less efficient than the other.

Acknowledgements The authors gratefully acknowledge funding from DOE STTR grant #DE-FG02-10ER86425 on *"Parallel Tandem Organic Solar Cells with Carbon Nanotube Sheet Interlayers"*.

References

1. Tanaka S, Mielczarek K, Ovalle-Robles R, Wang B, Hsu D, Zakhidov AA (2009) Monolithic parallel tandem organic photovoltaic cell with transparent carbon nanotube interlayer. Appl Phys Lett 94(11):113506. doi:10.1063/1.3095594. http://link.aip.org/link/APPLAB/v94/i11/p113506/s1&Agg=doi
2. Zakhidov A, Papadimitratos A, Mielczarek K (2010) Multijunction monolithic solar cells with transparent interlayers for inverted parallel-connection. http://patentscope.wipo.int/search/en/WO2012106002
3. GmbH H (2010) Heliatek achieves new world record for organic solar cells with certified 9.8 cell efficiency. http://www.heliatek.com/
4. Yang Y, Mielczarek K, Aryal M, Zakhidov A, Hu W, ACS Nano 0(0), null (0). doi:10.1021/nn3001388. http://pubs.acs.org/doi/abs/10.1021/nn3001388
5. Mielczarek K, Zakhidov A, Tanaka S (2012) Organic photovoltaics with carbon nanotube charge collectors: inverted structures for parallel tandems. Jpn J Electron Mater 12:47
6. Kim YH, Sachse C, Zakhidov AA, Meiss J, Zakhidov AA, Müller-Meskamp L, Leo K (2012) Combined alternative electrodes for semi-transparent and ITO-free small molecule organic solar cells. Org Electron 13(11):2422–2428. doi:10.1016/j.orgel.2012.06.034. http://www.sciencedirect.com/science/article/pii/S156611991200300X
7. Kim YH, Müller-Meskamp L, Zakhidov AA, Sachse C, Meiss J, Bikova J, Cook A, Zakhidov AA, Leo K (2012) Semi-transparent small molecule organic solar cells with laminated free-standing carbon nanotube top electrodes. Sol Energ Mater Sol Cells 96(0):244–250. doi:10.1016/j.solmat.2011.10.001. http://www.sciencedirect.com/science/article/pii/S0927024811005666
8. Tang CW (1986) Two-layer organic photovoltaic cell. Appl Phys Lett 48(2):183–185. doi:10.1063/1.96937. http://link.aip.org/link/?APL/48/183/1
9. Lögdlund M, Greczynski G, Crispin A, Fahlman M, Salaneck W, Kugler T (2001) Conjugated polymer and molecular interfaces. CRC Press, Boca Raton. doi:10.1201/9780203910870.ch4. http://dx.doi.org/10.1201/9780203910870.ch4
10. Coropceanu V, Cornil J, da Silva Filho DA, Olivier Y, Silbey R, Brédas JL (2007) Charge transport in organic semiconductors. Chem Rev 107(4):926–952. doi:10.1021/cr050140x. http://pubs.acs.org/doi/abs/10.1021/cr050140x
11. Lunt RR, Giebink NC, Belak AA, Benziger JB, Forrest SR (2009) Exciton diffusion lengths of organic semiconductor thin films measured by spectrally resolved photoluminescence quenching. J Appl Phys 105(5):053711. doi:10.1063/1.3079797. http://link.aip.org/link/?JAP/105/053711/1
12. Shaw PE, Ruseckas A, Samuel IDW (2008) Exciton diffusion measurements in poly(3-hexylthiophene). Adv Mater 20(18):3516–3520. doi:10.1002/adma.200800982. http://dx.doi.org/10.1002/adma.200800982

13. Brédas JL, Cornil J, Heeger AJ (1996) The exciton binding energy in luminescent conjugated polymers. Adv Mater 8(5):447–452. doi:10.1002/adma.19960080517. http://dx.doi.org/10.1002/adma.19960080517
14. Alvarado SF, Seidler PF, Lidzey DG, Bradley DDC (1998) Direct determination of the exciton binding energy of conjugated polymers using a scanning tunneling microscope. Phys Rev Lett 81:1082–1085. doi:10.1103/PhysRevLett.81.1082. http://link.aps.org/doi/10.1103/PhysRevLett.81.1082
15. Campbell IH, Hagler TW, Smith DL, Ferraris JP (1996) Direct measurement of conjugated polymer electronic excitation energies using metal/polymer/metal structures. Phys Rev Lett 76:1900–1903. doi:10.1103/PhysRevLett.76.1900. http://link.aps.org/doi/10.1103/PhysRevLett.76.1900
16. Halls JJM, Walsh CA, Greenham NC, Marseglia EA, Friend RH, Moratti SC, Holmes AB (1995) Efficient photodiodes from interpenetrating polymer networks. Nature 376(6540):498–500. doi:10.1038/376498a0. http://www.nature.com/doifinder/10.1038/376498a0
17. Yu G, Gao J, Hummelen JC, Wudl F, Heeger AJ (1995) Polymer photovoltaic cells: enhanced efficiencies via a network of internal donor-acceptor heterojunctions. Science 270(5243):1789–1791. doi:10.1126/science.270.5243.1789. http://www.sciencemag.org/content/270/5243/1789.abstract
18. Peumans P, Uchida S, Forrest SR (2003) Efficient bulk heterojunction photovoltaic cells using small-molecular-weight organic thin films. Nature 425(6954):158–162. http://dx.doi.org/10.1038/nature01949
19. Hiramoto M, Fujiwara H, Yokoyama M (1991) Three-layered organic solar cell with a photoactive interlayer of codeposited pigments. Appl Phys Lett 58(10):1062–1064. doi:10.1063/1.104423. http://link.aip.org/link/?APL/58/1062/1
20. Yu G, Gao J, Hummelen JC, Wudl F, Heeger AJ (1995) Polymer photovoltaic cells: enhanced efficiencies via a network of internal donor-acceptor heterojunctions. Science 270(5243):1789–1791. doi:10.1126/science.270.5243.1789. http://www.sciencemag.org/content/270/5243/1789.abstracthttp://www.sciencemag.org/cgi/doi/10.1126/science.270.5243.1789
21. Halls JJM, Walsh CA, Greenham NC, Marseglia EA, Friend RH, Moratti SC, Holmes AB (1995) Efficient photodiodes from interpenetrating polymer networks. Nature 376(6540):498–500. http://dx.doi.org/10.1038/376498a0
22. Padinger F, Rittberger R, Sariciftci N (2003) Effects of postproduction treatment on plastic solar cells. Adv Funct Mater 13(1):85–88. doi:10.1002/adfm.200390011. http://dx.doi.org/10.1002/adfm.200390011
23. Li G, Shrotriya V, Huang J, Yao Y, Moriarty T, Emery K, Yang Y (2005) High-efficiency solution processable polymer photovoltaic cells by self-organization of polymer blends. Nat Mater 4(11):864–868. http://dx.doi.org/10.1038/nmat1500
24. Shaheen SE, Brabec CJ, Sariciftci NS, Padinger F, Fromherz T, Hummelen JC (2001) 2.5 % efficient organic plastic solar cells. Appl Phys Lett 78(6):841–843. doi:10.1063/1.1345834. http://link.aip.org/link/?APL/78/841/1
25. Al-Ibrahim M, Ambacher O, Sensfuss S, Gobsch G (2005) Effects of solvent and annealing on the improved performance of solar cells based on poly(3-hexylthiophene): fullerene. Appl Phys Lett 86(20):201120. doi:10.1063/1.1929875. http://link.aip.org/link/?APL/86/201120/1
26. Peet J, Kim JY, Coates NE, Ma WL, Moses D, Heeger AJ, Bazan GC (2007) Efficiency enhancement in low-bandgap polymer solar cells by processing with alkane dithiols. Nat Mater 6(7):497–500. http://dx.doi.org/10.1038/nmat1928http://www.nature.com/nmat/journal/v6/n7/suppinfo/nmat1928_S1.html
27. Chen JT, Hsu CS (2011) Conjugated polymer nanostructures for organic solar cell applications. Polym Chem 2(2):2707–2722. doi:10.1039/C1PY00275A. http://dx.doi.org/10.1039/C1PY00275A
28. Weickert J, Dunbar RB, Hesse HC, Wiedemann W, Schmidt-Mende L (2011) Nanostructured organic and hybrid solar cells. Adv Mater 23(16):1810–1828. doi:10.1002/adma.201003991. http://dx.doi.org/10.1002/adma.201003991

29. Wang Q, Moser JE, Grätzel M (2005) Electrochemical impedance spectroscopic analysis of dye-sensitized solar cells. J Phys Chem B 109(31):14945–14953. doi:10.1021/jp052768h. http://pubs.acs.org/doi/abs/10.1021/jp052768h
30. Masahiro H, Minoru S, Masaaki Y (1990) Effect of thin gold interstitial-layer on the photovoltaic properties of tandem organic solar cell. Chem Lett 19(3):327–330
31. Yakimov A, Forrest SR (2002) High photovoltage multiple-heterojunction organic solar cells incorporating interfacial metallic nanoclusters. Appl Phys Lett 80(9):1667–1669. do:10.1063/1.1457531. http://link.aip.org/link/?APL/80/1667/1
32. Guo X, Liu F, Yue W, Xie Z, Geng Y, Wang L (2009) Efficient tandem polymer photovoltaic cells with two subcells in parallel connection. Organ Electron 10(6):1174–1177. doi:10.1016/j.orgel.2009.06.010. http://www.sciencedirect.com/science/article/pii/S156611 9909001724
33. O'Regan B, Grätzel M (1991) A low-cost, high-efficiency solar cell based on dye-sensitized colloidal TiO_2 films. Nature 353(6346):737–740. doi:10.1038/353737a0. http://www.nature.com/doifinder/10.1038/353737a0
34. Barbé CJ, Arendse F, Comte P, Jirousek M, Lenzmann F, Shklover V, Grätzel M (1997) Nanocrystalline titanium oxide electrodes for photovoltaic applications. J Am Ceram Soc 80(12):3157–3171. doi:10.1111/j.1151-2916.1997.tb03245.x. http://dx.doi.org/10.1111/j.1151-2916.1997.tb03245.x
35. Beek W, Wienk M, Janssen R (2004) Efficient hybrid solar cells from zinc oxide nanoparticles and a conjugated polymer. Adv Mater 16(12):1009–1013. doi:10.1002/adma.200306659. http://dx.doi.org/10.1002/adma.200306659
36. Beek WJE, Wienk MM, Kemerink M, Yang X, Janssen RAJ (2005) Hybrid zinc oxide conjugated polymer bulk heterojunction solar cells. J Phys Chem B 109(19):9505–9516. doi:10.1021/jp050745x. http://www.ncbi.nlm.nih.gov/pubmed/16852143
37. Kumar A, Sista S, Yang Y (2009) Dipole induced anomalous S-shape I-V curves in polymer solar cells. J Appl Phys 105(9):094512. doi:10.1063/1.3117513. http://link.aip.org/link/JAPIAU/v105/i9/p094512/s1&Agg=doi
38. Rowell MW, Topinka MA, McGehee MD, Prall HJ, Dennler G, Sariciftci NS, Hu L, Gruner G (2006) Organic solar cells with carbon nanotube network electrodes. Appl Phys Lett 88(23):233506. doi:10.1063/1.2209887. http://link.aip.org/link/?APL/88/233506/1
39. van de Lagemaat J, Barnes TM, Rumbles G, Shaheen SE, Coutts TJ, Weeks C, Levitsky I, Peltola J, Glatkowski P (2006) Organic solar cells with carbon nanotubes replacing In[sub 2]O[sub 3]:Sn as the transparent electrode. Appl Phys Lett 88(23):233503. doi:10.1063/1.2210081. http://link.aip.org/link/?APL/88/233503/1
40. Pasquier AD, Unalan HE, Kanwal A, Miller S, Chhowalla M (2005) Conducting and transparent single-wall carbon nanotube electrodes for polymer-fullerene solar cells. Appl Phys Lett 87(20):203511. doi:10.1063/1.2132065. http://link.aip.org/link/?APL/87/203511/1
41. Kaskela A, Nasibulin AG, Timmermans MY, Aitchison B, Papadimitratos A,Tian Y, Zhu Z, Jiang H, Brown DP, Zakhidov A, Kauppinen EI (2010) Aerosol-synthesized SWCNT networks with tunable conductivity and transparency by a dry transfer technique. Nano Lett 10(11):4349–4355. doi:10.1021/nl101680s. http://pubs.acs.org/doi/abs/10.1021/nl101680s
42. Kuznetsov A, Zakhidov A (2013) To Be Submitted (in press)

Chapter 16
Optimization of Carrier Harvest in MEG Based Hybrid Solar Cells

Nigora Turaeva, Boris Oksengendler, Murad Marasulov, and Sardor Nuraliev

Abstract In this work the statistic theory of multiple exciton generation in quantum dots based on the Fermi approach to the problem of multiple elementary particles generation at nucleon-nucleon collisions is generalized taking into account the generation of phonons along with electrons and holes. Size and shape optimization of quantum dot has been performed to receive the maximum multiplicity of MEG effect. The role of interface electronic states of quantum dot and ligand has been considered by means of quantum mechanics approaches. Besides the resonance tunneling of electrons and holes through interface described by two barriers potential well has been considered in the classical approximation. The efficiency of photon energy conversion into electrical one at presence of MEG effect in QDs has been calculated in the frame of Fermi statistical mechanism. The process of fast decay of exciton in polymer matrix by effective acceptor doping has been theoretically analyzed by means of Migdal's approach in weakly ionized plasma.

16.1 Introduction

Now it is well-known established among solar energetic specialists that one of the most promising approaches in developing of third generation solar cells is the effect of multiple exciton generation (MEG) in quantum dots [1]. One of possible structures of such solar cells consists of semiconductor quantum dots covered by ligands of organic molecule and imbedded into polymer matrix. The function of

N. Turaeva (✉)
Biological Department, Webster University, 470 E Lockwood Ave, St. Louis, MO 63119, USA
e-mail: nigoraturaeva82@webster.edu

B. Oksengendler • M. Marasulov • S. Nuraliev
Theoretical Department, Institute of Polymer Chemistry and Physics, 7B Kadyri A. Street, 100128 Tashkent, Uzbekistan
e-mail: oksengendlerbl@yandex.ru; mbm1005@mail.ru

R. Egger et al. (eds.), *Low-Dimensional Functional Materials*, NATO Science for Peace and Security Series B: Physics and Biophysics, DOI 10.1007/978-94-007-6618-1_16,

such solar cells is based on the following principles. By absorption of high-energy photon in a quantum dot several excitons are simultaneously generated. These excitons present electron hole pairs whose components move in different way: electrons tunnel between quantum dots by percolation whereas holes tunnel into polymer matrix and by dispersion transport move along the polymer chains. Special design of structural components of solar cells allows collecting electrons and holes on electrode surfaces.

16.2 MEG Effect

The principle effect in quantum dots based solar cells is a simultaneous generation of several excitons in quantum dot with small electron gap E_g at absorption of high-energy photon $h\nu >> E_g$. The effect was predicted 10 years ago [16] and proved experimentally [23] in quantum dots. The physical nature of this effect was discussed by theorists who proposed four options of the theory [8, 10, 18, 24]. But it seems that most productive approach allowing to study MEG effect on quantitative and qualitative levels is the statistic theory of MEG developed in Tashkent [18]. According to this approach the deep analogy is observed between MEG and Fermi's interpretation of the phenomena of multiple generation of mesons [9]. We suppose that the micromechanism is based on the effect of electron shaking that takes place in quantum dot at fast electron transition from the valence band to the conductivity band at absorption of high-energy photon [18, 21].

Generalizing the S calculation algorithm developed by Fermi and taking into account the generation of three types of particles ($n/2$ electrons, $n/2$ holes and p phonons) with different laws of dispersion ($\varepsilon_e = P_e^2/2m_e$, $\varepsilon_h = P_h^2/2m_h$, $\varepsilon_{ph} = C_s P_{Ph}$ where C_s is the sound speed, $P_e\ P_h\ P_{Ph}$ are the momenta of electron, hole and phonon, respectfully), we obtain a new expression for the statistical weight as compared to [18].

$$S(n,p) = \frac{(m_0)^{\frac{3n}{2}} (f_e f_n)^{\frac{3}{4}n} \Omega^{\frac{n}{2}+\frac{1}{3}}}{2^{\frac{3n}{2}} \pi^{\frac{n}{2}+\frac{2}{3}} \hbar^{\frac{3n}{2}+1} \left(3P+\frac{3n}{2}-1\right)!} \left[\frac{\Omega^{\frac{1}{3}}(h\nu - n\tilde{E}_g)}{\pi^{\frac{2}{3}}\hbar C_s}\right]^{3P+\frac{2}{3}n+1} \tag{16.1}$$

Here, the momentum of each electron and hole is three-dimensional and phonon has two transversal degrees of freedom and one longitudinal degree of freedom, $h\nu$ is the energy of primary high-energy phonon; only direct electron transitions are taken into account here, m_0 is the free electron mass, $m_0 f_e$ and $m_0 f_n$ are the effective masses of electron and hole.

On the basis of Eq. (16.1), it is easy to calculate a mean multiplicity of generated electrons, holes and phonons

$$\overline{n}_e = \overline{n}_h = < N_{ex} >; \tag{16.2}$$

$$\overline{n}_e = \overline{n}_h = \sum_{n,p} nS(n,p)/2\sum_{n,p} S(n,p) \tag{16.3}$$

$$\overline{n}_{ph} = \sum_{n,p} pS(n,p)/\sum_{n,p} S(n,p) \tag{16.4}$$

With the data on the quantum dot sizes and phonon energy a curve of the exciton distributions $R(n)$ can be plotted for quantum dots PbSe where the MEG effect was observed [23]. It can be easily shown that the basic criterion of the Poisson distribution of fluctuations $\{\overline{n^2} = (\overline{n})^2 + \overline{n}\}$, as interpreted by MEG according to the statistical theory (Formula 16.1), is not met. We can do it on the basis of Formulas (16.1, 16.2 and 16.3) with the phonon approximation for simplicity, i.e. for $p = 0$. For example, for a quantum dot of the radius R = 3 nm it turned out that $\overline{n} = 4.2$; $(\overline{n})^2 = 17.64$; $\overline{n^2} = 18.4$ for irradiation by photons with energy $h\nu = 3.63E_g$ and $\overline{n} = 5.7$; $(\overline{n})^2 = 32.49$; $\overline{n^2} = 33.46$ for $h\nu = 4.9E_g$, i.e. $\overline{n^2} \neq (\overline{n})^2 + \overline{n}$. Hence, the fluctuation distribution of exciton multiplicity is non-Poissonian [26]. A deviation from the Poisson law increases with the raise in photon energy, i.e. $\frac{d|\overline{n^2}-(\overline{n})^2-\overline{n}|}{d(h\nu)} > 0$. This formula is in agreement with the experimental results for quantum dots based on PbSe of different sizes and Si.

16.3 The Role of a Boundary Between Quantum Dot and Ligand

As experiments show, the role of electron states of the boundary between quantum dot and ligand is extremely important in terms of existing of MEG effect [13, 17]. It is connected to *the another fundamental property of nanoparticles asserting that a ratio of surface and volume electron states are commensurable values*. The role of surface can be understood on the basis of quantum-mechanical theory of disturbances of closely located levels (ε_1 and ε_2 are the energies of ligand and Tamm's state of quantum dot accordingly). It should be noted that ε_2 depends on size of quantum dot [18]. These levels are split at chemical bonding and give electron states: $\tilde{\varepsilon}_1$ and $\tilde{\varepsilon}_2$ [15]:

$$\tilde{\varepsilon}_{1,2} = \frac{\varepsilon_1 + \varepsilon_2 + H_{11} + H_{22}}{2} \pm \frac{1}{2}\sqrt{\frac{(\varepsilon_1 + \varepsilon_2 + H_{11} + H_{22})^2}{4} - (\varepsilon_1 + H_{11})(\varepsilon_2 + H_{22}) + |H_{12}|^2} \tag{16.5}$$

where H_{ii} is the change of energy of ε_1 and ε_2 caused by their interaction on a boundary between them and H_{12} is the exchange integral. Obviously under weak interaction of electron wave functions of ligand and quantum dot surface ($H_{12} \to 0$) unperturbed levels fall into the energetic gap whereas in case of strong overlapping of wave functions ($H_{12} \neq 0$) levels can fall into valence band and conductivity band.

It is clear that in these cases the role of boundary electron states is different and can influence onto MEG effect by different way. Note that the role of surface electronic levels are dual: they can participate in the primary transitions under shaking, effectively reducing E_g (i.e. increasing the average multiplicity of excitons) and also they can serve as centers of recombination of electron-hole pairs, decreasing the average multiplicity of excitons. The probability of each option depends on location of the $\tilde{\varepsilon}_1$ and $\tilde{\varepsilon}_2$.

16.4 Size and Shape Optimization of Quantum Dot

The fact that the formula for the probability of generation $e-h$ pairs include several factors depending on radius of quantum dots $m(R_0), \Omega(R_0), E_g(R_0)$ allows to arise a problem of finding of optimal value R0 maximizing the quantum efficiency of MEG. For this purpose we can find the extremum of the value $\ln S(n)$. Taking into account the following expressions:

$$m \approx \frac{m_0}{5}\left[1+\frac{4}{5}\chi^2\left(\frac{a^2}{R_0^2}\right)\right]; E_g = E_g^0 + \frac{\hbar^2\chi^2}{2m_0a^2}\left(\frac{a^2}{R_0^2}\right); \Omega = \frac{4\pi}{3}a^3\left(\frac{R_0^3}{a^3}\right) \quad (16.6)$$

we obtain $\ln S(n)$ (see Eq. 16.1).

The condition $\frac{d\ln(S(n))}{dR_0} = 0$ gives the first approximation:

$$R_0^{opt} = a\chi\left(1-\frac{5}{24}\left(\frac{3}{2}n-1\right)n\frac{1}{h\nu}\frac{\hbar^2}{2m_0a^2}\right)^{1/2}. \quad (16.7)$$

It is clear, that R_0^{opt} increases with the energy of photon; the type of materials is taken into account by size of interatomic distance a; the second approximation gives us the dependence R_0^{opt} on E_g^0 and a.

It can be raised the natural question about the optimal shape of quantum dot. It is not certainly obvious that spherical shape of quantum dot can give the maximum probability of the MEG effect. Let us analyse this problem is based on electron shaking theory. We suppose that spherical quantum dot is deformed at small one-axis strain in result of which the sphere is converted either into the ellipsoid or spheroid. The strain of the sphere is characterized by means of perturbation parameter $\delta = 2\frac{a-b}{a+b}$, where a and b are the semi-major and semi-minor axes accordingly. We assume that the deformation of quantum dot does not change its volume ($R^3 = ab^2$). Basing on results [15], we suppose that the local energy levels of electron and their wave functions are perturbated at deformation and the probability of electron shaking is defined as

$$W_{non-sphere} = \frac{|<\tilde{n}+1_{non-sphere}|V|\tilde{n}_{non-sphere}>|^2}{(E_{\tilde{n}+1}^{non-sphere} - E_{\tilde{n}}^{non-sphere})^2} \quad (16.8)$$

here $\tilde{n}$ is the number an electron state on well, modeling quantum dot. We have the following [15]:

$$E_{\tilde{n}}^{non-sphere} = E_{\tilde{n}}^{sphere} + < \tilde{n}_{sphere}|H'|n_{sphere} > \tag{16.9}$$

$$|\tilde{n}_{non-sphere} >= |\tilde{n}_{sphere} > + \frac{< \tilde{n}+1_{sphere}|H'|\tilde{n}_{sphere} >}{E_{\tilde{n}+1}^{sphere} - E_{\tilde{n}}^{sphere}} |\tilde{n}+1_{sphere} > \tag{16.10}$$

The perturbation of quantum dot shape H' is proportional to the deformation δ:

$$H' = -\delta \frac{\hbar^2}{3m} \left(\nabla^2 - 3\frac{\partial^2}{\partial z^2} \right). \tag{16.11}$$

It is obvious from the expression $W_{non-sphere}$ depends on δ in a com-plicated manner. Keeping the terms which are linear to δ, we can suppose that $W_{non-sphere} \approx W_{sphere} + \delta \times F(m.e.)$, where $F(m.e.)$ is the complicated function of different elements, shaking operator V and deformation H' by wave functions of non-perturbated spherical quantum dot. The function of $F(m.e.)$ depends on the states of $\tilde{n}$ and $\tilde{n}+1$, which present the high occupied and low unoccupied orbitals of quantum dot, accordingly. The probability of electron shaking is positive ($F(m.e.) > 0$) and it can be increased at elliptical deformation of quantum dot and decreased at spherical deformation. It is interesting to note that this conclusion is valid for the initial process of MEG effect that is absorption of photon, the probability of which is defined by the cross-section σ_1^{ex} [18]. Recently it was reported [6] a significant enhancement of multiple exciton generation in PbSe quasi-one-dimensional semiconductors (nanorods) over zero-dimensional nanostructures (nanocrystals), characterized by a 2-fold increase in efficiency ($\eta_{MEG} = 0.81$) and reduction of the threshold energy to $(2.23 \pm 0.03)E_g$, while for PbSe nanocrystals it is about $3.43E_g$. Moreover the threshold doesn't depend almost on energy gap of nanorods, which is a function of rods cross-section. It seems the ratio effective masses of electron and hole in rods to be decreased compared to the one for QDs.

In the section devoted to the analysis of quasi-particle passage through a boundary quantum dot polymer we did not consider radiative recombination of electron and hole (the probability $1/\tau_r$) as a relaxation process impeding such passage. At a usual quantum dot that is absolutely justified. However, there is a situation when the process of spontaneous photon radiation can play a fundamental role. Assume (as a dream) that a technology of quantum dot production is so high that it allows a cavity with uniquely high quality factor Q. Let Q approach to the values obtained in experiments by [11]. Then at such quantum dots it is possible to expect manifestation of a nice Purcell effect showing in our case that while generation of primary exciton by high-energy photon provided that the wave length of such exciton emission λ is more than the double diameter of the cavity ($\lambda/2d > 1$) the photon emission will be suppressed (Fig. 16.1). However, according to the Bothe concept [4] the Auger effect calculated by Mller [14] in the relativistic approximation takes place as photon conversion. Therefore, usually occurring at

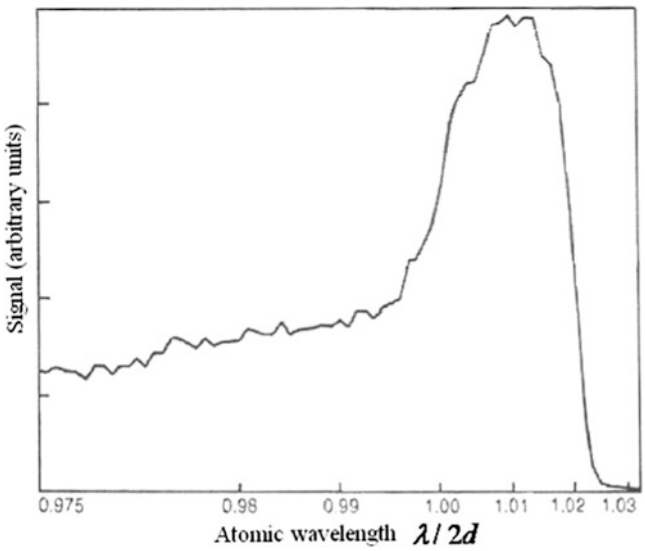

Fig. 16.1 Probability of spontaneous photon emission on cavity

quantum dots for 10^{-11} s, the Auger effect takes place after photon emission that according to the Purcell effect and proved for optical range in experiments of cavity quantum electrodynamics [11] is suppressed at the quantum dots where the MEG is realized ($\lambda/2d >> 1$ for $d = 2R$). As a result, τ_A can be an order of the time of resonance tunneling and the outer efficiency is $\beta \to 1$ (see Sect. 16.5). The present nanotechnologies allow this mechanism of sharp increase of β to be considered as a dream. Another possibility of effective harvest of the electrons and holes from MEG effect is the disposition of QDs into photonic crystals in which photon energy gap corresponds to the energy of involved photons so the spontaneous and Auger-recombination recombination can be suppressed which can increase the charge transfer processes in QDs.

16.5 Charge Separation at Boundary in Third-Generation Solar Cells

Right after exciton excitation owing to the MEG effect at quantum dots (stage I) in solar cells there are two successive stages: – exciton separation into electrons and holes at boundary and – separate transport of *e*- and *h*-carriers from quantum dot to boundary. The second stage with the results obtained in the previous section about the electronic structure of boundary is under consideration in this section. Let us consider an electronic structure of the boundary: these are five successive regions I, II, III, IV and V (Fig. 16.2). Here I and V are the regions of quantum

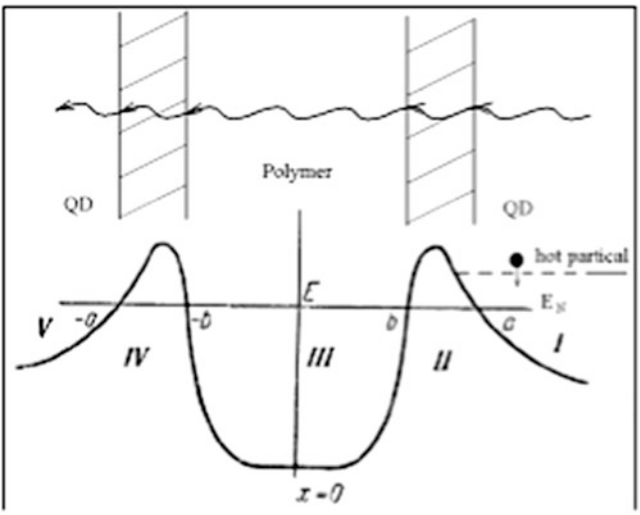

Fig. 16.2 Resonance tunneling of electron excitation through border

dots, III is the region of a solvent, II and IV are the regions of barriers. It is clear that electron transport is the resonance tunneling between neighboring quantum dots through two barriers; a hole moves from a quantum dot through polymer tunneling through one barrier.

The situation for electron is interesting. The tunneling probability in the classical approximation (see Bohm [3]) is as follows

$$T = \left[1 + \frac{\tau_0^2}{\hbar^2}\left(E - \frac{1.78e^2}{\varepsilon R} - E_i\right)^2 \Theta^4\right]^{-1} \tag{16.12}$$

Here, E is the level of exciton energy at the quantum dot, $1.78e^2/\varepsilon R$ is the binding energy at the quantum dot, E_i is the level of electron energy in the solvent, τ_0 is the oscillation period in the region III, $\Theta = exp\left[\int_b^a P_n \frac{dx}{\hbar}\right]$, P_n is the electron momentum in the region I. It is seen that for $E = E_i$ the tunneling through two successive barriers takes place with the 100 % probability. The hole tunneling is usual and its great probability is due to a small size of the ligand molecule.

However, if in the barrier there is an orbital occupied by electron then the resonance-type tunneling through this level is possible, which increases the probability of hole tunneling.

It is seen that the kinetics of electron accumulation in the outer chain is defined by the expression

$$N_q(t) = N_0 \exp\left[-\frac{t}{\tau_A} + \frac{T}{\tau_0}t\right] \tag{16.13}$$

where τ_A is the time of Auger recombination of electron and hole at the quantum dot, N_0 is the number of excitons generated at the quantum dot during a single act of the MEG effect. The exciton lifetime at the quantum dot is defined as $\tau_{ex} = \frac{\tau_0}{T}(\tau_A)/(\frac{\tau_0}{T} + \tau_A)$ and the outer quantum yield of carriers as $\beta = \frac{N_q(t)}{N_0}$. It is interesting to compare the result of this analysis with the experiment [2]. As shown by these experiments, when the quantum dot surface PbSe is treated by different solvents the outer quantum MEG yield that is defined as a share of photons absorbed by the quantum dots generating the carriers in the outer chain can be significantly varied. Different treatments lead to changing several system parameters: (1) exciton lifetime, (2) biexciton lifetime, (3) distance between the quantum dots, (4) quantum yield of MEG. For surface treatment a share of removed oleic molecules is different in different cases. Analysis of experimental data results in the following conclusion. (1) The lifetime of single exciton decreases for all the types of treatments except pure solvent ethanol (EtOH). (2) The lifetime of biexciton increases when the distance between the quantum dots decreases. (3) The quantum yield of MEG decreases for all the types of treatments except one with pure solvent ethanol (EtOH). These experimental facts can be interpreted on the basis of the Formula (16.12). A decrease in the exciton lifetime for treatment with different substances can be explained by a decrease in the time of Auger-relaxation owing to recombination at the free surface states when the passivating agents are removed, as well as by an influence of the treatment substances on the position of the exciton energy level in the quantum dot and electron in a solvent and on the barrier parameters width and height. Evidently, only in the case of ethanol treatment, ethanol makes influence on the barrier parameters: the tunneling coefficient increases, which leads to variation of the quantum yield.

16.6 Separation of Charge Carriers in Polymer Matrix of Solar Cells

In all solar cells based on polymer composition structures the exciton excitations are formed by photon absorption. The most important and completely non-evident stage of solar cell operation is exciton separation into electrons and holes. For excitons generated by the quantum dots such separation takes place while resonance tunneling through a boundary quantum dot polymer owing to difference in the effective mass of electron and hole and their different rate of energy relaxation inside the quantum dot (see Sect. 16.5). However, with the great probability the exciton tunnels as a whole through a boundary and then moves along the polymer chain as a whole quasi-particle. Besides, some part of photons is absorbed directly in the polymer chain. As a result, a great number of excitons migrate in the polymer chain. Therefore, there is an important problem of their separation onto components. More perspective way is electron capture by special dopants placed in the polymer matrix, for example by fullerene molecules [1] (Fig. 16.3). That is why there is an actual problem of developing a theoretical model of exciton breaking and electron re-capture by a dopant. By using a linear part of polymer along which the exciton

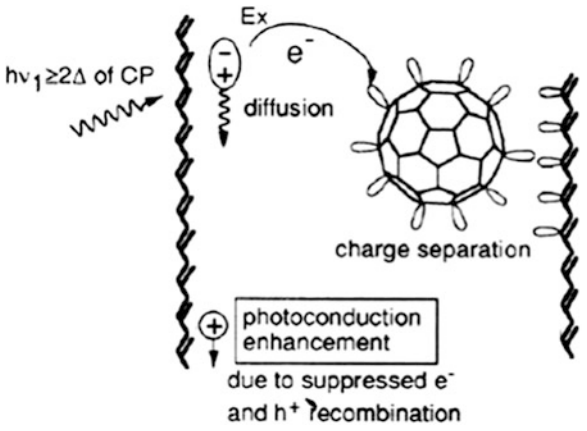

Fig. 16.3 Separation of electron and hole by means of recharging

moves and assuming a great mass of hole ($m_h \gg m_e$) it is possible to consider exciton dissociation owing to electron transition from exciton into a potential well of the dopant (Fig. 16.3) as a phenomenon of recharging in weakly ionized plasma between a linearly moving hydrogen-like atom with a hole as its nucleus and a free potential well formed (for simplicity) by an effective positive charge (Fig. 16.3). Drawing step by step this analogy, we obtain that the probability of exciton decay with electron capture by a dopant will be (see Migdal [15])

$$W = \sin^2 \frac{1}{2} \int_{-\infty}^{\infty} (U_u - U_g) dt \tag{16.14}$$

For great distances between the polymer chain and dopant ($\rho \gg 1$) in atomic units we have $U_g - U_u = \frac{4}{e} R e^{-R}$. Here, U_g and U_u are the bonding and anti-bonding terms of hole-dopant molecule. With $R^2 = \rho^2 + v^2 t^2$ (Fig. 16.3) we have the classical result (see Migdal [15]):

$$W(\rho) = \frac{2\pi^2}{e^2 v^2} \rho^3 e^{-2\rho} \tag{16.15}$$

Then the average cross section of exciton decay $ex \to h + e$ will be

$$\sigma_+ = \int_0^{\infty} W(\rho) 2\pi\rho d\rho \tag{16.16}$$

With the usual units we obtain

$$\sigma_+ = \frac{\pi}{2} \left(\frac{\hbar^2}{me^2} \right)^2 \ln^2 \frac{e^2}{v\hbar} \approx 14\pi \ln^2 \frac{2.2 \cdot 10^6}{v} (Mb) \tag{16.17}$$

Here, $1Mb \approx 10^{-22} m^2; [v] = \frac{m}{s}$.

Note that the model complication owing to consideration of the case of small deviation from resonance [7] instead of resonance recharging makes no changes in slope opposition of σ_+ and ν. The general estimation is of interest, but the result of slope opposition of the probability of exciton decay and its mobility in the polymer chain is also important. This is another criterion to choose a polymer matrix. The result obtained, to a certain extent, reduces interest to using as a polymer matrix such ultra perspective polymer rubrene known by its unique great mobility of quasi-particles.

16.7 Ultimate Efficiency of Conversion of Solar Energy onto Electrical One

The MEG effect if one of the perspective ways of creation of third generation solar cells, therefore it arise the principal problem of ultimate efficiency conversion of solar energy into electrical one. From the law of energy conservation and accounting the energy losses $(h\nu - n\tilde{E}_g)$ at simultaneous generation of n electrons $(n < n_{max} = h\nu < \tilde{E}_g)$ for partial efficiency of conversion of photon energy into the n electrons transition energy we receive

$$\eta(n) = \frac{h\nu - (h\nu - n\tilde{E}_g)}{h\nu} = \frac{n\tilde{E}_g}{h\nu} \tag{16.18}$$

The mean efficiency of conversion is defined as

$$\overline{\eta} = \frac{\tilde{E}_g}{h\nu}\frac{\sum nS(n)}{\sum S(n)} = \frac{\tilde{E}_g}{h\nu}n_{max} \tag{16.19}$$

Here it is taken into account the distribution function $(S(n)/\sum S(n))$ the maximum of which is observed at $n = n_{max}$. Introducing the different effective masses for electrons and holes ($m_e = m_o f_e$ and $m_h = m_o f_h$) and expressing all parameters through world units we can transform the function $S(n)$ into more convenient form. Going from discrete form of $S(n)/\sum S(n)$ to quasi-continuing one on the base of statistical approach we receive the following

$$n_{max} \approx y\ln(Zy) + \frac{1}{3} \tag{16.20}$$

where $y = h\nu/\tilde{E}_g$, $Z = \frac{\omega^2\sqrt{f_e f_h}}{2\pi}\left(\frac{\tilde{E}_g}{\hbar^2/m_0 a_0^2}\right)$, $\omega = \frac{4\pi}{3}(R/a_0)^3$, a_0 is the Bohr raius. Note that the mean value of $\overline{n}$ for the function (16.19) can be evaluated using the microscopic approach [18, 21]: $\overline{n} = \sum nF_n$, but we will perform the evaluation on the base of statistical (1) and (2). For example, for a quantum dot of PbSe with the following parameters $_g$ = 0.64 eV, R = 3.9 nm and the photon energy $h\nu = 4.9_g$

we receive $\eta \approx 60$ %, that is much greater that ultimate efficiency calculated by Shockley Queisser for bulk materials (31 %) [1]. It is obvious that the real efficiency of third generation solar cells will be less than the evaluated magnitude of efficiency if we take into account the losses of charges at passing the interface of quantum dot and ligand and transporting them through polymer matrix.

16.8 Conclusion

As problems for future researches of MEG effect we can formulate the following: (1) Regulating level of passivation of surface states; (2) Calculation of the efficiency taking into account MEG effect and open state of the system; (3) Solution of the problem of radiation stability and degradation resistance of solar cells based on quantum dots (recently the first results [20] have been received in this field showing possibility of regulation of radiation stability by the state of the boundary quantum dot matrix).

References

1. Basic research needs for solar energy utilization. Report of the basic energy sciences workshop on solar energy utilization, April 18021, 2005, Second Printing, October 2005, U.S. Department of Energy (DOE)
2. Beard MC et al (2009) Variations in the quantum efficiency of multiple exciton generation for a series of chemically treated PbSe nanocrystal films. Nano Lett 9:836
3. Bohm D (1952) Quantum theory. Prentice-Holl, New York
4. Bothe W (1926) Uber die Kopplung zwischen elementaren Strah-lungsvorgangen, Zeitschrift fur Physik 37:547
5. Chepic DI, Efros Al L, Ekimov AI et al (1990) Auger ionization of semiconductor quantum dots in a glass matrix. J Luminescence 47:113
6. Cunningham PD et al (2011) Enhanced multiple exciton generation in quasi-one- dimensional semiconductors. Nano Lett 11:3476
7. Demkov YN (1963) Recharging under little defect of resonance. J Exp Theor Phys 45:195
8. Ellingson R, Beard M, Jonson J et al (2005) Highly efficient multiple exciton generation in colloidal PbSe and PbS quantum dots. Nano Lett 5:865
9. Fermi E (1950) High energy nuclear events. Progr Theor Phys 5:570
10. Franceschetti A, Anh J, Zunger A (2006) Impact ionization can explain carrier multiplication in PbSe quantum dots. Nano Lett 6:2191
11. Haroche S, Kleppner D (1989) Cavity quantum electrodynamics. Phys Today 42(1):24
12. Hulet RG, Hilfer ES, Kleppner D (1985) Inhibited spontaneous emission by a Rydberg atom. Phys Rev Lett 55:2137
13. Klimov VI, McGuire JA, Sykora M et al (2010) Apparent versus true carrier multiplication yields in semiconductor nanocrystals. Nano Lett 10:20492057.
14. Mller C (1931) Uber den Sto? zweier Teilchen unter Berucksichtigung der Retardierung der Krafte. Z fr Phys 70:786
15. Migdal AB(1975) Quality methods of quantum theory. Nauka, Moscow
16. Nozik AJ (2002) Quantum dot solar cells. Physica E 14:115

17. Nozik AJ, Beard MC, Midgett AG et al (2010) Comparing multiple exciton generation in quantum dots to impact ionization in bulk semiconductors: Implications for enhancement of solar energy conversion. Nano Lett 10:30193027
18. Oksengendler BL, Turaeva NN, Rashidova SS (2009) Statistic theory of multiple exciton generation in quantum dots. Appl Sol Ener 3:36
19. Oksengendler BL, Turaeva NN (2010) Surface Tamm states of curved surface of ionic crystals. Dokl Acad Nauk Russia 434:1
20. Oksengendler BL, Turaeva NN, Maksimov SE et al (2010) Peculiarities of radiation defect production in nanocrystals embedded in solid matrix. J Exp Theor Phys 111:415
21. Oksengendler BL, Turaeva NN, Uralov I et al (2012) Statistics, synergetics, and mechanism of multiple photogeneration of excitons in quantum dots: Fundamental and applied aspects. Appl Sol Ener 3:6
22. Oksengendler BL, Turaeva NN, Rashidova S (2012) Advanced theory of multiple exciton generation effect in quantum dots. Eur Phys J B 85:218
23. Schaller R, Klimov VI (2004) Spontaneous emission probabilities at radio frequencies. Phys Rev Lett 92:186601
24. Schaller RD, Agranovich VM, Klimov VI (2005) High efficiency carrier multiplication in PbSe nanocrystals: Implications for solar energy conversion. Nat Phys 1:189
25. Schaller RD, Petruska MA, Klimov VI (2005) High-efficiency carrier multiplication through direct photogeneration of multi-excitons via virtual single-exciton states. Appl Phys Lett 87:253102
26. Turaeva NN, Oksengendler BL, Uralov I (2011) Non-Poissonian exciton populations in semiconductor nanocrystals via carrier multiplication. Appl Phys Lett 98:243103

Chapter 17
Thermoelectric Nanowire Arrays Response to Illumination

Tito Huber, Reum Scott, Scott Johnson, Tina Brower, Albina Nikolaeva, and Leonid Konopko

Abstract Bismuth nanowire arrays configured on devices where they are capped with a transparent indium tin oxide electrode generate electric power when exposed to light. The arrays feature poor optical reflectivity and, possibly, light trapping. We show experimental results that indicate that the arrays respond to illumination owing to the thermoelectric conversion of heat absorbed at the surface. The unique features of the energy pathway are manifested through a strong temporal and photon wavelength dependence of the photoresponse. Energy conversion in thermoelectrics with light trapping surfaces is a path to fast infrared light detection and across-the-spectrum solar energy harvesting.

17.1 Introduction

Optoelectronics is based on devices that convert optical energy into electrical energy and vice versa [15]. For semiconductor optoelectronic devices such as silicon solar cells, photon absorption leads to the transfer of charge between different electronic bands, resulting in a photocurrent (PC). It recently has been shown that the two dimensional material graphene exhibits hot carrier thermoelectric (TE) photoresponse, an effect where electrical power is generated by the heating associated with the absorption of light at the nanoscale [5, 19]. Here we show that

T. Huber (✉)
Department of Chemistry, Howard University, 500 College St. NW, Washington, DC 20059, USA
e-mail: thuber@howard.edu

R. Scott • S. Johnson • T. Brower
Department of Electrical Engineering, Nanoscale Science and Engineering Center, 2300 Sixth St. NW, Washington, DC 20059

A. Nikolaeva • L. Konopko
Institute of Electronic Engineering and Industrial Technologies, ASM, Chisinau MD-2018, Moldova

R. Egger et al. (eds.), *Low-Dimensional Functional Materials*, NATO Science for Peace and Security Series B: Physics and Biophysics, DOI 10.1007/978-94-007-6618-1_17,

nanowire arrays (NWAs) of bismuth feature a TE photoresponse and we study the nanoscale optical and TE properties that give rise to the effect.

TE effects are caused by the difference in the broadening of the energy distribution in the electronic bands owing to a temperature gradient. The efficiency of TE power conversion is gauged by the figure of merit $Z = \alpha^2\sigma/(T\kappa)$, where α is the thermopower, σ is the electrical conductivity, κ is the thermal conductivity, and T is the absolute temperature. Some materials—namely, traditional TE materials, in a short list that includes bismuth—have large thermopower values and a large σ/κ, leading to exceptionally large Z values [12] and, therefore, high efficiency. Bulk TE crystals are not good candidates in the search for TE photoresponse effects because energy dissipates quickly in these systems. Also, a motivation for our work was that κ is less in nanowires than in the bulk [11]. Also, the high optical reflectivity of the front surface of bulk thermoelectrics is not conducive for conversion. Indeed, in a variety of bulk systems including bulk crystalline semiconductors and Bi this effect appears only under pulsed illumination [10]. In their investigation of PC's in solar cells, researchers have discovered that the nanostructuring of bulk materials into nanowires or sharp points aligned along the optical incident direction results in reduced optical reflection and induced light trapping [4, 6]. There are many mechanisms that may play a role. NWAs optical reflection is weak because the electromagnetic field penetrate deeply in the material. This property has been attributed to dipole effects because the wires are pointing parallel to the light wave vector and the photon electric field is perpendicular to the wire length [20]. NWA optical trapping has been discussed also in the context of optical metamaterials [3, 7]. The aim of this paper is to report on the fabrication of TE devices composed of Bi NWAs and its photoresponse. We find that the photoresponse is excited by infrared and visible illumination. Under visible illumination, the response is complex. However, under infrared illumination the photoresponse is simply governed by heat diffusion and can be inequivocally attributed to TE effects.

17.2 Fabrication and Characterization

We fabricated devices composed of bismuth NWAs that were integrated with electrodes consisting of a bottom bulk bismuth layer and a thin film of indium tin oxide (ITO) (see Fig. 17.1). The length of the nanowire array L, not considering the bulk bismuth layer, was 50 mm and the active area S of the array was $\sim$1 mm^2. The thickness of the ITO film, composed of 90 % In_2O_3 and 10 % Sn_2O_2, was 50 nm. It was deposited with a Cressington sputter coater. The current versus voltage (I-V) relationship of the detector, was symmetric and Ohmic, without features that might have indicated the presence of Schottky barriers. The resistance was 6.3 kΩ. Because the contact resistance between the silver epoxy (Epotek 411V) and the bulk bismuth, as well as the one between the bismuth nanowires and the bulk bismuth, was low ($<$1 Ω), the I-V value that we measured was mainly related to the front

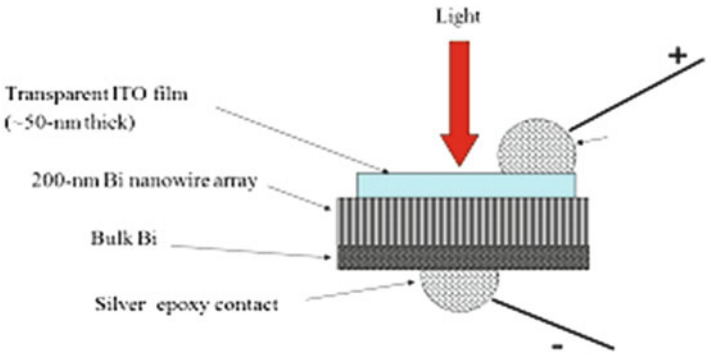

Fig. 17.1 Schematic of the bismuth (*Bi*) nanowire arrayindium tin oxide (*ITO*) device

surface. We have not measured the number of wires that are connected to the ITO and also we do not know the value of the contact resistance. However the individual Bi NW resistance is $\sim$500 Ω and therefore we find that the contact resistance is comparable to the measured total resistance (6 kΩ). The temperature of the TE junction that detects the light energy, which is located at the front surface and is presumed to be the one that is established at the nanowire array-ITO interface, is T_F. Because the circuit is closed between the ITO film and the back of the array, which is thermally ground at ambient temperature T_0, the thermoelectric signal can be considered proportional to $T_F - T_0$.

The arrays were fabricated using a template method—namely, the high pressure injection (HPI) method—in which the melt of the alloy of interest is injected in a porous insulator using high pressure [8]. The fabrication is illustrated in Fig. 17.2.

We used a commercial alumina membrane disk (Anopore, Whatman, MA, USA) with a thickness of about 55 μm. It supports an array of parallel, largely non-interconnected, cylindrical channels of 200 nm in diameter parallel to the disk axis. To inject bismuth in the pores, we placed high-purity bismuth pellets (99.999 %, Sigma-Aldrich) in contact with the Anopore alumina membrane inside a high pressure reactor. The reactor was heated to a temperature above the melting point of Bi (270 °C); in the experiments presented here, this temperature was 400 °C. Next the pressure was gradually increased to 1 kbar, forcing the molten material into the matrix channels. After a few minutes passed (during which time the injection was completed) the reactor was cooled and the impregnant allowed to solidify inside the channels). The sample was then extracted from the reactor, and standard mechanical polishing techniques were performed to remove the surrounding excess.

The array electronic properties were determined in separate experiments [8, 9]. The crystal sizes were larger than the wire diameter and were oriented with the c-axis along the wire length. Electron and hole band parameters were determined via magnetoresistance experiments. As with bulk bismuth, the bismuth in the nanowires was a semimetal. The diffusion thermopower of the nanowires was negative (nanowires, as well as bulk, are n-type because electrons have greater

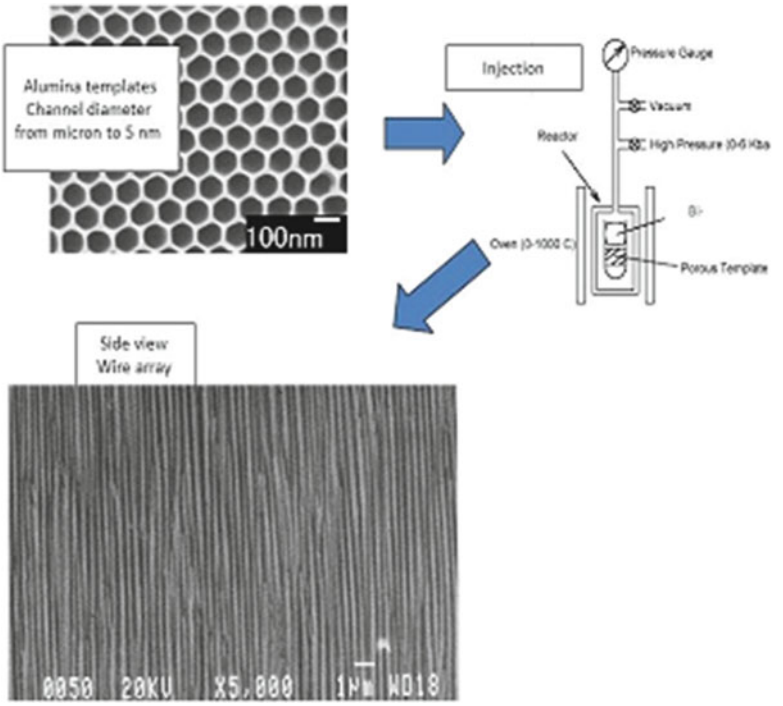

Fig. 17.2 Fabrication of the Bi nanowire array in our experiments

mobility than holes). This value (about −90 mV/K) did not differ greatly from that attained for single-crystal bulk bismuth along the trigonal orientation. The room temperature Z was estimated to be $2 \times 10^{-3}\mathrm{K}^{-1}$ (60 % of the value for bulk bismuth). The NWAs were extremely anisotropic because of the insulating effect of the alumina matrix.

At the NWA-ITO interface, the bismuth was paired with the ITO film. A sample of the ITO film, of the same thickness, was deposited on a glass substrate, and the resistance and thermopower were measured. We found that the ITO resistance square was 1.2 kΩ and that the thermopower was 20 mV/K. Our measurements were in line with those of previous research on the electronic transport properties of ITO films [18].

We characterized the NWAs under visible light illumination. The optical properties of the nanowire array were very different from those of bulk single crystal bismuth which has a shine, it is reflective. Also, the 50-μm thick alumina template, prior to processing, was translucent/transparent in the visible and infrared. By contrast, we found that the absorption by our NWAs was very strong. The arrays surface was black, not shiny. This finding is common for NWAs of many diverse materials (e.g. silicon nanowire arrays) and denotes poor reflectivity and light trapping [6]. We also observed that light reached deep inside the array. Under

oblique illumination, that is to say that the incident light beam is not parallel to the nanowires, the reflected visible light is polarized a finding that can be explained by considering that wire array works like a polarizing wire grid. For this to occur, light has to penetrate at least at a distance of the order of a wavelength l. Based on these observations, we estimated that the thickness of the interface for normal incidence exceeded 0.5 mm. By contrast, crystalline bismuth has an absorption length A of a 1 nm or less in the same range and somewhat larger in the infrared.

17.3 Experimental

Because the signal arises in the absence of a bias current, it is interpreted in terms of thermopower that is proportional to the $T_F - T_0$—that is, the temperature of the front surface with respect to the ambient temperature T_0— or a PC that exists in the absence of a thermal gradient. The setup employed to measure the photoresponse is shown in Fig. 17.3.

When we measured the time-dependent photoresponse, we found evidence of the thermal flow as well as of a major component in the signal that could be interpreted as a PC. The illumination was that of a chopped beam of frequency f; the beam was made by focusing the output of a quartz lamp on the front surface of the device. This beam had visible and near-infrared components. The amplitude of the signal I, which is synchronous with the illumination, was measured with a lock-in amplifier. We had the capability to filter the light with infrared band-pass filters that absorb the part of the spectrum within a range of wavenumbers.

Figure 17.4 displays I versus f for unfiltered and infrared light, produced with long wave pass filters with 700- and 1,000-nm cutoff wavelength. The signal increases with increasing frequency f non-monotonically, and there is great contrast between the case of unfiltered light and the pure infrared illumination, the latter clearly showing an inflection point at $f_0 = (400\ \text{Hz})$, where I is constant for frequencies below the inflection point. This photoresponse is related to the time dependency of the diffusion of heat through the sample from the front to the heat sink in the back of the sample and to the conversion of heat deposited by the incident pulse into electric power via TE effects in the nanowire array.

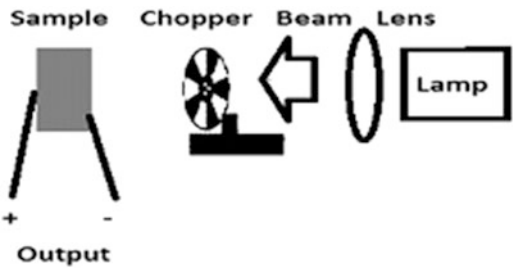

Fig. 17.3 Setup for photoresponse measurements

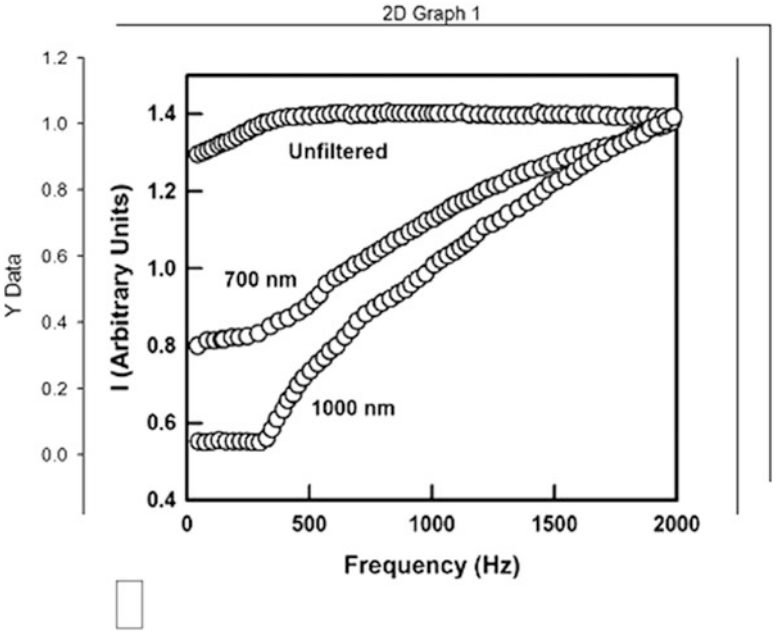

Fig. 17.4 Photoresponse I of the device to a chopped beam as a function of frequency f in three cases. Unfiltered light from a tungsten lamp and also in the cases where the light is filtered with long wave pass filters to exclude wavelengths shorter than 700 or 1,000 nm, as indicated. The 1,000 nm-filtered data shows the expected ($I \sim f^{1/2}$) relation between 500 Hz and 2 KHz

The diffusion of heat through a sample is characterized by the diffusion constant D, which is given by $k/\rho c$ (k is the thermal conductivity, ρ is the density, and c is the specific heat). Parker et al. [13] presented an analysis of heat diffusion through a plate of thickness L showing that there is a thermal time constant $\tau = 1.38L^2/(\pi^2 D)$ for equilibration of the front temperature T_F and back temperature. For low frequencies $f < 1/\tau$ the deviation of the front surface temperature T_F from the back temperature decreases with decreasing f because thermal contact through the plate becomes increasingly better. The optical method introduced by Parker et al. [13] can be used to measure D; this method involves applying a pulse of light, or chopped beam illumination, to the front of an insulated slab and measuring the back temperature with a fast thermometer. This property is the basis of the optical method that was successfully applied to thermoelectric Bi_2Te_3 and bismuth nanowire arrays by Borca-Tasciuc et al. [1, 2]. Here, we interpret the observation of an inflection point at f_0 as the point of equilibration of the front temperature T_F and back temperature, that is maintained at T_0 in our device, and, therefore, $\tau = 1/f_0$. The inflection point frequency of 400 Hz in Fig. 17.3 gives $D = (1.1 \pm 0.2) \times 10^{-2}\text{cm}^2/\text{s}$. Our experimental result for D is in remarkably good agreement with the experimental result of $1.3 \times 10^{-2}\text{cm}^2/\text{s}$ by Borca-Tasciuc et al. [1]. This interpretation of τ as the array thermalization time is confirmed by

the observation that, in our device, the electrical potential between the front and back surfaces— and, therefore, the signal—can be interpreted as the thermoelectric signal proportional to T_F that is generated by the heat current. The plateau in the signal versus f that we observe, arises because, under quasi-equilibrium conditions ($f < f_0$), $T_F - T_0 = \dot{Q}L/kS$ where $\dot{Q}$ is the absorbed optical power, which is independent of f. Further information about the TE processes in the sample can be obtained by the $f$evolution of the signal for $f > f_0$. The heat diffuses a distance of the order of $\sqrt{D/f}$, which is less than $L$and therefore the thermal contact becomes increasingly worse with f. Consequently $T_F - T_0$ increases with f as observed. Therefore, preliminarily the signal can be attributed to a TE response. Also, since the time dependent thermoelectric response, for pure infrared illumination, corresponds to the thermal model we gather that the electron phonon thermalization is fast in the time domain that we have investigated and we therefore rule out hot electron processes in the case of infrared light. This assignment is fitting in the case of infrared-only illumination. Under unfiltered light, which includes visible light, the inflection point is barely noticeable, and the signal strength is almost independent of frequency. This feature suggests that part of the signal is not thermal, which in turn indicates the existence of a PC or hot electron component in this case. We verified that the device has a fast response by measuring the photoresponse induced by a flash lamp with pulse duration of 100 ms. We observed a response time of ∼150 ms, which corresponds to a frequency of ∼7 kHz.

The responsivity of our device was 1.8 mV/W. As reported by St-Antoine et al. [14], the nanotube thermopile has a much higher responsivity of 0.9–1.8 V/W but with a long time constant (1 ms). By contrast, the photoresponse of Ca_xCoO_2 thin (∼100-nm thick) films with an off-diagonal TE effect were designed to be very fast (∼10 ns), but the conversion is very inefficient [16]. It needs excitation by a pulsed laser to show a response. In the present study, we have demonstrated the fast response mechanism and speeds up to 7 kHz were achieved. According to our thermal model, the TE response is limited in speed only by thermal diffusion through the optical absorption length A. In the present device, $A \sim 500$ nm for visible light; therefore, potentially, the response frequency is as high as $2\pi D/A^2 = 3$ MHz.

Semiconductors used in solar cells cannot convert the infrared part of the solar spectrum, which represents about half of the total solar energy output, because the absorption of a photons bearing less than the bandgap energy does not produce electron-hole pairs. Direct solar thermal energy conversion has been discussed [17]. Devices based on TE nanomaterials can convert the infrared radiation part of the spectrum into usable electrical power, which suggests that integration of TE processes in solar cells may increase solar energy harvesting efficiency.

We report on the fabrication and photoresponse of a device composed of a nanowire array of TE bismuth, which is capped with a transparent electrode consisting of a film of ITO. The front surface is absorbent because of the light-trapping property of the nanowire array. We show that, under infrared illumination, the photoresponse is thermoelectric At low f, quasi-equilibrium is achieved and the signal is f-independent. At high frequencies the absorbed heat is not dissipated in the back electrode during a period, and the signal can rise, as $f^{1/2}$, to high values

because the energy is delivered to a thin layer on the front of the sample. The TE effect is only evident under infrared-only illumination and appears in combination with PC and hot-carrier processes under visible illumination. The photoTE signal can be fast, with a response time much shorter than the array thermalization time and the arrays may have future optoelectronic application as fast nanoscale bolometers.

This material is based on work supported by the Materials Science Division of the U.S. Army Research Office (under Grant No. W911NF-09-1-05-29) and by The Boeing Company under RA-6. The authors are indebted to John Belk, Jeff Hunt, and Pablo Jarillo-Herrero for helpful discussions.

References

1. Borca-Tasciuc DA et al (2001) Thermal characterization of nanowire array in alpha-Al(2)O(3) matrix. MRS Proc 703:V2.7
2. Borca-Tasciuc DA et al (2004) Thermal properties of electrodeposited bismuth telluride nanowires embedded in amorphous alumina. Appl Phys Lett 85:6001
3. Fan RH (2012) Transparent metals for ultrabroadband electromagnetic waves. Adv Mat 24:1980
4. Foss Jr C, Tierney M, Martin MR (1992) Template-synthesis of infrared-transparent metal microcylinders: Comparison of optical properties with the predictions of effective medium theory. J Phys Chem 96:9001
5. Gabor NM (2011) Hot carrier assisted intrinsic photoresponse in graphene. Science 334:648
6. Garnett E, Yang P (2010) Nano Lett 10:1082
7. Hochbaum AI et al (2008) Enhanced thermoelectric performance of rough silicon nanowires. Nature 451:163
8. Huber TE et al (2011) Surface state band mobility and thermopower in semiconducting bismuth nanowires. Phys Rev B 83:235414
9. Huber TE et al (2012) Thermoelectric prospects of nanomaterials with spin-orbit surface bands. J Appl Phys 111:043709
10. Kelzenberg MD et al (2010) Enhanced absorption and carrier collection in Si wire arrays for photovoltaic applications. Nat Mater 9:239
11. Lawrance R, Bube R (1968) Photothermoelectric and thermally stimulated thermoelectric effects: Techniques in photoelectronic analysis. Appl Phys 39:1807
12. Nolas GS, Sharp J, Goldsmid HJ (2001) Thermoelectrics: basic principles and new materials developments. Springer, Heildelberg
13. Parker WJ et al (1961) Flash method of determining thermal diffusivity, heat capacity, and thermal conductivity. J Appl Phys 32:1679
14. St-Antoine BC, Menard D, Martel R (2011) Single-walled carbon nanotube thermopile for broadband light detection. Nano Lett 11:609
15. Sze SM (1981) Physics of semiconductor devices, 2nd edn. Wiley, London
16. Takahashi K et al (2012) Light-induced off-diagonal thermoelectric effect via indirect optical heating of incline-oriented Ca(x)CoO(2). Appl Phys Lett 100:18197
17. Tritt et al (2008) Thermoelectrics: Direct solar thermal energy conversion. Mater Res Soc Bull 33:366-369
18. Wu C-Y et al (2010) Free-electronlike diffusive thermopower on indium tin oxide thin films. J Appl Phys 108:123708
19. Xu X et al (2010) Photo-thermoelectric effect at the graphene interface junction. Nano Lett 10:562
20. Yao Y et al (2008) Optical negative refraction in bulk metamaterials of nanowires. Science 321:930

Chapter 18
Special Features of Thermoelectric Phenomena in Granulated Semiconductors

Khatam Ashurov, Boris Abdurakhmanov, Flyra Djurabekova, Sherzod Kuchkanov, Sergey Maksimov, and Boris Oksengendler

Abstract A model of the heterogeneous semiconductor medium consisting of multiphase granules, which are the crystal semiconductor grains covered by the oxide film has been proposed. The effective medium model (EMM) of the set of contacting granules has been constructed. Each granule phase is characterised by its own conductivity σ_i, heat conductivity χ_i, Seebeck factor α_i, characteristic size d_i and, accordingly, efficiency of thermoelectric transformation Z_i. Expressions for the estimation of σ_{eff}, χ_{eff}, α_{eff} and Z_{eff} are constructed, and their values depending on asymmetry degree of characteristics of the granule components are analysed. The complicated ternary thermoelectric media is considered. The possibilities of acquisition of the optimal medium characteristics under various technological conditions and the action of ionizing radiation have been studied.

18.1 Introduction

Direct transformation of a non-photoactive component of solar radiation and natural and man-caused heat into electric energy is a very topical and actual problem that can be solved with thermoelectric generators [1]. Their operation is based on the Seebeck effect [2] generation of voltage (E) in an electric circuit consisting of

S. Maksimov (✉)
Institute of Ion-Plasma and Laser Technologies, Uzbek Academy of Sciences, Do'rmon yo'li Str. 33, Tashkent 100125, Uzbekistan
e-mail: maksimov_s@yahoo.com

K. Ashurov • B. Abdurakhmanov • F. Djurabekova • S. Kuchkanov
Institute of Ion-Plasma and Laser Technologies, Uzbek Academy of Sciences, Tashkent, Uzbekistan

B. Oksengendler
Polymer Physics Institute, Uzbek Academy of Sciences, Uzbekistan

R. Egger et al. (eds.), *Low-Dimensional Functional Materials*, NATO Science for Peace and Security Series B: Physics and Biophysics, DOI 10.1007/978-94-007-6618-1_18,

successively connected heterogeneous materials, in particular a semiconductor with two identical metallic contacts having different temperatures $T_1 < T_2$.

$$E = \alpha(T_2 - T_1) \tag{18.1}$$

where α is the Seebeck factor characterizing a thermoelectric ability of a pair of materials and being *per se* a sum of the specific or differential thermoelectromotive forces (TEMF) of semiconductor or metal which form a contact. Since, according to the data presented in the thermoelectric series of Seebeck et al. [1], the specific TEMF of metals within the temperature range 300–500 K does not exceed some unities of microvolts, but the specific TEMF of elementary semiconductors is by an order higher, the contribution of metallic contacts is neglected and only the differential TEMF of semiconductor, for example 44 μV/C for silicon, is considered. As perspective thermoelectric materials one usually considers the semiconductive compounds like BiTe, various oxides, as well as sulfide and boride of rare-earth elements, including exotic compounds. Until recently silicon despite its wide use in production and its content in rocks of the earth's crust > 25 % has not been used as such owing to a comparatively small value of α. However, a very interesting physical effect was described in [3] and explained in [4]: EMF generation in an equally heated isotype thermal energy converter of (TEC) from micro-grain silicon. The EMF value exceeds by dozens of times the EMF that can emerge because of the non-controlled gradients of temperature inside TEC. It was also shown [3] that the purposeful creation of temperature gradient inside such TEC is accompanied by appearing of an anomalously high TEMF and a possibility of producing comparatively high values of the short circuit current density. Advisability of wide practical application of TEC and its competitiveness will be indubitable if they have high values of conductivity (σ), in particular within the temperature range 300–1,000 K, and, vice versa, small values of thermal conductivity (χ), which together with α defines a major parameter of a thermoelectric material, namely the quality factor (Z) [2, 5]

$$Z = \frac{\alpha^2 \sigma}{\chi} \tag{18.2}$$

According to the results of current-voltage diagram measurements for different temperature and of TEC resistance ones by a compensation method, it is possible to state that the sufficiently high values of σ [6], as well as a character of its temperature changes, as compared to monocrystalline silicon, are caused by its essential different nature and due to special points of construction both as a material and as TEC itself.

18.2 Effective Medium Model for Granulated Semiconductors

For the thermoelectric phenomena in granulated semiconductors to be described, a model of the heterogeneous semiconductor medium consisting of diphasic granules, which are the crystal semiconductor grains covered by the oxide film, has been

proposed in [7]. This effective medium model (EMM) consisting of a set of contacting granules has been constructed. Each granule phase is characterized by its own conductivity σ_i, heat conductivity χ_i, Seebeck factor α_i, characteristic size d_i and, accordingly, thermoelectric transformation efficiency Z_i $(i = 1, 2)$. On the basis of the linear Onsager thermodynamics the expressions for the estimation of σ_{eff}, χ_{eff}, α_{eff} and Z_{eff} are constructed; and their values depending on an asymmetry degree of the characteristics of the granule components are analysed. The obtained parameters of diphasic medium are the following [7]:

$$\sigma_{eff} = \frac{\sigma_1 \sigma_2}{\sigma_2 \frac{d_1}{d_1+d_2} + \sigma_1 \frac{d_2}{d_1+d_2}} \tag{18.3}$$

$$\chi_{eff} = \frac{d_1 + d_2}{\frac{d_1}{\chi_1} + \frac{d_2}{\chi_2}} \tag{18.4}$$

$$\alpha_{eff} = \alpha_1 \frac{\chi_2 d_1}{\chi_2 d_1 + \chi_1 d_2} + \alpha_2 \frac{\chi_1 d_2}{\chi_1 d_2 + \chi_2 d_1} \tag{18.5}$$

$$Z_{eff} = \left[\alpha_1 \frac{\chi_2 d_1}{\chi_2 d_1 + \chi_1 d_2 + \alpha_2 \frac{\chi_1 d_2}{\chi_1 d_2 + \chi_2 d_1}} \right]^2 \times \left[\frac{\sigma_1 \sigma_2}{\sigma_2 \frac{d_1}{d_1+d_2} + \sigma_1 \frac{d_2}{d_1+d_2}} \right] \left[\frac{1}{d_1 + d_2} \left(\frac{d_1}{\chi_1} + \frac{d_2}{\chi_2} \right) \right] \tag{18.6}$$

The basic feature of our system is that in a reality, in the case of the granulated silicon [3, 4], we do not have a two-component, but ternary system "Si core + core-core border (CCB) + oxide layer". For consideration of this real situation we may use an artificial method. According to this method the basic expressions for effective values σ_{eff}, χ_{eff} and α_{eff}, obtained in Formulas (18.3), (18.4), and (18.5) for components 1 and 2, can become, in turn, the components in combinations of σ_{eff}, and σ_3, χ_{eff} and χ_3, α_{eff} and α_3, according to classical Landauer algorithm [8]:

$$\frac{\tilde{\sigma}_{eff} - \sigma_{eff}}{2\sigma_{eff} + \tilde{\sigma}_{eff}} P_{eff} + \frac{\tilde{\sigma}_{eff} - \sigma_3}{2\sigma_3 - \tilde{\sigma}_{eff}} (1 - P_{eff}) = 0 \tag{18.7}$$

$$\frac{\tilde{\chi}_{eff} - \chi_{eff}}{2\chi_{eff} + \tilde{\chi}_{eff}} P_{eff} + \frac{\tilde{\chi}_{eff} - \chi_3}{2\chi_3 - \tilde{\chi}_{eff}} (1 - P_{eff}) = 0 \tag{18.8}$$

$$\tilde{\alpha}_{eff} = \frac{< \alpha_i \sigma_i / \Delta_0 >}{< \sigma_i / \Delta_0 >}; \Delta_0 = (2\tilde{\sigma}_{eff} + \sigma_i)(2\chi_{eff} + \chi_i) \tag{18.9}$$

Here $\tilde{\sigma}_{eff}$, $\tilde{\chi}_{eff}$ and $\tilde{\alpha}_{eff}$ are desired values of parameters in effective ternary system, $< \ldots >$ is the short indication of weight averaging; P_{eff} is the part of combined two-component "2-1" phase in total "2-1"+"3" system. Resolving the Eq. (18.7) relative to $\tilde{\sigma}_{eff}$, $\tilde{\chi}_{eff}$ and $\tilde{\alpha}_{eff}$, it is possible to obtain all thermoelectric

characteristics of ternary medium as the functions of σ_i, χ_i and $\tilde{\alpha}_i$, and, therefore, to found $\tilde{Z}_{eff}$ for the total "1+2+3" system. The expressions (18.7) obtained during the theoretical investigation of ternary system, indicate on the large opportunities of management of $\tilde{Z}_{eff}$ value by the technological changes in electrophysical, thermophysical and geometrical parametres of all three components (core, CCB and SiO2 shell) of the real semiconductor granules.

18.3 Influence of Irradiation on the Thermophotovoltaic Effect in Granulated Silicon

The very important question is, how the optimal asymmetry of phases 1 and 2 can be achieved. We assume that radiation influence is one of such methods. The range of applicability of this method is a priori limited by the annealing temperature of radiation defects; however, it does not reduce its importance, because the greatest interest in practice is connected with the relative low temperatures of TEC heating for the purpose of utilization of low-grade heat.

Some thermovoltaic features of the monocrystalline silicon (MS) $n^+ - p$ structures in which the radiation defects and, accordingly, the high concentrations of deep energy levels are created by irradiation of the samples with fast electrons have been presented in [9] (Fig.18.1). The radiation defects were created by irradiation of the $n^+ - p$ structures by electrons with energy $E \sim 1$ MeV and doze $D = 10^{15}$ cm^{-2}.

They are the $n^+ - p$ planar structures produced by phosphorus diffusion at the depth ~ 1 μm on the targets KDB-1 (111) of 1 cm^2 with ohmic contacts; the back contact is solid and the front one is like a grid, a material of these contacts is the

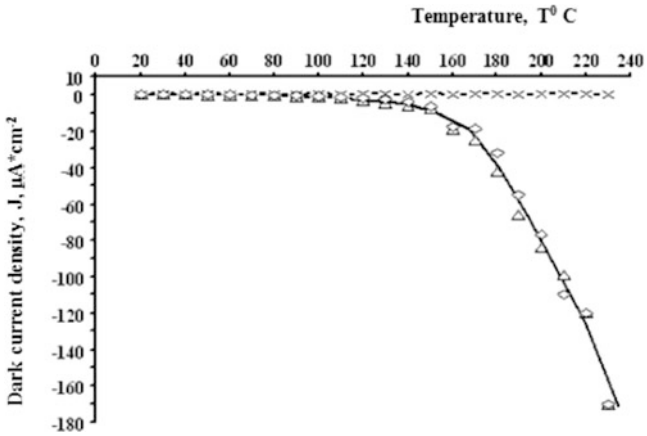

Fig. 18.1 The temperature changes in the of dark current density for the electron-irradiated monocrystalline $n^+ - p$ structures while heating $(-\triangle-)$ and cooling $(-\diamond-)$ as compared to the control sample $(-\times-)$ [9]

composition TiCuNi or TiCu deposited through masks. The dark current and voltage were measured for the irradiated and control samples in the alternate mode (heating-cooling) with preset speeds over the temperature range 20–250 °C. The curves illustrate changes in the dark current for the heated $(-\triangle-)$ and $(-\diamond-)$ cooled electron-irradiated MC n^+p structures and for the same non-irradiated control one $(-\times-)$. It is seen that unlike the control sample $(-\times-)$ in which there is no current while both heating and cooling the irradiated structures generate current within the whole range of temperature, which is particularly seen for heating above 140 °C. To interpret the radiation influence on the thermovoltaic effect for the material under study the following statements of radiation physics of heterogeneous materials will be used.

1. An object is heterogeneous; therefore an effective medium model (EMM) [10] is applied to it.
2. In the grains and oxidized layers there are processes of elastic and ionization-radiation defect formation (RD) [11].
3. Radiation-stimulated diffusion (RSD) of Si takes place from the Si grains to the inter-grain areas of SiO_2 [11].

As a result of combinations of these processes, for the good quality Z under irradiation we have (it follows from EMM)

$$Z = \alpha^2 \frac{\sigma_{Si}\sigma_{SiO_2}}{\sigma_{Si}+\sigma_{SiO_2}} \frac{\chi_{Si}+\chi_{SiO_2}}{\chi_{Si}\chi_{SiO_2}} \tag{18.10}$$

Here both σ_i and χ_i are the functions of irradiation doze (Φ) [11]

$$\sigma_{Si} = \sigma_{Si}^0(1-const\cdot\Phi), \sigma_{SiO} = \sigma_{SiO}^0\left[1+const\cdot(\Phi-\Phi_C)^\beta\right] \tag{18.11}$$

The first equation is a result of increasing the recombination A-centers, the second one is a result of penetrating the Si atoms in the SiO_2 layers and percolation conductivity in them, Φ is the critical doze, $\beta < 1$ is the critical index. The influence of the SiO_2 film thickness on the critical parameters Φ and β should be noted [12].

$$\chi_{Si} = \chi_{Si}^0(1-const\cdot\Phi), \chi_{SiO} = \chi_{SiO}^0(1+const\cdot\Phi) \tag{18.12}$$

The latter equation is a consequence of homogenization because of RSD in the boundaries.

Analysis of Eqs. (18.9) and (18.10) shows that because of the specific values of all the constants (they can be calculated by the methods of radiation physics [11]) a different dependence $Z(\Phi)$ is possible. In particular, the following equation is characteristic of electron and γ irradiation

$$Z(\Phi) = \alpha^2 \frac{\sigma_{SiO_2}^0}{\chi_{SiO_2}^0} \frac{1+const\cdot(\Phi-\Phi_C)^\beta}{1+const\cdot\Phi} \equiv Z(0)f(\Phi) \tag{18.13}$$

i.e. $Z(\Phi)$ can be a non-monotonous function of doze. For the numerator being predominant there is an increase of $Z(\Phi)$ with doze, which can be realized in experiment. However, such a behavior is characteristic of dozes $\Phi > \Phi_C$ only. It is important to note that for the irradiation doze within the range $0 < \Phi < \Phi_C$ there should be a decrease in $Z(\Phi)$ (see Eq. 18.11), which is observed in experiment. Note that there is no thermovoltaic effect without radiation for $\frac{\sigma^0_{SiO_2}}{\chi^0_{SiO_2}} << 1$.

However, special interest in systems of the granulated semiconductors is connected with the fact that two next phases (CCB and oxide layer) are nanophases, and quasi-particles can transit through them in ballistic regime (phonons), or in tunneling one (electrons and holes). One of the variants of the description of similar processes is presented in [8, 12–14], and the result in the case of nanocontact is the following [14]:

$$\alpha_n \sim \frac{d}{dt}\left(\ln\frac{t}{1-t}\right); \sigma_n \sim \frac{t}{1-t}; \chi_n^e \sim \frac{t}{1-t} \tag{18.14}$$

Here

$$t = \exp\left(-\frac{2}{\hbar}\sqrt{2mQ}l\right), \tag{18.15}$$

where t is the tunnel exponent, χ_n^e is the electron heat conductivity (in ordinary case there is $\chi_n = \chi_n^e + \chi_n^{ph}$, where ph means phonons).

Radiation effects are frequently opposite in the cases of nanoscale objects and macroscopic ones. So, the standard result of irradiation leads to the formation of the defects creating local levels in the gap. For macroobjects (grains) it leads to the reduction of number of carriers in the permitted band, i.e. σ_{macro} falls. For nanoobjects, on the contrary, the creation of the local energy level under the barrier increases t (Fig. 18.2), because for the intact barrier t is described by Eq. (18.13), and for the barrier with defect due to hopping conduction

$$t = \frac{t_1 t_2}{t_1 + t_2} \sim \frac{1}{2}\exp\left(-\frac{2}{\hbar}\sqrt{2mQ}\frac{l}{2}\right) \tag{18.16}$$

where $t_1 \approx t_2$ are the tunnel exponents of the hops with participation of the localized states placed inside the barriers (Fig. 18.2). So, σ_{nano} increases under irradiation.

Concerning heat conductivity there is other situation: χ_{macro} always falls with the growth of defect number (both for χ^e_{macro}, and for χ^{ph}_{macro}); $\chi_{nano} = \chi^e_{nano} + \chi^{ph}_{nano}$ passes through a minimum with dose growth, because χ^e_{nano} grows in insulators from zero, and χ^{ph}_{nano} falls due to the degradation of ballistic conditions. The dependence of the Seebeck factor α_{macro} from the dose Φ is much weaker, because the dependence of the carriers number is logarithmic; α_{nano} also weakly depends on t, as

$$\alpha_{nano} \sim \frac{1}{t} + \frac{1}{1-t} \tag{18.17}$$

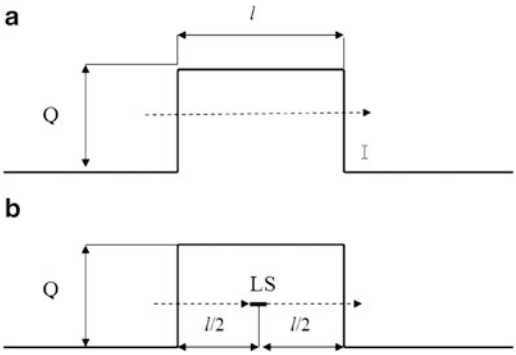

Fig. 18.2 Scheme of Landauer tunneling contact: (**a**) non-defect case; (**b**) defect case with the localized state (*LS*) inside the contact

Thus, the existence of nanocontacts is in many cases a narrow throat of radiation effects in multiphase system, modulation of their thermoelectric characteristics is possible by use of the irradiation.

However, the granulated systems with small (up to nanoscale) components have an additional essentially new property sharply distinguishing their behaviour from macrosystems under the action of radiation. The matter is that in principle radiation acts have a stochastic character. It is known that such processes taking place in big (macro) systems belong to the self-averaging class [15]. However, in the small systems the big fluctuations comparable with average values take place. Owing to these circumstances it is possible to apply to the analysis of radiation effects in granulated nanosystems an approach applied in the study of radiation processes in biological objects, namely, the hit and target [16] principle. This principle allows to refuse the method of the kinetic equations [11] operating with av-erage values.

Using the hit and target principle, it is possible to write the following expression for the probability of obtaining certain proper-ties f_i $(i = 1,2,3)$, which are the parametres of each component in the ternary equivalent media:

$$\Omega_i = [\exp(-\nu_i \Phi)] \sum_{k=0}^{n-1} (\nu_i \Phi)^k ; \Omega(\Phi) = \Omega_1 \Omega_2 \Omega_3 \tag{18.18}$$

Here ν_i is the cross-section of the single radiation hit of the target (phase i), k is the number of radiation hits of the target, leading to the change of the parameter f_i up to value $f_i(k) = f_i^0 - k\Delta f_i$; Δf_i is the partial change of the parameter f_i at a single hit, f_i^0 is the initial (before radiation) value of the parameter f_i. Thus, the parameter Ω_i shows the probability of obtaining the value $f_i = f_i^0 - (n)\Delta f_i$ under irradiation up to dose Φ. Substituting $\sigma_{eff} = \sigma_{eff}^0 - k\Delta\sigma_{eff}$, $\chi_{eff} = \chi_{eff}^0 - k\Delta\chi_{eff}$, $\alpha_{eff} = \alpha_{eff}^0 - k\Delta\alpha_{eff}$, in the expression for Z_{eff}, it is possible to obtain the dependence $Z_{eff}(\Phi)$. This value $Z_{eff}(\Phi)$ should be interpreted as stochastic, i.e. quality factor Z_{eff} can be obtained not deterministically, but with probability Ω_{eff}. Obviously, the less the components 1, 2 and 3 are less, the more standard deviation is:

$$\delta = \sqrt{\frac{< [\Delta(\nu_i \Phi)]^2 >}{(< \nu_i \Phi >)^2}} = \frac{1}{\sqrt{< \nu_i \Phi >}} \tag{18.19}$$

distribution of fluctuations is wider and so averaging is inefficient. Let's add that as Ω_i is based on the Poisson distribution with average value $\nu_i \Phi$, the analysis on the basis of the kinetic equations operating with average values of variables is absolutely inadequate at small doses ($\nu_i \Phi < 1$). We will also notice that the described complication of the analysis of dose dependences is relatively laborious in comparison with macrosystems, but it is absolutely necessary at transition to complicate nanosystems.

18.4 Conclusion

Thus, it is possible to make the general conclusion that electron and γ-irradiations are rather fine tools in material technology of the granulated semiconductor media, which are perspective and promising materials for the solution of the problem of heat transfor-mation into electricity. An other important conclusion predicted not only theoretically, but also in our preliminary experiments both on microgranular silicon and on the samples of polycrystalline silicon with larger grains, is the dependence of efficiency of the radiation effects on electrophysical characteristics of CCB with an oxide lay-er, defined by both the technology and the kind of raw materials go-ing on manufacturing. Radiation effects, for example, the γ-irradiation or ionic implantation, stimulates the occurrence of the thermovoltaic effect [9] and increases the Seebeck factor. The opti-mum combination of characteristics of the initial materials (both the grains and CCB) with the radiation doses allows to obtain the ther-moelectric materials with high efficiency factor of produced TEC.

Acknowledgements This work was supported by the Committee for Coordination Science and Technology Development under Cabinet of Ministers of Uzbekistan, contract F3-F-F158.

References

1. Ioffe AI (1960) Semiconductor thermoelements. Izdat. AN SSSR, Moscow/Leningrad (in Russian)
2. Dmitriev AV, Zvyagin IP (2010) Current trends in the physics of thermoelectric materials. Adv Phys Sci 53(8):789–804
3. Ashurov M Kh, Abdurakhmanov BM, Adilov MM, Ashurov Kh B (2010) Isotopic thermal energy converter based on micro-grain silicon. Dokl Acad Nauk Resp Uzbek 3:45–49 (in Russian)
4. Abdurakhmanov BM, Oksengendler BL (2011) Dokl Acad Nauk Resp Uzbek 1:26–28 (in Russian)
5. Stilbans LS (1967) Physics of semiconductors. Soviet Radio, Moscow, 452p (in Russian)
6. Abdurakhmanov BM, Adilov MM, Ashurov M Kh, Ashurov Kh B, Oksengendler BL (2010) Development and study of sili-con isotype one- and multi-transitive thermovoltaic converters of energy. Preprint -8-693 of Nuclear Physics Institute, Uzbek Academy of Sciences, Tashkent, p 36 (in Russian)

7. Abdurakhmanov BM, Adilov MM, Ashurov M Kh, Ashurov Kh B, Maksimov SE, Oksengendler BL (2012), published in Geliotekhnika (2012) 2:17–23
8. Landauer R (1978) Electrical transport and optical properties of inhomogeneous media. In: Garland JC, Tanner DB (eds) AIP Conference Proceedings. AIP, New York, pp 2–10
9. Abdurakhmanov BM, Olimov LO, Abdurazzakov FS, Aladina ZN (2010) Silicon solar cells exposed to electron bom-bardment: thermovoltaic properties. Appl Sol Ener 46(2):161–162
10. Landau LD, Lifshitcs EM (1982) Electrodynamics of solid media. Nauka, Moscow (in Russian)
11. Vinetskiy VL, Kholodar GA (1979) Radiation physics of semiconductors. Naukova Dumka, Kiev (in Russian)
12. Dragoman M, Dragoman D (2009) Nanoelectronics. Principles and devices. Oxford University Press, Oxford
13. Snarskii AA, Sarychev AK, Bezsudnov IV, Lagarkov AN (2012) Thermoelectric figure of merit of bulk nanostructured composites with distributed parameters. Semicon-ductors, Fizika i Tekhnika Poluprovodnikov 46(5):677–683
14. Guttman CD, Ben-Jacob E, Bergman DJ (1995) Thermoelectric properties of a series of Landauer barriers. Phys Rev B 52(7):5256–5263
15. Lifshits IM, Gredeskul SA, Pastur LA (1982) Introduction in the theory of disorder systems. Nauka, Moscow
16. Timofeeff-Ressovsky NW, Ivanov VI, Korogodin VI (1968) Application of hit and target principle in radiobiology. Atomizdat, Moscow

Chapter 19
Thermoelectricity in Ternary Rare-Earth Systems

Vladimir Nikiforov, Valentin Irkhin, and Alexander Morozkin

Abstract The measurements of electrical resistivity, thermal conductivity and thermoelectric power for a number of newly synthesized metal compounds and alloys based on transition and rare-earth elements were done. The maximum value of thermoelectric figure of merit ZT for the proposed system at room temperature is about 7 %. Special attention is paid to possible manifestations of the Kondo effect.

19.1 Introduction

Thermoelectric materials are of great interest due to their ability to use waste heat to generate electricity and act as solid state Peltier coolers. Thermoelectric devices based on thermoelectric materials have numerous advantages, such as being low-noise, high reliability, without any moving parts and long period of operation. Since power units of thermoelectric generation produce electric current from temperature difference, we can convert waste heat energy to electric energy. Therefore, thermoelectric power generation is one of the most promising tools for environmental conservation. However, the conversion efficiency of conventional thermoelectric generation is insufficient in performance. The reason for this low efficiency is in poor thermoelectric properties of most conventional thermoelectric materials.

The thermoelectric fitness of a material is estimated by the value of the dimensionless parameter, figure of merit $ZT = S^2\sigma T/\kappa$ where S is the Seebeck coefficient, σ electrical conductivity, and κ thermal conductivity. The material having higher ZT

V. Nikiforov (✉) • A. Morozkin
Department of Physics, Lomonosov Moscow State University, Len Gory, Moscow GSP-2, 119899, Russia
e-mail: nvn@lt.phys.msu.ru

V. Irkhin
Institute of Metal Physics, Ekaterinburg, Russia

R. Egger et al. (eds.), *Low-Dimensional Functional Materials*, NATO Science for Peace and Security Series B: Physics and Biophysics, DOI 10.1007/978-94-007-6618-1_19,

value possesses better thermoelectric performance. High-performance thermoelectric materials must have large S, high σ, and low κ to retain the heat at the junction and reduce the heat transfer losses.

How to Increase ZT?

The Wiedemann–Franz law limits the ratio of the electronic contribution to the thermal conductivity and electrical conductivity of a metal. That ratio should be proportional to the temperature, $\kappa/\sigma = LT$. Rosenberg [21] notes that the Wiedemann–Franz law is generally valid for high and low (i.e., a few of Kelvins) temperatures, but can be violated at intermediate temperatures. In degenerate semiconductors, the Lorentz number L has a strong dependence on system parameters: dimensionality, strength of interatomic interactions and Fermi level position. The Lorentz number can be reduced by manipulating electronic density of states, varying doping density and layer thickness in superlattices and composite materials with correlated carriers [12, 20].

We can use the following strategies:

1. To reduce thermal conductivity and increase the efficiency by minimizing the thermal losses through the device.
2. To increase the Seebeck coefficient and the electrical conductivity. Recent advances that achieved $ZT \tilde{}\ 2$ are mostly due to the reduction of χ by nanostructuring, i.e., by using multilayered materials [6] and nanocomposites [12]
3. To introduce resonant states within the Fermi window by doping [11].

19.2 Skutterudite Systems

Skutterudite compounds MX_3 with a cubic structure (M = Co, Rh, Ir, Fe, Ru, X = P, As, Sb) are a class of promising high performance thermoelectric material for power generation [2, 13, 14, 16] and thus have attracted a great deal of interest in recent years.

Although binary skutterudite compounds possess good electrical transport properties, their overall figure of merit ZT is not too high because of relatively high thermal conductivity. It is found by Sales et al. [23] and Nolas et al. [17, 18] that rare-earth atoms such as La, Ce, etc. may be inserted into the voids of the crystal structure where they "rattle" around their equilibrium positions. This rattling motion can efficiently scatter the phonons and thus greatly reduce the lattice thermal conductivity without deteriorating the electrical transport properties. The ZT value of the rare-earth filled skutterudite is more than unity between 773 and 973 K [23].

Ternary skutterudites RyM4X12; with R being rare earth, M transition metal and X pnictogen; are a novel class of materials exhibiting extraordinary large thermoelectric potential, Kondo- and heavy-fermion properties [1, 19].

The interest in skutterudite-related systems is connected with search of new thermoelectric materials [22]. Unfilled skutterudites of the type $M(P,Sb,As)_3$ (M is a transition metal) contain voids into which low-coordination ions, in particular rare earth elements, can be inserted. This increases phonon scattering and decreases lattice thermal conductivity without increasing electrical resistivity ρ [17]. Thus the figure of merit can become rather large.

The electronic properties of the $Ir_4LaGe_3Sb_9$, $Ir_4NdGe_3Sb_9$, and $Ir_4SmGe_3Sb_9$ systems were investigated by Nolas et al. [17]. Another class of skutterudite-related systems are $R_3M_4X_{13}$ compounds (where R is a rare earth element, X = Ge or Sn) which attract attention due to the interesting electron properties, interplay of superconductivity and magnetic order [15]. In particular, the Yb-based systems demonstrate the intermediate valence nature of the Yb ions and slightly enhanced value of the linear electronic specific heat coefficient.

19.3 Theoretical Sketch for Thermoelectric Power in Rare-Earth and Kondo Systems

The Seebeck coefficient can become very large due to the reduction of free carriers. There is a crossover from positive to negative thermopower as soon as electron transport dominates over hole transport.

The Kondo skutterudites may exhibit large S due to an appropriate reduction of free charge carriers caused by rare earth elements like Ce or Yb [1]. Strong electron correlations, as obvious in $Pr_{0.73}Fe_4Sb_{12}$; can enhance significantly thermopower values above those found in skutterudites containing valence-stable rare earth elements [19].

Based on the *s-d* interaction model for dilute magnetic alloys Kondo [8] has calculated the scattering probability of the conduction electrons to the second Born approximation. Thus the effect gives rise to a singular term in the resistivity which involves a factor of $cJ^3 \ln T$, where c is the concentration of impurity atoms, J the *s-d* exchange integral. When combined with the lattice resistivity, this gives rise to a resistance minimum, provided J is negative, and large temperature-independent Seebeck coefficient [7, 8].

Here we discuss briefly the Seebeck coefficient $S(T)$ in Kondo lattices following to Irkhin and Katsnelson [4], Irkhin and Irkhin [5]. We can distinguish two cases:

1. *Perturbation theory regime.* The Kondo correction in the electron self-energy $\Sigma(E)$ (or conduction-electron T-matrix) is proportional to $J^3 \ln(E)$. Large Kondo contributions to $S(T)$ correspond to the anomalous odd contribution to the relaxation rate $\tau^{-1}(E)$ [8]. The latter should arise, by analytical properties of $\Sigma(E)$, from the logarithmic singularity in $\mathrm{Re}\Sigma(E)$ [4]. Although such a singularity

is absent in the usual Kondo problem, it occurs in the presence of the potential scattering V which leads to emergence of complex factors $1+V\Sigma_k(E-\mathrm{t}_k+\mathrm{i}0)^{-1}$ which "mix" $\mathrm{Im}\Sigma$ and $\mathrm{Re}\Sigma$ in the incoherent regime.

In the presence of interaction between magnetic moments (Kondo lattices), spin dynamics leads to the replacements $\ln|E| \to (1/2)\ln(E^2+\omega^2)$, $\mathrm{sign}E \to (2/\pi)\tan^{-1}(E/\omega)$ in $\mathrm{Im}\Sigma$ and $\mathrm{Re}\Sigma$, respectively (ω is a characteristic spin-fluctuation frequency). Then the anomalous contribution reads $S(T)-e\rho(T)\times T/max\{T,\omega\}$. Thus the quantity ω plays the role of a characteristic fluctuating magnetic field which is introduced by Kondo [8] to describe thermoelectric power of diluted Kondo systems.

In real concentrated systems Kondo systems, at moderately high (as compared to T_K) temperatures $S(T)$ is usually large and has an extremum (a maximum at $S<0$, a minimum at $S<0$).

2. *The low-temperature regime.* Besides the Kondo temperature, one introduces the second energy scale – the coherence temperature T_{coh}, which corresponds to onset of coherent Kondo scattering by different lattice sites. This is usually small in comparison with T_K. The picture of the coherent state formation enables one to treat experimental data on low-temperature anomalies of thermoelectric power in heavy-fermion systems. With decreasing T below the above-discussed high-temperature extremum, $S(T)$ often changes its sign, has an extremum again and vanishes linearly at $T \to 0$. Such a behavior may be attributed to occurrence of a pseudogap with reversing the sign of the quantity $\mathrm{d}N(E)/\mathrm{d}E$ ($N(E)$ is the electron density of states) at the Fermi level, which determines the $S(T)$ sign in the Mott diffusion mechanism.

   Generally, the systems having low characteristic temperature scales exhibit enhanced S values. In particular, heavy-fermion systems, which exhibit sharp features in density of states due to the hybridization between conduction electrons and f or d-electrons, have been considered as candidates for low-temperature thermoelectric cooling applications [3, 9, 25]. Large thermopower values have been predicted and observed in Kondo insulators like $Ce_3Pt_3Sb_4$ at low temperatures [10, 24].

   In nanowire structures, electron transport is hardly affected by the boundary scattering due to their small intrinsic mean free paths while phonons are strongly scattered due to classical size effect. These results suggest that the nanostructures of Kondo insulators can be designed for high performance thermoelectric cooling devices at low temperatures.

19.4 Experimental Results

We have synthesized and investigated a number of binary and ternary rare-earth compounds and alloys, including new ones. Here we pay attention to Ce-based Kondo compounds (Table 19.1).

Table 19.1 Electric resistivity ρ (mOhm·m), Seebeck coefficient S (mV/K), thermal conductivity κ (W/m·K) and ZT pameter at 300 K

Alloys (sample)	S	r	κ	WF	ZT
$Ce_{0.5}Y_{0.5}NiSb$	−53.2	1.66	11.0	2.49	**0.0465**
$Ce_{0.25}Y_{0.75}NiSb$	−52.6	9.99^{SC}	5.7	7.77	0.015
$Ce_{0.75}Y_{0.25}NiSb$	10.0	5.4	6.2	4.57	$9.0{\cdot}10^{-4}$
$Ce_{0.5}Y_{0.5}NiSb$	−22.8	48.25	2.45	16.1	$1.3{\cdot}10^{-3}$
$Ce_{0.5}La_{0.5}NiSb$	−3.85	7.1	4.48	4.34	$1.4{\cdot}10^{-4}$
$Ce_{0.5}Y_{0.5}Ni_{0.95}Cu_{0.05}Sb$	−18.1	5.17	0.42	0.30	**0.045**
$Ce_{0.5}Y_{0.5}NiSb_{0.8}Bi_{0.2}$	−36.8	2.42	7.7	2.54	0.022
Ce_2MgNi_2	−22.5	0.46	8.6	0.54	0.038
$Ce_{0.5}Mg_{0.5}Ni_2$	−29.4	0.88	14.0	1.68	0.021
$Ce_{0.5}Mg_{0.5}Ni_2$	−33.6	1.00	12.3	1.68	0.028
$Ce_{0.5}Mg_{0.5}Ni_2$	−35.6	1.07	11.7	1.71	0.030
$CeSi_2$	−55.0	0.98	13.8	1.85	**0.067**
$Ce_{0.5}Y_{0.5}Si_2$	−20.0	2.5	13.0	4.43	$3.7{\cdot}10^{-3}$
$CeSi_{1.6}Ge_{0.4}$	−20.0	2.0^{SC}	14.0	3.8	$4.3{\cdot}10^{-3}$
$Ce_{0.5}Y_{0.5}CoSi_3$	−37.6	0.45	16.4	1.01	**0.057**
$CeCo_{0.8}Cu_{0.2}Si_3$	−36.9	0.91	18.8	2.33	0.024
$CeCoSi_3$	−34.6	2.1	9.1	2.61	0.018
$CeCoSi_{1.5}Ge_{1.5}$	25.74	1.11	10.9	1.65	0.0164
CeSiGe	−3.4	5.9	8.0	6.44	$7.4{\cdot}10^{-5}$
$CeSi_{1.6}Ge_{0.4}$	−20.0	2.0	14.0	3.8	$4.3{\cdot}10^{-3}$

The Wiedemann-Franz parameter is $WF = \rho \cdot \kappa/\gamma_{WF} \cdot 300$, $\gamma_{WF} = (\pi^2/3) \cdot (k_B/e)^2$ (k_B is the Boltzmann constant and e the electronic charge)

Maximum ZT values for the presented systems are about 7 %. One can see that Kondo-lattice systems like $CeSi_2$, $Ce_{1-x}Y_xNiSb$ indeed have largest Seebeck coefficient values. Moreover, such systems demonstrate strong temperature dependences of resistivity and Seebeck coefficient (Fig. 19.1).

We report also in more details the results on thermoelectric properties of the scutterudites $Yb_3Co_4Sn_{13}$ and $Yb_3Co_4Ge_{13}$ compounds and $Yb_{3-x}R_xCo_4Ge_{13}$ (R = Ce, La) solid solutions.

Analysis of the powder X-ray diffractograms shows that the $R_3T_4X_{13}$ compounds (R = rare earth, T = Ru, Rh, Os, X = Ge, Sn) adopt the $Pr_3Rh_4Sn_{13}$ -type cage-like structure. This favours small lattice thermal conductivity.

The electrical resistance along the long axis of the sample was measured with a standard four-terminal geometry using a dc current of 0.8 mA The Seebeck coefficient (the thermoelectric voltage under zero electric current) has been measured with disconnection of the sample from the current source. The heat flux in the sample was generated with electric heater. The thermopower E was measured over the same potential contacts used in the resistance measurements. The Seebeck coefficient was calculated as the ratio E/dT. The uncertainty of S was estimated to be less than 10 %. The thermal conductivity was measured by a longitudinal steady state method.

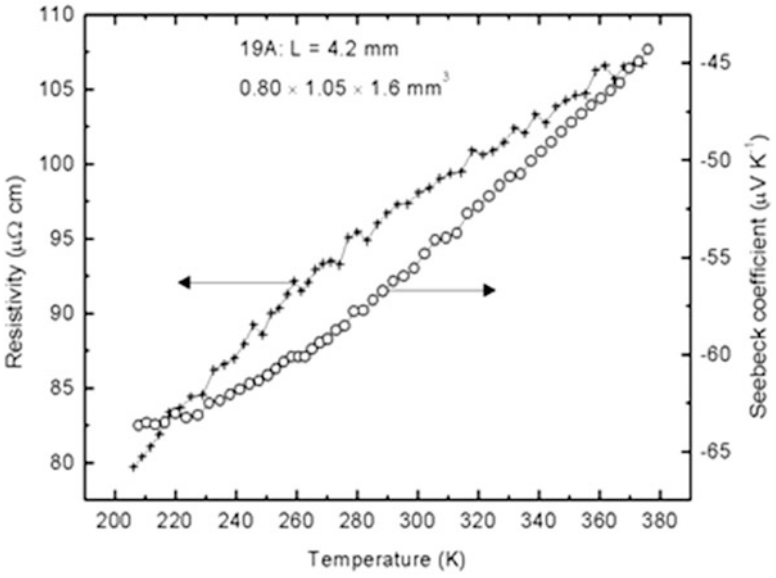

Fig. 19.1 Resistivity and Seebeck coefficient vs. temperature for $CeSi_2$ alloys

All these compounds demonstrate the metallic-type conductivity. Probably, the $Yb_3Co_4Ge_{13}$ has higher electric resistance due to presence of Ge semiconductor in the alloy: the resistance of the $Yb_2CeCo_4Ge_{13}$ and $Yb_{2.3}La_{0.7}Co_4Ge_{13}$ alloys is less than of $Yb_3Co_4Ge_{13}$ alloy which demonstrates absence of the Ge admixture phase.

The Seebeck coefficients, electrical resistance and thermal conductivity have monotonic behavior with increasing temperature from 240 to 380 K (Fig. 19.2).

One can see that the lattice thermal conductivity $\kappa_{lattice}$ of Ge-containing $Pr_3Rh_4Sn_{13}$-type compounds is higher than for Sn-containing compound (thermal coductivity κ is the sum of lattice and electronic conductivity, $\kappa = \kappa_{lat} + \kappa_{el}$) due to that the mass of Sn is higher than the mass of Ge. Also, due to this, the Wiedemann-Franz parameter $\mathrm{WF} = \pi\kappa/\gamma_{WF}$ T has higher values for Ge-containing compounds.

The Seebeck coefficient is $S = 14 \div 27$ V/K for $Yb_3Co_4Sn_{13}$, and $S = -21 \div -12\mu$V/K for $Yb_3Co_4Ge_{13}$. Among the scutterudite systems under consideration, the parameter ZT is maximal for $Yb_3Co_4Sn_{13}$ compounds and acquires the value of 0.017 at 380 K. Although its thermal conductivity is not maximal, this compound demonstrates lowest resistivity at high temperatures. Thus a good metallic electrical resistivity and high Seebeck coefficient (rather than small heat conductivity) turn out to be decisive for large ZT values in this case. Provided that the dependences of electric resistance, thermal conductivity and Seebeck coefficient vs. temperature retain for $Yb_3Co_4Sn_{13}$ compound up to 1,000 K, this compound may have the ZT value about 0.3 at 1,000 K.

Substitution of Yb for Ce or La, as well as substitution of Ge for Sn shifts the Seebeck coefficient to positive values observed in the $Yb_3Co_4Ge_{13}$ compound. The

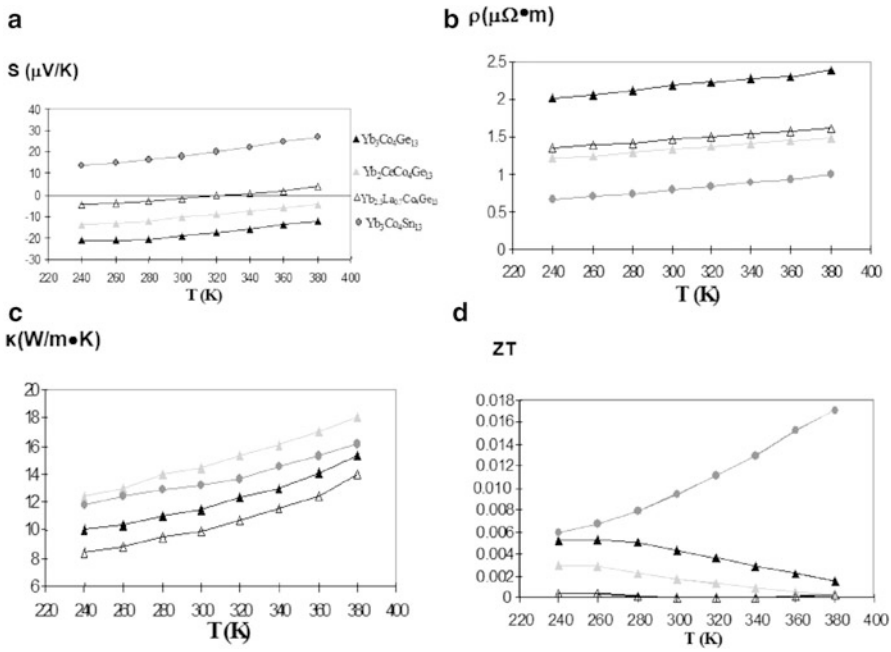

Fig. 19.2 Seebeck coefficient S, electric resistance ρ, thermal conductivity κ and ZT parameter vs. temperature for $Yb_3Co_4Ge_{13}$, $Yb_2CeCo_4Ge_{13}$, $Yb_{2.3}La_{0.7}Co_4Ge_{13}$ and $Yb_3Co_4Sn_{13}$ compounds

Seebeck coefficient of $Yb_{2.3}La_{0.7}Co_4Ge_{13}$ demonstrates non-monotonous temperature dependence. This sign change may be connected with a non-trivial electronic structure near the Fermi level, characteristic for Kondo-like and intermediate-valence systems.

The parameter $ZT = TS^2/(\rho\kappa)$ is maximal for $Yb_3Co_4Sn_{13}$ compounds and acquires the value of 0.017 at 380 K (Fig. 19.2). Although its κ is not maximal, this compound demonstrates lowest resistivity at high temperatures. Thus a good metallic electrical resistivity and high Seebeck coefficient (rather than small heat conductivity) turn out to be decisive for large ZT values.

We can conclude as follows:

1. The $Pr_3Rh_4Sn_{13}$-type Ge-containing compounds have lattice thermal conductivity higher than Sn-containing compounds due to relatively low Ge atom mass as compared to Sn, which is important for thermoelectric characteristics.
2. The systems investigated demonstrate a non-trivial behavior vs. alloy composition. Substitution of Yb for cerium or La shifts the Seebeck coefficient to positive values. A more systematic treatment is of interest. Probably, some $Yb_{3-x}R_xCo_4Sn_{13}$ compounds will have the Seebeck coefficient and ZT parameter value higher than $Yb_3Co_4Sn_{13}$ compound.

Although *ZT* values obtained in the rare-earth compounds are still not too large, they are promising materials. There exist some ways to improve their characteristics. Further experimental investigations in this directions and comparison with other ternary rare-earth systems would be useful.

Acknowledgements This work was supported by Asahi Kasei Corporation (Japan) in the ISTC project N 2382p and by the Programs of fundamental research of RAS Physical Division "Strongly correlated electrons in solids and structures", project No. 12-T-2-1001 (Ural Branch) and of RAS Presidium "Quantum mesoscopic and disordered structures", project No. 12-P-2-1041.

References

1. Bauer E et al (2003) Physica B 328:49
2. Caillat T, Fleurial J-P, Borshchevsky A (1996) J Cryst Growth 166:722
3. Grenzebach C et al (2006) Phys Rev B 74:195119
4. Irkhin V Yu, Katsnelson MI (1989) Z Phys B 75:67
5. Irkhin V Yu, Irkhin Yu P (2007) Electronic structure, correlation effects and properties of d- and f-metals and their compounds. Cambridge International Science Publishing, Cambridge
6. Kanatzidis MG (2010) Chem Mater 22:648
7. Kondo J (1965) Progr Theor Phys 34:372
8. Kondo J (1969) Solid state physics. In: Seitz F, Turnbull D (eds) vol 23. Academic, New York, p 183
9. Mahan GD (1998) Sol State Phys 51:81
10. Mahan GD, Sales BC, Sharp JW (1997) Phys Today 50:42
11. Mahan GD, Sofo JO (1996) Proc Natl Acad Sci USA 93:7436
12. Minnich AJ et al (2009) Energ Environ Sci 2:466
13. Morelli DT, Meisner GP (1997) Phys Rev B 56:7376
14. Morelli DT et al (1995) Phys Rev B 51:9622
15. Mudryk Ya et al (2001) J Phys Cond Matter 13:7391
16. Nolas GS et al (1996) J Appl Phys 79:2622
17. Nolas GS et al (1996) J Appl Phys 79:4002
18. Nolas GS, Cohn JL, Slack GA (1998) Phys Rev B 58:164
19. Nolas GS et al (1999) Annu Rev Mater Sci 29:89
20. Pichanusakorn P, Bandaru P (2010) Mater Sci Eng 67:19
21. Rosenberg H (2004) The solid state. Oxford University Press, Oxford
22. Rowe DM (2006) Thermoelectrics handbook: macro to nano. CRC/Taylor & Francis, Boca Raton
23. Sales BC, Mandrus D, Williams RK (1996) Science 22:1325
24. Takabatake T et al (2003) Physica B 328:53
25. Zlatic V, Hewson AC (eds) (2009) Properties and applications of thermoelectric materials. Springer, New York

Chapter 20
Simulation of Random Telegraph Noise in Nanometer nMOSFET Induced by Interface and Oxide Trapped Charge

Atabek E. Atamuratov, Ralf Granzner, Mario Kittler, Zuhra Atamuratova, Mahkam Halillaev, and Frank Schwierz

Abstract In this work, the influence of a single positive elementary charge trapped either in the oxide or at the oxide-semiconductor interface on Random Telegraph Noise (RTN) has been investigated and the relative RTN amplitude $\Delta I_D/I_D$ in nanometer MOSFET was simulated. Since our investigations were focused on the RTN amplitude, we considered only the steady-state and did not investigate the dynamics of charging/discharging the trap.

For considering the impact of a single charge trapped in the oxide or at the interface, we assumed that this single positive charge was homogeneously distributed across a certain gate oxide volume or across a certain interface area. By varying the length of the charged region, containing a homogeneously distributed single charge, from 54 nm down to 0.8 nm, it is found that the RTN amplitude increases for decreasing length and reaches saturation for lengths below 20 nm.

For identical extensions and positions in the gate length direction, a trapped interface charge generates a RTN amplitude up to two times larger compared to a charge trapped in the oxide. For both oxide and interface charges the maximal RTN amplitude is observed for a trap located right above the center of the channel. Results show that the main contribution to the RTN amplitude comes from the variation of the carrier density in the channel due to the trapped charge.

A.E. Atamuratov • Z. Atamuratova • M. Halillaev
Department of Physics, Urganch State University, H. Olimjon Street, 740013 Urganch, Uzbekistan
e-mail: aatabe@hotmail.ru

R. Granzner • M. Kittler • F. Schwierz
Department of Solid-State Electronics, Institute of Micro- and Nanotechnologies, Ilmenau University of Technology, Ilmenau, Germany

R. Egger et al. (eds.), *Low-Dimensional Functional Materials*, NATO Science for Peace and Security Series B: Physics and Biophysics, DOI 10.1007/978-94-007-6618-1_20,

20.1 Introduction

Over the last decade, subthreshold/near-threshold digital CMOS logic has attracted increasing attention. In this type of logic, the MOSFETs switch between off (gate-source voltage $V_{GS} = 0$) and "a little bit" on ($V_{GS-on} = V_{DD} < V_{TH}$ for subthreshold logic or $V_{GS-on} \approx V_{DD} = V_{TH}$ for near-threshold logic, where V_{TH} is the transistor's threshold voltage and V_{DD} is the supply voltage). This is fundamentally different from conventional superthreshold logic, where the transistors switch from off to "fully-on" ($V_{GS-on} = V_{DD} \approx 4 \times V_{TH}$). Sub/near-threshold logic is a very effective way to achieve ultralow power consumption for digital circuits which can be applied in both power efficient high-performance logic circuits and a wide range of power-sensitive circuits [1–3]. The enhanced power efficiency of subthreshold/near-threshold circuits comes, however, at the expense of reduced speed. Furthermore, since device currents in the sub/near-threshold regime are very small, the impact of noises to device and circuit operation can become significant [4–8]. As reported in [4], in highly scaled nMOSFETs extremely large current fluctuations due to Random Telegraph Noise (RTN) have been observed under subthreshold conditions (relative RTN amplitudes $\Delta I_D/I_D$ is around 75 % where I_D is the drain current and ΔI_D is the drain current fluctuation caused by RTN).

The occurrence of RTN in MOSFET is traditionally explained by the capture/release of charge carriers in/from a single trap within the gate oxide or at the oxide-semiconductor interface. In some experiments RTN amplitude is very large [4]. Unfortunately, the origin of such large RTN fluctuations is still unknown. Early reports linked RTN to both bulk dielectric defects and/or interface state defects [9, 10]. While the mitigation of both bulk dielectric and interface state defects is always good practice, it is unclear which type of defect should receive the most attention [4]. During the last few years, the detailed investigation of RTN in nanometer MOSFETs led to results which put the existing traditional models of RTN generation in doubt [4, 5]. Therefore it is interesting and urgently needed to investigate the origin and the effects of RTN in nanometer MOSFETs.

In this work, the influence of a single positive elementary charge trapped either in the oxide or at the oxide-semiconductor interface on RTN has been investigated and the relative RTN amplitude $\Delta I_D/I_D$ in nanometer MOSFET was simulated. In particular, the dependence of the relative RTN amplitude on both the localization area of the trapped charge, i.e., the area across which the single charge is "distributed", and the position of this area relative to the center of the channel was investigated. For the simulations, the drift-diffusion option of the device simulator Sentaurus was used.

20.2 Simulation Results

Generally, the origin of RTN is connected to the capture and subsequent emission of single charges on/from a trap which causes drain current fluctuations in MOSFETs. The process of capturing or emitting a single charge, and the resulting fluctuations of the drain current, has a discrete character. The current jumps between two distinct levels and it is either high or low. Since our investigations were focused on the RTN amplitude, we considered only the steady-state and did not investigate the dynamics of charging/discharging the trap.

For considering the impact of a single charge trapped in the oxide or at the interface, we assumed that this single positive charge was homogeneously distributed across a certain gate oxide volume or across a certain interface area. This defines an appropriate charge density in the chosen gate oxide or interface region.

For the 2D simulations we considered an nMOSFET structure with constant substrate doping $N_A = 5 \cdot 10^{18}\,\mathrm{cm}^{-3}$, an oxide layer thickness of 1.4 nm and a channel length L of 54 nm. The RTN amplitude was determined for a source voltage of $-50\,\mathrm{mV}$ and zero drain and substrate voltages. To find the optimum size to be assumed for the charged oxide/interface region (containing one single charge homogeneously distributed across the region), we calculated the maximal RTN amplitude for different extensions of the charged region (in all cases located at the channel center). Figure 20.1 shows the RTN amplitude versus length of the charged region for both trapped oxide and interface charges. It is seen that the maximal RTN amplitude increases for decreasing lengths of the charged region and then saturates for lengths below 20 nm. Maximal RTN amplitude does almost not depend on the size of the charged region for both oxide and interface trapped charge in range from 0.8 to 18 nm. For the following detailed considerations of the RTN amplitude dependence on the position of the charge we choose a size of 2 nm length for the charged region.

We shall arrange the charged area above the channel center in the oxide or the interface region because at low drain-source voltage the potential barrier between source and drain is maximum approximately in the middle of the channel and it is to be expected that a single charge trapped right above the center of the channel would have the greatest influence on the drain current and accordingly to cause the maximal RTN amplitude. A comparison of the RTN amplitude for various position of the charged area along all channel (channel length 54 nm) for both oxide and interface trapped charges is shown in Fig. 20.2.

It can be seen from Fig. 20.2 that a maximal RTN amplitude is reached if the charged area is arranged above the center of channel. A displacement the charged area from the center to a distance of $L/4$ (L is the channel length), the RTN amplitude is decreased up to 50 % for both oxide and interface trapped charges. The dependence of the RTN amplitude on the gate overdrive also is shown in Fig. 20.3 for a position of 18 nm from the center.

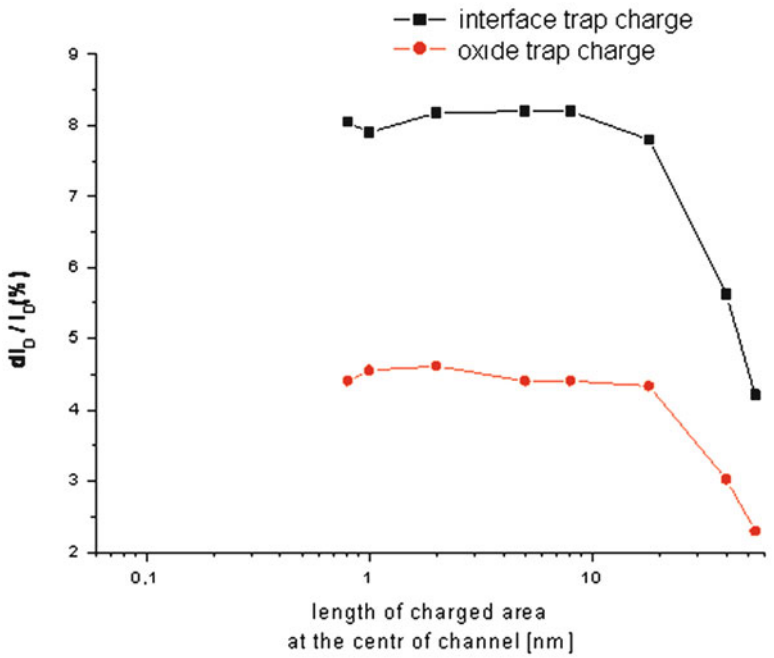

Fig. 20.1 Dependence of maximum RTN amplitude (gate overdrive $V_G V_T = -300\,\mathrm{mV}$) on the length of oxide and interface trap charge area at the centre a channel

Relatively high RTN amplitudes are observed only in the subthreshold region and the RTN amplitude is higher when the charged area is placed above the channel centre for both the cases of oxide trapped and interface trapped charge. The RTN amplitude is approximately two times higher for the case of an interface trapped charge than for the case of an oxide trapped charge. Obviously, RTN and the related change of the drain current is connected to the variation of carrier concentration induced by a charge trapped in oxide or interface. In Fig. 20.4 the distribution of the carrier concentration along the channel in a depth 1 nm below the oxide-silicon interface for charge located above the channel center is presented. The variation of the charge concentration induced by an interface trapped charge is larger than that induced by an oxide trapped charge. The current variation induced by changing of carrier concentration can be evaluated based on the drift model by

$$\Delta I_D = \frac{eSv}{l} \int_{-\frac{l}{2}}^{\frac{l}{2}} (n(x) - n_0(x))dx \tag{20.1}$$

Here, e is the elementary charge, S is the cross-section of the current path, v is the carrier drift velocity, l is the length of the region in the channel where a sizeable variation of the carrier concentration after charge trapping occurs (along the x axis), and $n_0(x)$ is the carrier concentration without charge trapping. An estimation of

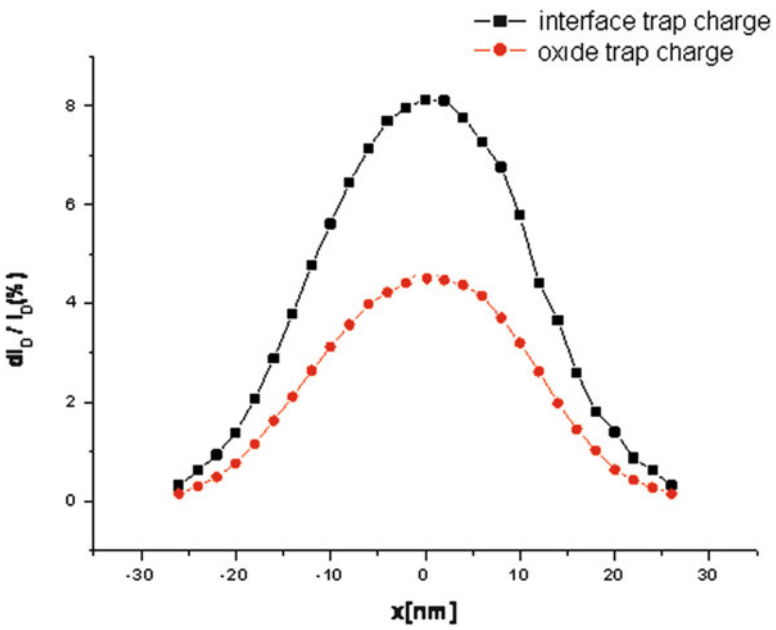

Fig. 20.2 Dependence of the maximum RTN amplitude on the position of oxide and interface trapped charge area with length 2 nm along the channel. The gate overdrive is −300 mV

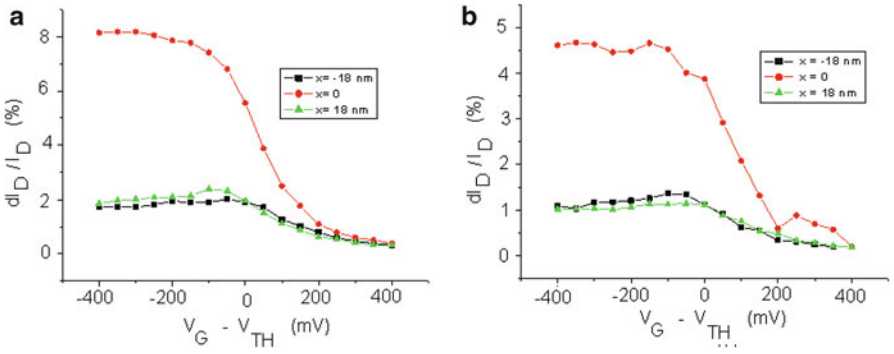

Fig. 20.3 RTN amplitude dependence on gate overdrive for the cases of a charge trapped at the interface (**a**) and in the oxide (**b**)

the relation of drain current variation due to charge trapping ΔI_D(interface trap) / ΔI_D(oxide trap) by combining Eq. (20.1) and carrier density profile from Fig. 20.4 leads to a value of 1.41. For comparison the relation of the drain current variation induced by trapping of a charge in oxide and on interface at $V_G - V_T = 0$, carried out from data in Fig. 20.3 give value 1.43. The obtained very similar values show that, as could be expected, the carrier concentration variation correlates well with current variation.

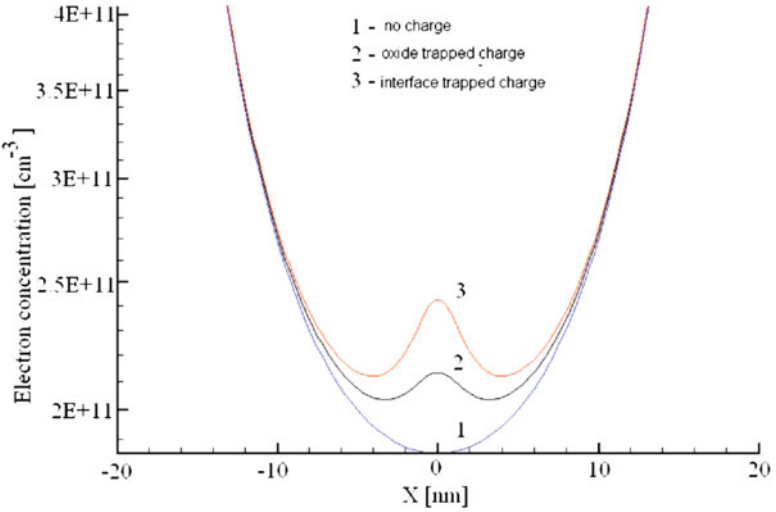

Fig. 20.4 Electron concentration along the channel 1 nm below the oxide/semiconductor interface with and without trapped charge. The charged region is 2 nm long and located above the channel center

20.3 Conclusion

By varying the length of the charged region, containing a homogeneously distributed single charge, from 54 nm down to 0.8 nm, we found that the RTN amplitude increases for decreasing length and reaches saturation for lengths below 20 nm.

For identical extensions and positions in the gate length direction, a trapped interface charge generates a RTN amplitude up to two times larger compared to a charge trapped in the oxide.

For both oxide and interface charges the maximal RTN amplitude is observed for a trap located right above the center of the channel. Our results show that the main contribution to the RTN amplitude comes from the variation of the carrier density in the channel due to the trapped fixed charge.

References

1. Bol D, Ambroise R, Flandre D, Legat J-D (2009) Interests and limitations of technology scaling for subthreshold logic. IEEE Tans Very large Scale Integr Syst 17(10):1508–1519
2. Markovic D, Wang CC, Alarco'n LP, Liu T-T, Rabaey JM (2010) Ultralow-power design in near-threshold region. Proc IEEE 98(2):237–252
3. Dreslinski RG, Wieckowski M, Blaauw D, Sylvester D, Mudge T (2010) Near-threshold computing: reclaiming Moore's Law through energy efficient integrated circuits. Proc IEEE 98(2):253–266

4. Campbell JP, Yu LC, Cheung KP, Qin J, Suehle JS, Oates A, Sheng K (2009). Large random telegraph noise in sub-threshold operation of nano-scale nMOSFETs. In: Proceedings of the IEEE international conference on IC design and technology ICICDT 2009, pp 17–20
5. Campbell JP, Qin J, Cheung KP, Yu L, Suehlel JS, Oates A, Sheng K (2008) The origins of random telegraph noise in highly scaled SiON nMOSFETs. Integrated reliability workshop, pp 105–109
6. Cheung KP, Campbell JP (2011) On the magnitude of random telegraph noise in ultra-scaled MOSFETs. In: Proceedings of the IEEE international conference on ICICDT, pp 1–4
7. Asenov A, Balasubramaniam R, Brown AR, Davies JH (2003) RTS amplitude in decananometer MOSFETs: 3-D simulation study. IEEE Trans Electron Dev 50:839–845
8. Asenov A, Balasubramaniam R, Brown AR, Davies JH, Saini S (2000) Random telegraph signal amplitudes in sub 100 nm (Decanano) MOSFETs: 3D "atomistic" simulation study. In: Proceedings of the IEDM technical digest, pp 279–282
9. Hung KK, Ko PK, Hu CM, Cheng YC (1990) A unified model for the flicker noise in metal oxide-semiconductor field-effect transistors. IEEE Trans Electron Dev 37:654–665
10. Ohata A, Toriumi A, Iwase M, Natori K (1990) Observation of random telegraph signals – anomalous nature of defects at the Si/SiO_2 interface. J Appl Phys 68: 200–204

Chapter 21
Anyon Bosonized 2D Fermions or a Single Boson Physics of Cuprates: Experimental Evidences

Bakhodir Abdullaev

Abstract Within the single boson and single fermion two liquid picture [1] we have been succeeded to understand all elements of the doping-temperature phase diagram [1–3] and the non-Fermi liquid low-temperature heat conductivity and entropy [4] of cuprates. Single bosons are a result of the anyon bosonization of $2D$ fermions.

21.1 Introduction

The origin of pseudogap (PG) and high-temperature superconductivity phases in copper oxides is the most puzzling and challenging problem in condensed matter physics. Despite on the intensive experimental and theoretical studies we have no clear understanding of these phases so far. A relationship between two phases has become a subject of wide range theoretical proposals and their possible experimental testing.

The fundamental property of the PG is a partial gap in the density of states [5] which is observed in various experiments. To understand the nature of this gap the real space atomic scale scanning tunneling microscopy measurements of the copper oxide $Bi_2Sr_2CaCu_2O_{8+\delta}$ have been performed. For the case of high-T_c superconductivity the spatial gap inhomogeneities have been observed in Refs. [6, 7], while Pan et al. [8] explicitly determine their minimal size. The evolution of the nanoscale gap formation with temperature decrease in the PG region has been investigated by Gomes et al. [9].

In the recent paper [1] we have studied the origin of minimal size nanoregions (NRs), which were visualized in Refs. [8, 9] through the measurement of the

B. Abdullaev (✉)
Institute of Applied Physics, National University of Uzbekistan, 100174-Vuzgorodok, Tashkent, Uzbekistan
e-mail: bakhodir_abdullaev@yahoo.com

R. Egger et al. (eds.), *Low-Dimensional Functional Materials*, NATO Science for Peace and Security Series B: Physics and Biophysics, DOI 10.1007/978-94-007-6618-1_21,

energy gap. We used the experimental fact that PG and superconductivity phases are formed from the NRs. Particularly, we have been interested in the electric charge of NRs. We employed the information about the charge to understand some ingredients of doping-temperature phase diagram of $Bi_2Sr_2CaCu_2O_{8+\delta}$ copper oxide. It is worth to notice that all physical findings in the paper were inferred from the analysis of data for the NRs in [8,9]. The most important fermionic nature of the second hole inside NR at the second critical doping x_{c2} and dopings below x_{c2} was implied from the meaning of the x_{c2}: at this doping the superconductivity and hence, the bosonic property of the matter disappears. The justification of the appearance of single hole bosons has been given using the concept of anyons. In such a treatment the anyon vector potential and the corresponding statistical magnetic field represent Berry connection and fictitious magnetic field [10], respectively. It was demonstrated in [1] that $2D$ fermions can be bosonized. So that the fermion ground state becomes an excited state with respect to the boson one. The linear density dependence of the energy gap between these two states describes the well-known Uemura relation for $2D$ superconductors.

Another puzzling side of the PG normal phase is that in this region some experimental data clearly demonstrate a failure of a Landau Fermi liquid theory (LFLT), which is the basis of the theory of normal metals. Hill with collaborators [11] reported that the heat conductivity of the electron doped copper-oxide $Pr_{2-x}Ce_xCuO_4$ measured at low temperature (low-T) is deviated from one predicted by the LFLT, i.e., as the temperature decreases, the temperature dependence of the heat conductivity (κ) is changed from the normal linear $\kappa \sim T$ behavior into an anomalous $T^{3.6}$ one, which was described by the "downturn" behavior of the heat conductivity. They also reported another important non-Fermi liquid behavior: the Lorentz ratio of the Wiedemann – Franz law (WFL) in the region of the linear T-dependence of κ was significantly larger (1.7 times) than Sommerfeld's value. These violations were also observed in the $Bi_{2+x}Sr_{2-x}CuO_{6+\delta}$ copper-oxide in the vicinity of the metal-insulator-crossover by Proust et al. [12].

The normal state electronic specific heat c of superconductors $YBa_2Cu_3O_{6+x}$ and $La_{2-x}Sr_xCuO_4$ above the high-T_c transition temperature T_c was experimentally investigated in Refs. [13] and [14], respectively. A magnetic field dependence of c has considered in [15] for $Y_{0.8}Ca_{0.2}Ba_2Cu_3O_{6+x}$ compound. Due to existence of high-T_c superconductivity, it is impossible to extract the information on the low-T dependence of the normal state c. On the other hand, Loram et al. [13] showed the T-dependence of the entropy ($\mathscr{S}$) $\mathscr{S} \sim T^i$ with $i > 1$ for the underdoped (insulating) material, which was driven from the measured electronic specific heat of high-T_c superconductors $YBa_2Cu_3O_{6+x}$, ignoring the superconducting effects, while for the optimal doping compound $\mathscr{S} \sim T$ was measured.

In Sect. 21.2 we demonstrate the rigorous proof that $2D$ fermions can bosonize. Then in Sect. 21.3 the result of the ground-state energy calculation of charged anyon gas will be given. We apply the difference between the ground state energies of fermions and bosons to derive the single boson doping-temperature phase diagram of cuprates in Sect. 21.4. In Sect. 21.5 it will be demonstrated that this difference in

the ground state energies yields the microscopic origin of the phenomenological Uemura relation. Section 21.6 will be devoted to the charge and percolation analysis of NRs on the base of experimental data given in Refs. [9] and [8]. The analysis provides the interpretation of some elements of the phase diagram doping-temperature in $Bi_2Sr_2CaCu_2O_{8+\delta}$ compound. Section 21.7 will describe the origin of the non-Fermi liquid heat conductivity and the entropy of copper-oxides. We summarize and conclude our paper in Sect. 21.8.

21.2 Real Bosonization of 2*D* Fermions

The fact that $a-b$ planes of CuO_2 atoms play a dominant role in the determination of the physics of cuprates provides an opportunity to exploit the fundamental property of the two-dimensionality. Specifically, the $2D$ topology allows the fractional statistics [16] characterized by a continuous parameter ν taking values between 0 (for bosons) and 1 (for fermions). The particles with $0 < \nu < 1$ are generically called anyons [17, 18]. One can apply the last one in the study of properties of the mentioned above $a-b$ planes.

Following to Ref. [1], in this section we briefly outline the rigorous derivation of the real bosonization of $2D$ fermions. It can be achieved by exact cancellation of terms in the ground state energy arisen from fermion (anyon) statistics and a Zeeman interaction of spins $\hbar/2$ of particles with statistical magnetic field [19, 20] produced by vector potential of anyons.

Let us consider the Hamiltonian

$$\hat{H} = \frac{1}{2M}\sum_{k=1}^{N}\left[(\mathbf{p}_k + \mathbf{A}_\nu(\mathbf{r}_k))^2 + M^2\omega_0^2|\mathbf{r_k}|^2\right] + \frac{1}{2}\sum_{k=1}^{N}\left[V(\mathbf{r}_k) + \sum_{j\neq k}^{N}\frac{e^2}{|\mathbf{r}_{kj}|}\right] \tag{21.1}$$

of the gas of N anyons with mass M and charge e, confined in $2D$ parabolic well, interacting through Coulomb repulsion potential in the presence of uniform positive background [21] $V(\mathbf{r}_k)$. Here, $\mathbf{r}_k$ and $\mathbf{p}_k$ represent the position and momentum operators of the kth anyon in $2D$ space dimension,

$$\mathbf{A}_\nu(\mathbf{r}_k) = \hbar\nu\sum_{j\neq k}^{N}\frac{\mathbf{e}_z\times\mathbf{r}_{kj}}{|\mathbf{r}_{kj}|^2} \tag{21.2}$$

is the anyon gauge vector potential [22], $\mathbf{r}_{kj} = \mathbf{r}_k - \mathbf{r}_j$, and $\mathbf{e}_z$ is the unit vector normal to the $2D$ plane. In the expression for $\mathbf{A}_\nu(\mathbf{r}_k)$ and hereafter we assume that $0 \leq \nu \leq 1$.

In the bosonic representation of anyons we take the system wave function in the form [23]:

$$\Psi(\mathbf{R}) = \prod_{i\neq j} r_{ij}^{\nu} \Psi_T(\mathbf{R}). \tag{21.3}$$

Here $\mathbf{R} = \{\mathbf{r}_1 \ldots . \mathbf{r}_N\}$ is the configuration space of the N anyons. The product in the right hand side of this equation is the Jastrow-type wave function. It describes the short distance correlations between two particles due to anyonic (fermionic) statistics interaction.

Let us consider first the term in the Hamiltonian $\hat{H}$, Eq. (21.1) containing the anyon vector potential $\mathbf{A}_\nu(\mathbf{r}_k)$. Substituting $\Psi(\mathbf{R})$, Eq. (21.3), in Schredinger equation with this Hamiltonian, we obtain an equation $\tilde{\hat{H}}\Psi_T(\mathbf{R}) = E\Psi_T(\mathbf{R})$ with the novel Hamiltonian $\tilde{\hat{H}} = \tilde{\hat{H}}_1 + \tilde{\hat{H}}_2$, where

$$\tilde{\hat{H}}_1 = \sum_{k=1}^{N} \left(\frac{-\hbar^2 \Delta_k}{2M} - \frac{\hbar^2 \nu}{M} \sum_{j\neq k} \frac{\mathbf{r}_{kj} \cdot \nabla_k}{|\mathbf{r}_{kj}|^2} \right) \tag{21.4}$$

and

$$\tilde{\hat{H}}_2 = -i\frac{\hbar}{M} \sum_{k=1}^{N} \left(\mathbf{A}_\nu(\mathbf{r}_k) \cdot \nabla_k + \nu \sum_{j\neq k} \frac{\mathbf{A}_\nu(\mathbf{r}_k) \cdot \mathbf{r}_{kj}}{|\mathbf{r}_{kj}|^2} \right). \tag{21.5}$$

As shown in Ref. [23], the ν interaction Hamiltonian in $\tilde{\hat{H}}_1$, i.e., the second its term, is equivalent to a sum of two-body potentials

$$\frac{\pi\hbar^2 \nu}{M} \sum_{j\neq k} \delta^{(2)}(\mathbf{r}_k - \mathbf{r}_j) \, . \tag{21.6}$$

Therefore, the Hamiltonian $\tilde{\hat{H}}_1$ now reads

$$\tilde{\hat{H}}_1 = \sum_{k=1}^{N} \left(\frac{-\hbar^2 \Delta_k}{2M} + \frac{\pi\hbar^2 \nu}{M} \sum_{j\neq k} \delta^{(2)}(\mathbf{r}_k - \mathbf{r}_j) \right). \tag{21.7}$$

Now we demonstrate the real bosonization of $2D$ fermions on the example of anyons in parabolic well. To do this we consider the Zeeman interaction term

$$\frac{\hbar}{M} \sum_{k=1}^{N} \hat{\mathbf{s}} \cdot \mathbf{b}_k \tag{21.8}$$

of spins with the statistical magnetic field [20] (see also Ref. [19])

$$\mathbf{b}_k = -2\pi\hbar\nu \mathbf{e}_z \sum_{j\neq k} \delta^{(2)}(\mathbf{r}_k - \mathbf{r}_j) \, , \tag{21.9}$$

which can be derived if one calculates $\mathbf{b}_k = \nabla \times \mathbf{A}_\nu(\mathbf{r}_k)$ by using Eq. (21.2).

For $s_z = \hbar/2$ and using the expression, Eq. (21.9), for $\mathbf{b}_k$ one obtains

$$\frac{\hbar}{M}\sum_{k=1}^{N}\hat{\mathbf{s}}\cdot\mathbf{b}_k = -\pi\nu\frac{\hbar^2}{M}\sum_{k(j\neq k)}\delta^{(2)}(\mathbf{r}_k-\mathbf{r}_j)\ . \tag{21.10}$$

Being added to the expression, Eq. (21.7), for the Hamiltonian $\tilde{\hat{H}}_1$, this Zeeman term cancels exactly the second one of $\tilde{\hat{H}}_1$, which is responsible for the statistics of fermions (for $\nu = 1$) and anyons. Since the energy of bosons is lower than one for fermions and anyons, there appears a coupling of spin with statistical magnetic field for every particle or bosonization of $2D$ fermions and anyons. From this one can conclude, if anyon concept is correct for the description of any $2D$ quantum system, its ground state should be bosonic with $\nu = 0$, while its excited state should be fermionic ($\nu = 1$) or anyonic ($0 < \nu < 1$) depending of the fixed value of ν. As demonstrated in Ref. [1], the vector potential $\mathbf{A}_\nu(\mathbf{r}_k)$ represents the Berry connection and the statistical magnetic field is the fictitious magnetic field originated from the Berry phase [10] of anyons (see book of Wilczek [18]).

21.3 The Ground-State Energy of Charged Anyon Gas

In Ref. [24] we have derived an approximate analytic formula for the ground-state energy of the charged anyon gas. Our approach was based on the harmonically confined two-dimensional ($2D$) Coulomb anyon gas and a regularization procedure for vanishing confinement. To take into account the fractional statistics and Coulomb interaction we introduced a function, which depends on both the statistics and density parameters (ν and r_s, respectively). We determined this function by fitting to the ground state energies of the classical electron crystal at very large r_s (the $2D$ Wigner crystal), and to the Hartree-Fock (HF) energy of the spin-polarized $2D$ electron gas, and the dense $2D$ Coulomb Bose gas at very small r_s. The latter was calculated by use of the Bogoliubov approximation. Applied to the boson system ($\nu = 0$) our results were very close to recent results from Monte Carlo (MC) calculations. For spin-polarized electron systems ($\nu = 1$) our comparison led to a critical judgment concerning the density range, to which the HF approximation and MC simulations apply. In dependence on ν, our analytic formula yielded ground-state energies, which monotonously increased from the bosonic to the fermionic side if $r_s > 1$. For $r_s \leq 1$ it shows a nonmonotonous behavior indicating a breakdown of the assumed continuous transformation of bosons into fermions by variation of the parameter ν.

We have found in Ref. [24] the expression for the ground-state energy per particle (in Ry units) in the form

$$\mathscr{E}_0(\nu, r_s) \approx \frac{2f(\nu, r_s)}{r_s^2}\left[\frac{\nu}{2K_X^2} + \frac{K_X^2}{2} - \frac{K}{K_X}\right]. \tag{21.11}$$

Here

$$K_X = (K_A + K_B)^{1/2} + [-(K_A + K_B) + 2(K_A^2 - K_A K_B + K_B^2)^{1/2}]^{1/2}, \tag{21.12}$$

and

$$K_A = \left[K^2/128 + \left((\nu/12)^3 + (K^2/128)^2\right)^{1/2}\right]^{1/3}, \quad K_B = \left[K^2/128 - \left((\nu/12)^3 + (K^2/128)^2\right)^{1/2}\right]^{1/3}, \tag{21.13}$$

with $K = c_{WC} r_s / f^{1/2}(\nu, r_s)$.

For the Bose gas ($\nu = 0$) we obtained from Eq. (21.11)

$$\mathscr{E}_0(0, r_s) = -\frac{c_{WC}^{2/3} f^{2/3}(0, r_s)}{r_s^{4/3}} \tag{21.14}$$

and found for small r_s $f(0, r_s) \approx c_{BG}^{3/2} r_s / c_{WC}$, which fitted the ground-state energy of Coulomb Bose gas calculated in Ref. [24] in the Bogoliubov approximation with $c_{BG} = 1.29355$. For large r_s, the ground-state energy does not depend on statistics and equals the energy of the classical $2D$ Wigner crystal [25], $E_{WC} = -2.2122/r_s$. This matches with Eq. (21.14) if at low densities $f(0, r_s) \approx r_s^{1/2}$ with $c_{WC}^{2/3} = 2.2122$. For large r_s we obtained

$$\mathscr{E}_0(\nu, r_s \to \infty) = \frac{c_{WC}^{2/3} f^{2/3}(\nu, r_s)}{r_s^{4/3}} \left(-1 + \frac{7\nu f^{2/3}(\nu, r_s)}{3 c_{WC}^{4/3} r_s^{4/3}}\right). \tag{21.15}$$

For arbitrary r_s, the interpolating functional form

$$f(\nu, r_s) \approx \nu^{1/2} c_0(r_s) e^{-5 r_s} + \frac{c_{BG}^{3/2} r_s / c_{WC}}{1 + c_1(r_s) c_{BG}^{3/2} r_s^{1/2} / c_{WC}} + \frac{0.2 c_1(r_s) r_s^2 Ln(r_s)}{1 + r_s^2} \tag{21.16}$$

with $c_0(r_s) = 1 + 6.9943 r_s + 22.4717 r_s^2$ and $c_1(r_s) = 1 - e^{-r_s}$ satisfied all constraints for $f(\nu, r_s)$ function (see Ref. [24]) and, in addition, yields in the fermion case ($\nu = 1$) for the ground-state energy per particle the HF result [26]

$$E_{HF} = \frac{2}{r_s^2} - \frac{16}{3\pi r_s}. \tag{21.17}$$

In Fig. 21.1 we show results for the ground-state energy per particle on the large scale $1.0 \le r_s \le 15.0$. The upper four curves refer in descending order to

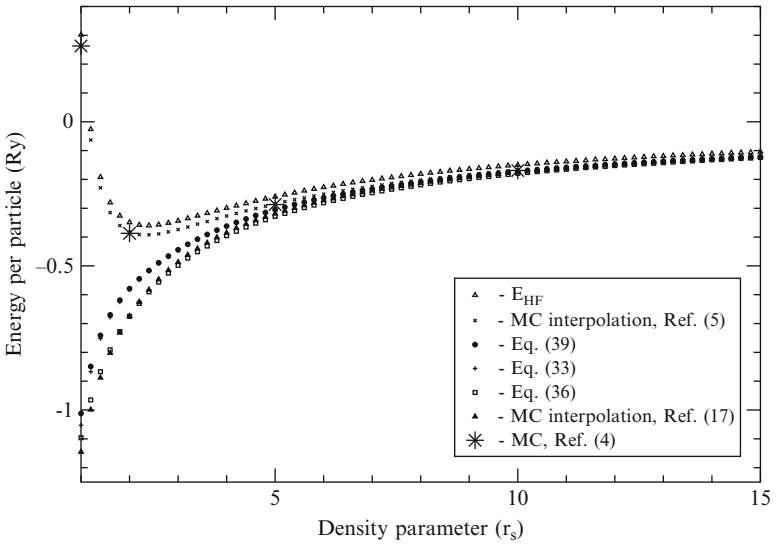

Fig. 21.1 Ground-state energies per particle vs. density parameter r_s for range $1.0 \leq r_s \leq 15.0$ from *top* to *bottom*: for fermions ($\nu = 1$) HF approximation (Eq. 21.17) and Ref. [26], *open triangles*), MC interpolation data (from Ref. [27] (Ref. [5] in Ref. [24])), (*crosses*), and present results from Eq. (21.15) (Eq. (39) in Ref. [24]) (*closed circles*) and Eq. (21.11) (Eq. (33) in Ref. [24]) (*plus signs*), and for bosons ($\nu = 0$) present results from Eq. (21.14) (Eq. (36) in Ref. [24]) (*open squares*) and MC data from Ref. [28] (Ref. [17] in Ref. [24]) (*closed triangles*). MC data of Ref. [29] (Ref. [4] in Ref. [24]) for some particular values of r_s are indicated by *star symbols*

the fermion case ($\nu = 1$): HF energies for spin-polarized electrons from Ref. [26] (open triangles), interpolated by Padè approximant MC data from Ref. [27] for spin-polarized electrons (crosses), and our results from Eq. (21.11) (on the given scale identical with those of Eq. (21.15)) for spin-polarized electrons (closed circles). The lower two curves are for charged bosons ($\nu = 0$) and result from MC calculations of Ref. [28] (closed triangles) and from our Eq. (21.14) (open squares). By star symbols we indicated the MC data [29] (without interpolation) obtained for some particular r_s values.

21.4 Single Boson Doping-Temperature Phase Diagram

Following to Refs. [2, 3], one can assume the fluctuations of spins of fermions coupled to magnetic field. Therefore, bosons with effective spins might look like as Fermi particles. However, fermions with different spins are independent [30]. Thus, the spins of bosons interact with each other and do not interact with spins of another fermions if they exist in the system. We introduce a some correlation length, inside of which spins of bosons interact with each other. For temperature $T = 0$ we denote

it by ξ_0. The increase of fluctuations destroys the coupling, and bosons become the anyons or fermions. This occurs when the gain in the energy due to fluctuations of spins of bosons is equal to energy difference between the anyon (or Fermi) and Bose ground states.

The interaction of spins of bosons we bring in the form

$$e^{-r_0/\xi_0}\sum_{k=1}^{N}\hat{\mathbf{s}}_{k+\delta}\cdot\hat{\mathbf{s}_k}\ . \tag{21.18}$$

Here it was introduced a factor e^{-r_0/ξ_0} with r_0 is being the mean distance between particles. For screened by magnetic field spins ξ_0 is to be assumed phenomenological and taken from experiment.

We establish the explicit form of Eq. (21.18). The growth of boson spin fluctuations should cancel term, Eq. (21.8), in the Hamiltonian. Therefore, for dense ($r_0 < \xi_0$) Bose gas there should be $\hat{\mathbf{s}}_{k+\delta} = -\hbar\mathbf{b}_k/M$.

The Hamiltonian of bosonized infinite anyon Coulomb gas with interaction of spins has a form

$$\hat{H} = \frac{1}{2M}\sum_{k=1}^{N}\left[(\mathbf{p}_k+\mathbf{A}_\nu(\mathbf{r}_k))^2+MV(\mathbf{r}_k)\right]$$
$$+\frac{1}{2}\sum_{k,j\neq k}^{N}\frac{e^2}{|\mathbf{r}_{kj}|}+\frac{\hbar(1-e^{-r_0/\xi_0})}{M}\sum_{k=1}^{N}\hat{\mathbf{s}}\cdot\mathbf{b}_k\ . \tag{21.19}$$

For anyon Coulomb gas with density parameter $r_s > 2$, where r_s is r_0 in Bohr radius a_B units, the approximate ground state energy per particle is expressed by Eq. (21.15). In our treatment we consider the bosonized fermions with $\nu = 1$. To become fermions, bosons should overcome the energy difference

$$\Delta_0^B = \frac{7(1-e^{-r_s/\xi_0})f^{4/3}(0,r_s)}{3c_{WC}^{2/3}r_s^{8/3}}\ , \tag{21.20}$$

the gap of superconductivity. Our approach in [24] corresponds to spinless or fully spin polarized fermions. One needs to have deal with normal, i.e., no spin polarized electron liquid. However, the accuracy of our calculations is lower than the difference of Tanatar and Ceperley data [27] for ground state energy for these both phases of electrons.

The Fig. 21.2 displays the PG boundary energy E_g (Fig. 11 from paper [31]), superconductivity gap energy $\Delta_0 = 4K_B\ T_c$, which was evaluated using the empirical formula $T_c = T_{c,max}[1-82.6(p-0.16)^2]$ with $T_{c,max} = 95\ K$ for Bi-2212 ($Bi_2Sr_2CaCu_2O_{8+\delta}$) compound, and energy gap calculated from Eq. (21.20) as function of doping p. As seen from this figure, our Δ_0^B has the same magnitude as experimental gap, but is qualitatively different from generally accepted "dome" like doping-temperature phase diagram. However, it is in accordance with Fig. 10

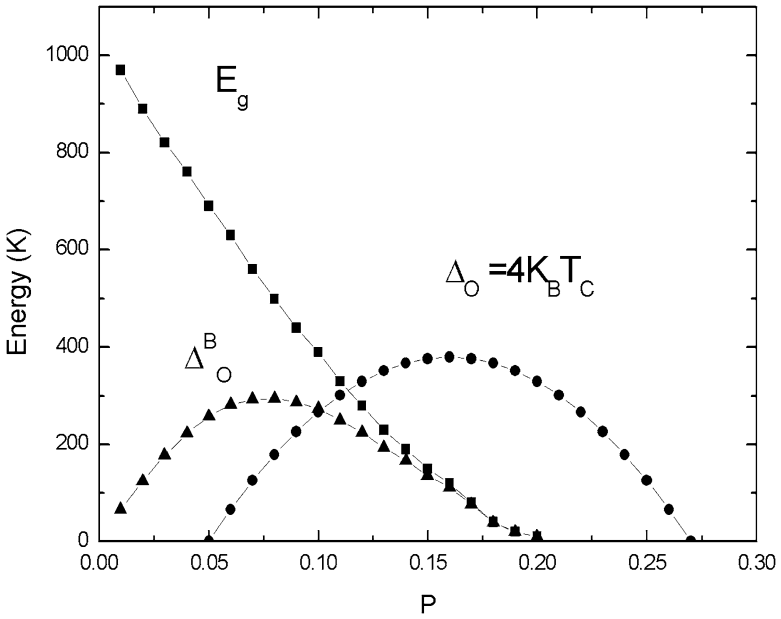

Fig. 21.2 The experimental PG E_g, superconductivity gap $\Delta_0 = 4K_B\ T_c$ (experiment for hole doped *Bi*-2212 compound), and calculated from formula Eq. (21.20) one for bosons Δ_0^B energies in Kelvin temperature (K) units as function of concentration of holes p

of paper [31] of Tallon and Loram and their conclusion that PG energy E_g up to $p_c \approx 0.19$ separates Bose-Einstein condensate into regions, where density of Cooper pairs is small and big (weak and strong superconductivity).

For phase diagram data of electron doped cuprates we use Ref. [32] for NCCO ($Nd_{2-x}Ce_xCuO_4$) and Ref. [33] for PCCO ($Pr_{2-x}Ce_xCuO_4$). It was shown there that $E_g/(k_BT^*) \approx 10$ for NCCO and $E_g/(k_BT^*) \approx 11$ for PCCO, therefore, we assume $E_g/(k_BT^*) \approx 10$ for both materials. For experimental superconductivity gap we also assume $\Delta_0/(k_BT_c) \approx 10$. Figure 21.3 shows the doping p dependence of experimental E_g, $\Delta_0 = 10k_BT_c$ and Δ_0^B calculated from Eq. (21.20) by using the above spacing constants of a and b for elementary structural cell. Comparing with Fig. 21.2, we see the same qualitative and quantitative result. More obvious is extension of our Δ_0^B to small values of p, while experimental Δ_0 starts with $p = 0.13$. However, absolute values of both superconductivity gaps of hole and electron doped materials are nearly equal.

21.5 Origin of Uemura Relation

In this section, following to Ref. [1], we describe the single boson origin of the phenomenological Uemura relation for $2D$ superconductors.

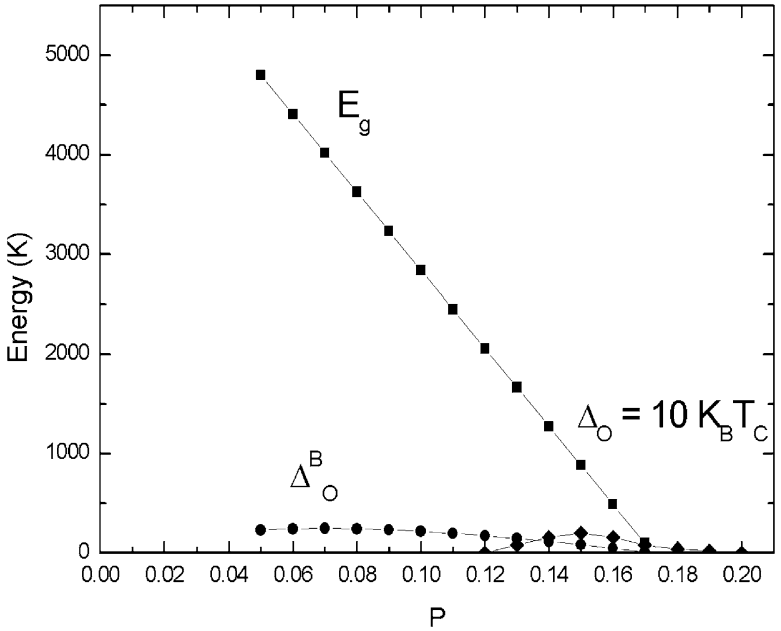

Fig. 21.3 The experimental PG E_g, superconductivity gap $\Delta_0 = 10K_B\,T_c$ (experiments for electron doped NCCO and PCCO compounds), and calculated from formula Eq. (21.20) one for bosons Δ_0^B energies in Kelvin temperature (K) units as function of concentration of electrons p

Now, it is widely accepted (see Ref. [34]) that the Uemura relation (UR), the linear dependence of T_c on concentration of charge carriers, originally observed in Refs. [35] and [36] for underdoped cuprate, bismuthate, organic, Chevrel-phase and heavy-fermion superconductors, survives also for extended class of other superconductors and has a fundamental universal character. There is no doubt that this relation plays an important role for the construction of the mechanism of superconductivity in these materials and can even be a source for discovering fundamental properties of the underlying physics. An experiment clearly relates the UR with $2D$ geometry of samples. Motivated by this observation, in Ref. [1] we investigated the possible role of the fermion bosonization, which is a result of the topology of $2D$, to the origin of UR.

The experimental doping dependence of r_0, mean distance between two holes, can be approximated by the relationship $r_0 \approx a/x^{1/2}$ (see Fig. 34 in Ref. [37]), where a is a lattice constant in the elementary structural plaquette for the CuO_2 $a-b$ plane of a copper oxide. Since in Ref. [1] the doping value denotes by the variable x, we keep this notation in this and another sections below. This relationship is derived in Ref. [37] for $La_{2-x}Sr_xCuO_4$ compound with $a \approx 3.8\mathring{A}$. This lattice constant a is the nearly same for other copper oxide compounds, thus it is also valid for investigated here compound $Bi_2Sr_2CaCu_2O_{8+\delta}$. It is worth to mention that $b \approx a$ for the lattice constant b of the same structural plaquette.

Applying the relationship $r_0 \approx a/x^{1/2}$, where $a \approx 3.8\text{Å}$, we do an estimate values of r_0, expressed in Bohr radius a_B unit ($r_s = r_0/a_B$), corresponding the doping interval $x_{c1} \leq x \leq x_{c2}$, where x_{c1} and x_{c2} are the first and second critical dopings in the doping-temperature phase diagram. One obtains $13.12 \leq r_s \leq 32.14$. For this interval of r_s we have obtained the expression, Eq. (21.15), for the ground state energy per particle of the Coulomb interacting anyon gas. It is expressed in Ry Rydberg energy unit and for large r_s equals to the energy of the classical $2D$ Wigner crystal [25], $E_{WC} = -c_{WC}^{2/3}/r_s$ with $c_{WC}^{2/3} = 2.2122$.

Taking into account from the previous section that the excited state of the $2D$ system is fermionic and the ground state is bosonic, one can write the explicit expression for an energy gap between these two states

$$\Delta(r_s) = \mathscr{E}(\nu = 1, r_s) - \mathscr{E}(\nu = 0, r_s) = \frac{7E_{WC}^2}{3c_{WC}^2} \,. \tag{21.21}$$

The meaning of this expression in that to become the fermion the boson should gain the energy $\Delta(r_s)$. Substituting in Eq. (21.21) the expression for E_{WC} and introducing the $2D$ density $n = 1/(\pi r_0^2)$ one derives

$$\Delta(n) = \frac{7\pi n a_B^2}{3c_{WC}^{2/3}} \,. \tag{21.22}$$

Since the critical temperature T_c is proportional to $\Delta(n)$, one can conclude that the $2D$ topology driven bosonization of fermions may explain the UR for variety superconductors, whose physics is quasi-two dimensional.

21.6 Experiment Implied Single Boson Elements of the Doping-Temperature Phase Diagram

Recently, Gomes et al. [9] have visualized the gap formation in NRs above the critical temperature T_c in the high-T_c superconductor $Bi_2Sr_2CaCu_2O_{8+\delta}$. It has been found that, as the temperature lowers, the NRs expand in the bulk superconducting state consisted of inhomogeneities. The fact that the size of the inhomogeneity [8] is close to the minimal size of the NR [9] leads to a conclusion that the superconducting phase is a result of these overlapped NRs. In the present section we reproduce the main results of Ref. [1], where it was performed the charge and percolation regime analysis of NRs and showed that at the first critical doping x_{c1}, when the superconductivity starts on, each NR carries the positive electric charge one in units of electron charge, thus we attributed the NR to a single hole boson, and the percolation lines connecting these bosons emerged. At the second critical doping x_{c2}, when the superconductivity disappears, our analysis demonstrated that the charge of each NR equals two. The origin of x_{c2} can be

Table 21.1 The doping x dependencies of NR charges

x	$(10\mathring{A}/r_0)^2$	$(13\mathring{A}/r_0)^2$	$\xi_{coh}(\mathring{A})$	$(\xi_{coh}/r_0)^2$	ξ_{coh}/r_0	N_{ob}
0.28	1.939	3.277	10	1.939	1.393	~ 1
0.22	1.524	2.575	10	1.524	1.235	~ 2
0.16	1.108	1.873	11	1.341	1.158	~ 3
0.14	0.969	1.638	12	1.396	1.182	~ 3
0.10	0.693	1.170	13	1.170	1.082	~ 6
0.05	0.346	0.585	17	1.000	1.000	
0.04	0.277	0.468	18	0.897	0.947	
0.02	0.139	0.234	20	0.554	0.744	

The doping x dependencies for $(10\,\mathring{A}/r_0)^2$, $(13\,\mathring{A}/r_0)^2$ at fixed $\xi_{coh} = 10\,\mathring{A}$ and $\xi_{coh} = 13\,\mathring{A}$, respectively, for the coherent length ξ_{coh}, the charge $(\xi_{coh}/r_0)^2$ and the percolation parameter ξ_{coh}/r_0 at this ξ_{coh} are presented. The values for the number N_{ob} of bosons surrounding every fermion are shown in the last column

understood by introducing additional normal phase hole fermions in NRs, whose concentration appearing above x_{c1} increases smoothly with the doping and breaks the percolation lines of bosons at x_{c2}. The last one resulted in disappearing the bulk bosonic property of the PG region, which explained the upper bound for existence of vortices in Nernst effect [38]. Since Ref. [9] has demonstrated the absence of NRs at the PG boundary one can conclude that along this boundary, as well as in x_{c2}, all bosons disappear.

The authors of Ref. [9] have visualized the NRs in the PG region of $Bi_2Sr_2CaCu_2O_{8+\delta}$ compound at fixed hole dopings $x = 0.12, 0.14, 0.16, 0.19, 0.22$. It has been determined that for $x = 0.16$ and $x = 0.22$ the minimal size of the NRs is $\xi_{coh} \approx 1 - 3$ nm. The estimated minimal size of NRs, ξ_{coh}, is about 1.3 nm in the superconducting phase [8] ($T_c = 84K$). Another notable result obtained in Ref. [8] is the observation of spatial localization of the doped charges. The charges are localized in the same area as NRs [8] with the same coherence length ξ_{coh}.

A principal part of our analysis in Ref. [1] has been the doping x dependence of the NR charge $(\xi_{coh}/r_0)^2$. We started with a case of zero temperature. The parameter ξ_{coh}/r_0 contained an essential information in our consideration. The factor $(\xi_{coh}/r_0)^2$ reduces to the expression $x(\xi_{coh}/a)2$ which has a simple physical meaning: it is a total electric charge of $(\xi_{coh}/a)^2$ number of plaquettes each of them having a charge x. On the other hand, the parameter ξ_{coh}/r_0 describes the average spatial overlapping degree of two or more holes by one NR. If $\xi_{coh}/r_0 > 1$ then all NRs will be in close contact to each other providing by this the bulk superconductivity in percolation regime.

In the Table 21.1 we outlined the doping x dependencies for the function $(\xi_{coh}/r_0)^2$ for fixed experimental values $\xi_{coh} = 10\mathring{A}$ (the minimal size of the NR) and $\xi_{coh} \approx 13\mathring{A}$ taken from Refs. [9] and [8], respectively, and for the function ξ_{coh} which fits $(\xi_{coh}/r_0)^2$ to $(10\mathring{A}/r_0)^2$ at $x = 0.28$ and for $x = 0.05$ provides $(\xi_{coh}/r_0)^2 \approx 1.0$. Numerical values of the ξ_{coh}/r_0 are also shown in the table.

As seen from Table 21.1, the charges $(10\text{Å}/r_0)^2$, $(13\text{Å}/r_0)^2$, and $(\xi_{coh}/r_0)^2$ vary continuously with the doping x. This is not surprising because they are functions of $r_0(x)$ and $\xi_{coh}(x)$. From the analysis at the first critical doping, $x_{c1} = 0.05$, it follows that the charge $(\xi_{coh}/r_0)^2$ of the visualized NR in Ref. [9] equals $+1$. So that, it corresponds to the charge of a single hole. Notice, at the critical doping $x_{c1} = 0.05$ the percolation parameter is given by $\xi_{coh}/r_0 = 1.0$. That means the whole sample is entirely covered with mini areas $\xi^2_{coh} = r^2_0$ contacting each other. It is unexpected that at the second critical doping, $x_{c2} = 0.28$, the charge of the visualized NR takes the value $+2$. This implies that at $\xi^2_{coh} = 2r^2_0$ one has a pair of holes inside the NR and, as a result, the superconductivity disappears completely. For $x_{c2} = 0.28$ we have $\xi_{coh}/r_0 > 1.0$, so that the charge conductivity of the fermions still remains.

Notice, that there are no particles in the nature with the fractional charge, except the quasiparticles which can be produced by many-body correlations like in the fractional quantum Hall effect [21]. Hence, the problem of the presence of the extra fractional charge inside the NR has to be solved yet. We remind [8, 9] that PG visualized NRs constitute the bulk superconductivity phase below the critical temperature T_c, and therefore, they are a precursor for that phase. This implies undoubtedly that the NRs represent bosons at least. At $x_{c1} = 0.05$ one has the charge $(\xi_{coh}/r_0)^2 = 1$, so that one may conjecture that the NR represents just a boson localized in the square box ξ^2_{coh}.

For $x > 0.05$ the charge $(\xi_{coh}/r_0)^2$ has an additional to $+1$ fractional part. We assign the last one to the fractional part of the charge of fermion. Thus the total charge $(\xi_{coh}/r_0)^2$ of the NR includes the charge $+1$ of the boson and the fractional charge of the fermion. However, as it was mentioned above, the fractional charge cannot exist. Therefore, we take the number N_{ob} of NRs to be equaled to the inverse value of the fractional part to form a charge $+1$ of the fermion. As a result, we obtain one fermion surrounding by N_{ob} bosons. T he values of N_{ob} are outlined in the last column of the Table 21.1.

The NRs introduced in such a manner allow to understand clearly the evolution of the fermions in the whole range $0.05 \leq x \leq 0.28$ of doping and to explain the origin of the second critical doping $x_{c2} = 0.28$. It is clear, as x increases, the number of fermions grows up inside the superconducting phase. By this, at x_{c2}, when the number of fermions becomes equal to the number of bosons, one has the breaking of the boson percolation lines, and, thus the superconductivity disappears.

The schematic single hole bosonic phase diagram for $Bi_2Sr_2CaCu_2O_{8+\delta}$ is depicted in the Fig. 21.4. The coloured zones indicate the percentage of the sample that is gapped at given temperature and doping. The solid lines correspond to the following observed temperatures: PG boundary T^* and onset temperature T_{onset} for Nernst effect signals taken from Ref. [38], and the critical temperature T_c from Ref. [9]. The extrapolation of the connection of T^* with the second critical doping, x_{c2}, is depicted by the dashed line. The yellow points correspond to fixed T_{onset} values from Ref. [38], and the blue points represent the temperature data for 50 % of gapped area of the sample from Ref. [9] measured at fixed dopings. The thin brown coloured solid line fits the blue points. The percentage for the gapped doping is calculated by

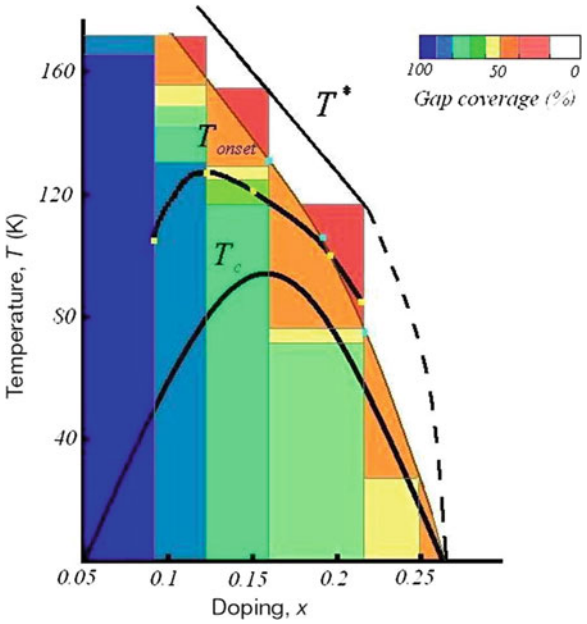

Fig. 21.4 Schematic single hole bosonic phase diagram for $Bi_2Sr_2CaCu_2O_{8+\delta}$

using the equation $(1-1/(N_{ob}+1))\cdot 100\,\%$ under the assumption that the NRs overlap each other. It is remarkable that T_{onset} line is substantially located in the brown coloured zones which means there is no bulk bosonic property above these zones.

The important qualitative issue, which leads from a result of [9] experiment, is in the following. The random positions in the real space of the observed pairs totally exclude any mechanism for the pair formation. Since occasionally positioned in this space coherent excitations (phonons, magnons or other quasi-particles), which create pairs, are problematic, if the system is homogenous. The last observation deduced from Gomes et al. paper is the fundamental argument for the justification of the single hole nature of the cuprate physics.

21.7 Non-Fermi Liquid Heat Conductivity and Entropy

In Ref. [4] we have tried to understand the non-Fermi liquid properties of the low-T heat conductivity, the specific heat and entropy of copper-oxides, mentioned in the introduction section, within a two-liquid model consisting from single boson and fermion holes.

In Fig. 21.5 we have plotted a WFL and a specific heat as function of temperature for compounds investigated experimentally in Refs. [11,13,14]. The experiment [11] shows $\kappa \sim T^{3.6}$ for normal state quasiparticles, while our dependence is $\kappa \sim T^4$ and connected with the specific heat dependence $c_1 \sim T^4$ for the Coulomb Bose gas (single bosons).

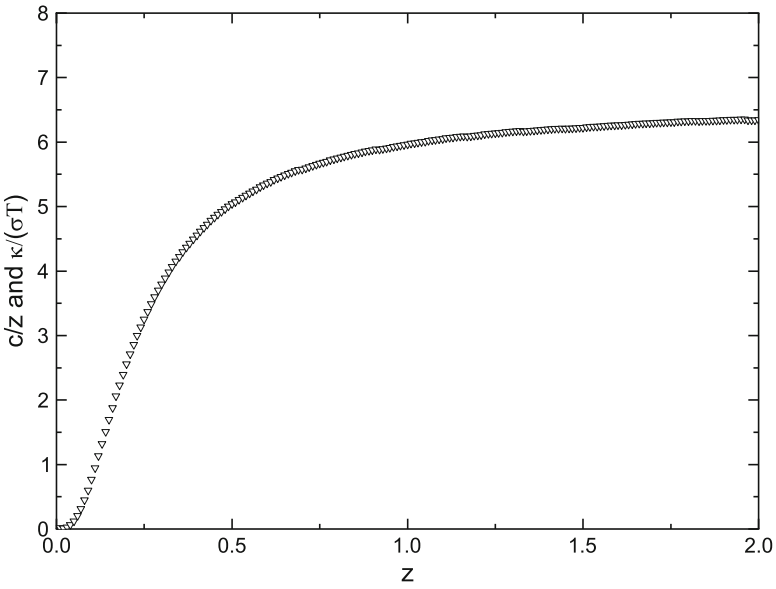

Fig. 21.5 The specific heat c/z and WFL $\kappa/(\sigma T)$ as function of z, where z is linearly proportional to temperature

For Lorentz ratio of the WFL we have derived in Ref. [4] the formula

$$L = L_0 \left[\frac{3.106}{t^{1/3}} \left(1 - \frac{t}{t_c} \right) + \frac{t}{t_c} \right], \tag{21.23}$$

where t and $t_c \approx 0.19$ (see Ref. [31]) are dopings, $L_0 = (\pi^2/3)(k_B/e)^2$ is the Fermi liquid Sommerfeld's value of the Lorentz ratio and the first term in square brackets originated from the single boson WFL $\kappa/(\sigma T) = 3.106 \cdot L_0/t^{1/3}$. In the Fig. 21.6 we displayed L/L_0 as function of t in comparison with its values measured for different cuprates. The good agreement for L/L_0 with experimental data is obvious.

In Ref. [4] we have also obtained the expression of the normal state entropy $\mathscr{S}$

$$\mathscr{S} = \frac{c_1}{4} \left(1 - \frac{T}{T^*} \right) + c_F \frac{T}{T^*}. \tag{21.24}$$

Here, c_F is the heat capacity for gas of fermions and T^* is a PG boundary temperature. The entropy as function of temperature at various dopings t is depicted in Fig. 21.7. Comparing calculated dependencies for $\mathscr{S}$ with experimental ones from Ref. [13], we see again the good agreement. As shown in [4], the nonlinear T dependence of the entropy $\mathscr{S}$ at small temperatures is related to the insulating ground state.

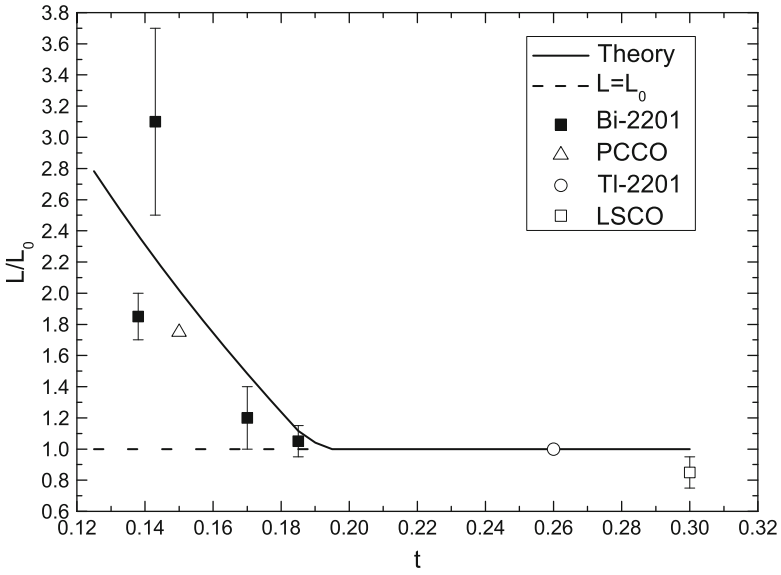

Fig. 21.6 The Lorentz ratio L/L_0 (Eq. (21.23)) vs. t (values for $t \geq 1$ are added artificially). Observed dots are from Ref. [12]

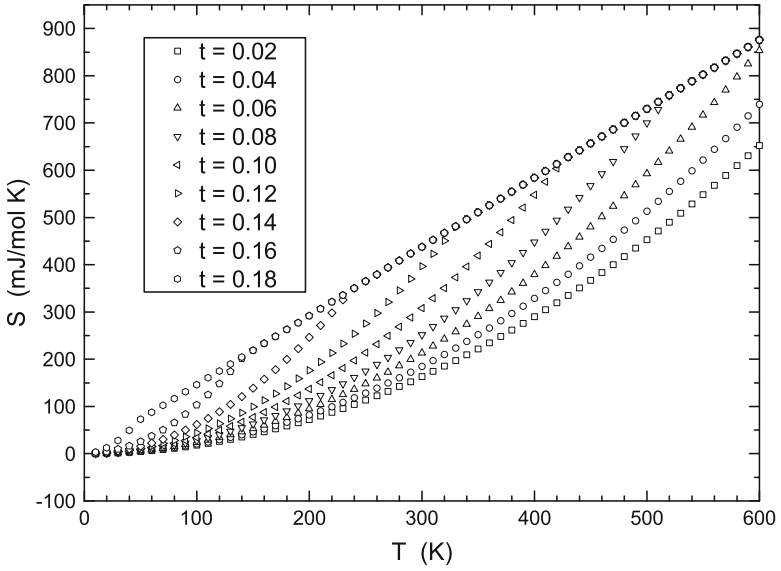

Fig. 21.7 The entropy $\mathscr{S}$ (Eq. (21.24)) vs. T at various t (values of $\mathscr{S}$ behind the crossing of linear and nonlinear parts of $\mathscr{S}$ are added artificially)

21.8 Conclusion

Summarizing the paper, we have succeeded in understanding the following constituents of the doping-temperature phase diagram of the hole doped copper oxides: (i) the first and second critical dopings have been a result of emergence and disappearance of the single hole boson percolation lines, respectively; (ii) the disappearance of the percolation lines leads to the end of the PG bulk bosonic property or to the end of Nernst effect signals; (iii) the fact that the PG boundary was a bound, where the single hole bosons disappear, confirmed by Ref. [9]. Our findings are consistent with the recent observation [39] of the superconducting phase consisted of the array of nanoclusters embedded in the insulating matrix and of percolative transition to this phase from the normal phase in $YBa_2Cu_3O_{6+\delta}$. Superconducting islands introduced in insulating background have been used for the interpretation of the superconductor-insulator transition in $Bi_2Sr_{2-x}La_xCaCu_2O_{8+\delta}$ compound [40].

We remind the possible scenario for the origin of PG phase in the copper-oxides. In Ref. [2] we pointed out that the PG boundary exactly coincides in the experiment with the structural phase transition line, where the symmetry of the sample structure changes. However, the structural phase transition induces in a system the mechanical strain. This mechanical strain changes the magnetic phase transition, existing in a system, from the second order into the first order one. However, this first order phase transition is close to the second order one. This effect calls in the literature as a striction. The phase transition of single bosons into fermions, discussed in Sect. 21.4, is possibly obeyed by a striction. Therefore, transition peaks in the specific heat increment are washed out in the underdoping regime of cuprates [13]. On the other hand, the first order phase transition accepts the existence of the meta-stable phase. We believe that PG phase of cuprates is the meta-stable phase of single bosons, which effective spins are fluctuating and interacting with each others. At the PG boundary this interaction entirely destroys bosons, transforming them into fermions.

At the end, we predict the existence of not percolated single bosons at low-T before the first critical doping x_{c1} in the doping-temperature phase diagram of copper-oxides. For these dopings, a scanning tunneling microscopy measurement may probe the same picture for minimal size NRs as for PG region, close to PG boundary. The Bose statistics of these particles may be experimentally detected by some methods described in Ref. [41]. These methods might be also applied to detect the fermion statistics of particles, which is the main hypotheses of the present treatment, outside of the PG boundary.

References

1. Abdullaev B, Park C-H, Musakhanov MM (2011) Phys C 471:486
2. Abdullaev B (2006) Implicit anyon or single particle boson mechanism of HTCS and pseudogap regime. In: Ling AV (ed) Trends in boson research. Nova Science Publisher, Inc., New York, pp 139–161
3. Abdullaev B, Park C-H (2006) J Korean Phys Soc 49:S642
4. Abdullaev B, Park C-H, Park K-S cond-mat/0703290
5. Timusk N, Statt B (1999) Rep Prog Phys 62:61
6. Howald C, Fournier P, Kapitulnik A (2001) Phys Rev B 64:100504(R)
7. McElroy K et al (2005) Science 309:1048
8. Pan SH et al (2001) Nature 413:282
9. Gomes KK et al (2007) Nature 447:569
10. Koizumi H (2010) J Phys A 43:354009
11. Hill RW, Proust C, Taillefer L, Fournier P, Greene RL (2001) Nature 414:711
12. Proust C, Behnia K, Bel R, Mande D, Vedeneev SI (2005) Phys Rev B 72:214511
13. Loram JW, Mirza KA, Cooper JR, Liang WY (1993) Phys Rev Lett 71:1740
14. Loram JW, Luo J, Cooper J, Liang W, Tallon J (2001) J Phys Chem Solids 62:59
15. Luo JL, Loram JW, Xiang T, Cooper JR, Tallon JL cond-mat/0112065
16. Leinaas JM, Myrheim J (1977) Nuovo Cimento Soc Ital Fis B 37:1
17. Wilczek F (1982) Phys Rev Lett 48:1144
18. Wilczek F (1990) Fractional statistics and anyon superconductivity. World Scientific, Singapore
19. Lerda A (1992) Anyons. Springer, Berlin
20. Dunne G, Lerda A, Sciuto S, Trugenberger CA (1992) Nucl Phys B 370:601
21. Laughlin RB (1987) In: Prange RE, Girvin SM (eds) The quantum Hall effect. Springer, New York
22. Wu Y-S (1984) Phys Rev Lett 53:111 (Erratum ibid 53:1028 (1984); Laughlin RB (1988) Phys Rev Lett 60:2677
23. Comtet A, McCabe J, Ouvry S (1991) Phys Lett B 260:372
24. Abdullaev B, Roessler U, Musakhanov M (2007) Phys Rev B 76:075403
25. Bonsal L, Maradudin AA (1977) Phys Rev B 15:1959
26. Rajagopal AK, Kimball JC (1977) Phys Rev B 15:2819
27. Tanatar B, Ceperley DM (1989) Phys Rev B 39:5005
28. De Palo S, Conti S, Moroni S (2004) Phys Rev B 69:035109
29. Attaccalite C, Moroni S, Gori-Giorgi P, Bachelet GB (2002) Phys Rev Lett 88:256601; (2003) Phys Rev Lett 91:109902(E)
30. Landau LD, Lifshitz EM (1977) Quantum mechanics, non-relativistic theory. Pergamon Press, Oxford, § 65
31. Tallon JL, Loram JW (2001) Phys C 349:53
32. Onose Y, Taguchi Y, Ishizaka K, Tokura Y (2004) Phys Rev B 69:024504
33. Zimmers A et al (2005) Europhys Lett 70:225
34. Zaanen J (2004) Nature 430:512
35. Uemura YJ et al (1989) Phys Rev Lett 62:2317
36. Uemura YJ et al (1991) Phys Rev Lett 66:2665
37. Kastner MA, Birgeneau RJ, Shirane G, Endoh Y (1998) Rev Mod Phys 70:897
38. Wang Y, Li L, Ong NP (2006) Phys Rev B 73:024510
39. Gavrilkin SY, Ivanenko OM, Martovitskii VP, Mitsen KV, Tsvetkov AY (2009) Proceedings of M2S-IX 2009, Tokyo, Arxiv: 0909.0612
40. Oh S, Crane TA, Van Harlingen DJ, Eckstein JN (2006) Phys Rev Lett 96:107003
41. Stern A (2008) Anyons and the quantum Hall effect – a pedagogical review. Ann Phys 323:204

Index

R. Egger et al. (eds.), *Low-Dimensional Functional Materials*, NATO Science for Peace and Security Series B: Physics and Biophysics, DOI 10.1007/978-94-007-6618-1,